Simulations of Cosmological Structure Formation with Nonrelativistic Scalar Fields

Dissertation

zur Erlangung des mathematisch-naturwissenschaftlichen Doktorgrades
„Doctor rerum naturalium“
der Georg-August-Universität Göttingen

im Promotionsstudiengang Physik
der Georg-August University School of Science (GAUSS)

vorgelegt von

Benedikt Eggemeier

aus Ibbenbüren

Göttingen, 2022

Betreuungsausschuss:

Prof. Dr. Jens Niemeyer
Institut für Astrophysik und Geophysik
Georg-August-Universität Göttingen

Prof. Dr. David J. E. Marsh
Department of Physics
King’s College London

Prof. Dr. Steffen Schumann
Institut für Theoretische Physik
Georg-August-Universität Göttingen

Mitglieder der Prüfungskommission:

Referent:	Prof. Dr. Jens Niemeyer Institut für Astrophysik und Geophysik Georg-August-Universität Göttingen
Korreferent:	Prof. Dr. David J. E. Marsh Department of Physics King’s College London
2. Korreferent:	Prof. Dr. Günter Sigl II. Institut für Theoretische Physik Universität Hamburg

Weitere Mitglieder der Prüfungskommission:

Prof. Dr. Laura Covi
Institut für Theoretische Physik
Georg-August-Universität Göttingen

Prof. Dr. Stefan Dreizler
Institut für Astrophysik und Geophysik
Georg-August-Universität Göttingen

Prof. Dr. Ariane Frey
II. Physikalisches Institut
Georg-August-Universität Göttingen

Prof. Dr. Steffen Schumann
Institut für Theoretische Physik
Georg-August-Universität Göttingen

Tag der mündlichen Prüfung: 23.05.2022

Abstract

Nonrelativistic, self-gravitating scalar fields are of current interest in several scenarios of cosmological structure formation. This includes the gravitational clustering of dark matter in the late-time Universe which can be described by a class of nonrelativistic scalar fields, as well as the gravitational fragmentation of the inflaton field after the end of inflation. A well-motivated and promising dark matter candidate is the QCD axion. Large axion density fluctuations can be produced in the post-inflationary scenario leading to the gravitational formation of highly compact objects known as axion miniclusters. They are expected to exist as substructures within the Milky Way at the present time which is of significance for axion detection experiments. The scalar inflaton field is generally assumed to be responsible for a phase of rapid, accelerated expansion in the very early Universe. Subsequently, the Universe may have passed through a long epoch of matter-dominated expansion during which initially small inflaton density perturbations grow and eventually collapse into gravitationally-bound structures. There exists a strong analogy in the nonlinear evolution of the studied scalar field for these two different eras of structure formation. Accordingly, the same numerical methods can be applied to explore the phenomenology of gravitationally-bound objects in both scenarios. In this thesis, we make use of large numerical simulations to study the post-inflationary gravitational clustering of the inflaton field and the gravitational collapse of axion density fluctuations into axion miniclusters. Our simulation results provide the first insights into the mass distribution and morphology of axion miniclusters and reveal the first quantitative predictions of gravitationally-bound inflaton structures in the very early Universe. While the existence of axion miniclusters directly affects searches for the axion, we show that a period of structure formation in the post-inflationary Universe can lead to the production of primordial black holes and to the generation of a stochastic gravitational wave background that might be detectable by future experiments.

Contents

List of Figures

List of Tables

List of Acronyms

ΛCDM	Λ Cold Dark Matter
ALP	Axion-Like Particle
AMR	Adaptive Mesh Refinement
BBN	Big Bang Nucleosynthesis
CDM	Cold Dark Matter
CIC	Cloud-In-Cell
CMB	Cosmic Microwave Background
CP	Charge-Parity
CWF	Classical Wave Function
DFT	Discrete Fourier Transform
FDM	Fuzzy Dark Matter
FFT	Fast Fourier Transform
FLRW	Friedmann-Lemaître-Robertson-Walker
HMF	Halo Mass Function
IHMF	Inflaton Halo Mass Function
ISMF	Inflaton Star Mass Function
LPT	Lagrangian Perturbation Theory
MC	Minicluster
MCH	Minicluster Halo
MC-HMF	Minicluster Halo Mass Function
NFW	Navarro-Frenk-White

PBH	Primordial Black Hole
PM	Particle-Mesh
PP	Particle-Particle
PQ	Peccei-Quinn
PS	Press-Schechter
PS-HMF	Press-Schechter Halo Mass Function
QCD	Quantum Chromodynamics
SGWB	Stochastic Gravitational Wave Background
SP	Schrödinger-Poisson
SVT	Scalar-Vector-Tensor
WDM	Warm Dark Matter
WKB	Wentzel-Kramers-Brilloin
ZA	Zel’dovich Approximation

Chapter 1

Introduction

The aim of cosmology is to describe the evolution of our Universe, starting from its initial state usually referred to as "Big Bang" to the formation of large-scale structures such as galaxies. Since the beginning of the last century, there has been enormous experimental progress that has bit by bit unveiled the composition of the Universe throughout most of its history. After Edwin Hubble's pioneering discovery that the Universe is expanding [1], more and more observations have completed the picture and eventually have led to the formulation of the Standard Model of Cosmology. All visible objects in the Universe consist of ordinary, baryonic matter which constitutes only 5% of the total energy budget of the Universe [2]. According to the Standard Model of Cosmology, the dominant contributions come from so far unidentified forms of matter and energy that are called *dark matter* and *dark energy*, respectively. While the latter amounts to about 70% of the total energy content and is responsible for the observed accelerated expansion of the Universe at present time, 25% of the Universe is made of dark matter, which plays a crucial role in the process of structure formation.

The first evidence for the existence of dark matter dates back to the 1930s. Observing galaxies orbiting the Coma cluster, Fritz Zwicky discovered discrepancies in their orbital velocities which he could only explain with an additional nonbaryonic matter component [3]. Before the end of the 20th century, further evidence was gathered, for example from galaxy rotation curves [4–6] and from the first measurements of the anisotropies in the *Cosmic Microwave Background* [7, 8]. In the past two decades, observations from ambitious experiments with increasing sensitivity could further confirm the dark matter hypothesis. Additional evidence for dark matter on galactic scales comes from gravitational lensing of distant galaxies [9], X-ray measurements [10], and the Bullet cluster [11]. Precise estimates of the energy content of the Universe were obtained from missions probing the Cosmic Microwave Background in great detail [2, 12]. The most recent results demonstrate that the dark matter density exceeds the density of baryons by a factor of five (see above). Nevertheless, the nature of dark matter still remains a mystery. It is known that dark matter has to interact very weakly with ordinary matter, mainly through the gravitational force. Moreover, the fact that dark matter still exists today requires it to be stable on time scales of the age of the Universe.

To explain the observed large-scale distribution of galaxies necessitates the dark matter to be cold [13]. It consists of particles that have become nonrelativistic before the onset of structure formation. This is in contrast to dark matter candidates with higher particle velocities that suppress the growth of structures on small scales, however, such models are highly constrained by observations [14, 15]. Admittedly, there are some observations that seem to contradict the cold dark matter predictions on small scales [16–21]. It is a controversial issue whether the small-scale challenges actually exist or if they can be resolved by a deeper understanding of astrophysical processes [22].

A large number of cold dark matter candidates have been proposed to date. Prominent particle candidates are weakly interacting massive particles, which have been extensively searched for in direct and indirect detection experiments [23]. They have not been detected, though, which is why other dark matter candidates such as primordial black holes [24] and axions [25] are of increasing interest. The latter include the QCD axion and axion-like particles that are motivated by particle physics and string theory, respectively. Since they are in general light and stable scalar particles and can be described as a classical, nonrelativistic field, they are perfectly suited candidates for cosmological structure formation. A characteristic feature of any scalar field with the aforementioned properties is that wave effects are induced on length scales of their de Broglie wavelength. This leads to fascinating phenomena such as wave interference patterns and the formation of gravitationally-bound solitonic cores. A popular model of axion-like particles that has received much attention in the last few years is *fuzzy dark matter* [26]. It assumes a particle mass of $m \sim 10^{-22}$ eV and does not couple to itself or to any other particles, except for gravitational interactions. For such masses the prominent cores can become as large as several kpc, forming in the centre of galaxies. Originally introduced to provide a solution to the small-scale challenges of cold dark matter, fuzzy dark matter can successfully recover the distribution of standard cold dark matter on super-galactic scales.

In models of structure formation with QCD axions, wave phenomena arise only at much smaller length scales due to their larger particle mass. The most striking feature in this cosmological scenario is instead associated with the possible generation of large axion density inhomogeneities in the early Universe. These overdensities start to collapse already in the radiation-dominated epoch to form gravitationally-bound objects called *axion miniclusters* [27–30]. In the course of time, the miniclusters evolve into large-scale dark matter halos but it is expected that a significant fraction of axion miniclusters survive the gravitational evolution and exist as substructures at the present day. The clumping of axion dark matter into such highly compact objects establishes different possibilities for axion searches. A central quantity for minicluster searches is their predicted distribution within the Milky Way which requires the execution of large numerical simulations.

The formation of gravitationally-bound structures is not restricted to the late-time Universe but can also take place in the earliest moments of our Universe during the so-called primordial dark age.[1] It is generally assumed that the Universe passed through a period of rapid, accelerated expansion during its first instants. This theory is called *inflation* [31–34] and provides answers not only to the observed flatness and large-scale isotropy of our Universe. Importantly, inflation can also explain the origin of the initial density fluctuations which have subsequently developed into the large-scale structure of the Universe today. It is presumably impossible to probe the high energy scales of inflation directly, and inflation itself is largely unconstrained by observations, which is why a range of different models have been proposed since the 1980s. The most basic assumption is that the extensive expansion during inflation is driven by a real scalar field called the inflaton. In a broad class of scenarios, inflation can be followed by an extended period of effectively matter-dominated expansion. During this era, initially small inflaton overdensities start to grow on subhorizon scales and gravitationally collapse into bound objects [35, 36]. Recently, it has been discovered that this phase of gravitational structure formation during the primordial dark age is very similar to cosmological structure formation with axion-like particles [37]. Hence, the same already existing numerical methods can be applied to shed some light on the very early Universe.

In this thesis, we make use of this analogy to study the formation of gravitational structures in two cosmological scenarios of interest by means of large numerical simulations. This involves the gravitational evolution of axion dark matter and the associated formation of axion miniclusters, as well as the gravitational fragmentation of the inflaton field in the matter-dominated, post-inflationary universe. The simulations presented in this thesis provide detailed insights into the mass distribution and structure of axion miniclusters, and reveal the first quantitative predictions for gravitationally-collapsed *inflaton halos* in the matter-dominated epoch following inflation. Applying numerical methods developed originally in the context of axion-like particles, we confirm the existence of solitonic cores that form after the end of inflation. By analogy with boson stars, we denote them *inflaton stars* [38]. We show that they might become gravitationally unstable and collapse into primordial black holes. Finally, the early-Universe simulations

---

[1] This should not be confused with an epoch in the late-time Universe, normally simply termed the dark ages, that is followed by the formation of the first galaxies.

are extended to include the computation of a stochastic gravitational wave background that is produced from the gravitational fragmentation of the inflaton field.

Outline

This thesis is structured as follows. In the remainder of this chapter, we cover the necessary background about the Standard Model of Cosmology, the physics of the early Universe and axion dark matter. This includes a discussion of the successes and challenges of the cosmological Standard Model, as well as an introduction to the concept of inflation and the processes that can occur afterwards. Furthermore, an overview of the origin of the axion and its production mechanisms is provided.

Chapter 2 then deals with the growth and collapse of density perturbations. Understanding the origin of the initially tiny fluctuations requires the treatment of cosmological perturbations. Supplemented by Appendices A and B, we collect the relevant equations of motion in Section 2.1 and apply them to the perturbed inflaton field in Section 2.2. Afterwards, the gravitational evolution and growth of density perturbations on subhorizon scales are considered. Eventually, linear perturbation theory breaks down, necessitating other methods such as numerical N-body simulations to study the gravitational collapse of perturbations. Chapter 3 focuses on structure formation with self-gravitating, nonrelativistic scalar fields. We derive the evolution equations, valid for both the QCD axion and the inflaton in our scenarios of interest, and discuss the formation of solitonic cores. Moreover, we give a brief summary of different simulation schemes.

We present simulation results from the formation of axion miniclusters in Chapter 4. Beforehand, we review the spherical collapse model that was originally used to describe the collapse of axion overdensities into miniclusters and we examine the early evolution of the axion field resulting in these overdensities. After a discussion of the simulation results in Section 4.3 based on work published in Ref. [39], the relevance of axion miniclusters for the detection of axion dark matter is portrayed. We turn to the post-inflationary Universe and the gravitational collapse of inflaton fluctuations into bound objects in Chapter 5. The presented work is largely based on Refs. [40, 41]. Beginning with an overview of the post-inflationary dynamics and a derivation of the inflaton density power spectrum on subhorizon scales, Section 5.2 summarises the setup for structure formation simulations in the early matter-dominated era. We present N-body simulations of this epoch in Section 5.3. Extending the simulations to much smaller length scales to achieve sufficient spatial resolution, the formation of solitonic cores is studied in Section 5.4. Also, we describe in Section 5.5 how an associated stochastic gravitational wave background can be computed and discuss first results. Finally, we conclude this thesis in Chapter 6 with a summary of our results and a discussion of possible directions for future research.

As indicated above, most of the results of this thesis[2] were published in Refs. [39–41]. Section 4.3 follows and extends the original publication titled "First Simulations of Axion Minicluster Halos" [39] and published in *Physical Review Letters*. The author of this thesis performed the analysis of the already existing N-body simulation data and produced all of the figures in Ref. [39], except for Fig. 4.3 in Section 4.3 which corresponds to Fig. 1 in Ref. [39]. The N-body simulations were carried out by the third author of Ref. [39] who also created this particular figure. The author of this thesis wrote large parts of the publication and communicated with the referees in the peer-review process. A large portion of Sections 5.2 to 5.4 are directly taken from the original articles "Formation of inflaton halos after inflation" [40] and "Gravitational collapse in the postinflationary Universe" [41], both published in *Physical Review D*. The author of this thesis was mainly responsible for both publications. He created the setup for the simulations, performed them, produced all of the figures in Refs. [40, 41], wrote the entire draft in both cases, and communicated with the referees in the peer-review process. The numerical simulations involved some code development by the author of this thesis. In particular, the simulations reported in Ref. [41] required the implementation of the so-called classical wave approximation (see Section 3.2.3) within the cosmology code AxioNyx [43]. This process was assisted by the second author of Ref. [41].

1.1 The Standard Model of Cosmology

Modern cosmology has its origin in 1915 when Albert Einstein completed the theory of general relativity. Only a few years later Edwin Hubble discovered that our Universe is actually expanding [1]. Together with the cosmological principle [44], which assumes that the Universe is homogeneous and isotropic on sufficiently large scales, this led to the foundation of the Standard Model of Cosmology. Its fundamental concepts and composition, as well as its successes and unresolved problems, are briefly summarised in this section.

1.1.1 The FLRW Universe

The fundamental principle of general relativity is that gravity results from the curvature of spacetime. Spacetime itself is not static. Instead, its geometry is affected by the energy

---

[2] There also exists a publication by the author of this thesis about the formation of solitonic cores in the centre of axion miniclusters [42] that are usually referred to as "axion stars" in this context. It is not part of this thesis since most of the work was done prior to the starting date of the doctoral studies.

and momentum of the matter contained within it. The relationship between the curvature of spacetime and matter is given by the Einstein field equations[3] [45]

$$G_{\mu\nu} = R_{\mu\nu} - \frac{1}{2}Rg_{\mu\nu} = 8\pi G T_{\mu\nu}\,, \tag{1.1}$$

where spacetime is expressed by the metric tensor $g_{\mu\nu}$ and G denotes the gravitational constant. The left-hand side consisting of the Ricci tensor $R_{\mu\nu}$ and the Ricci scalar $R = g^{\mu\nu}R_{\mu\nu}$, where $g^{\mu\nu}$ is the inverse of $g_{\mu\nu}$, is called the Einstein tensor $G_{\mu\nu}$. It describes the geometry of spacetime which responds to the matter content expressed by the stress-energy tensor $T_{\mu\nu}$ on the right-hand side. The Ricci tensor can be written as

$$R_{\mu\nu} = \partial_\mu \Gamma^{\sigma}{}_{\nu\sigma} - \partial_\nu \Gamma^{\sigma}{}_{\mu\sigma} + \Gamma^{\sigma}{}_{\mu\lambda}\Gamma^{\lambda}{}_{\nu\sigma} - \Gamma^{\sigma}{}_{\nu\lambda}\Gamma^{\lambda}{}_{\mu\sigma}\,, \tag{1.2}$$

where the Christoffel connection $\Gamma^{\lambda}{}_{\mu\nu}$ is defined as [46]

$$\Gamma^{\lambda}{}_{\mu\nu} = \frac{1}{2}g^{\lambda\rho}\left(\partial_\mu g_{\nu\rho} + \partial_\nu g_{\rho\mu} - \partial_\rho g_{\mu\nu}\right)\,. \tag{1.3}$$

Assuming homogeneity and isotropy, the spacetime of our Universe on large scales can be described by the Friedmann-Lemaître-Robertson-Walker (FLRW) metric [47–50]

$$\mathrm{d}s^2 = g_{\mu\nu}\mathrm{d}x^\mu \mathrm{d}x^\nu = -\mathrm{d}t^2 + a^2(t)\left[\frac{\mathrm{d}r^2}{1-Kr^2} + r^2\mathrm{d}\Omega^2\right]\,, \tag{1.4}$$

where the scale factor $a(t)$, which is normalised to $a(t_0) = a_0 = 1$ at the present time t_0, parameterises the expansion of space. The parameter K accounts for the spatial curvature of the Universe and $K^{-1/2}$ has the dimension of distance. This has a value of $K > 0$ in a closed universe, $K < 0$ in an open universe and $K = 0$ for a flat universe. Furthermore, $\mathrm{d}\Omega^2$ is the line element of a unit sphere and r is the radial coordinate in *comoving* units. While the *physical* distance d_{phys} between two points in space increases due to the expansion of space, the comoving distance d_{comv} is defined to remain constant. They are directly related to each other via the scale factor as $d_{\mathrm{phys}} = a(t)d_{\mathrm{comv}}$. From an observational point of view, it is useful to express the scale factor $a(t)/a_0 = (z+1)^{-1}$ in terms of the *redshift* z which measures the difference in the wavelength of light between its emission at time t and its observation at the present time t_0. Thus, the redshift can be used as a measure of cosmological time.

On large scales, the stress-energy tensor that appears in Eq. (1.1) takes the form of a perfect fluid [51]

$$T^{\mu}{}_{\nu} = (\rho + p)u^\mu u_\nu + p\delta^\mu_\nu\,, \tag{1.5}$$

---

[3] Throughout this thesis, we will use natural units where $c = \hbar = 1$, unless stated otherwise.

which characterises the matter content by the density ρ, the pressure p and the normalised 4-velocity u_μ of the fluid. In the local rest frame of the fluid, $u^\mu u_\mu = g_{\mu\nu}u^\mu u^\nu = -1$ implies that $u^0 = (1,0,0,0)$ and $u_0 = (-1,0,0,0)$. Thus, $T^0_{\ 0} = -\rho$, $T^0_{\ i} = T^i_{\ 0} = 0$ and $T^i_{\ j} = p\delta^i_j$ which illustrates that a perfect fluid is isotropic in the local rest frame. Assuming that both ρ and p do not vary spatially, the form of Eq. (1.5) is therefore consistent with the cosmological principle. Inserting the stress-energy $T^\mu_{\ \nu} = \mathrm{diag}(-\rho, p, p, p)$ of a perfect fluid together with the FLRW metric into the Einstein Eq. (1.1), and noting that the rest frame of the fluid coincides with the comoving coordinates in the FLRW metric, the Einstein equations yield the evolution equations[4] for the scale factor known as the Friedmann equations [47],

$$H^2 = \frac{8\pi G}{3}\rho - \frac{K}{a^2}\,, \tag{1.6}$$

$$\frac{\ddot{a}}{a} = -\frac{4\pi G}{3}(\rho + 3p)\,. \tag{1.7}$$

In the first Friedmann equation, the Hubble parameter $H \equiv \dot{a}/a$ was introduced which is a meaningful physical scale in an expanding universe since its inverse determines both the current age and size of a universe.

Demanding conservation of energy and momentum, the time component ($\nu = 0$) of the conservation equation $\partial_\mu T^\mu_{\ \nu}$ gives the continuity equation

$$\dot{\rho} + 3H(\rho + p) = 0\,. \tag{1.8}$$

Introducing the equation of state parameter $w \equiv p/\rho$ and assuming that it does not change with time, the continuity equation is solved by

$$\rho(a) = \rho_0 \left(\frac{a}{a_0}\right)^{-3(1+w)}\,, \tag{1.9}$$

where $\rho_0 = \rho(a_0)$. For a nonrelativistic matter component ($w = 0$) the energy density scales as $\rho_{\mathrm{mat}} \sim a^{-3}$, for radiation ($w = 1/3$) we have $\rho_{\mathrm{rad}} \sim a^{-4}$ and the energy component ρ_Λ of a cosmological constant Λ ($w = -1$) is constant [52]. This means that the evolution of a universe consisting of these three components can be described by a series of three different epochs. At early times the universe was radiation-dominated, followed by an epoch of matter-domination and eventually, the energy density of the cosmological constant dominates the evolution. Defining the density parameters at the present time t_0 as [53]

$$\Omega_{i,0} \equiv \frac{\rho_i(t_0)}{\rho_{\mathrm{crit}}} = \frac{8\pi G}{3H_0^2}\rho_i(t_0)\,, \quad \text{with} \quad \rho_{\mathrm{crit}} = \frac{3H_0^2}{8\pi G}\,, \tag{1.10}$$

---

[4] Throughout this thesis, a dot denotes a derivative with respect to physical time t.

the energy density on the right-hand side of the Friedmann Eq. (1.6) can be written as

$$\rho = \rho_{\text{crit}} \left(\Omega_{\Lambda,0} + \Omega_{K,0} a^{-2} + \Omega_{m,0} a^{-3} + \Omega_{r,0} a^{-4} \right) , \tag{1.11}$$

where the energy density of curvature $\rho_K = -3K/(8\pi G a^2)$ was introduced to absorb the curvature term in Eq. (1.6) into ρ. This allows us to write the first Friedmann Eq. (1.6) as

$$1 - \Omega_K = \Omega_m + \Omega_r + \Omega_\Lambda , \quad \text{or} \quad 1 - \frac{\Omega_{K,0}}{a^2} = \frac{\Omega_{0,m}}{a^3} + \frac{\Omega_{r,0}}{a^4} + \Omega_{\Lambda,0} , \tag{1.12}$$

where the curvature density parameters can in principle be either positive or negative. However, observations have revealed that $\Omega_{K,0} = 0.0007 \pm 0.0019$ [2] which means that we live in a flat universe. Thus, the spatial curvature term in the first Friedmann Eq. (1.6) can be omitted and the FLRW metric for a flat universe simplifies to

$$\mathrm{d}s^2 = -\mathrm{d}t^2 + a^2(t) [\mathrm{d}x^2 + \mathrm{d}y^2 + \mathrm{d}z^2] . \tag{1.13}$$

Often it is beneficial to use the *conformal* time τ defined by $\mathrm{d}\tau = \mathrm{d}t/a$ instead of the ordinary time coordinate t.[5] Then, the flat FLRW metric can be expressed in terms of the Minkowski metric $\eta_{\mu\nu} = \mathrm{diag}(-1, 1, 1, 1)$ as

$$\mathrm{d}s^2 = a^2(\tau) \eta_{\mu\nu} \mathrm{d}x^\mu \mathrm{d}x^\nu = a^2(\tau) [-\mathrm{d}\tau^2 + \mathrm{d}x^2 + \mathrm{d}y^2 + \mathrm{d}z^2] . \tag{1.14}$$

1.1.2 Successes of the ΛCDM Model and Unresolved Problems

Cosmology is not restricted to describing the evolution of the Universe on large length scales: it also makes predictions about the thermal history and composition of the Universe as well as about the formation of gravitationally-bound structures. Starting from the discovery that our Universe is expanding, an increasing number of observations and measurements have improved our understanding of the Universe. Currently, the favoured description of our Universe is given by the so-called ΛCDM model which assumes that it consists largely of a dark energy component denoted Λ and cold dark matter (CDM).

The cosmological constant Λ was originally introduced by Albert Einstein to enforce a static universe and again abandoned after Hubble's observation that the Universe is actually expanding. It became of relevance again when supernovae observations indicated an *accelerated* expansion of space at the present time [54, 55]. This could only be explained by the existence of some unknown form of dark energy which dominates the Universe today. Although other attempts to explain this observed phenomenon have been suggested [56], the cosmological constant remains the most popular.

---

[5] Throughout this thesis, a prime denotes a derivative with respect to conformal time τ.

Table 1.1 | Selection of ΛCDM parameters and their 68% error intervals as determined by Planck [2], taking into account CMB lensing reconstruction and measurements of baryon acoustic oscillations. The Hubble parameter at the present time is referred to as Hubble constant and often written in terms of the dimensionless variable h as $H_0 = 100h\,\mathrm{km/s/Mpc}$. The spectral index n_s (see Eq. (2.69)) and the amplitude of fluctuations A_s are parameters of the CMB power spectrum.

Description	Parameter	Value
Hubble constant	H_0 [km/s/Mpc]	67.66 ± 0.42
Baryon density parameter	$\Omega_{b,0}h^2$	0.0224 ± 0.0002
CDM density parameter	$\Omega_{c,0}h^2$	0.1193 ± 0.0009
Matter density parameter	$\Omega_{m,0}$	0.3111 ± 0.0056
Λ density parameter	$\Omega_{\Lambda,0}$	0.6889 ± 0.0056
Spatial curvature density parameter	$\Omega_{K,0}$	0.0007 ± 0.0019
Spectral index	n_s	0.9665 ± 0.0038
Amplitude of fluctuations	$10^9 A_s$	2.105 ± 0.030

Originating from the time when photons finally decoupled from matter after being in thermal equilibrium before, the Cosmic Microwave Background (CMB) provides information about small inhomogeneities present in the early Universe. Being highly homogeneous and isotropic on large scales, the temperature power spectrum of the CMB contains tiny anisotropies which can be translated to fluctuations in the matter density. An explanation for the origin of these inhomogeneities is given in Section 2.2. Together with measurements of baryon acoustic oscillations from large-scale structure surveys such as BOSS [57], the WMAP [12] and Planck [2] CMB missions allowed for the parameters of the ΛCDM model to be determined to high precision. The most recent results confirm that the geometry of our Universe is flat, $|\Omega_{K,0}| < 0.003$, and suggest that $\Omega_{\Lambda,0} = 0.689$, $\Omega_{m,0} = 0.311$ and $\Omega_{r,0} = 9.18 \times 10^{-5}$ with baryonic matter contributing as $\Omega_{b,0} = 0.049$ and CDM as $\Omega_{c,0} = 0.262$ (see Table 1.1 for a selection of ΛCDM parameters and their 68% error intervals taken from Ref. [2]). Since the energy density of CDM is large compared to baryonic matter and it is assumed that CDM couples only very weakly to photons, the nonrelativistic CDM component is indispensable for the process of structure formation [13]. During the time when baryons were still coupled to photons, initial fluctuations in the CDM component could already start to grow and collapse into gravitationally stable *dark matter halos*. Baryonic structures, i.e. stars and galaxies, formed only at much later times. This chronological sequence can explain the distribution of large-scale structure in our Universe today. The growth of structure from initially small density fluctuations and their gravitational collapse is discussed in Chapter 2.

There is additional evidence, for example from the large-scale distribution of galaxies and from gravitational lensing measurements, supporting the predictions of the ΛCDM model (see for example Ref. [58] for an overview). Thus, it provides a remarkably good fit to a number of existing observational data. However, tensions between data sets from different experiments have arisen for some ΛCDM parameters. Two prominent examples are the tension in measurements of the Hubble constant from the low-redshift and the high-redshift universe [59–61] and that some measurements actually favour a closed universe with a curvature density parameter $\Omega_{K,0} < 0$ [62–64] instead of a flat geometry. Future high-precision measurements will show whether these inconsistencies result from undetected systematics or whether their potential affirmation will be a hint for new physics.

On the other hand, the ΛCDM model itself poses several so far unresolved questions about the origin of our Universe and the nature of dark matter and dark energy. Starting with the latter, the Λ term can be interpreted as the energy density of the vacuum [65]. Theoretical calculations based on quantum field theory estimate this quantity to be considerably larger than the observed value which can be computed from $\Omega_\Lambda = 0.689$. Depending on the theoretical prediction, there exists a deviation between 30 and 120 orders of magnitudes [66, 67]. Potentially, this could be solved by a so far unknown symmetry mechanism that cancels the vacuum energy. If so, the accelerated expansion of the Universe would then be described by some new energy source such that the equation of state parameter fulfils $w < -1/3$ (see Eq. (1.20)). Alternatively, there are thoughts about abandoning ΛCDM completely and introducing a modified theory of gravity on large scales to explain the observed accelerated expansion [68, 69].

Furthermore, ΛCDM does not make any predictions about what CDM is actually made of and so far no CDM particle has been discovered in a direct detection experiment. Instead, a number of observations even seem to be in conflict with predictions from numerical CDM simulations on small scales, known as the small-scale challenges [22]. For instance, simulations predict a much higher number of dark matter subhalos inside a host halo of Milky Way size compared to the number of observed Milky Way satellite galaxies [18, 19]. Similarly, there exists a mismatch between the abundance of observed dwarf galaxies in the Local Volume and that predicted in simulations [70]. This conflict is usually known as the *missing satellite* or *missing dwarf problem*. It can be explained by the possibility that dark matter substructures can lose a substantial amount of baryons which makes them difficult to detect with optical instruments due to their large mass-to-light ratio. However, it was pointed out that some of the dark matter subhalos are too dense and massive to let this happen which became known as the *too-big-to-fail* problem [20, 21]. Another challenge for ΛCDM is to explain the observed "cored" density profile in the centre of dwarf and low-surface-brightness galaxies while CDM simulations predict a universal profile that behaves as r^{-1} in the centre (see Eq. (2.131)) forming a "cusp" for all dark matter halos independent of mass [71]. This discrepancy is called the *cusp-core problem* [16, 17]. Whether the small-scale challenges of CDM exist at all or whether they can be solved by a better understanding of baryonic physics and including them accordingly in numerical simulations, is a controversial topic [22]. For example, the missing satellite problem in terms of observed Milky Way satellite counts is resolved by results from the Sloan Digital Sky Survey [72].

Nevertheless, it might be possible that not all of the small-scale problems can be alleviated and if so, alternatives to CDM that can solve the tensions are required. Popular models are warm dark matter (WDM) consisting of sterile neutrinos or gravitinos [73–76], self-interacting dark matter taking into account self-interactions between dark matter particles [77], and fuzzy dark matter (FDM) that is described by a light nonrelativistic scalar field [26]. However, WDM is effectively ruled out by observations [15], self-interacting dark matter alone is unable to solve the missing satellite problem [22], and FDM suffers from strong observational constraints (see Section 3.1.2 for a brief discussion) which raises questions about the validity of these models.

Apart from the lack of knowledge about the nature of dark matter and dark energy, the ΛCDM model is not able to entirely explain the processes of the early Universe. It is known from the CMB that the early Universe must have been in a hot state of thermal equilibrium which is usually referred to as the beginning of the "hot Big Bang". The ΛCDM model does not make any claims about what processes led to the hot Big Bang in the first place and why the CMB is so highly isotropic on large scales. The latter can only be resolved if different parts of the Universe were in causal contact with each other at a time prior to the hot Big Bang. This is known as the *horizon problem* [78, 79] and is described in the following. Introducing the concept of the particle horizon[6] [74],

$$\tau = \int_0^t \frac{\mathrm{d}t'}{a(t')}, \tag{1.15}$$

which is the comoving distance a photon can propagate between the initial time $t = 0$ and some later time t, allows us to understand the causal structure of the universe. Since $a > 0$, the particle horizon increases with time. It also implies that points in space separated by a comoving distance larger than the particle horizon are causally disconnected. This means that their past light cones do not intersect and no information could be transferred from one point to the other. This might change at later times when the particle horizon has become sufficiently large. Turning now to the CMB, which shows the Universe at the redshift $z \sim 1100$, and computing Eq. (1.15) at that time on the basis of the ΛCDM model one finds that the particle horizon is much smaller than the part of the universe

---

[6] Note that the particle horizon is sometimes simply called the horizon in the literature.

visible in the CMB. In fact, one can show that points with an angular separation of more than only 1° on the sky today were not in causal contact with each other at the time the CMB was released [52]. Nevertheless, the CMB is uniform on much larger length scales which implies that somehow different regions of the Universe must have been causally connected before.

Another issue for the ΛCDM model is that it introduces a fine-tuning problem known as the *flatness problem* [80]. Using the expression of the Friedmann equation in terms of the density parameters in Eq. (1.12) and writing $\Omega = \Omega_m + \Omega_r + \Omega_\Lambda$, one obtains that

$$1 - \Omega = \frac{K}{a^2 H^2} \,. \tag{1.16}$$

If a universe is perfectly flat, we have $\Omega = 1$ for all times. However, if $\Omega \neq 1$, the density parameter evolves with time. Since $(aH)^{-1}$ grows both in a radiation- and a matter-dominated universe, a small deviation from flatness will grow accordingly. Measuring a value of $\Omega \approx 1$ today implies that the Universe must have been even flatter at earlier times. The purpose of the flatness problem is to find the origin of the initial flatness.

1.2 The Early Universe

The ΛCDM model seems to be incomplete as it cannot explain the observed flatness of our Universe, the large-scale homogeneity of the CMB and where the tiny inhomogeneities in the CMB on small scales actually come from. In this section, the theory of inflation is introduced which describes a period of accelerated expansion in the very early Universe prior to the hot Big Bang. We will see that an epoch of inflation can solve both the horizon and the flatness problem. Even more importantly, it provides the seeds for the large-scale structure in the Universe we observe today. Understanding the origin of the primordial fluctuations from inflation requires cosmological perturbation theory (see Section 2.1) and is therefore deferred to Section 2.2. While there are numerous possibilities for different inflationary scenarios, the exact process is still not known. Its simplest realisation is single-field slow-roll inflation which is discussed in Section 1.2.2. A complete theory of inflation needs to induce the transition to the hot Big Bang. The period that follows slow-roll inflation is called *reheating* and reviewed in Section 1.2.3.

1.2.1 An Inflationary Phase of Accelerated Expansion

Inflation was originally introduced to solve the horizon and the flatness problems [32]. Recall from the discussion of the horizon problem in Section 1.1.2 that the particle horizon in Eq. (1.15) is the relevant quantity to study the causality of different points in space. In terms of the comoving Hubble length $\mathcal{H}^{-1} = (aH)^{-1}$, which is often simply called the (comoving) horizon in the literature,[7] the particle horizon can be expressed as

$$\tau = \int_0^{t'} \frac{\mathrm{d}t}{a(t)} = \int_0^{a'} \frac{\mathrm{d}a}{Ha^2} = \int_0^{a'} \frac{\mathrm{d}\ln a}{\mathcal{H}} \,. \tag{1.17}$$

This allows us to interpret the Hubble length as the comoving distance travelled by a photon while the universe has expanded by $\Delta \ln a$. One can easily verify that the comoving Hubble length $\mathcal{H}^{-1}$ grows monotonically during matter- and radiation-domination. However, introducing an early phase with a shrinking $\mathcal{H}^{-1}$ implies that the comoving distance photons can travel during the same amount of expansion shrinks while the particle horizon grows. In other words, an initially large region of causally connected space becomes smaller in the course of time. Demanding a shrinking Hubble length during inflation thus provides a solution to the horizon problem. The origin of the flatness problem is that $|1 - \Omega| = K\mathcal{H}^{-2}$ grows as a function of time during radiation- and matter-domination. The requirement of a decreasing Hubble length during a period of inflation thus drives $\Omega \longrightarrow 1$, providing a solution to the flatness problem. Note that grand unified theories predict that magnetic monopoles and other unwanted relics are produced prior to inflation [32]. However, the extensive expansion during inflation dilutes the density of the relics to practically zero which is consistent with the fact that they have not been observed.

Applying the Friedmann equations now allows us to obtain conditions for inflation that are equivalent to the decreasing Hubble length $\mathcal{H}^{-1}$. Since

$$0 \overset{!}{>} \frac{\mathrm{d}\mathcal{H}^{-1}}{\mathrm{d}t} = -\frac{\ddot{a}}{\dot{a}^2} \,, \tag{1.18}$$

we see that inflation is a period of *accelerated* expansion, i.e. $\ddot{a} > 0$. Expressing the second Friedmann Eq. (1.7) as

$$\frac{\ddot{a}}{a} = H^2(1 - \varepsilon) \,, \quad \text{where} \quad \varepsilon = -\frac{\dot{H}}{H^2} \,, \tag{1.19}$$

one finds that $\varepsilon < 1$ for $\ddot{a} > 0$ meaning that the Hubble parameter varies only slowly during inflation. Similarly, the second Friedmann Eq. (1.7) implies that

$$\rho + 3p < 0 \quad \Rightarrow \quad w < -\frac{1}{3} \,, \tag{1.20}$$

so inflation demands negative pressure. Note that all these different conditions are equivalent to each other.

---

[7] Note that this is also the case for the particle horizon.

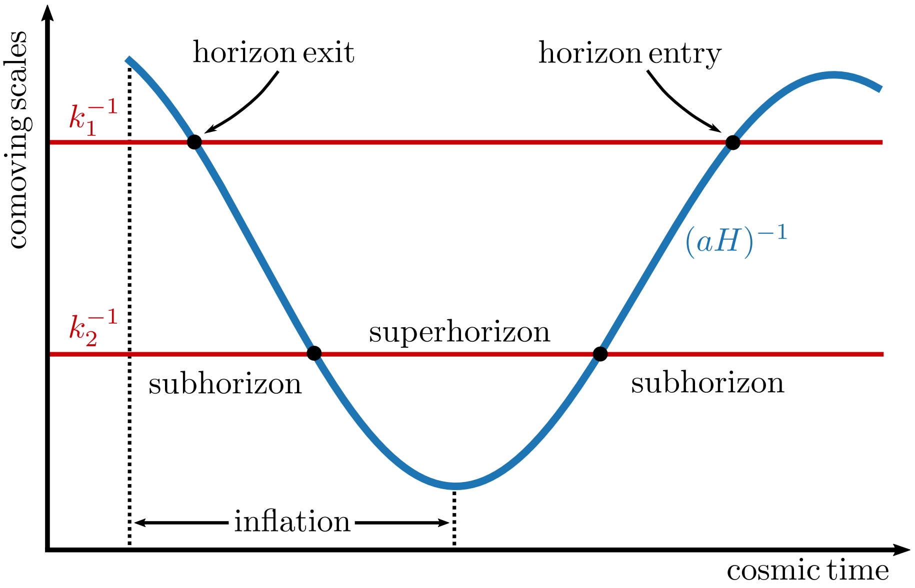

Figure 1.1 | Schematic representation of the evolution of the comoving Hubble length, $(aH)^{-1}$, during and after inflation. The Hubble length decreases during inflation and perturbations of different comoving scales, denoted by k_1^{-1} and k_2^{-1}, leave the horizon at different times. Once inflation is completed, the Hubble length increases and the comoving distance scales eventually become subhorizon.

From a cosmological point of view, it is of major importance that inflation provides an explanation for the creation of primordial density perturbations (see Section 2.2) which are the seeds for all the structures in our Universe. For the later discussion of the evolution of these density perturbations the history of each comoving distance scale k is relevant. A scale can be subhorizon ($k > \mathcal{H}$), superhorizon ($k < \mathcal{H}$) or at horizon ($k = \mathcal{H}$). Since the comoving Hubble length $\mathcal{H}^{-1}$ decreases during inflation and increases afterwards, initially subhorizon scales exit the horizon during inflation and re-enter at later times when the Universe is radiation- or matter-dominated (see Fig. 1.1). Importantly, the amplitude of the density perturbations generated during inflation at a certain comoving scale k depends on the time when this scale exits the horizon during inflation (see Section 2.2). Superhorizon density perturbations remain constant during inflation[8] but start to collapse when they become subhorizon at later times. This meaningful circumstance is the origin of the standard formation scenario of primordial black holes (PBHs). Applying Newtonian gravity it was found that a density fluctuation, which re-enters the horizon during radiation-domination, can collapse into a black hole if the density contrast $\delta = \delta\rho/\rho$ exceeds the critical value $\delta_c = 1/3$ [81, 82]. The mass of such PBHs is roughly given by the mass contained within the horizon at the

---

[8] More precisely, curvature perturbations remain constant during inflation on superhorizon scales if they are adiabatic (see discussion in Section 2.2.2). As shown in Section 2.3.2, they can be related to density perturbations.

time t_c of collapse [82],

$$M_{\mathrm{PBH}} \sim 10^{15}\,\mathrm{g}\left(\frac{t_c}{10^{-23}\,\mathrm{s}}\right) . \tag{1.21}$$

As a result, PBHs cover a wide mass range and can in principle reach masses as low as 10^{-5} g.

1.2.2 Single Field Slow-Roll Inflation

As we have seen in the previous section, the accelerated expansion of the universe during inflation is equivalent to an equation of state parameter $w < -1/3$. The required negative pressure cannot be realised by ordinary matter or radiation, however, this can be achieved by introducing a real scalar field φ which is called the *inflaton*. Parameterising the inflaton by φ, its Lagrangian is given by [52]

$$\mathcal{L}_\varphi = -\frac{1}{2} g^{\mu\nu} \partial_\mu \varphi \partial_\nu \varphi - V(\varphi) , \tag{1.22}$$

where $V(\varphi)$ is the effective potential of the scalar field φ. The shape of $V(\varphi)$ depends on the considered inflationary model, we keep it unspecified for now. When coupling to gravity, the relativistic action of the scalar field is [52]

$$S = \frac{1}{16\pi G} \int \mathrm{d}^4x \sqrt{-g} R + \int \mathrm{d}^4x \sqrt{-g} \mathcal{L}_\varphi , \tag{1.23}$$

with Ricci scalar R and $g = \det(g_{\mu\nu})$. Varying the action with respect to φ and considering the flat FLRW spacetime leads to the equation of motion [52]

$$\ddot{\varphi} + 3H\dot{\varphi} - \frac{\nabla^2 \varphi}{a^2} + \frac{\mathrm{d}V}{\mathrm{d}\varphi} = 0 , \tag{1.24}$$

which as known as the *Klein-Gordon* equation. Provided that $\varphi = \varphi(t)$ is homogeneous, the $\nabla^2\varphi$ term vanishes. Varying the action in Eq. (1.23) with respect to the metric, one can obtain the stress-energy tensor of a scalar field [52],

$$T_{\mu\nu} = \partial_\mu \varphi \partial_\nu \varphi - g_{\mu\nu} \left(\frac{1}{2} \partial_\alpha \varphi \partial^\alpha \varphi + V(\varphi) \right) . \tag{1.25}$$

Identifying the components of the stress-energy tensor with that of a perfect fluid (see Eq. (1.5)), the energy density and pressure of a homogeneous scalar field are

$$\rho_\varphi = \frac{1}{2}\dot{\varphi}^2 + V(\varphi) , \qquad p_\varphi = \frac{1}{2}\dot{\varphi}^2 - V(\varphi) . \tag{1.26}$$

Thus, the equation of state parameter can be expressed as

$$w = \frac{p_\varphi}{\rho_\varphi} = \frac{1 - 2V(\varphi)/\dot{\varphi}^2}{1 + 2V(\varphi)/\dot{\varphi}^2} , \tag{1.27}$$

which reveals that $w < 0$ if $V(\varphi) > \dot{\varphi}^2/2$, i.e. the inflaton potential has to dominate over the kinetic term during inflation. Inserting the expressions for energy density and pressure from Eq. (1.26) into the Friedmann Eq. (1.6), we see that the universe evolves as

$$H^2 = \frac{1}{3M_{\text{Pl}}^2}\left(\frac{1}{2}\dot{\varphi}^2 + V(\varphi)\right), \tag{1.28}$$

where $M_{\text{Pl}} = (8\pi G)^{-1/2}$ is the reduced Planck mass. As was already discussed in Section 1.2.1, the parameter $\varepsilon = -\dot{H}/H^2$ introduced in Eq. (1.19) must be small to explain the shrinking Hubble horizon during the inflationary stage. Using the two Friedmann equations and the density and the pressure of a scalar field from Eq. (1.26), the *slow-roll parameter* ε can be written as [52]

$$\varepsilon \equiv -\frac{\dot{H}}{H^2} = \frac{\dot{\varphi}^2}{2M_{\text{Pl}}^2 H^2}\,. \tag{1.29}$$

Since $\varepsilon < 1$ during inflation implies that the potential $V(\varphi)$ must dominate over the kinetic term $\dot{\varphi}^2$. To achieve this for a long period of time requires that the acceleration of the scalar field $\ddot{\varphi}$ has to be small as well. This provides motivation to define a second slow-roll parameter [52]

$$\eta = -\frac{\ddot{\varphi}}{H\dot{\varphi}}\,. \tag{1.30}$$

As long as ε and η are small, the period of inflation does not come to an end. Applying the slow-roll approximation $\varepsilon,\ \eta \ll 1$, it is possible to simplify the equations of motion. This approximation means that the inflaton potential dominates over the kinetic term in Eq. (1.28), i.e. $V(\varphi) \gg \dot{\varphi}^2$, and the friction term $3H\dot{\varphi}$ dominates over $\ddot{\varphi}$ in Eq. (1.24). Then, the Friedmann Eq. (1.28) and the Klein-Gordon Eq. (1.24) simplify to the slow-roll equations

$$H^2 = \frac{V(\varphi)}{3M_{\text{Pl}}^2}, \qquad 3H\dot{\varphi} = -\partial_\varphi V(\varphi)\,. \tag{1.31}$$

Thus, the Hubble parameter is approximately constant during slow-roll and the scale factor evolves as $a(t) \sim \exp(Ht)$. Using the slow-roll equations to express ε and η in terms of the potential $V(\varphi)$ and its derivatives, defines the potential slow-roll parameters [52]

$$\varepsilon = \frac{\dot{\varphi}^2}{2M_{\text{Pl}}^2 H^2} \approx \frac{1}{2}M_{\text{Pl}}^2\left(\frac{\partial_\varphi V}{V}\right)^2 \equiv \varepsilon_V\,, \tag{1.32}$$

and

$$\eta = -\frac{\ddot{\varphi}}{H\dot{\varphi}} = \frac{\partial_{\varphi\varphi} V}{3H^2} - \varepsilon \approx M_{\text{Pl}}^2\frac{\partial_{\varphi\varphi} V}{V} \equiv \eta_V\,. \tag{1.33}$$

Here, the time derivative of the second slow-roll equation in Eq. (1.31) was used to replace $\ddot{\varphi}$. Inflation comes to an end once the slow-roll conditions are violated, i.e. when $\varepsilon(\varphi_{\text{end}}) \equiv 1$ or $\varepsilon_V(\varphi_{\text{end}}) \approx 1$. A useful quantity which provides a measure for the amount of expansion until the end of inflation is the number of e-foldings $\mathcal{N}$,

$$\mathcal{N} \equiv \ln \frac{a(t_{\text{end}})}{a(t)} = \int_t^{t_{\text{end}}} H(t)\,\mathrm{d}t = \int_\varphi^{\varphi_{\text{end}}} \frac{H}{\dot{\varphi}}\,\mathrm{d}\varphi \approx \frac{1}{M_{\text{Pl}}^2} \int_{\varphi_{\text{end}}}^{\varphi} \frac{V}{\partial_\varphi V}\,\mathrm{d}\varphi\,, \tag{1.34}$$

where the approximation is only valid during slow-roll. To be consistent with CMB observations at least $\mathcal{N} = 60$ e-folds of inflation are usually required[9] [52]. This guarantees that the largest observable scales were subhorizon at the beginning of inflation which is necessary for solving the horizon problem.

Eventually, inflation is followed by an epoch which is called reheating during which the inflaton decays into radiation and other particles. Before coming to this stage of the early Universe, different models of inflation are briefly summarised in the following.

Inflationary Models

Any model of inflation consists of a potential $V(\varphi)$ and must provide a mechanism for ending inflation. This occurs once φ approaches the minimum of $V(\varphi)$ or when $\varepsilon(\varphi_{\text{end}}) = 1$. In so-called *hybrid* inflation models, another scalar field is present that can lead to an end of inflation even though the slow-roll approximation is still valid [83]. In general, one distinguishes between small-field and large-field models of inflation that are characterised by the range $\Delta\varphi$ in Planck units that φ is allowed to move during inflation (see Fig. 1.2).

In small-field models, the inflaton field varies only over a small range, i.e. $\Delta\varphi < M_{\text{Pl}}$. The shape of a possible corresponding potential is similar to the potential in spontaneously broken symmetries, where a field evolves from an initially unstable equilibrium condition towards the minimum of its potential (see left-hand side of Fig. 1.2). Hence, such models can be described by potentials of the form [52]

$$V(\varphi) = V_0 \left[1 - \lambda \left(\frac{\varphi}{M_{\text{Pl}}}\right)^4 + \ldots\right], \tag{1.35}$$

where the dots represent terms of a higher order that are negligible during inflation. A particularly interesting model is *Starobinsky inflation* where the single-field potential is given by [31]

$$V(\varphi) = \lambda^4 M_{\text{Pl}}^4 \left[1 - \exp\left(-\sqrt{\frac{2}{3}}\frac{\varphi}{M_{\text{Pl}}}\right)\right], \tag{1.36}$$

---

[9] Note that this number is reduced in models when inflation is followed by an extended phase of matter-dominated expansion (see Eq. (1.65)).

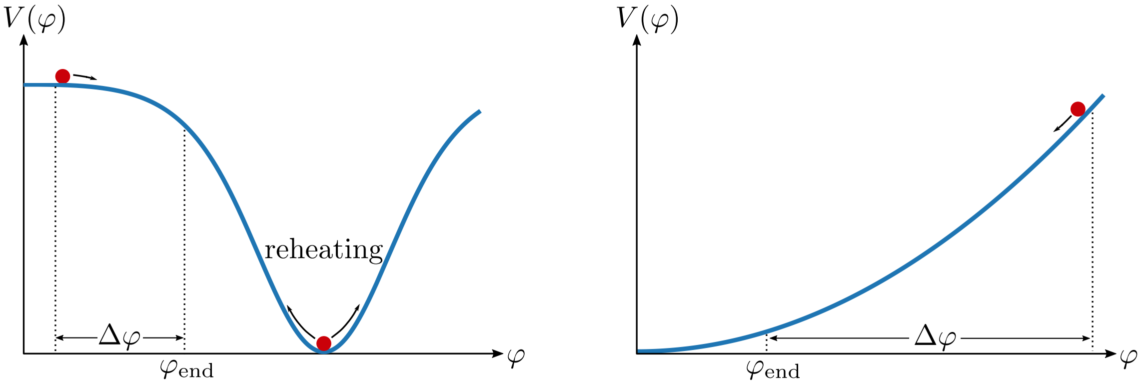

Figure 1.2 | Illustration of the inflaton potential in small-field (left) and large-field (right) models of inflation. While the inflaton field evolves over a small distance $\Delta\varphi < M_{\mathrm{Pl}}$ during small-field inflation, a large range $\Delta\varphi > M_{\mathrm{Pl}}$ is covered in large-field inflation. During reheating (see Section 1.2.3), the inflaton oscillates around the minimum of its potential.

which results from including an additional R^2 term in the action of Eq. (1.23). On the contrary, large-field inflation covers models where the inflaton starts at an initially large value and thus varies by large values of $\Delta\varphi > M_{\mathrm{Pl}}$ before reaching a minimum of the potential at $\varphi = 0$ (see right-hand side of Fig. 1.2). A simple large-field model is *chaotic inflation* [33] where the potential is of the monomial form $V(\varphi) \sim \varphi^n$. Another model is *natural inflation* where the inflaton is the Nambu-Goldstone boson of a spontaneously broken symmetry with the periodic potential[10] [85, 86]

$$V(\varphi) = V_0 \left[1 \pm \cos\left(\frac{\varphi}{f}\right)\right] , \tag{1.37}$$

which in principle can be considered both as a small-field and a large-field model as this depends on the free parameter f. Note that there are even more possibilities of building inflationary models, for example by considering more than one inflaton field [87]. However, in this thesis, we will consider only a simple single-field slow-roll model.

Apart from describing the accelerated expansion of the universe during inflation and finding a way of ending it, a successful inflationary model needs to be consistent with observational data. While large-field models produce a significant amount of primordial gravitational waves [88], small-field models predict a comparatively small gravitational wave signal (cf. Eq. (2.85) in Section 2.2.5). The most recent CMB measurements have revealed strong tensions for large-field models, i.e. for both chaotic and natural inflation, while Starobinsky inflation is compatible with all observations so far [89].

---

[10] Note that the same mechanism motivates the axion (see Section 1.3), thus this potential resembles the axion potential in Eq. (1.71). This type of inflation is the origin of other axion inflation models, where an axion drives the accelerated expansion of space during inflation. An overview of axion inflation can be found for example in Ref. [84].

1.2.3 Reheating

Once the end of inflation is reached, $\varepsilon(\varphi_{\text{end}}) = 1$, the inflaton starts to oscillate around the minimum of its potential (see Fig. 1.2). Since the vast expansion during inflation leaves the universe in a rather empty and cold state, a mechanism is required that transforms the energy stored in the inflaton field to other forms of matter and radiation. This mechanism is called reheating and describes the transition of the universe from the cold state to the hot Big Bang, where the universe is in thermal equilibrium and dominated by radiation. The temperature of the universe when thermal equilibrium is reached is called the reheating temperature. The general idea of reheating is that the oscillations of the inflaton produce elementary particles via its coupling to other matter fields.

Soon after the inflationary theory was introduced, efforts were made to develop the theory of reheating. Initially, it was tried to modify the equation of motion of the inflaton field directly to transfer energy to other particles [90]. This approach raised more questions than answers as it was not specified what additional terms need to be added to the equation of motion and whether they should be present already during slow-roll inflation [91]. Instead, it was discovered that a perturbative theory of reheating could be successfully used to determine the reheating temperature [92, 93]. However, perturbative reheating is only efficient at the late stages of reheating. At earlier stages, the theory of parametric resonance provides a way to efficient particle production [94, 95], a process known as *preheating* [96]. Up to the present day, no complete theory of reheating exists, in the sense that it should describe the evolution from the end of inflation until thermalisation has been developed. Nevertheless, substantial progress has been made in uncovering plenty of fascinating physical phenomena that can occur prior to thermalisation.

Evolution of the Inflaton Field

Before specifying the processes that can lead to particle production and eventually to the thermalisation of the Universe it is necessary to describe the dynamics after inflation when the inflaton oscillates around the minimum of its potential, ignoring for the moment couplings to other particles. Choosing for convenience the quadratic potential

$$V(\varphi) = \frac{1}{2}m^2\varphi^2\,, \tag{1.38}$$

where m denotes the inflaton mass, the Klein-Gordon Eq. (1.24) for the homogeneous inflaton field φ and the Friedmann Eq. (1.28) read

$$\ddot{\varphi} + 3H\dot{\varphi} + m^2\varphi = 0\,, \quad \text{and} \quad H^2 = \frac{1}{6M_{\text{Pl}}^2}\left(\dot{\varphi}^2 + m^2\varphi^2\right)\,. \tag{1.39}$$

Introducing the angular variable ϑ, the Friedmann equation can be parameterised as [53]

$$\dot{\varphi} = \sqrt{6} H M_{\rm Pl} \cos\vartheta \,, \qquad m\varphi = \sqrt{6} H M_{\rm Pl} \sin\vartheta \,. \tag{1.40}$$

Since $\ddot{\varphi} = \sqrt{6} M_{\rm Pl} (\dot{H} \cos\vartheta - H\dot{\vartheta} \sin\vartheta)$, the Klein-Gordon equation can be used to obtain

$$\dot{H} = -3H^2 \cos^2\vartheta \tag{1.41}$$

$$\dot{\vartheta} = m + 3H \sin\vartheta \cos\vartheta \,. \tag{1.42}$$

As is evident from Eq. (1.41), the Hubble parameter decreases with time. Consequently, the second term on the right-hand side of Eq. (1.42) oscillates with decreasing amplitude and can be neglected for $m \gg H$. Setting the integration constant to zero,[11] we have $\vartheta \simeq mt$ and the scalar field φ oscillates with frequency $\omega \simeq m$. Solving Eq. (1.41) by integrating $\mathrm{d}H/H^2 = -3\cos^2(mt)\mathrm{d}t$ we obtain [53]

$$H = \frac{2}{3t}\left(1 + \frac{\sin(2mt)}{2mt}\right)^{-1} \simeq \frac{2}{3t} \,, \tag{1.43}$$

where the approximation is only valid for $mt \gg 1$ ($m \gg H$). Since $H = \dot{a}/a$, one can extract the behaviour of the scale factor by integrating Eq. (1.43),

$$a(t) \simeq a_{\rm end}\left(\frac{t}{t_{\rm end}}\right)^{2/3} \sim t^{2/3} \,, \tag{1.44}$$

where the subscript "end" refers to a quantity evaluated at the end of inflation. Then, the Hubble parameter in terms of the scale factor reads

$$H \simeq \frac{2}{3t_{\rm end}}\left(\frac{a_{\rm end}}{a}\right)^{3/2} = H_{\rm end}\left(\frac{a_{\rm end}}{a}\right)^{3/2} \,. \tag{1.45}$$

The evolution of the field φ is given by

$$\varphi \simeq \mathcal{A}(t)\sin(mt) \,, \quad \text{with} \quad \mathcal{A}(t) = \frac{\sqrt{6} M_{\rm Pl}}{m} H \sim \frac{M_{\rm Pl}}{mt} \,, \tag{1.46}$$

where $\mathcal{A}(t)$ is the amplitude of the field oscillations. Neglecting the $\dot{H}$ term in the time derivative of φ as it is suppressed with a^{-3}, the energy density of the scalar field (cf. Eq. (1.26)) can be thus written as

$$\rho_\varphi \simeq \frac{1}{2} m^2 \mathcal{A}^2(t) \,, \tag{1.47}$$

and behaves as $\rho_\varphi \sim a^{-3}$. Hence, the post-inflationary evolution can be treated as a matter-dominated universe on timescales larger than the frequency of the field oscillations.[12] Now we are in a position to take into account couplings to other particles. This can be done either perturbatively or via a process of parametric resonance.

---

[11] The integration constant corresponds to a constant phase in $\sin\vartheta$ and $\cos\vartheta$, and can be safely neglected.

[12] Note that the post-inflationary evolution behaves like a radiation-dominated universe if a quartic potential $V(\varphi) \sim \varphi^4$ instead of the quadratic potential in Eq. (1.38) is used.

Perturbative Reheating

Following Ref. [91], we discuss the perturbative theory of reheating which was originally developed in Refs. [92, 93]. Considering interactions of the inflaton field with another scalar field χ_s and a fermionic field χ_f and neglecting cubic interaction terms, the effective potential in the Lagrangian is given by

$$V = V(\varphi) + \frac{1}{2} g_s^2 \varphi^2 \chi_s^2 + g_f \bar{\chi}_f \chi_f \varphi \,, \tag{1.48}$$

where g_s and g_f are small coupling constants. Assuming a quadratic potential $V(\varphi)$ with a minimum at $\varphi = \sigma$,

$$V(\varphi) = \frac{1}{2} m^2 (\varphi - \sigma)^2 \,, \tag{1.49}$$

and performing the shift $\varphi \longrightarrow \varphi + \sigma$, one obtains an additional interaction term $V_+ = g_s^2 \sigma \varphi \chi_s^2$ in Eq. (1.48) while $V(\varphi)$ is the quadratic potential from Eq. (1.38). The interaction terms $\Delta\mathcal{L} = -g_s^2 \sigma \varphi \chi_s^2 - g_f \bar{\chi}_f \chi_f \varphi$ describe the decay of the inflaton into a pair of scalar χ_s and fermionic χ_f particles. Assuming that their masses m_{χ_s}, m_{χ_f} are much lighter than the mass m of the inflaton, the decay rates are [91]

$$\Gamma(\varphi \longrightarrow \chi_s \chi_s) = \frac{g_s^4 \sigma^2}{8\pi m} \,, \quad \text{and} \quad \Gamma(\varphi \longrightarrow \bar{\chi}_f \chi_f) = m \frac{g_f^2}{8\pi} \,. \tag{1.50}$$

Evidently, the decay rates are proportional to g_s^4 and g_f^2, respectively. Since the coupling constants are small, perturbative reheating is a rather slow process. Nevertheless, the number density $n_\varphi = \rho_\varphi / m \simeq m\mathcal{A}^2/2$ (see Eq. (1.47)) of the inflaton particles in a comoving volume decreases with the total decay rate $\Gamma = \Gamma(\varphi \longrightarrow \chi_s \chi_s) + \Gamma(\varphi \longrightarrow \bar{\chi}_f \chi_f)$ as

$$\frac{\mathrm{d}(a^3 n_\varphi)}{\mathrm{d}t} = -\Gamma a^3 n_\varphi \,. \tag{1.51}$$

This exponential decrease in the number of inflaton particles can be understood as an additional friction term in the equation of motion for φ [91],

$$\ddot{\varphi} + (3H + \Gamma)\dot{\varphi} + m^2 \varphi = 0 \,. \tag{1.52}$$

Note that this equation is only valid for $m \gg H$, i.e. at the time when φ performs rapid oscillations at the minimum of $V(\varphi)$ and not during slow-roll inflation. At the initial reheating stage, the expansion of the universe leads to a decreasing energy density of the inflaton field. Once $H \lesssim \Gamma$, the energy density is transferred to the decay products. Since

$m \ll m_{\chi_s}, m_{\chi_f}$, the created particles are relativistic and the universe becomes radiation-dominated. Assuming that reheating is completed when $H \sim \Gamma$ which corresponds to the time $t_{\mathrm{reh}} \sim 2\Gamma^{-1}/3$, one obtains that the energy density at time t_{reh} is

$$\rho(t_{\mathrm{reh}}) \simeq 3M_{\mathrm{Pl}}^2\Gamma^2 \,. \tag{1.53}$$

Provided that thermodynamic equilibrium is established after the inflaton has decayed, one can relate this energy density to the reheating temperature T_{reh} [91],

$$\rho(t_{\mathrm{reh}}) \simeq 3M_{\mathrm{Pl}}^2\Gamma^2 \simeq \frac{\pi^2}{30} g_* T_{\mathrm{reh}}^4 \,. \tag{1.54}$$

Here, g_* is the number of relativistic degrees of freedom at reheating which is of the order 10^2 in the Standard Model. Hence, the reheating temperature is[13]

$$T_{\mathrm{reh}} \simeq \left(\frac{90}{\pi^2 g_*}\right)^{1/4} \sqrt{\Gamma M_{\mathrm{Pl}}} = 0.55 \left(\frac{100}{g_*}\right)^{1/4} \sqrt{\Gamma M_{\mathrm{Pl}}} \,. \tag{1.55}$$

Admittedly, this perturbative treatment of reheating is quite intuitive, however, it raises some issues. As already mentioned, the small couplings require that the reheating process evolves slowly and it is possible that the energy transfer is not completed leaving energy in the inflaton field [96]. Furthermore, the above approach does not consider Bose condensation effects which can enhance particle production enormously once the number density of the bosonic decay products crosses a certain threshold [91]. Apart from this, perturbative reheating does not work if larger couplings to the inflaton are considered which necessitates a non-perturbative description. Exploiting the large number density of the inflaton, the idea is to consider the oscillating homogeneous inflaton field as a classical condensate. Treating the decay products quantum mechanically, which is necessary due to their initially vanishing occupation numbers, the oscillating background field can lead to huge particle production rates via parametric resonance. This production mechanism is known as preheating (see below) and was introduced in Ref. [96]. Nevertheless, the perturbative treatment is in any case applicable to the late stage of (p)reheating when most of the inflaton energy density has already been transferred into other particles to avoid that energy remains stored in the inflaton field.

Preheating

To take into account Bose enhancement effects in the production of bosonic particles at the earlier stages of reheating, one has to rely on a non-perturbative description referred

---

[13] Note that this expression appears to be different from the result $T_{\mathrm{reh}} \simeq 0.2\sqrt{\Gamma M_{\mathrm{P}}}$ in Ref. [91]. However, this can be explained by the fact that M_{P} refers to the Planck mass $M_{\mathrm{P}} = \sqrt{8\pi} M_{\mathrm{Pl}}$ and that the authors of Ref. [91] assumed a value of $g_* = 200$.

to as preheating. The coupling between the oscillating *classical* inflaton field φ and the *quantum* bosonic field $\hat{\chi}$ leads to a resonant amplification of $\hat{\chi}$ which translates to an exponential growth in their number density.[14] As before, we consider the quadratic inflaton potential from Eq. (1.48) without the fermionic part and the shift $\varphi \longrightarrow \varphi + \sigma$ such that the interaction terms are

$$\Delta\mathcal{L} = -\frac{1}{2}g^2\varphi^2\chi^2 - g^2\sigma\varphi\chi^2 - \frac{1}{2}g^2\sigma^2\chi^2 \,. \tag{1.56}$$

Expressing the field χ in terms of annihilation ($\hat{a}_k$) and creation operators ($\hat{a}_k^\dagger$) in Fourier space,

$$\hat{\chi}(t,\mathbf{x}) = \int \frac{\mathrm{d}^3\mathbf{k}}{(2\pi)^{3/2}} \left(\hat{a}_k\chi_k \exp(-i\mathbf{k}\mathbf{x}) + \hat{a}_k^\dagger\chi_k^* \exp(i\mathbf{k}\mathbf{x})\right) , \tag{1.57}$$

the equation of motion for the mode functions χ_k in an expanding background is [91]

$$\ddot{\chi}_k + 3H\dot{\chi}_k + \left(\frac{k^2}{a^2} + g^2\varphi^2 + g^2\sigma^2 + 2g^2\sigma\varphi\right)\chi_k = 0 \,. \tag{1.58}$$

Since this equation resembles an oscillator with frequency $\omega_k^2 = k^2/a^2 + g^2\varphi^2 + g^2\sigma^2 + 2g^2\sigma\varphi$, a periodically changing background field φ can lead to parametric resonance of certain k modes.

It is illustrative to analyse this equation in different preheating regimes for a non-expanding background ($a = 1$, $\dot{a} = 0$). If $\varphi \ll \sigma$, the equation of motion reduces to

$$\ddot{\chi}_k + \left(k^2 + g^2\sigma^2 + 2g^2\sigma\varphi\right)\chi_k = 0 \,. \tag{1.59}$$

Introducing the variables $A_k = 4(k^2 + g^2\sigma^2)/m^2$, $\kappa = 4g^2\sigma\varphi/m^2$ and $\varsigma = mt/2$, it can be written as [91]

$$\frac{\mathrm{d}^2\chi_k}{\mathrm{d}\varsigma^2} + (A_k - 2\kappa\cos(2\varsigma)) = 0 \,, \tag{1.60}$$

which is known as Mathieu equation [97]. Solutions to this equation are of the form $\chi_k \sim \exp(\mu\varsigma)$, where μ is the Floquet exponent, and exhibit instabilities for real values of μ that are larger than zero for certain modes k. Since these instabilities translate to an exponential increase in the occupation numbers $n_k \sim |\chi_k|^2 \sim \exp(2\mu\varsigma)$ of quantum fluctuations [91], the Floquet exponent μ is a measure for the efficiency of particle production.

---

[14] Efficient parametric resonance is restricted to bosonic particles. Hence, fermionic particles are not considered in the following and the subscript in χ and g, which were used to distinguish between scalar and fermionic fields before, is dropped.

For $\kappa \ll 1$, i.e. $m \gg g\sigma$, solutions for Eq. (1.60) can be found analytically. Parametric resonance occurs in the narrow regimes $A_k \sim n^2$, where n is an integer, with a width of order $\Delta k \sim \kappa^n$ in momentum space. Since $\kappa \ll 1$, the first resonance band with $A_k = 1 \pm \kappa$ is the widest and a calculation of the Floquet exponent reveals that one observes resonance for all k in the interval between $k = m(1 - \kappa/2)/2$ and $k = m(1 + \kappa/2)/2$ [97]. The maximum of $\mu = \kappa/2$ is at $k = m/2$ which can be understood as the decay of an inflaton particle φ into two χ particles. This seems to be similar to the case of perturbative reheating discussed before. However, the process of particle production in this scenario is completely different as the production rate depends on the number of particles that were created before. Hence, Bose enhancement effects are the reason for the exponential particle growth rate. The smallness of κ leads to both a small resonance regime and a small exponent μ which is why preheating is not very effective in the *narrow resonance* regime. If the expansion of the universe is taken into account, the efficiency even decreases. On the one hand, the amplitude of φ becomes smaller reducing the value of κ and thus the width of the resonance bands. On the other hand, the modes k are redshifted and eventually leave the regime in which resonance can take place. One finds that narrow resonance only occurs for $\kappa m \gtrsim 3H + \Gamma$ [91], so eventually it is not effective anymore and the remaining inflaton particles decay via perturbative reheating.

The previous results are only valid for $\varphi \ll \sigma$ which in the considered model can only be satisfied at the end of preheating. At the beginning of the reheating stage, the field value is actually quite large so that the $g^2\varphi^2$ term in Eq. (1.58) cannot be neglected and $\kappa > 1$. Preheating thus starts in the regime of *broad resonance* where parametric resonance occurs in much broader resonance bands than in the case of narrow resonance. In the chaotic inflation model, the amplitude of the inflaton field φ can initially be of the order M_{Pl}. Assuming $\varphi \gg \sigma$ and a static universe, the equation of motion for the mode functions then reads

$$\ddot{\chi}_k + (k^2 + g^2\varphi^2)\chi_k = 0\,, \tag{1.61}$$

which can be written as Eq. (1.60) with $A_k = k^2/m^2 + 2\kappa$, $\kappa = g^2\varphi^2/(4m^2)$ and $\varsigma = mt$ [91]. For a large value of κ, parametric resonance takes place in the wide range $k^2 \lesssim 2m^2\kappa^{1/2}$ and particle production becomes very efficient [91]. Solving Eq. (1.61) numerically, one finds an enormous increase in the occupation numbers n_k each time the oscillating inflaton field φ crosses zero [91]. If the expansion of the universe is taken into account, the initially large amplitude of φ rapidly decreases. While the change of the oscillation frequency is periodic for a non-expanding universe, this is not the case when expansion is included. This leads to a different phase of χ_k each time φ crosses zero and thus to a process called stochastic resonance during which the occupation number n_k in general increases but it may occasionally also decrease [91]. Eventually, κ becomes small and the narrow resonance regime is reached, followed by the perturbative inflaton decay.

Nonlinear Evolution

Although reheating is a crucial part in a complete theory of inflation, cosmological observations have not shed light on the involved physical processes so far. It is known that the Universe must reach thermal equilibrium at the end of reheating and Big Bang Nucleosynthesis[15] (BBN) provides a lower limit of $T \sim \text{MeV}$ for the reheating temperature [100–102]. Beforehand, plenty of interesting physical phenomena could have taken place. In the following, a brief overview of these phenomena is presented.

The resonant particle production during preheating has to stop at some point. If the expansion of the Universe does not lead to its termination, the back-reaction of the produced χ particles, which has been neglected in the above discussion of preheating, ends the process [103]. This can be taken into account by including higher order correction terms in the equation of motion of the quantum fluctuations (see Eq. (1.58)). To begin with, the effective mass of the inflaton oscillations is altered by the existence of χ particles. As long as this change in mass $\Delta m^2 \simeq g n_\chi / |\varphi|$ is smaller than the squared inflaton mass m^2, back-reaction effects can be neglected. Once $\Delta m^2 > m^2$ they become relevant and as a result, resonant particle production comes to an end. Additionally, one can show that the back-reaction of χ particles is subdominant as long as the energy density ρ_χ in the χ particles is smaller than the energy density ρ_φ of the inflaton field [103]. Apart from this, the scattering of χ particles from each other and their interaction with the oscillating inflaton field can lead to the production of φ particles. This process is known as *rescattering* and results in an increase of the effective mass of the χ field and in the fragmentation of the homogeneous inflaton field [91]. In principle, parametric particle production can end with a significant fraction of the total energy stored both in φ and in χ. Numerical simulations are required for a detailed analysis of the back-reaction effects during preheating and for the subsequent nonlinear evolution that leads to thermalisation. The first detailed three-dimensional simulations of broad resonance in an expanding universe including the back-reaction and rescattering were reported in Ref. [104].

To evolve the combined system of the inflaton and potential daughter fields, numerical codes such as LATTICEEASY [105], DEFROST [106] and PSPECTRE [107] have been developed. They can be used to solve the equations of motion of the coupled system of fields in an expanding universe. In the simplest considered model, the inflaton is only weakly coupled

---

[15] BBN denotes the production of nuclei for light chemical elements and isotopes such as deuterium, helium and lithium. This process occurred between 10 s and 20 min after the hot Big Bang [98, 99].

to other fields, so any interactions with other fields can be omitted. If self-interactions are included, the inflaton potential $V(\varphi)$ takes the general form [108]

$$V(\varphi) = \frac{1}{2}m^2\varphi^2 + \frac{\lambda_3}{3}\varphi^3 + \frac{\lambda_4}{4}\varphi^4 + \dots\,, \tag{1.62}$$

and the inflaton oscillations at the initial stage of reheating can induce a resonant amplification of its own fluctuations. This is in contrast to the standard preheating mechanism where parametric resonance leads to the production of daughter particles which is why this scenario is called *self-resonance*. It can lead to the fragmentation of the inflaton field in the subsequent evolution. The nonlinear dynamics during the latter phase is particularly interesting for inflaton potentials that are in agreement with current observational constraints. Such potentials can be approximated by Eq. (1.62) around their minimum while they flatten and reach a plateau-like region away from the minimum. Simulations have shown that long-lived soliton-like objects such as *oscillons* form abundantly in such a scenario [109–112]. Since the energy density is dominated by oscillons which behave like dust, this allows for a long phase of matter-dominated expansion following self-resonance [111, 112]. If the minimum in the inflaton potential is nonquadratic, objects similar to oscillons but less stable form and the universe will become radiation-dominated instead [113–115].

In models where the inflaton couples to other fields, simulations have shown the formation of bubble-wall-like configurations [116, 117] after the termination of preheating. Moreover, it is possible to produce topological defects such as domain walls and cosmic strings [118], so there is a rich amount of possible nonlinear physics involved in the phase following preheating. Importantly, even for an inflaton without couplings to other fields and without self-interactions, i.e. in the absence of resonance, gravitational interactions lead eventually to the fragmentation of the inflaton field and to the formation of gravitationally-bound, nonlinear structures [35–38, 40, 41]. This is similar to cosmological structure formation in the late-time universe and is further studied in Chapter 5.

In any case, the Universe must become radiation-dominated in the last stages of reheating and finally reach thermal equilibrium at some reheating temperature $T_{\rm reh} \geq 1\,\mathrm{MeV}$. Completing thermalisation can be a long process and an equation-of-state parameter of $w \sim 1/3$ is reached already at an earlier time called pre-thermalisation [108]. However, pre-thermalisation can be delayed in scenarios where oscillons or gravitationally-bound structures are formed. In this case, the universe is matter-dominated which requires the decay into relativistic matter to accomplish $w \sim 1/3$. Furthermore, one has to ensure that the inflaton decays completely since otherwise, the universe can again become matter-dominated before BBN [108]. This shows the significance of perturbative reheating in the last stages of reheating when preheating is not efficient anymore. Thermalisation can be achieved only afterwards and requires out-of-equilibrium quantum field theory [108]. However, the exact thermalisation process is still not understood and the computation of a robust reheating temperature for a particular model remains an open problem.

Observational Consequences

Since the thermal state of the Universe at BBN veils the relevant processes that led to this state in the first place, it is unfortunately difficult to construct reheating constraints from observations. However, the rich dynamics during reheating make it possible to generate direct and indirect signatures that might be detectable in the future. They are addressed briefly below.

While the primordial density power spectrum is not affected by the thermal history (see Section 2.2), a full understanding of the history from inflation until today is required to relate length scales in the early Universe to the length scales observed in the present Universe. Since it is not known how reheating has actually proceeded, there is some uncertainty in mapping scales observed in the CMB to the corresponding scales during inflation. To obtain a relation that performs this matching, the history of the Universe is divided into different periods. Considering some scale k which leaves the horizon during inflation at time t_k when $k = a_k H_k$, it has to be evolved until the end of inflation, from there to the end of reheating and finally to the present time. Relating it to the present size of the horizon, one obtains the expression

$$\frac{k}{a_0 H_0} = \frac{a_k H_k}{a_0 H_0} = \frac{a_k}{a_{\mathrm{end}}} \frac{a_{\mathrm{end}}}{a_{\mathrm{reh}}} \frac{a_{\mathrm{reh}}}{a_{\mathrm{eq}}} \frac{H_k}{H_{\mathrm{eq}}} \frac{a_{\mathrm{eq}} H_{\mathrm{eq}}}{a_0 H_0} \,. \tag{1.63}$$

Here the subscript “eq” refers to a quantity evaluated at matter-radiation equality. Assuming matter-dominated expansion during reheating, $\rho \sim a^{-3}$, and a radiation-dominated universe, $\rho \sim a^{-4}$ from the end of reheating until matter-radiation equality Eq. (1.63) can be written as [52]

$$\frac{k}{a_0 H_0} = e^{-\mathcal{N}(k)} \left(\frac{\rho_{\mathrm{reh}}}{\rho_{\mathrm{end}}}\right)^{1/3} \left(\frac{\rho_{\mathrm{eq}}}{\rho_{\mathrm{reh}}}\right)^{1/4} \frac{H_k}{H_{\mathrm{eq}}} \frac{a_{\mathrm{eq}} H_{\mathrm{eq}}}{a_0 H_0} \,. \tag{1.64}$$

For scales that left the horizon during inflation one can make use of the slow-roll approximation to express H_k in terms of the inflaton potential $V(\varphi_k) = V_k$. Using additionally that $a_{\mathrm{eq}} H_{\mathrm{eq}}/(a_0 H_0) = 219 \Omega_{m,0} h$ [52], and solving Eq. (1.64) for $\mathcal{N}$, we obtain the number of e-folds before the end of inflation as a function of k [119],

$$\mathcal{N}(k) = 66 - \ln\left(\frac{k}{a_0 H_0}\right) - \frac{1}{12} \ln\left(\frac{\rho_{\mathrm{end}}}{\rho_{\mathrm{reh}}}\right) + \ln\left(\frac{V_k^{1/4}}{M_{\mathrm{Pl}}}\right) + \ln\left(\frac{V_k^{1/4}}{\rho_{\mathrm{end}}^{1/4}}\right) \,. \tag{1.65}$$

This relation is also known as the matching equation. The uncertainty in the duration of reheating and thus the uncertainty in the energy density ρ_{reh} at the end of reheating affects $\mathcal{N}(k)$ and inflationary observables.

The fragmentation of the inflaton field during reheating might lead to the generation of gravitational waves (see Section 5.5) that might be observable in the present as a stochastic gravitational wave background (SGWB) [120–131]. As will be discussed in Section 2.2.5, inflation itself produces a gravitational wave spectrum that originates from the quantisation of tensor perturbations and can be observed via the polarisation of the CMB. This is in contrast to the gravitational waves from reheating that result from the production and evolution of inhomogeneities on subhorizon scales which is described by classical equations of motion. The frequencies of the emerging gravitational waves during reheating are redshifted due to the expansion of space. Thus, the uncertainty in the exact evolution and duration of the reheating epoch (cf. Eqs. (1.63) and (1.64)) translates to uncertainties in the frequencies that one would observe today.

Furthermore, different reheating processes can provide explanation attempts for the observed baryon asymmetry in our Universe [132–137] and produce primordial magnetic fields which might explain the large-scale magnetic fields in the present Universe [138, 139]. Of increasing interest is also the possible formation of PBHs which can arise from the fragmentation of the inflaton field on subhorizon scales and the subsequent creation of large inhomogeneities [41, 140–152]. PBHs with small masses will evaporate quickly and might contribute to the thermalisation of the Universe while PBHs that survive the reheating process would act as a potential dark matter component. Note that the production of PBHs during reheating is different to the standard PBH formation scenario (see Section 1.2.1) that is related to the collapse of inflationary density perturbations when they re-enter the horizon during radiation-domination.

1.3 Axion Dark Matter

As discussed previously in Section 1.1.2, it is still unclear what dark matter is made of. A popular candidate motivated by particle physics is the axion which was originally introduced to solve the so-called strong CP problem of Quantum Chromodynamics (QCD). The initial concept of the QCD axion has been extended to axion-like-particles (ALPs) which can appear over a wide mass range in string theory. Since they can be treated as a classical, nonrelativistic scalar field, they are of interest for cosmological structure formation. In this section, the origin of the QCD axion and its potential production mechanisms in the early Universe are discussed. This is relevant for the possible formation of axion miniclusters studied in Chapter 4.

1.3.1 The Origin of the Axion

The QCD Lagrangian has two contributions violating charge (C) and parity (P), meaning that it is not invariant under the parity transformation $\mathbf{x} \longrightarrow -\mathbf{x}$ and the charge conjugation which reverses the charge of a particle. The first CP-violating term was originally added to the QCD Lagrangian in order to solve the U(1) problem of QCD and reads [153, 154]

$$\mathcal{L}_{\theta_{\mathrm{QCD}}} = \frac{g_s^2}{32\pi^2}\theta_{\mathrm{QCD}} G^a_{\mu\nu}\widetilde{G}^{a\,\mu\nu} \,. \tag{1.66}$$

Here, $G^a_{\mu\nu}$ is the gluon field tensor, $\widetilde{G}^{a\,\mu\nu} = \epsilon^{\mu\nu\lambda\rho}G^a_{\lambda\rho}/2$, θ_{QCD} is a dimensionless parameter and g_s is the coupling constant between gluons and quarks. The other CP-violating contribution comes from the coupling of the quarks to the electroweak sector which arises due to a phase in the complex mass matrix M_q. This can be taken into account by replacing θ_{QCD} from the Lagrangian in Eq. (1.66) with [155]

$$\bar{\theta} = \theta_{\mathrm{QCD}} + \arg(\det M_q) \,. \tag{1.67}$$

This parameter is 2π-periodic and combines the two CP-violating contributions. Thus, if $\bar{\theta} = 0$ there is no CP-violation. Importantly, it is directly related to the electric dipole moment d_n of the neutron [156]

$$d_n \approx 3.6 \times 10^{-16}\bar{\theta}\, e\,\mathrm{cm} \,, \tag{1.68}$$

where e denotes the charge of the neutron. This relation can be used to deduce the value of $\bar{\theta}$ from measurements of d_n. Recent results constrain the dipole moment to $|d_n| \lesssim 1.8 \times 10^{-26}\, e\,\mathrm{cm}$ [157] which according to Eq. (1.68) translates to $|\bar{\theta}| \lesssim 10^{-10}$. This poses a fine-tuning issue known as the strong CP problem since there exists no explanation from first principles why $\bar{\theta} \longrightarrow 0$.

Roberto Peccei and Helen Quinn proposed a mechanism to solve the strong CP problem by introducing a global chiral U(1) symmetry [158, 159], usually referred to as the Peccei-Quinn (PQ) symmetry. It is spontaneously broken by the vacuum expectation value of a complex scalar field with angular part $e^{i\phi/f_a}$. The energy scale of symmetry breaking is f_a and the QCD axion ϕ is the Nambu-Goldstone boson of the broken symmetry [160, 161]. Initially, it is massless and obeys the shift symmetry $\phi \longrightarrow \phi + \mathrm{const}$. To obtain a mass, the shift symmetry must be broken at some energy scale. This occurs at the time of QCD phase transition when nonperturbative effects such as instantons [25] become relevant at temperature $T \sim \Lambda_{\rm QCD} \sim 200\,\rm MeV$. The axion shift symmetry is then explicitly broken which generates an effective axion potential. By relaxing to its minimum at $\phi = -f_a\bar{\theta}$, the axion obtains a mass and the value of the CP-violating parameter $\bar{\theta}$ is shifted to zero which solves the strong CP problem. The originally introduced QCD axion has a mass of $m_a \simeq 25\,\rm keV$, however, it was soon excluded [162, 163]. Since the axion decay constant f_a can be chosen freely if new particles are introduced, much smaller axion masses are allowed in other models. Examples are the KSVZ [164, 165] and the DFSZ [166, 167] model, where heavy quarks and an additional Higgs field, respectively, are introduced beside the complex PQ scalar field. Importantly, the axion is stable on cosmological timescales and is thus an attractive dark matter candidate [168–170].

It is possible to compute the mass of the QCD axion in chiral perturbation theory which gives [171, 172]

$$m_a \simeq 5.7 \times 10^{-6}\,\rm eV \left(\frac{10^{12}\,\rm GeV}{f_a}\right) \tag{1.69}$$

at zero temperature. Upper limits on the axion decay constant come from supernova cooling [25, 173, 174] while black hole superradiance can constrain the axion in limited lower mass ranges [25, 175]. Taking them into account, the allowed QCD axion mass lies in the range $8 \times 10^{-11}\,\rm eV \lesssim m_a \lesssim 4 \times 10^{-2}\,\rm eV$ [25, 176]. Note that the QCD axion mass is temperature-dependent which is encoded via $m_a^2(T) f_a^2 = \chi(T)$ in the topological susceptibility $\chi(T)$. A calculation based on the interacting instanton liquid model valid at high temperatures $T > 1\,\rm GeV$ predicts the power-law relation [177]

$$m_a^2(T) = \frac{\alpha_a \Lambda_{\rm QCD}^4}{f_a^2}\left(\frac{T}{\Lambda_{\rm QCD}}\right)^{-n}, \tag{1.70}$$

with coefficients $n = 6.68$ and $\alpha_a = 1.68 \times 10^{-7}$. Similar results were obtained from lattice QCD computations [178, 179]. This relation has to be truncated at low temperatures $T < \Lambda_{\rm QCD}$ in order to match the axion mass at zero temperature from Eq. (1.69).

Not being able to necessarily solve the strong CP problem, a large number of ALPs can be produced in string theory [180–182]. In principle, they can arise alongside the QCD axion with a similar production mechanism. For example, they can also result as a Nambu-Goldstone boson from the breaking of a U(1) symmetry at scale f_a. The boson acquires a mass when the temperature of the universe drops below some reference scale Λ_a. As Λ_a can be quite low and f_a in principle also arbitrarily large, the mass of an ALP $m_a \sim \Lambda_a^2/f_a$ can become quite small. Accordingly, the parameter space for ALPs is distinctly larger than the one for QCD axions. In particular, this allows the production of an ALP with mass $m \sim 10^{-22}\,\rm eV$ which is adopted in the FDM model to approach the small-scale challenges of the ΛCDM model.

1.3.2 Production of Axion Dark Matter

Once the PQ symmetry is broken, the massless axion field takes a random initial value within the horizon at that time. In terms of the dimensionless angular field $\theta = \phi/f_a$, the shift symmetry of the axion field requires that the initial value θ_i lies within[16] $-\pi$ and π [25]. Depending on the time when the PQ symmetry is spontaneously broken, one can make different predictions about the abundance of the produced axions. If the PQ is unbroken during inflation, also known as the *post-inflationary* scenario, θ takes a different random value on each Hubble patch. Thus, the massless axion field is inhomogeneous on scales larger than the size of the horizon. These small-scale inhomogeneities are the seeds of axion miniclusters [27–30] that arise from their gravitational collapse after the axion field has acquired a mass at some energy scale Λ_a. The formation of axion miniclusters is discussed in Chapter 4. Additionally, according to the Kibble mechanism [183] the breaking of the PQ symmetry gives rise to topological defects such as axion strings and domain walls [25]. Since θ takes different values on different Hubble patches it can wind from $-\pi$ to π around a given point in space. Decreasing the loop around this point, one ends up in the point itself where θ cannot continuously change from $-\pi$ to π anymore. This results in a string-like topological defect [25]. Domain walls occur once the axion becomes massive and are 2D surfaces of a nearly constant θ connecting different strings. They pull strings together which eventually leads to the destruction of the string-domain wall network and the production of both relativistic and nonrelativistic axions [25]. The post-inflationary scenario is the relevant scenario for the QCD axion if they have a symmetry breaking scale of $f_a \lesssim 10^{12}$ GeV which is a good target region for axion detection experiments using a microwave cavity [184].

For ALPs with much lighter masses, the symmetry breaking scale is usually much larger and PQ symmetry breaking takes place during inflation. This situation is known as the *pre-inflationary* scenario where each Hubble patch of different θ is stretched nearly exponentially such that the size of a single patch can be actually larger than the size of the horizon at present time. Thus, the axion field is homogenised in this scenario taking a uniform value of θ everywhere. Note that topological defects are also created similarly to the post-inflationary scenario. However, they are diluted during inflation in the same way as other defects such as magnetic monopoles (cf. Section 1.2.1). Since the axion field already exists during inflation as a “spectator” field,[17] it is subject to quantum fluctuations that result in isocurvature perturbations. They are created alongside the inflationary adiabatic perturbations (see Section 2.1.4 for a classification of perturbations). In the

---

[16] Note that this is the common convention. In principle, one could also consider for example $\theta_i \in [0, 2\pi]$.

[17] This is in contrast to models of axion inflation where inflation is driven by an axion field [84–86].

pre-inflationary scenario, the isocurvature fluctuations are small on subhorizon scales and are thus not relevant for gravitational structure formation with ALPs. Instead, an axion-like field is attracted by the potential wells generated by the adiabatic perturbations from inflation. This is in contrast to the post-inflationary PQ symmetry breaking case relevant for QCD axions, where the resulting inhomogeneities on small scales are also of the isocurvature type, but of much larger amplitude, and thus can gravitationally collapse into axion miniclusters at early times.

Both scenarios have in common that axion dark matter is produced non-thermally via the *misalignment mechanism*. Once the shift symmetry of the axion field is explicitly broken at the energy scale $\Lambda_a \sim (m_a f_a)^{1/2}$, it develops a potential and acquires a mass. If the axion field value, expressed in terms of the misalignment angle[18] $\theta = \phi / f_a$, does not align with the minimum of the potential but is instead displaced, it will roll down the potential and perform oscillations around its minimum.[19] Usually, the axion potential is written as [25]

$$V(\phi) = m_a^2 f_a^2 \left[1 - \cos\left(\frac{\phi}{f_a}\right)\right] , \tag{1.71}$$

which can be approximated as the quadratic potential $V(\phi) = m_a^2 \phi^2/2 = m_a^2 f_a^2 \theta^2/2$ if θ is not displaced far from the minimum. The corresponding equation of motion is given by the Klein-Gordon Eq. (1.24) that is valid for any massive oscillating scalar field, so, for example, both for the inflaton during reheating and the axion. In terms of θ it can be written as

$$\ddot{\theta} + 3H\dot{\theta} - \frac{\nabla^2 \theta}{a^2} + \frac{1}{f_a^2} \frac{\partial V(\theta)}{\partial \theta} = 0 \tag{1.72}$$

with the axion potential given in Eq. (1.71). Note that the mass m_a in the axion potential is temperature- and thus time-dependent for QCD axions such that the full evolution equation of θ can only be solved numerically. Considering the pre-inflationary scenario for convenience, where one can assume a constant ALP mass, the axion field is homogeneous, i.e. $\nabla\theta = 0$. Together with the quadratic approximation of the axion potential, it is then possible to find an exact solution of Eq. (1.72) provided the background universe is either radiation- or matter-dominated [25]. This is useful to gain insight into the general evolution of the axion field after symmetry breaking. Adopting a radiation-dominated background universe and the initial conditions $\theta_i = 1$, $\dot{\theta}_i = 0$, the solution for θ as well as the energy density ρ_a (cf. Eq. (1.26)), the comoving number density $n_a = \rho_a a^3/m_a$,

---

[18] Here we assume a domain wall number set to one.

[19] Note that this is similar to the behaviour of the inflaton field at the end of inflation described in Section 1.2.3.

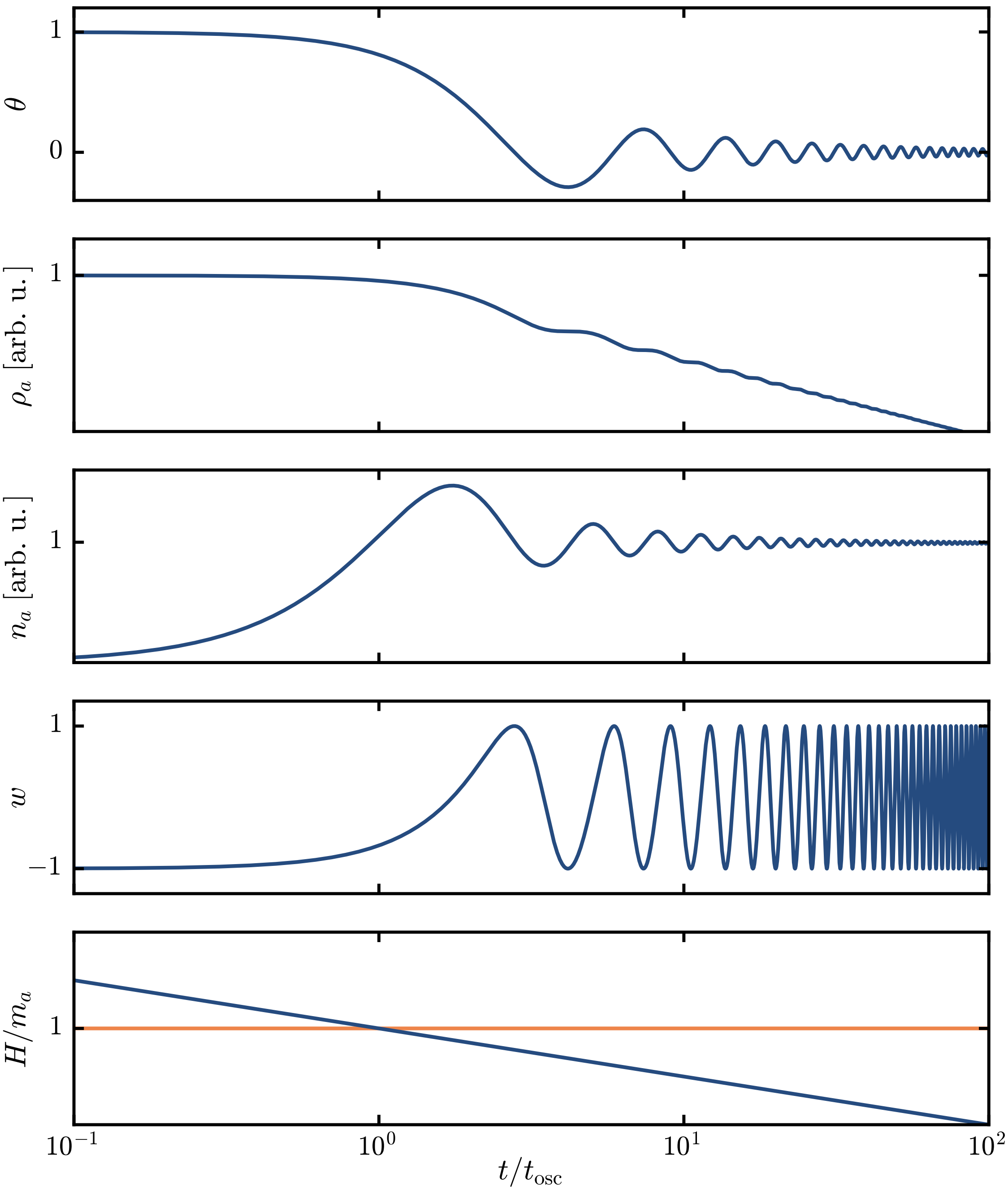

Figure 1.3 | Evolution of the axion field θ, its energy density ρ_a, comoving number density n_a, equation of state parameter w and H/m_a for an initially misaligned field $\theta_i = 1$ in a radiation-dominated background universe. The time coordinate is normalised to the time $t_{\rm osc}$ when the axion field begins to oscillate at $H \simeq m_a$.

the equation of state parameter w and the Hubble parameter are shown in Fig. 1.3. Initially, the Hubble parameter is much larger than the axion mass and the axion field is overdamped. Once $H \sim m_a$, the field starts to oscillate around zero. Averaged over many oscillations, the energy density of the axion scales as $\rho_a \sim a^{-3}$ and accordingly the comoving number density approaches a constant. This is similar to nonrelativistic matter which makes the axion a well-motivated CDM candidate. While the equation of state parameter is initially fixed at $w = -1$, i.e. behaving as a dark energy component, it oscillates between $w = -1$ and $w = 1$ at late times with an average value of $\langle w \rangle = 0$ which is similar to $w = 0$ for CDM.

The production of axions via the misalignment mechanism allows the energy density parameter $\Omega_{a,0}$ of axion dark matter at the present time to be computed as a function of initial field displacement and the axion mass. Defining a_{osc} as the scale factor at the time when the field starts to oscillate ($H(a_{\mathrm{osc}}) = m_a$), the axion energy density at later times $a > a_{\mathrm{osc}}$ is determined by

$$\rho_a(a) \simeq \rho_a(a_{\mathrm{osc}}) \left(\frac{a_{\mathrm{osc}}}{a}\right)^3 . \tag{1.73}$$

Since ρ_a is nearly constant until the field starts to oscillate, one can approximate $\rho_a(a_{\mathrm{osc}})$ as $\rho_a(a_{\mathrm{osc}}) \approx m_a^2 \phi_i^2/2$. Considering low-mass ALPs in the mass range $10^{-24}\,\mathrm{eV} \leq m_a \leq 10^{-12}\,\mathrm{eV}$, the density parameter can be approximated as [185]

$$\Omega_{a,0} \approx \frac{1}{6}(9\Omega_{r,0})^{3/4} \left(\frac{m_a}{H_0}\right)^{1/2} \left(\frac{\phi_i}{M_{\mathrm{Pl}}}\right)^2 , \tag{1.74}$$

which depends on the initial field displacement ϕ_i, the ALP mass m_a and the present values of the Hubble parameter and the radiation energy density parameter. Demanding that dark matter consists entirely of ALPs, $\Omega_{a,0} = \Omega_{c,0} = 0.262$, one can find a set of parameters (m_a, ϕ_i) that gives the correct dark matter density. This requires for low-mass ALPs that $\phi_i > 10^{14}\,\mathrm{GeV}$ [25]. Hence, they are relevant only in the pre-inflationary PQ symmetry breaking scenario as the Hubble parameter is $\lesssim 10^{13}\,\mathrm{GeV}$ at the end of inflation [89].

Due to the temperature-dependent mass term (see Eq. (1.70)) and the formation of topological defects the computation of the relic density is more complicated for QCD axions. Beginning with the contribution from the misalignment mechanism, one can define as before $H(T_{\mathrm{osc}}) = m_a(T_{\mathrm{osc}})$ as the time the axion starts to oscillate. For QCD axions with $f_a < 2 \times 10^{15}\,\mathrm{GeV}$ this occurs when $T > 1\,\mathrm{GeV}$ which is slightly above Λ_{QCD} [186]. Thus the mass $m_a(T_{\mathrm{osc}})$ of the axion at the beginning of the oscillations together with the misalignment angle θ_i determines the energy density which scales as a^{-3} afterwards. Considering *only* the misalignment mechanism, this allows the present QCD axion density parameter to be estimated as [186]

$$\Omega_{a,0} h^2 \sim 2 \times 10^4 \left(\frac{f_a}{10^{16}\,\mathrm{GeV}}\right)^{7/6} \langle \theta_i^2 \rangle . \tag{1.75}$$

This assumes that the axion potential can be approximated as a quadratic potential which is only justified for small misalignment angles close to the minimum of the potential. If the initial displacements are large, axion self-interactions that are implicitly present in the cosine potential from Eq. (1.71) lead to an anharmonic correction factor $\mathcal{F}$ such that θ_i in Eq. (1.75) needs to be replaced with $\mathcal{F}\theta_i$ [25, 187]. In the post-inflationary scenario relevant for the formation of axion miniclusters (see Chapter 4), each causally disconnected patch takes a different value of $\theta_i \in [-\pi, \pi]$ such that $\langle \theta_i^2 \rangle = \pi^2/3$ is fixed [25]. To avoid overproduction of dark matter by the misalignment mechanism, one demands that $\Omega_{a,0}h^2 < 0.12$ which in this scenario yields constraints on the PQ symmetry breaking scale, 10^9 GeV $\lesssim f_a \lesssim 10^{11}$ GeV [25]. It is known for a long time that the production of axions can be significantly enhanced by the decay of the network of axion strings and domain walls [188–195]. Nevertheless, the precise amount of produced axions from the decay of topological defects is still uncertain and overall, the evolution of axion strings and the evolved physical processes is a highly debated subject [196–206]. Note that if the axion contribution from strings were significantly larger than from misalignment, dark matter consisting of QCD axions would be completely excluded by astrophysical constraints [25].

QCD axions are weakly coupled to the Standard Model of particle physics.[20] Highly relevant for axion detection experiments is the coupling of the QCD axion to photons. Additionally, they interact with other particles gravitationally which is of significance for cosmological structure formation. Since ALPs motivated by string theory are expected to interact even solely via gravity, both QCD axions and ALPs are in general excellent dark matter candidates [168, 170]. As discussed above, they are produced to a large amount non-thermally via the misalignment mechanism which guarantees that they are nonrelativistic and thus well-motivated CDM candidates. They can even account for the entire abundance of CDM in our Universe. Apart from the non-thermal decay of topological defects, QCD axions can in principle also be generated by a thermal process of pion scattering [208–210] which could contribute as hot dark matter. However, the thermal population is negligible for QCD axions with $f_a \gtrsim 10^9$ GeV [25] that are relevant for the formation of axion miniclusters.

---

[20] See Ref. [207] for the computation of their couplings to photons and electrons.

Chapter 2

Growth and Collapse of Density Perturbations

We considered a perfectly homogeneous universe in Section 1.1. While the assumption of homogeneity is justified on the largest scales, we know that our Universe is far from homogeneous on smaller scales. This poses the question of where the observed structures in our Universe come from and how they have formed. In other words, we require a mechanism to generate the initial conditions building the seeds of all structures at the present time and their subsequent evolution. Interestingly, the idea of an inflationary phase of accelerated expansion in the very early Universe does not only solve the flatness, horizon and monopole problems (see Section 1.2.1) but also provides an explanation for the existence of primordial density fluctuations. Although they are initially quite small, they start to grow gravitationally and collapse eventually into bound structures such as dark matter halos and galaxies.

This chapter gives an overview of the generation of inflationary perturbations, their linear gravitational growth and the methods that can be applied to study their nonlinear collapse. The foundation is laid in Section 2.1 which briefly introduces the concept of cosmological perturbations by perturbing both the metric and the stress-energy tensor in the Einstein field equations. Considering the perturbed FLRW spacetime and adding fluctuations to the homogeneous background inflaton field in Section 2.2, allows us to derive the evolution equation of inflationary perturbations known as the Mukhanov-Sasaki equation. Quantising the fluctuations is the key to obtaining the primordial curvature power spectrum that can be probed by the CMB. In a similar manner, one can compute the power spectrum of primordial gravitational waves. The evolution of matter density perturbations on subhorizon scales, where Newtonian perturbation theory applies, is then discussed in Section 2.3. As this is restricted to their linear evolution, Section 2.4 outlines models to study their eventual gravitational collapse which includes both analytical and semi-analytical models as well as numerical N-body simulations.

2.1 Cosmological Perturbations

In order to study the evolution of initially small density perturbations, one relies on the use of perturbation theory. While it is possible to use Newtonian perturbation theory for the growth of cosmological structures on scales smaller than the Hubble horizon (see Section 2.3), the perturbation theory of General Relativity gives a complete description on all scales. The idea is to consider a *perturbed* spacetime that is very close to the *background* spacetime.[21] The Einstein equations couple perturbations both in the metric $g_{\mu\nu}$ and in the stress-energy tensor $T_{\mu\nu}$. The perturbed tensors can be written as

$$g_{\mu\nu}(\tau, \mathbf{x}) = \bar{g}_{\mu\nu}(\tau) + \delta g_{\mu\nu}(\tau, \mathbf{x}) \,, \tag{2.1}$$

$$T_{\mu\nu}(\tau, \mathbf{x}) = \bar{T}_{\mu\nu}(\tau) + \delta T_{\mu\nu}(\tau, \mathbf{x}) \,. \tag{2.2}$$

In the following, we consider *cosmological perturbation theory* where the background spacetime is described by the flat FLRW metric and the background stress-energy tensor takes the form of a perfect fluid (cf. Eq. (1.5)). This is suited to our needs and simplifies calculations significantly. Additionally, the equations of motion are perturbed only to linear order which allows us to evolve different types of perturbations independently from each other and to treat them separately. Concretely, one makes use of the so-called *SVT-decomposition* to decompose the metric and stress-energy perturbations into scalar (S), vector (V) and tensor (T) perturbations. While tensor perturbations describe *gravitational waves* that do not appear in Newtonian perturbation theory, vector perturbations are related to the rotational velocity perturbations of the cosmic fluid. They decay in an expanding universe and are thus not relevant from a cosmological point of view. In this section, only scalar perturbations are covered as they couple to density perturbations and show gravitational instability resulting in the formation of structures in our Universe [53].

Importantly, the decomposition of the spacetime into a background and a perturbation depends on the chosen coordinate system $x = (\tau, \mathbf{x})$. So far we have considered the case of a homogeneous and isotropic universe where the coordinate system was chosen such that the spacetime is given by the FLRW metric. However, there are in principle no preferred coordinates for the perturbed spacetime as there are many coordinate systems that can fulfil Eq. (2.1). Selecting a specific coordinate system defines the so-called *gauge* in cosmological perturbation theory. Sometimes it proves to be useful to change

---

[21] Background quantities are marked with a bar on top of a variable in this thesis.

the chosen coordinate system by a small coordinate transformation which is known as *gauge transformation*. While choosing an appropriate gauge can simplify calculations significantly, one has to be clear about which perturbations are actual physical and which only arise from the chosen gauge and are thus spurious. To avoid any misinterpretations, it is therefore helpful to introduce gauge-invariant quantities as they do not change under a coordinate transformation. Another possibility is to fix the gauge by constraining the perturbations such that the coordinate system is fully defined [211].

In this section, we briefly summarise some main results from cosmological perturbation theory and introduce the *Newtonian* gauge that is used in the derivation of the equations of motion. As mentioned before, we focus only on scalar perturbations as they are associated with the gravitationally unstable density perturbations that are of particular interest in this thesis. Appendix A briefly introduces the SVT-decomposition and deals with gauge transformations of different types of perturbations as well as with particular gauge choices without going into too much detail. Furthermore, Appendix A provides derivations of some relevant equations that are used in this section.

2.1.1 Metric Perturbations

Considering first-order perturbations to the homogeneous background metric $\bar{g}_{\mu\nu}$ given by the FLRW metric, the perturbed line element can be written as [53]

$$\mathrm{d}s^2 = a^2\left[-(1+2A)\mathrm{d}\tau^2 - 2B_i\mathrm{d}\tau\,\mathrm{d}x^i + ((1-2D)\delta_{ij} + 2E_{ij})\mathrm{d}x^i\,\mathrm{d}x^j\right]\ . \tag{2.3}$$

Here, $A(\tau, x^i)$ is the so-called *lapse* function, $B_i(\tau, x^i)$ is the *shift* vector, $D = -h^i_i/6$ carries the trace of the spatial metric perturbation h_{ij} and E_{ij} is a symmetric and trace-less *shear* tensor, $E^i_i = 0$. Thus, the perturbed metric consists of the two scalar perturbations A and D, the vector perturbation B_i and the tensor perturbation E_{ij}.

We are interested in the scalar perturbations only, so we make use of the SVT-decomposition (see Appendix A.1 for details) of the perturbations. This splits the vector B_i into the gradient of a scalar B and a divergenceless vector B^V_i, i.e. $\delta_{ij}\partial_j B^V_i = 0$, such that $B_i = -\partial_i B + B^V_i$. Similarly, one can decompose the symmetric tensor $E_{ij} = E^S_{ij} + E^V_{ij} + E^T_{ij}$ into a scalar E^S_{ij}, a vector E^V_{ij} and a tensor E^T_{ij}, where the scalar component is given by $E^S_{ij} = (\partial_i\partial_j - \frac{1}{3}\delta_{ij}\nabla^2)E$. Replacing the full perturbations in Eq. (2.3) by the scalar ones, the perturbed metric for scalar perturbations reads

$$\mathrm{d}s^2 = a^2\left[-(1+2A)\mathrm{d}\tau^2 + 2\partial_i B\mathrm{d}\tau\,\mathrm{d}x^i + ((1-2\psi_{\mathcal{R}})\delta_{ij} + 2\partial_i\partial_j E)\mathrm{d}x^i\,\mathrm{d}x^j\right]\ , \tag{2.4}$$

where we defined the so-called *curvature perturbation*[22] [53]

$$\psi_{\mathcal{R}} = D + \frac{1}{3}\nabla^2 E \,. \tag{2.5}$$

As mentioned earlier, a change in the coordinate system can affect the perturbations and might introduce spurious perturbations. The gauge transformation rules of the scalar perturbations A, B, D, E in Eq. (2.4) can be found in Eqs. (A.25) to (A.28). Accordingly, the curvature perturbation transforms as [212]

$$\psi_{\mathcal{R}} \longrightarrow \psi_{\mathcal{R}} + \mathcal{H}\xi^0 \,. \tag{2.6}$$

under the gauge transformation $x^\mu \longrightarrow x^\mu + \xi^\mu$. It is possible to construct combinations of the scalar metric perturbations that do not change under a gauge transformation. Two gauge-invariant quantities, which will prove to be particularly useful, are the so-called *Bardeen potentials.* They are defined as [53]

$$\begin{aligned} \Phi &= A + \mathcal{H}(B - E') + (B - E')' \,, \\ \Psi &= D + \frac{1}{3}\nabla^2 E - \mathcal{H}(B - E') = \psi_{\mathcal{R}} - \mathcal{H}(B - E') \,. \end{aligned} \tag{2.7}$$

Furthermore, it is sometimes wise to pick a certain gauge and keep it fixed as this can simplify computations enormously. An overview of some particular gauge choices that prove to be useful can be found in Appendix A.3. In the remainder of this section, we will make use of the *conformal Newtonian* gauge that is defined by $B^N = E^N = 0$.

Metric in Conformal Newtonian Gauge

The Bardeen potentials in the conformal Newtonian gauge are equal to the metric perturbation ($\Phi = A^N$) and to the curvature perturbation ($\Psi = \psi_{\mathcal{R}}^N$), respectively. The metric in Eq. (2.4) then reduces to [53]

$$\mathrm{d}s^2 = a^2 \left[-(1 + 2\Phi)\mathrm{d}\tau^2 + (1 - 2\Psi)\delta_{ij}\mathrm{d}x^i\, \mathrm{d}x^j \right] \,. \tag{2.8}$$

The advantage of the Newtonian gauge is that the gauge invariance of Ψ and Φ allows the derivation of gauge-invariant equations of motion in a rather simple way. Therefore, it is particularly suited for studying the growth of large-scale structures in the universe (see Section 2.3).

---

[22] Note that we use $\psi_{\mathcal{R}}$ here instead of the common ψ because we reserve the variable ψ for the wave function of a scalar field in Chapter 3.

2.1.2 Matter perturbations

The stress-energy tensor $\bar{T}^{\mu\nu}$ of the unperturbed FLRW universe is described by the background quantities density $\bar{\rho}$, pressure $\bar{p}$ and 4-velocity $\bar{u}^\mu$ (cf. Eq. (1.5)). We now define density, pressure and velocity perturbations as $\delta\rho = \rho - \bar{\rho}$, $\delta p = p - \bar{p}$ and $\delta u^i = u^i - \bar{u}^i$, respectively. Exploiting isotropy, the background velocity is $\bar{u}^\mu = (\bar{u}^0, 0, 0, 0)$ and since $\bar{u}^\mu \bar{u}_\mu = a^2 \eta_{\mu\nu} \bar{u}^\mu \bar{u}^\nu = -a^2 (\bar{u}^0)^2 = -1$, one finds $\bar{u}^\mu = a^{-1}(1, 0, 0, 0)$ and $\bar{u}_\mu = a(-1, 0, 0, 0)$. Writing now the velocity perturbation as $u^i = \delta u^i = v^i/a$, the 4-velocity can be expressed as

$$u^\mu = a^{-1}(1 + a\delta u^0, v^i)\,, \quad \text{and} \quad u_\mu = (-a + \delta u_0, \delta u_i)\,. \tag{2.9}$$

Using now the metric $g_{\mu\nu}$ given by (cf. Eq. (2.3))

$$[g_{\mu\nu}] = a^2 \begin{bmatrix} -1 - 2A & -B_i \\ -B_i & (1 - 2D)\delta_{ij} + 2E_{ij} \end{bmatrix},$$

and considering only perturbations to first-order, one obtains that $\delta u_0 = -(a^2 \delta u^0 + 2aA)$, $\delta u^0 = -A/a$, $\delta u_i = -aB_i + av_i$. Thus, we have

$$u^\mu = a^{-1}(1 - A, v^i)\,, \quad \text{and} \quad u_\mu = a(-1 - A, v_i - B_i)\,. \tag{2.10}$$

Inserting these expressions into $T^\mu_{\ \nu} = (\rho + p)u^\mu u_\nu + p\delta^\mu_{\ \nu}$, the perturbed stress-energy tensor to linear order in perturbations can be written as [212]

$$\begin{aligned} T^0_{\ 0} &= -(\bar{\rho} + \delta\rho)\,, & (2.11)\\ T^0_{\ i} &= (\bar{\rho} + \bar{p})(v_i - B_i)\,, & (2.12)\\ T^i_{\ 0} &= -(\bar{\rho} + \bar{p})v_i\,, & (2.13)\\ T^i_{\ j} &= (\bar{p} + \delta p)\delta^i_j + \Sigma^i_{\ j}\,. & (2.14) \end{aligned}$$

Here, $\Sigma^i_{\ j}$ is the so-called anisotropic stress and defined as $\Sigma^i_{\ j} \equiv \delta T^i_{\ j} - \frac{1}{3}\delta^i_{\ j}\delta T^k_{\ k}$. The anisotropic stress vanishes in the unperturbed FLRW universe, i.e. for a perfect fluid, as it appears only as a first-order perturbation. As before, one can make use of the SVT-decomposition (see Appendix A.1) to consider only scalar perturbations. In Newtonian gauge ($B^N = 0$), the perturbed components of the stress-energy tensor then read[23] [212]

$$\delta T^0_{\ 0} = -\delta\rho^N\,, \tag{2.15}$$

$$\delta T^0_{\ i} = -(\bar\rho + \bar p)\partial_i v^N \tag{2.16}$$

$$\delta T^i_{\ 0} = (\bar\rho + \bar p)\partial_i v^N\,, \tag{2.17}$$

$$\delta T^i_{\ j} = \delta p^N \delta^i_{\ j} + \bar p\left(\partial_i\partial_j - \frac{1}{3}\delta_{ij}\nabla^2\right)\Pi\,, \tag{2.18}$$

where Π is the scalar perturbation from the tensor perturbation $\Pi^i_{\ j}$ that is directly related to the anisotropic stress via $\Pi^i_{\ j} \equiv \Sigma^i_{\ j}/\bar p$. Note that the anisotropic stress is gauge-invariant (see Eq. (A.32)) which is the reason why Π in Eq. (2.18) does not carry the superscript N.

2.1.3 Equations of Motion in Newtonian Gauge

In this section, we collect the equations of motion for scalar perturbations to linear order, working in the Newtonian gauge where the perturbed metric is given by Eq. (2.8). Keeping only terms up to first-order in the Bardeen potentials Ψ and Φ, the associated connection coefficients $\Gamma^\rho_{\ \mu\nu} = \bar\Gamma^\rho_{\ \mu\nu} + \delta\Gamma^\rho_{\ \mu\nu}$ defined by Eq. (1.3) are [213]

$$\bar\Gamma^0_{\ 00} = \mathcal{H}\,, \qquad \delta\Gamma^0_{\ 00} = \Phi'\,, \tag{2.19}$$

$$\bar\Gamma^i_{\ 00} = 0\,, \qquad \delta\Gamma^i_{\ 00} = \partial_i\Phi\,, \tag{2.20}$$

$$\bar\Gamma^0_{\ i0} = 0\,, \qquad \delta\Gamma^0_{\ i0} = \partial_i\Phi\,, \tag{2.21}$$

$$\bar\Gamma^0_{\ ij} = \mathcal{H}\delta_{ij}\,, \qquad \delta\Gamma^0_{\ ij} = -\left(\Psi' + 2\mathcal{H}(\Psi + \Phi)\right)\delta_{ij}\,, \tag{2.22}$$

$$\bar\Gamma^i_{\ j0} = \mathcal{H}\delta^i_j\,, \qquad \delta\Gamma^i_{\ j0} = -\Psi'\delta^i_j\,, \tag{2.23}$$

$$\bar\Gamma^i_{\ jk} = 0\,, \qquad \delta\Gamma^i_{\ jk} = -(\partial_k\Psi\delta^i_j + \partial_j\Psi\delta^i_k) + \partial_i\Psi\delta_{jk}\,. \tag{2.24}$$

The connection coefficients will be used in the derivation of the perturbed Einstein and conservation equations below.

Perturbed Einstein Equations

Expanding the Einstein equations to first-order in perturbations and subtracting the background equation $\bar G^\mu_{\ \nu} = 8\pi G\bar T^\mu_{\ \nu}$, the perturbed Einstein equations read

$$\delta G^\mu_{\ \nu} = 8\pi G\delta T^\mu_{\ \nu}\,. \tag{2.25}$$

---

[23] Similar to the metric fluctuations, the perturbations of the stress-energy tensor are gauge-dependent. Its transformation rule can be found in Eq. (A.15) and the explicit transformation behaviour of the scalar perturbations is given in Appendix A.2.2.

While the components of the perturbed stress-energy tensor are given by Eqs. (2.15) to (2.18), a derivation of the perturbed Einstein tensor can be found in Appendix A.4. In short, using the connection coefficients $\Gamma^{\rho}{}_{\mu\nu} = \bar{\Gamma}^{\rho}{}_{\mu\nu} + \delta\Gamma^{\rho}{}_{\mu\nu}$ from Eqs. (2.19) to (2.24), one can compute the Ricci tensor $R^{\mu}{}_{\nu}$ and thus the Einstein tensor $G^{\mu}{}_{\nu}$. Subtracting the background $\bar{G}^{\mu}{}_{\nu}$ from Eqs. (A.46) to (A.48) and using the perturbed components of the stress-energy tensor in Newtonian gauge (see Eqs. (2.15), (2.17) and (2.18)) then gives the perturbed components of the Einstein equations in Newtonian gauge [53]:

$$\delta G^{0}{}_{0} = a^{-2}\left(-2\nabla^2\Psi + 6\mathcal{H}\Psi' + 6\mathcal{H}^2\Phi\right) = -8\pi G\delta\rho^N\,, \tag{2.26}$$

$$\delta G^{i}{}_{0} = 2a^{-2}\partial_i(\Psi' + \mathcal{H}\Phi) = 8\pi G(\bar{\rho} + \bar{p})\partial_i v^N\,, \tag{2.27}$$

$$\begin{aligned}\delta G^{i}{}_{j} &= a^{-2}\left(\partial_i\partial_j(\Psi - \Phi) + [2\Psi'' + \nabla^2(\Phi - \Psi) + \mathcal{H}(2\Phi' + 4\Psi') + (4\mathcal{H}' + 2\mathcal{H}^2)\Phi]\delta^i_j\right)\\ &= 8\pi G\left[\delta p^N\delta^i_j + \bar{p}\left(\partial_i\partial_j - \frac{1}{3}\delta_{ij}\nabla^2\right)\Pi\right]\,.\end{aligned} \tag{2.28}$$

Since the spatial part of the perturbed Einstein equations is quite cumbersome, it is helpful to separate it into its trace and a traceless part. The latter can be obtained by contracting $\delta G^{i}{}_{j}$ and $\delta T^{i}{}_{j}$ with the tensor $P^{j}{}_{i} = \partial^j\partial_i - \frac{1}{3}\delta^j_i\nabla^2$ [212]. This leads to the equation

$$\Psi - \Phi = 8\pi G a^2\bar{p}\,\Pi\,. \tag{2.29}$$

Taking the trace of spatial Einstein equation gives [212]

$$\Psi'' + \mathcal{H}(2\Psi' + \Phi') + (\mathcal{H}^2 + 2\mathcal{H}')\Phi + \frac{1}{3}\nabla^2(\Phi - \Psi) = 4\pi G a^2\delta p^N\,. \tag{2.30}$$

We can drop the spatial derivatives in Eq. (2.27) since the equality of the spatial derivative of two perturbations implies that the perturbations are the same. Then, Eq. (2.27) simplifies to

$$\Psi' + \mathcal{H}\Phi = 4\pi G a^2(\bar{\rho} + \bar{p})v^N\,. \tag{2.31}$$

The Eqs. (2.29) to (2.31) and Eq. (2.26), also known as (relativistic) *Poisson equation*, will be used in Section 2.2 for the derivation of the evolution equation of inflationary perturbations.

Perturbed Conservation Equations

The conservation of the stress-energy tensor, $\nabla_\mu T^{\mu}{}_{\nu} = \partial_\mu T^{\mu}{}_{\nu} + \Gamma^{\mu}{}_{\mu\alpha}T^{\alpha}{}_{\nu} - \Gamma^{\alpha}{}_{\mu\nu}T^{\mu}{}_{\alpha} = 0$, allows us to derive conservation equations for the $\nu = 0$ and the $\nu = i$ components. Considering perturbations to first-order in Ψ and Φ, we obtain the background continuity equation $\bar{\rho}' = -3\mathcal{H}(\bar{\rho} + \bar{p})$ for $\nu = 0$ at zeroth order. Using $v_i^N = -\partial_i v^N$, we can derive an equation for the first-order perturbations [212],

$$\left(\delta\rho^N\right)' = -3\mathcal{H}\left(\delta\rho^N + \delta p^N\right) + (\bar{\rho} + \bar{p})(\nabla^2 v^N + 3\Psi') \,. \tag{2.32}$$

This perturbation equation can thus be understood as a continuity equation and describes the evolution of density perturbations. While the first term on the right of Eq. (2.32) represents the expansion of the background, the $\nabla^2 v^N$ term is an effect of the local fluid flow and the Ψ' term is a relativistic effect that arises from the metric fluctuations. Taking $\nu = i$ and keeping only perturbations to first-order, one finds the perturbation equation [212]

$$(\bar{\rho} + \bar{p})\left(v^N\right)' = -(\bar{\rho} + \bar{p})' v^N - 4\mathcal{H}(\bar{\rho} + \bar{p}) v^N + \delta p^N + \frac{2}{3}\bar{p}\,\nabla^2\Pi + (\bar{\rho} + \bar{p})\Phi \,, \tag{2.33}$$

which corresponds to the Euler equation for a viscous fluid. The term on the left-hand side and the first on the right-hand side of Eq. (2.33) express the change in momentum, the second term on the right-hand side is due to the background expansion, and the remaining terms describe different forces.

Using the background continuity equation, the equation of state parameter $w = \bar{p}/\bar{\rho}$, and introducing the relative density perturbation $\delta \equiv \delta\rho/\bar{\rho}$, the above perturbation equations can be rewritten as [213]

$$\left(\delta^N\right)' = 3\mathcal{H}\left(w\delta^N - \frac{\delta p^N}{\bar{\rho}}\right) + (1 + w)(\nabla^2 v^N + 3\Psi') \,, \tag{2.34}$$

$$\left(v^N\right)' = -\left(\frac{w'}{1 + w} + \mathcal{H}(1 - 3w)\right) v^N + \frac{\delta p^N}{\bar{\rho} + \bar{p}} + \frac{2w}{3(1 + w)}\nabla^2\Pi + \Phi \,. \tag{2.35}$$

Note that Eqs. (2.34) and (2.35) are not independent from the perturbed Einstein Eqs. (2.29) to (2.31). However, Eqs. (2.34) and (2.35) can in principle be used to replace the last two of the perturbed Einstein equations.

The two fluid equations simplify enormously for the case of a nonrelativistic fluid when $p = w = 0$ and the anisotropic stress Π vanishes. Taking the spatial derivative of Eq. (2.35), one obtains in this case that

$$\left(\delta^N\right)' = -\nabla \cdot \mathbf{v}^N + 3\Psi' \,, \tag{2.36}$$

$$\left(\mathbf{v}^N\right)' = -\mathcal{H}\mathbf{v}^N - \nabla\Phi \,, \tag{2.37}$$

where we again made use of $v_i^N = -\partial_i v^N$. Combining both equations by taking the time derivative of Eq. (2.36) and a spatial derivative of Eq. (2.37) leads to [213]

$$\delta'' + \mathcal{H}\delta' = \nabla^2\Phi + 3(\Psi'' + \mathcal{H}\Psi') \,, \tag{2.38}$$

where we dropped the superscript N for convenience. For a perfect fluid, we have $\Psi = \Phi$ (cf. Eq. (2.29)) and the right-hand side of Eq. (2.38) is purely described by the gravitational potential Φ which is sourced by the density perturbation on the left-hand side. We will use this equation in Section 2.3 to study the evolution of density fluctuations on subhorizon scales.

2.1.4 Classification of Perturbations

For future reference, we now introduce adiabatic, isocurvature and Gaussian perturbations. Considering a barotropic equation of state, $p = p(\rho)$, one can relate the pressure perturbations δp and density perturbations $\delta\rho$ to each other via [52]

$$\frac{\delta p}{\delta\rho} = \frac{\dot{\bar{p}}}{\dot{\bar{\rho}}} = c_s^2 \,, \tag{2.39}$$

where c_s^2 is the speed of sound. Perturbations that fulfil

$$\delta p = c_s^2 \delta\rho = \frac{\dot{\bar{p}}}{\dot{\bar{\rho}}} \delta\rho \tag{2.40}$$

are called adiabatic perturbations in cosmology. They arise when there is, for example, a slight time delay in the evolution of different parts of the universe which is the case during inflation. For multiple fluid components consisting, for example, of matter and radiation, all matter components have the same δ_m perturbation and all radiation components have the same δ_r perturbation. Deviations from adiabaticity lead to isocurvature perturbations[24] which introduce variations in the ratio of the number density of two different fluid components [52]. Since there is only one component in single-field inflation, namely the inflaton field, purely adiabatic perturbations are generated in this scenario. As long as those perturbations are superhorizon, they stay adiabatic. However, once they become subhorizon during radiation- or matter-domination they can develop isocurvature perturbations, as discussed in Ref. [52].

Gaussian perturbations obey, as the name suggests, a Gaussian probability distribution which means that the Fourier components of the perturbations have independent probability distributions [52]. The variance, i.e. the two-point correlation function evaluated at the same position $\langle g^2(\mathbf{x})\rangle$, of a Gaussian perturbation $g(\mathbf{x})$ does not depend on the position $\mathbf{x}$ and the direction of the Fourier mode $\mathbf{k}$. Hence, the variance of Gaussian perturbations is invariant both under rotations and translations. Additionally, it contains all statistical information about the perturbations since higher-order correlation functions can be calculated from it [52]. Importantly, the fluctuations generated during inflation are

---

[24] Note that isocurvature perturbations are sometimes also called entropy perturbations.

Gaussian, so only their two-point function has to be extracted from the CMB to unveil their statistics.

2.2 Inflationary Perturbations

Now we decompose the scalar inflaton field φ into an inhomogeneous perturbation $\delta\varphi$ and a position-independent background $\bar{\varphi}$,

$$\varphi(t, \mathbf{x}) = \bar{\varphi}(t) + \delta\varphi(t, \mathbf{x}). \tag{2.41}$$

Figuratively, these perturbations lead to local time delays in the inflationary evolution such that inflation comes to an end at slightly different times in different parts of the universe. Inserting Eq. (2.41) into Eq. (1.24), the homogeneous background equation is given by

$$\ddot{\bar{\varphi}} + 3H\dot{\bar{\varphi}} + V'(\bar{\varphi}) = 0\,, \tag{2.42}$$

and the perturbations are described by [52]

$$\delta\ddot{\varphi} + 3H\delta\dot{\varphi} - a^{-2}\nabla^2\delta\varphi + V''(\bar{\varphi})\delta\varphi = 0\,. \tag{2.43}$$

However, this approach ignores perturbations in the spacetime and that the inflaton field is coupled to the metric. Fortunately, we can make use of cosmological perturbation theory (see Section 2.1) in order to explicitly take into account metric perturbations.

In this section, the evolution equation of inflationary perturbations is discussed. As before, we will at first work in the Newtonian gauge and consider only scalar metric perturbations. We then derive the so-called *Mukhanov-Sasaki* equation which, on the one hand, is a way of expressing the perturbation equation of the inflaton field in a simple form. On the other hand, it provides insight into the initial conditions of inflation and can be used to compute both the primordial curvature power spectrum and the primordial spectrum of gravitational waves.

2.2.1 Evolution Equations

Using the perturbed FLRW metric in Newtonian gauge (see Eq. (2.8)), a direct computation of the Klein-Gordon Eq. (B.12) to linear order in perturbations gives [52] (see Appendix B.2 for details)

$$\left(\delta\varphi^N\right)'' + 2\mathcal{H}\left(\delta\varphi^N\right)' - \nabla^2\delta\varphi^N - (\Phi' + 3\Psi')\bar{\varphi}' + a^2(\partial_{\varphi\varphi}\bar{V})\delta\varphi^N + 2a^2\Phi\partial_\varphi\bar{V} = 0\,, \tag{2.44}$$

where $\bar{V} \equiv V(\bar{\varphi})$. Perturbing the stress-energy tensor of a scalar field (cf. Eq. (1.25)) to linear order (see Appendix B.3 for details), one finds that the anisotropic stress Π vanishes, which implies that $\Psi = \Phi$ as can be seen from Eq. (2.29). While Eq. (2.44) then simplifies to

$$\left(\delta\varphi^N\right)'' + 2\mathcal{H}\left(\delta\varphi^N\right)' - \nabla^2\delta\varphi^N - 4\Psi'\bar{\varphi}' + a^2(\partial_{\varphi\varphi}\bar{V})\delta\varphi^N + 2a^2\Psi\partial_\varphi\bar{V} = 0\,, \tag{2.45}$$

the perturbed Einstein equations for a scalar field are given in Eqs. (B.20) to (B.22) and only depend on Ψ and $\delta\varphi^N$. The perturbed Einstein equations can be rewritten as a differential equation which depends only on Ψ. This requires taking the time derivative of Eq. (B.21) which yields

$$\left(\delta\varphi^N\right)' = \frac{(\Psi'' + \mathcal{H}'\Psi + \mathcal{H}\Psi')\bar{\varphi}' - (\Psi' + \mathcal{H}\Psi)\bar{\varphi}''}{4\pi G\bar{\varphi}'^2}\,, \tag{2.46}$$

and to insert $3\mathcal{H}\Psi'$ from Eq. (B.20) into Eq. (B.22). Using the relation from Eq. (B.11), we obtain the evolution equation

$$\Psi'' - \nabla^2\Psi + 2\left(\mathcal{H} - \frac{\bar{\varphi}''}{\bar{\varphi}'}\right)\Psi' + 2\left(\mathcal{H}' - \mathcal{H}\frac{\bar{\varphi}''}{\bar{\varphi}'}\right)\Psi = 0\,. \tag{2.47}$$

In terms of the equation of state parameter w and the speed of sound c_s^2 (see Eqs. (B.4) and (B.9)), it can also be written as

$$\Psi'' - \nabla^2\Psi + 3\mathcal{H}(1 + c_s^2)\Psi' + 3\mathcal{H}^2(c_s^2 - w)\Psi = 0\,. \tag{2.48}$$

2.2.2 Comoving Curvature Perturbation

A useful quantity for studying inflationary perturbations is the so-called *comoving curvature perturbation* $\mathcal{R}$ (see Appendix B.4 for details). It is defined in Eq. (B.23) and can be expressed in terms of the curvature perturbation $\psi_\mathcal{R}$ and the inflaton perturbations $\delta\varphi$ (see Eq. (A.40)). Importantly, $\mathcal{R}$ is in fact a gauge-invariant quantity which can be realised by writing it in Newtonian gauge (see Appendix A.3). The Bardeen potential is then given by $\Psi = \psi_\mathcal{R}$ and the comoving curvature perturbation is $\mathcal{R} = \Psi + \mathcal{H}v^N$ (see Eq. (A.39)). Using the Einstein Eq. (2.31) with $\Psi = \Phi$, the velocity perturbation v^N in Newtonian gauge is

$$v^N = \frac{\Psi' + \mathcal{H}\Psi}{4\pi G a^2(\bar{\rho} + \bar{p})}\,. \tag{2.49}$$

Applying the first Friedmann equation in Eq. (B.1), the comoving curvature perturbation then is [212]

$$\mathcal{R} = \Psi + \frac{2}{3}\frac{\Psi' + \mathcal{H}\Psi}{\mathcal{H}(1 + w)}\,. \tag{2.50}$$

Evidently, $\mathcal{R}$ depends only on the Bardeen potential Ψ and is therefore gauge-invariant. This allows us to compute $\mathcal{R}$ in any gauge. Its time derivative $\mathcal{R}'$ can be written as

$$\frac{3}{2}(1+w)\mathcal{H}\mathcal{R}' = \Psi'' + \left(\frac{3}{2}(1+w)\mathcal{H} + \mathcal{H} - \frac{\mathcal{H}'}{\mathcal{H}} - \frac{w'}{1+w}\right)\Psi' - \frac{\mathcal{H}w'}{1+w}\Psi\,. \tag{2.51}$$

With the relations in Eqs. (B.4) and (B.5) and using the evolution Eq. (2.48), we find that the time derivative

$$\frac{3}{2}(1+w)\mathcal{H}\mathcal{R}' = \Psi'' + 3\mathcal{H}(1+c_s^2)\Psi' + 3\mathcal{H}^2(c_s^2 - w)\Psi = \nabla^2\Psi\,. \tag{2.52}$$

is essentially given by $\nabla^2\Psi$. In Fourier space, the last equation reads [212]

$$\frac{3}{2}\frac{(1+w)}{\mathcal{H}}\mathcal{R}_k' = -\frac{k^2}{\mathcal{H}^2}\Psi_k\,, \tag{2.53}$$

and reveals that $\mathcal{R}$ is conserved on superhorizon scales $k \ll \mathcal{H}$. Thus, the purely adiabatic perturbations generated during single-field inflation basically freeze out once they cross the horizon. From there on, a perturbation stays constant until it reenters the horizon at a later time. In principle, one does not need to know anything about the physical processes inside the horizon in the meantime, for example during reheating. On the contrary, this remarkable result allows us to directly shift the perturbations generated during inflation to much later times when they start to become subhorizon again.

Note that the constancy of $\mathcal{R}$ on superhorizon scales is only true for adiabatic perturbations. Writing the time derivative $\mathcal{R}'$ as

$$\frac{3}{2}\frac{(1+w)}{\mathcal{H}}\mathcal{R}' = \frac{\Psi''}{\mathcal{H}^2} + \frac{2+3c_s^2}{\mathcal{H}}\Psi' + 3(c_s^2 - w)\Psi + \frac{\Psi'}{\mathcal{H}}\,, \tag{2.54}$$

and using the Einstein Eqs. (2.30) and (2.31) in Newtonian gauge for a perfect fluid, we obtain in Fourier space that [212]

$$\begin{aligned}\frac{3}{2}\frac{(1+w)}{\mathcal{H}}\mathcal{R}_k' &= \frac{3}{2}\frac{\delta p^N}{\bar{\rho}} + 3c_s^2\left(\frac{\Psi_k'}{\mathcal{H}} + \Psi_k\right)\\ &= -c_s^2\frac{k^2}{\mathcal{H}^2}\Psi_k + \frac{3}{2}\left(\frac{\delta p^N}{\bar{\rho}} - c_s^2\frac{\delta\rho^N}{\bar{\rho}}\right)\,.\end{aligned} \tag{2.55}$$

For adiabatic perturbations we have $\delta p = c_s^2\delta\rho$ (see Eq. (2.40)), and the term in brackets on the right-hand side of this equation vanishes revealing that $\mathcal{R}$ is constant on superhorizon scales only in this case.

2.2.3 Mukhanov-Sasaki Equation

In this section, we lay the foundation for relating the gauge-invariant comoving curvature perturbation $\mathcal{R}$ to the quantum-mechanical fluctuations generated at the beginning of inflation. This can be achieved by deriving an equation of motion for $\mathcal{R}$ in a form of a simple harmonic oscillator which is straightforward to quantise [212].

It was shown in Ref. [214] that quantising the variable q, which is known as the Mukhanov variable and is defined as

$$q = \zeta\mathcal{R} = a\left(\delta\varphi + \frac{\bar{\varphi}'}{\mathcal{H}}\psi_{\mathcal{R}}\right), \quad \text{where} \quad \zeta = a\frac{\bar{\varphi}'}{\mathcal{H}}, \tag{2.56}$$

leads to the initial conditions of inflation. In the first step, we need to derive the equation of motion for the variable q. There are several ways of doing so, for example by starting from the full action in Eq. (1.23). Perturbing the action to second-order in $\mathcal{R}$ and expressing it in terms of q then allows the action to be varied with respect to q to obtain the equation of motion [212]. In a similar approach, one makes use of the Arnowitt-Deser-Misner formalism [215] where the spacetime metric is sliced into three-dimensional hypersurfaces. The metric perturbations are then encoded in the so-called lapse function and the shift function. It is possible to rewrite the action such that lapse and shift occur as Lagrange multipliers. Varying the action with respect to these two functions leads to constraint equations which are then used to derive the equation of motion for q [212].

Instead, we take the equation of motion of the scalar field perturbation (see Eq. (2.45)) and combine it with the perturbed Einstein equations from Eqs. (B.20) to (B.22) to find the equation of motion for q. A detailed derivation of the so-called Mukhanov-Sasaki equation [214, 216] can be found in Appendix B.5. Using the result from Eq. (B.33), it can be written as [212]

$$q'' - \nabla^2 q - \frac{\zeta''}{\zeta}q, \quad \text{and} \quad q_k'' + \left(k^2 - \frac{\zeta''}{\zeta}\right)q_k = 0 \tag{2.57}$$

in Fourier space. While this equation resembles a harmonic oscillator, it is nevertheless not easy to solve it in general since ζ''/ζ depends on the background dynamics. It is possible to express ζ''/ζ in terms of slow-roll parameters ε and η (see Eqs. (1.29) and (1.30)) as [217]:

$$\frac{\zeta''}{\zeta} = \mathcal{H}^2\left(2 + 2\varepsilon - 3\eta + \eta^2 - \varepsilon\eta + \frac{\dot{\varepsilon}}{H} - \frac{\dot{\eta}}{H}\right). \tag{2.58}$$

During inflation, where $\varepsilon, |\eta| < 1$, this can be approximated to leading order in slow-roll parameters as $\zeta''/\zeta = \mathcal{H}^2(2 + 2\varepsilon - 3\eta)$.

Mukhanov-Sasaki Equation in de Sitter Space

In de Sitter space (ε, $\eta \longrightarrow 0$, $H = \text{const}$), where $a \sim \exp(Ht)$ and thus $\tau = -(aH)^{-1}$, one can approximate Eq. (2.58) as (see Eq. (B.2))

$$\frac{\zeta''}{\zeta} = \frac{a''}{a} = \frac{2}{\tau^2} = 2a^2H^2. \tag{2.59}$$

This allows us to consider highly relevant limits of Eq. (2.57) on super- and subhorizon scales. For the former case it is $k^2 \ll (aH)^2 = \zeta''/\zeta$ and Eq. (2.57) reduces to

$$q_k'' - \frac{2}{\tau^2} q_k = 0 \,. \tag{2.60}$$

Similarly, one finds that on subhorizon scales $k^2 \gg (aH)^2 = \zeta''/\zeta$, Eq. (2.57) approaches

$$q_k'' + k^2 q_k = 0 \,, \tag{2.61}$$

which resembles the equation of a harmonic oscillator with a frequency that does not depend on time. Hence, the solutions of Eq. (2.61) oscillate, $q_k \propto \exp(\pm ik\tau)$, while Eq. (2.60) can be solved by [212]

$$q_k = \alpha \frac{\exp(-ik\tau)}{\sqrt{2k}} \left(1 - \frac{i}{k\tau}\right) + \beta \frac{\exp(ik\tau)}{\sqrt{2k}} \left(1 + \frac{i}{k\tau}\right) \,. \tag{2.62}$$

The free parameters α and β can only be determined if additional boundary conditions for q_k are provided. This can be achieved by quantising the variable q_k.

Quantisation of Perturbations

Exploiting the analogy between Eq. (2.57) and the equation of motion of the harmonic oscillator, one can quantise the perturbation q in a similar manner. Then, the Fourier components $q_{\mathbf{k}}$ correspond to quantum operators [212],

$$q_{\mathbf{k}} \longrightarrow \hat{q}_{\mathbf{k}} = q_k(\tau)\hat{a}_{\mathbf{k}} + q^*_{-k}\hat{a}^\dagger_{-\mathbf{k}} \,, \tag{2.63}$$

where the creation ($\hat{a}^\dagger_{-\mathbf{k}}$) and annihilation operator ($\hat{a}_{\mathbf{k}}$) obey the commutation relation $[\hat{a}_{\mathbf{k}}, \hat{a}^\dagger_{\mathbf{k}'}] = (2\pi)^3\delta(\mathbf{k} - \mathbf{k}')$. Moreover, the complex mode functions are normalised such that $\langle q_k, q_k \rangle = i(q_k' q_k^* - q_k q_k^{*\prime}) = 1$ [212]. The normalisation of the mode functions imposes a boundary condition on solutions of the Mukhanov-Sasaki equation (see for example Eq. (2.62)). An additional boundary condition can be obtained by specifying the vacuum state $\hat{a}_{\mathbf{k}} \left|0\right\rangle$. At early times ($\tau \longrightarrow -\infty$), all relevant comoving length scales were subhorizon ($\zeta''/\zeta = 2/\tau^2 \longrightarrow 0$, $k \gg a^2H^2$). In this case, the Mukhanov-Sasaki equation is given by Eq. (2.61) which corresponds to the mode equation of a harmonic oscillator in the non-expanding Minkowski space. By analogy, one can require the vacuum to be the state of lowest energy that is given by the positive frequency mode $q_k \propto \exp(-ik\tau)$. Properly normalised, this provides the initial condition [212]

$$q_k(\tau) \longrightarrow \frac{1}{\sqrt{2k}} \exp(-ik\tau) \,, \tag{2.64}$$

known as the *Bunch-Davies vacuum.*

2.2.4 Primordial Curvature Power Spectrum

The initial condition given by Eq. (2.64) fixes the two free parameters from Eq. (2.62) to be $\alpha = 1$, $\beta = 0$. Thus, the mode functions on superhorizon scales are

$$q_k = \frac{\exp(-ik\tau)}{\sqrt{2k}} \left(1 - \frac{i}{k\tau}\right) . \tag{2.65}$$

With this knowledge we can compute the power spectrum $P_{\mathcal{R}}(k)$ of curvature perturbations $\mathcal{R}_k = q_k/\zeta$, defined via the two-point function [212]

$$\langle \mathcal{R}_k \mathcal{R}_{k'} \rangle = (2\pi)^3 \delta(\mathbf{k} - \mathbf{k}') P_{\mathcal{R}}(k) , \quad \text{with} \quad P_{\mathcal{R}}(k) = \frac{|q_k(\tau)|^2}{\zeta^2} . \tag{2.66}$$

Hence, the dimensionless curvature power spectrum $\Delta^2_{\mathcal{R}}$ is

$$\Delta^2_{\mathcal{R}}(k) = P_{\mathcal{R}}(k) \frac{k^3}{2\pi^2} = \frac{1}{\zeta^2} \frac{a^2 H^2}{2k^3} \left(1 + \frac{k^2}{a^2 H^2}\right) \frac{k^3}{2\pi^2} . \tag{2.67}$$

Inserting the definition of ζ (see Eq. (2.56)), the curvature power spectrum approaches on superhorizon scales ($k \ll aH$)

$$\Delta^2_{\mathcal{R}}(\tau, \mathbf{k}) = \frac{H^2}{(2\pi)^2} \frac{H^2}{\dot{\varphi}^2} = \frac{H_*^2}{(2\pi)^2} \frac{H_*^2}{\dot{\varphi}_*^2} . \tag{2.68}$$

The power spectrum is evaluated at horizon crossing ($k_* = a_* H_*$) since $\mathcal{R}$ remains constant on superhorizon scales until the corresponding mode re-enters the horizon (cf. Section 2.2.2). In a pure de Sitter universe, the resulting power spectrum does not depend on k since H and $\dot{\varphi}$ are constant, so it is scale-invariant. However, this does not apply during slow-roll inflation and different modes exit the horizon at slightly different values of H_* leading to deviations from the scale invariance. They are usually quantified in terms of the scalar spectral index n_s [212],

$$n_s - 1 \equiv \frac{\mathrm{d} \ln \Delta^2_{\mathcal{R}}}{\mathrm{d} \ln k} , \tag{2.69}$$

that can be also written as

$$n_s = 1 + 2\eta - 4\varepsilon \tag{2.70}$$

to first-order in the slow-roll parameters ε, η. A deviation from $n_s = 1$ can thus be understood as a probe of the inflationary dynamics in terms of the slow-roll parameters.[25] It is convenient to parameterise the primordial power spectrum as [212]

$$\Delta^2_{\mathcal{R}}(k) = A_s \left(\frac{k}{k_p}\right)^{n_s - 1} , \tag{2.71}$$

---

[25] Note that one obtains the same result for the spectral index n_s when ζ''/ζ in Eq. (2.58) is expanded to first-order in slow-roll parameters [212].

where $n_s \simeq 0.967$ and $A_s \simeq 2.1 \times 10^{-9}$ for a pivot scale of $k_p = 0.05\,\mathrm{Mpc}^{-1}$ (cf. Table 1.1). Apart from the nearly scale-invariant curvature power spectrum, two other significant properties of the inflationary perturbations in single-field inflation are that they are adiabatic and Gaussian[26] (cf. Section 2.1.4). In inflationary models with multiple fields, both isocurvature perturbations and primordial non-Gaussianities can be generated, however, they are subdominant according to the latest Planck results [89]. Note that such primordial non-Gaussianities are different from the non-Gaussianities that build up from the gravitational evolution of density perturbations during the matter-dominated universe on subhorizon scales.

2.2.5 Gravitational Waves From Inflation

Apart from explaining the origin of small fluctuations in the inflaton field and the corresponding primordial power spectrum, inflation also predicts the generation of primordial gravitational waves. This leads to a stochastic background of gravitational waves which imprints its signature in the polarisation of the CMB. Certainly, measuring inflationary gravitational waves or an SGWB originating from the post-inflationary era would extend the knowledge about the relevant inflationary parameters. Therefore, many experiments such as the space-based interferometers LISA [220], DECIGO [221, 222] and BBO [223] as well as the terrestrial interferometers (Advanced) LIGO [224–227] and Advanced VIRGO [228] have been proposed to search for a signal.

Having treated so far only scalar perturbations, one can adapt the same approach to compute the primordial power spectrum of tensor perturbations. Extracting the tensor perturbations from the perturbed metric in Eq. (2.3), one obtains to leading order [229]

$$\mathrm{d}s^2 = a^2(\tau)\left[-\mathrm{d}\tau^2 + (\delta_{ij} + h_{ij})\right]\mathrm{d}x^i\mathrm{d}x^j\,. \tag{2.72}$$

The tensor perturbations h_{ij} are transverse and traceless, $\partial_i h_{ij} = \delta_{ij} h_{ij} = 0$ (cf. Appendix A.1), and gauge-invariant (cf. Appendix A.2.1). Additionally, they are completely decoupled from the inflationary background and its scalar perturbations at linear order in perturbation theory. Perturbing the Einstein equations to first-order in the tensor perturbations h_{ij}, one eventually obtains the evolution equation[27] [53, 229]

$$h''_{ij} + 2\mathcal{H}h'_{ij} - \nabla^2 h_{ij} = 16\pi G a^2 \Sigma^{TT}_{ij}\,, \tag{2.73}$$

---

[26] Strictly speaking, deviations from Gaussianity are predicted to be rather small in single-field inflation [218, 219].

[27] Note that there is only one non-trivial component of the Einstein equations and not three as before for scalar perturbations.

where Σ_{ij}^{TT} is the traceless and transverse anisotropic stress tensor. It can be assumed to vanish during inflation as there are no source terms. Then, Eq. (2.73) corresponds to a wave equation with drag term $2\mathcal{H}h'_{ij}$. Exploiting the symmetry of h_{ij}, the trace condition $\delta_{ij}h_{ij} = 0$ and that $\partial_i h_{ij}$ translates to $k_i h_{ij} = 0$ in Fourier space, one finds for a wave propagating along the z-axis, i.e. $\mathbf{k} = (0, 0, k)$, that [212]

$$\left[h_{ij}\right] = \begin{bmatrix} h_\times & h_+ & 0 \\ h_+ & -h_\times & 0 \\ 0 & 0 & 0 \end{bmatrix} . \tag{2.74}$$

The wave exhibits two different polarisations, denoted by the plus sign and the cross. This labelling originates from the fact that the plus-polarisation perturbs test particles in the same direction as their original separation while the cross-polarisation rotates the test particles by 45°. In Fourier space, the tensor perturbation can be written as [212]

$$h_{ij}(\tau, \mathbf{x}) = \int \frac{\mathrm{d}^3\mathbf{k}}{(2\pi)^{3/2}} \sum_{\gamma=+,\times} \epsilon_{ij}^{\gamma}(k) h_{\mathbf{k},\gamma}(\tau) \exp(i\mathbf{k}\mathbf{x}) , \tag{2.75}$$

where the polarisation amplitude is denoted by $h_{\mathbf{k},\gamma}$. The polarisation tensor ϵ_{ij}^{γ} satisfies $\epsilon_{ii}^{\gamma} = k^i \epsilon_{ij}^{\gamma} = 0$ and $\epsilon_{ij}^{\gamma}\epsilon_{ij}^{\gamma'} = 2\delta_{\gamma\gamma'}$. Inserting this Fourier representation into Eq. (2.73) with vanishing stress, the equations of motion for the tensor perturbations can be expressed as

$$h''_\gamma + 2\mathcal{H}h'_\gamma + k^2 h_\gamma = 0 , \tag{2.76}$$

for $\gamma = +, \times$. Defining the variable $q_\gamma = aM_{\mathrm{Pl}}h_\gamma/2$, Eq. (2.76) can be written as [212]

$$q''_{k,\gamma} + \left(k^2 - \frac{a''}{a}\right) q_{k,\gamma} = 0 , \tag{2.77}$$

which resembles the Mukhanov-Sasaki Eq. (2.57) for scalar perturbations. This immediately suggests quantising q_γ in order to obtain the power spectrum of inflationary gravitational waves, as was done before with the scalar perturbations. According to Eq. (2.59), we have $a'' = 2/\tau^2$ in de Sitter space and thus

$$q''_{k,\gamma} = \frac{2}{\tau^2} q_{k,\gamma} \tag{2.78}$$

on superhorizon scales. Choosing again the Bunch-Davies vacuum in Eq. (2.64) to provide the initial conditions for solving Eq. (2.78), the dimensionless power spectrum for each polarisation on superhorizon scales is [212]

$$\Delta_\gamma^2(\tau, \mathbf{k}) = \frac{4}{a^2 M_{\mathrm{Pl}}^2} |q_{k,\gamma}|^2 \frac{k^3}{2\pi^2} = \frac{4}{M_{\mathrm{Pl}}^2} \frac{H_*^2}{(2\pi)^2} . \tag{2.79}$$

As before, the power spectrum is evaluated at horizon crossing, $k_* = a_* H_*$. The full tensor power spectrum is the sum of the spectra for each polarisation and thus reads

$$\Delta_t^2 = \frac{2}{\pi^2}\frac{H_*^2}{M_{\mathrm{Pl}}^2} \,. \tag{2.80}$$

In a pure de Sitter universe, H is constant and this spectrum would be scale-invariant. This is not the case in slow-roll inflation. The amplitude of modes that exit the horizon at an earlier time is larger, thus one expects slight deviations from scale invariance. In complete analogy to the scalar spectral index in Eq. (2.69), one can define a spectral index n_t for the tensor perturbations [212],

$$n_t \equiv \frac{\mathrm{d}\ln\Delta_t^2}{\mathrm{d}\ln k} = -2\varepsilon \,. \tag{2.81}$$

From an observational point of view, it is useful to define the *tensor-to-scalar ratio* $r_{\mathrm{ts}} \equiv \Delta_t^2/\Delta_{\mathcal{R}}^2$. Expressing $\dot{\bar{\varphi}}$ in Eq. (2.68) in terms of ε and H, one finds that [212]

$$r_{\mathrm{ts}} = \frac{\Delta_t^2}{\Delta_{\mathcal{R}}^2} = \frac{8}{M_{\mathrm{Pl}}^2}\frac{\dot{\bar{\varphi}}^2}{H^2} = 16\varepsilon. \tag{2.82}$$

The latest Planck results constrain the tensor-to-scalar ratio to be $r_{\mathrm{ts}} < 0.10$ [89]. Future experiments will be able to achieve more accurate results on r_{ts} and measure the full power spectrum of tensor perturbations. Since the amplitude of the scalar perturbations is fixed to $\sim 10^{-9}$ (cf. Table 1.1) and $\Delta_t^2 \sim H^2 \sim V$ [2], the tensor-to-scalar ratio is especially useful for determining the energy scale of inflation. A large value of r_{ts} corresponds to a large inflationary energy scale.

Related to the tensor-to-scalar ratio is another relation known as the *Lyth bound*. Expressing r_{ts} in Eq. (2.82) in terms of the number of e-folds $\mathcal{N}$ (see Eq. (1.34)) with $\mathrm{d}\mathcal{N} = -\mathrm{d}\ln a = -H\mathrm{d}t$, we obtain

$$r_{\mathrm{ts}} = \frac{8}{M_{\mathrm{Pl}}^2}\left(\frac{\mathrm{d}\varphi}{\mathrm{d}\mathcal{N}}\right)^2 \,. \tag{2.83}$$

This relation can be used to determine the amount $\Delta\varphi$ the field φ has changed between the end of inflation at $\mathcal{N}_{\mathrm{end}}$ and the time fluctuations observed in the CMB left the horizon. This occurred $\mathcal{N}_{\mathrm{CMB}} \approx 40 - 60$ e-folds before the end of inflation and $\Delta\varphi$ can be computed from

$$\frac{\Delta\varphi}{M_{\mathrm{Pl}}} = \int_{\mathcal{N}_{\mathrm{end}}}^{\mathcal{N}_{\mathrm{CMB}}} \left(\frac{r_{\mathrm{ts}}}{8}\right)^{1/2} \mathrm{d}\mathcal{N} \,. \tag{2.84}$$

It was found that this expression can be approximated during slow-roll inflation yielding the Lyth bound [88]

$$\frac{\Delta\varphi}{M_{\mathrm{Pl}}} = \mathcal{O}(1) \times \left(\frac{r_{\mathrm{ts}}}{0.01}\right)^{1/2} \,, \tag{2.85}$$

where $r_{\rm ts} = r_{\rm ts}(\mathcal{N}_{\rm CMB})$. Thus, one can expect large values of the tensor-to-scalar ratio for large-field models of inflation that are classified by $\Delta\varphi > M_{\rm Pl}$ and accordingly small values of $r_{\rm ts}$ for small-field models.

2.3 Evolution of Matter Perturbations

Having seen that inflation produces tiny perturbations that are essentially frozen on superhorizon scales, we now study their evolution once they re-enter the horizon at the time when the Universe was radiation- or matter-dominated. We will see that there is efficient growth of matter perturbations only during matter-domination[28] and how the primordial curvature perturbations can be related to fluctuations in the matter density. In the following, we consider the evolution of subhorizon density perturbations assuming slowly varying gravitational fields and nonrelativistic velocities. This allows a Newtonian treatment and the relativistic effects in the equations of motion obtained in Section 2.1 can be neglected.

2.3.1 Gravitational Instability and Linear Growth

We start from the perturbed continuity and Euler equations for a relativistic fluid (see Eqs. (2.34) and (2.35)) and consider a perfect fluid with vanishing anisotropic stress, i.e. $\Psi = \Phi$. In terms of the equation of state parameter $w = \bar{p}/\bar{\rho}$ and speed of sound $c_s^2 = \delta p/\delta\rho$, the continuity and Euler equations for adiabatic perturbations ($c_s^2 \approx w$) then simplify to [213]

$$\delta' = -(1+w)\left(\nabla\cdot\mathbf{v} - 3\Phi'\right)\,, \tag{2.86}$$

$$\mathbf{v}' = -\mathcal{H}(1-3w)\mathbf{v} - \frac{c_s^2}{1+w}\nabla\delta - \nabla\Phi\,, \tag{2.87}$$

where Eq. (B.5) was used to replace w'. Taking the time derivative of Eq. (2.86) and the divergence of Eq. (2.87), we obtain a second-order differential equation for the evolution of the density perturbations on subhorizon scales [213],

$$\delta'' + (1-3w)\mathcal{H}\delta' - c_s^2\nabla^2\delta = (1+w)\nabla^2\Phi\,. \tag{2.88}$$

Note that we neglected the time derivatives of the metric perturbation Φ in the derivation of Eq. (2.88). As discussed in Ref. [213], this is justified on subhorizon scales and valid

---

[28] This does not mean that gravitational structures cannot form before matter-radiation-equality at all. For example, axion miniclusters (see Chapter 4) start to form already during radiation-domination.

when the metric perturbation is averaged over a Hubble time. As the density perturbations are coupled to the gravitational potential via the Poisson equation (see Eq. (2.26))

$$\nabla^2\Phi = 4\pi G a^2 \bar{\rho}\delta \,, \tag{2.89}$$

the perturbation Eq. (2.88) can be written in Fourier space as

$$\delta_k'' + (1-3w)\mathcal{H}\delta_k' + \left(c_s^2 k^2 - (1+w)4\pi G a^2 \bar{\rho}\right)\delta_k = 0 \,. \tag{2.90}$$

The scale k_J at which the gravity term is equal to the pressure term $c_s^2 k^2 \delta_k$ is the so-called *Jeans scale* [213]

$$k_J^2 = (1+w)\frac{4\pi G a^2 \bar{\rho}}{c_s^2} \,. \tag{2.91}$$

For large scales ($k < k_J$), the pressure term in Eq. (2.90) can be neglected and gravity leads to growing perturbations. Vice versa, gravity is subdominant on small scales ($k > k_J$) and perturbations oscillate without growing.

Considering now a nonrelativistic fluid, like CDM with $w = 0$, the pressure term can be omitted and the equation of motion takes the form (cf. Eq. (2.38))

$$\delta_k'' + \mathcal{H}\delta_k' - 4\pi G a^2 \bar{\rho}\delta_k = 0 \,. \tag{2.92}$$

Evidently, this equation does not depend on k which means that all perturbations δ_k grow at the same rate.[29] This allows us to decompose solutions of this equation into factors of a time-dependent and a spatial part. As there exist two solutions to Eq. (2.92), the general form of the solution in real space can be expressed as

$$\delta(\mathbf{x},\tau) = D_+(\tau)A_+(\mathbf{x}) + D_-(\tau)A_-(\mathbf{x}) \,. \tag{2.93}$$

The functions $D_+(\tau)$ and $D_-(\tau)$ describe the evolution of the perturbations, while $A_+(\mathbf{x})$ and $A_-(\mathbf{x})$ contain information about the initial conditions of δ. For a purely matter-dominated universe ($\Omega_m = 1$), one finds that there is a solution with linear growth, $D_+(\tau) = a(\tau)$, and a decaying solution $D_-(\tau) = a^{-3/2}(\tau)$ that can be neglected. Thus, density perturbations grow linearly with scale factor in a matter-dominated universe. It is now illustrative to study the behaviour of perturbations at early times when the universe was dominated by radiation and matter, and at late times when the radiation component can be neglected and dark energy becomes dominant. Starting with early times, the total background energy density can be approximated as $\bar{\rho} = \bar{\rho}_m + \bar{\rho}_r$. As

---

[29] Note that this is only correct for *linear* perturbations. Once higher-order corrections become relevant, products of the density and velocity perturbations lead to coupled Fourier modes [230].

perturbations in the radiation component only oscillate and do not grow[30], they can be neglected and Eq. (2.92) becomes for matter perturbations [52]

$$\delta_m'' + \mathcal{H}\delta_m' - 4\pi G a^2 \bar{\rho}_m \delta_m \approx 0\,. \tag{2.94}$$

Note that the radiation component is assumed to be smooth and has only been considered in the expansion rate. Introducing the variable $y = a/a_{\mathrm{eq}}$, the Hubble parameter can be written as

$$\mathcal{H}^2 = \frac{\mathcal{H}_0^2 \Omega_m^2}{\Omega_r}\left(\frac{1}{y} + \frac{1}{y^2}\right)\,. \tag{2.95}$$

Then, Eq. (2.94) becomes [52]

$$\frac{\mathrm{d}^2\delta_m}{\mathrm{d}y^2} + \frac{2+3y}{2y(1+y)}\frac{\mathrm{d}\delta_m}{\mathrm{d}y} - \frac{3}{2y(1+y)}\delta_m = 0\,, \tag{2.96}$$

which is known as the Mészáros equation and solved by [52]

$$\delta_m = A_+\left(1 + \frac{3}{2}y\right) + A_-\left[\left(1 + \frac{3}{2}y\right)\ln\frac{(1+y)^{1/2}+1}{(1+y)^{1/2}-1} - 3(1+y)^{1/2}\right]\,. \tag{2.97}$$

The matter perturbations behave as $\delta_m \sim \ln a$ during radiation-domination ($y \ll 1$) and as $\delta_m \sim a$ during matter-domination ($y \ll 1$). Thus, they experience significant growth only once the Universe has become matter-dominated. In the late-time Universe, dark energy starts to dominate and $\mathcal{H}^2 = 8\pi G\bar{\rho}_\Lambda a^2/3 \gg 4\pi G a^2 \bar{\rho}_m$, so the last term in Eq. (2.94) can be omitted. Using furthermore that $\mathcal{H} = -\tau^{-1}$ in a dark energy-dominated universe, the equation of motion for matter perturbations then becomes $\delta_m'' - \delta_m'/\tau \approx 0$. It is solved by $\delta_m = A_+ + A_- \exp(-2\mathcal{H}\tau)$. Hence, matter perturbations stop growing once dark energy dominates the energy budget of a universe.

2.3.2 Matter Power Spectrum

Since the primordial curvature perturbations generated during inflation are assumed to be the origin of all the structures in our Universe, all sorts of perturbations in the post-inflationary Universe are related to the inflaton perturbations $\delta\varphi$. In the following, the curvature power spectrum $\Delta^2_{\mathcal{R}}$ from inflation (see Eq. (2.68)) is linked to the power spectrum of density perturbations.

---

[30] This can be best seen by analysing Eq. (2.90) and the Jeans scale for a radiation component. Using the first Friedmann Eq. (B.1) in conformal time, we obtain that in this case $k_J \sim \mathcal{H}$. Thus, subhorizon scales $k \gg \mathcal{H}$ are also sub-Jeans scales and the pressure term in Eq. (2.90) dominates. This results in an oscillatory solution for radiation.

Using the result for the comoving curvature perturbation $\mathcal{R}$ from Eq. (2.50), one obtains a differential equation for the metric perturbation Φ,

$$\frac{5+3w}{3}\Phi + \frac{2\Phi'}{3\mathcal{H}} = (1+w)\mathcal{R}\,. \tag{2.98}$$

Exploiting that $\mathcal{R}$ is constant on superhorizon scales for adiabatic perturbations and assuming that w does not change as well, this equation can be solved by [213]

$$\Phi = \frac{3+3w}{5+3w}\mathcal{R}\,. \tag{2.99}$$

Note that we omitted the decaying part of this solution. According to the Poisson Eq. (2.89), the metric perturbation is related to the density perturbation,

$$\delta_k = -\left(\frac{k}{a}\right)^2 \frac{\Phi_k}{4\pi G\bar{\rho}} = -\frac{2}{3}\left(\frac{k}{\mathcal{H}}\right)^2 \Phi_k\,, \tag{2.100}$$

once Φ_k has entered the horizon. It is insightful to study how Φ evolves in the matter- and radiation-dominated eras which is given by Eq. (2.30). In the matter era, Eq. (2.30) reduces to

$$\Phi'' + \frac{6}{\tau}\Phi' = 0\,, \tag{2.101}$$

which is solved by $\Phi = A_+ + A_- a^{-5/2}$. Thus, Φ is constant during matter-domination. In a radiation-dominated universe, the equation of motion for Φ is [213]

$$\Phi'' + \frac{4}{\tau}\Phi' - \frac{1}{3}\nabla^2\Phi = 0\,. \tag{2.102}$$

One finds that Φ oscillates with a decreasing amplitude and behaves as $\Phi \sim a^{-2}$ on subhorizon scales [213]. Since Φ does not change on subhorizon scales in a matter-dominated universe, one can directly relate the density perturbations δ_k to the primordial curvature perturbation $\mathcal{R}_k$,

$$\delta_k = -\frac{2}{3}\left(\frac{k}{\mathcal{H}}\right)^2 \Phi_k = -\frac{2}{5}\left(\frac{k}{\mathcal{H}}\right)^2 \mathcal{R}_k\,, \tag{2.103}$$

where we used that $\Phi_k = 3\mathcal{R}_k/5$ for $w = 0$. However, this is not the case for perturbations entering already during radiation-domination. One needs to consider that $\Phi \sim a^{-2}$ during this time, and that the related density perturbation δ_k grows only logarithmically until matter-radiation equality. Denoting the scale entering the horizon at matter-radiation equality as k_{eq}, smaller scales with $k > k_{\text{eq}}$ become subhorizon at earlier times and experience thus more suppression. All of these effects can be incorporated into a *transfer function* $T(k,\tau)$ such that [52]

$$\delta_k(\tau) = -\frac{2}{5}\left(\frac{k}{\mathcal{H}}\right)^2 T(k,\tau)\mathcal{R}_k\,, \tag{2.104}$$

where by definition $T(k,\tau) = 1$ for $k \ll k_{\mathrm{eq}}$. This guarantees that one recovers Eq. (2.103) for large scales entering the horizon during matter-domination. The suppression of small scales is accounted for by requiring $T(k,\tau) \sim (k_{\mathrm{eq}}/k)^2$ [52]. In practice, a full analytical solution for the transfer function does not exist. Its computation is usually done numerically with codes such as Camb [231] which can take into account all relevant physical effects. Due to the homogeneity and isotropy of the background universe, the transfer function does not depend on the direction of **k**. Taking the squared average of Eq. (2.104) gives the power spectrum of density perturbations which is also called the matter power spectrum

$$\Delta_m^2(k,\tau) = \frac{4}{25}\left(\frac{k}{\mathcal{H}}\right)^4 T^2(k,\tau)\Delta_{\mathcal{R}}^2 \,. \tag{2.105}$$

In this expression, $\Delta_{\mathcal{R}}^2$ is the inflationary spectrum from Eq. (2.71). In contrast to the primordial curvature power spectrum, the matter power spectrum is not scale-invariant. While the transfer function modifies the matter power spectrum for small scales $k > k_{\mathrm{eq}}$, the shape of the primordial spectrum is preserved for the large scales $k \ll k_{\mathrm{eq}}$ which enter the horizon during matter-domination.

2.3.3 Lagrangian Perturbation Theory

So far, perturbations have been described in the Eulerian framework which allows for the evaluation of the density and velocity fields at any point in space and time. For the sake of completeness, we briefly introduce the concept of Lagrangian perturbation theory (LPT) where the trajectories of fluid elements are followed instead of solving the equations of motion for the density and velocity fields. In LPT, one defines the displacement field[31] $\boldsymbol{\Psi}(\mathbf{q},\tau)$ which connects initial particle positions $\mathbf{q}$ to the final Eulerian positions $\mathbf{x}$ [232],

$$\mathbf{x}(\tau) = \mathbf{q} + \boldsymbol{\Psi}(\mathbf{q},\tau)\,, \quad \mathbf{x}'(\tau) = \frac{\mathrm{d}}{\mathrm{d}\tau}\boldsymbol{\Psi}(\mathbf{q},\tau)\,. \tag{2.106}$$

Rewriting the equation of motion for particle trajectories $\mathbf{x}(\tau)$ in terms of the displacement field, one ends up with a nonlinear equation for $\boldsymbol{\Psi}(\mathbf{q},\tau)$. It can be solved perturbatively, i.e. by expanding the displacement field as

$$\boldsymbol{\Psi}(\mathbf{q},\tau) = \boldsymbol{\Psi}^{(1)}(\mathbf{q},\tau) + \boldsymbol{\Psi}^{(2)}(\mathbf{q},\tau) + \ldots\,, \tag{2.107}$$

where the omitted higher-order terms improve the solution only marginally [232]. Exploiting conservation of mass, $\bar{\rho}(1+\delta(\mathbf{x}))\mathrm{d}^3\mathbf{x} = \bar{\rho}\mathrm{d}^3\mathbf{q}$, one can show that the Jacobian $J(\mathbf{q})$

---

[31] Note that the displacement field is denoted by $\boldsymbol{\Psi}$ while the metric perturbation from the previous sections is denoted by Ψ.

of the transformation in Eq. (2.106) is related to the density perturbation $\delta(\mathbf{x})$ as [233]

$$1 + \delta(\mathbf{x}) = \frac{1}{J(\mathbf{q})} = \left|\det\left(\frac{\partial x_i}{\partial q_j}\right)\right|^{-1} . \tag{2.108}$$

Once fluid elements with different initial positions reach the same position $\mathbf{x}$ and cross each other, a situation known as *shell-crossing*, the Jacobian becomes zero, leading to a singularity in the density perturbation. Note that already displacements to *linear* order in LPT contain *nonlinear* information about the Eulerian density field, so Eq. (2.108) is essentially a nonlinear relation [232]. Considering only the linear order term $\mathbf{\Psi}^{(1)}(\mathbf{q}, \tau)$ in the displacement field is known as the Zel'dovich approximation (ZA) [234]. It leads to the result that

$$\nabla_{\mathrm{q}} \cdot \mathbf{\Psi}^{(1)}(\mathbf{q}, \tau) = -D^{(1)}(\tau)\delta_i(\mathbf{q}) , \tag{2.109}$$

where $\delta_i(\mathbf{q})$ is the initial density fluctuation and $D^{(1)}(\tau)$ is a linear growth factor. This can be understood as initialising fluid particles with straight trajectories where their initial velocities are specified by the initial density perturbation. The ZA provides a suitable description of the evolution in the single-streaming regime where a unique velocity value can be assigned to each point in space. However, even before shell-crossing occurs and multiple streams of matter exist in the same space, the ZA becomes invalid. Taking into account the second-order perturbation $\mathbf{\Psi}^{(2)}(\mathbf{q}, \tau)$, referred to as 2LPT, improves the ZA in describing the Eulerian density and velocity fields drastically [232]. Both the ZA and 2LPT are used for the generation of the initial conditions in N-body simulations [235]. We will make use of the publicly available MUSIC code [236] to generate the initial conditions for the simulations presented in Chapter 5.

2.4 Gravitational Collapse of Perturbations

In the previous discussion of the growth of density perturbations in Section 2.3.1 only perturbations up to linear order were considered. This provides an accurate description only for $\delta \ll 1$. Once $\delta \sim 1$, nonlinear effects become important which requires taking into account higher-order perturbations. They can either be directly included in the Eulerian framework or via LPT which yields nonlinear density perturbations already when perturbing the displacement field to linear order. Eventually, density fluctuations will grow beyond $\delta \gtrsim 1$ and nonlinear perturbation theory breaks down. This occurs before gravitationally-bound objects such as inflaton halos, axion miniclusters or galaxies start to form. Numerical simulations can be used to study the gravitational collapse of initially small density fluctuations and to predict the evolution of structures in the

Universe. However, under certain conditions (semi)analytical models of gravitational collapse can be applied to gain an understanding of gravitational clustering and the distribution of collapsed objects in the Universe.

2.4.1 Spherical Collapse Model

Considering a spherically symmetric perturbation with radial size R and an initial overdensity δ in a flat and matter-dominated universe provides valuable insight into the behaviour of perturbations in the nonlinear regime. Since the evolution of the spherical mass distribution is independent of the background universe, it can be considered as a universe on its own with positive curvature $K > 0$. It will reach a maximal extent R_{max} at some time t_{max} and eventually collapse. The corresponding Friedmann equations are solved by [52]

$$R(\vartheta) = \frac{R_{\mathrm{max}}}{2}(1 - \cos\vartheta)\,, \quad t(\vartheta) = \frac{t_{\mathrm{max}}}{\pi}(\vartheta - \sin\vartheta)\,, \tag{2.110}$$

where the angle ϑ runs from 0 to 2π. Evidently, the sphere grows and reaches its maximal size R_{max} at $\vartheta = \pi$. From there on, the overdensity starts to collapse which is why R_{max} is also called the *turn-around* radius. At earlier times, $\vartheta \ll 1$ and the overdensity is still in the linear regime. Then, the expressions for both $R(\vartheta)$ and $t(\vartheta)$ can be expanded in a Taylor series and one obtains that [52]

$$R(t) \simeq \frac{R_{\mathrm{max}}}{4}\left(6\pi\frac{t}{t_{\mathrm{max}}}\right)^{2/3}\left[1 - \frac{1}{20}\left(6\pi\frac{t}{t_{\mathrm{max}}}\right)^{2/3}\right]\,, \tag{2.111}$$

which describes the evolution of a spherical perturbation to linear order. Using that the density of a sphere scales as $\rho \sim R^{-3}$, the corresponding overdensity $\delta_{\mathrm{lin}} = \delta\rho/\bar{\rho} = -3\delta R/R$ can be calculated from Eq. (2.111) which yields [52]

$$\delta_{\mathrm{lin}} \simeq \frac{3}{20}\left(6\pi\frac{t}{t_{\mathrm{max}}}\right)^{2/3}\,. \tag{2.112}$$

Thus, the linear overdensity at the time of turn-around is $\delta_{\mathrm{lin}}^{\mathrm{ta}} = 1.06$ which means that density perturbations in linear theory start to collapse when $\delta_{\mathrm{lin}} \sim 1$. Note that the actual overdensity in the spherical collapse model at the same time is $\delta^{\mathrm{ta}} = 4.55$, i.e. larger by a factor of 4 [52]. After turn-around, the collapse proceeds similarly to the preceding phase of expansion and completes at $t = 2t_{\mathrm{max}}$. According to Eq. (2.112), the density contrast is $\delta_{\mathrm{lin}}^{\mathrm{coll}} = 1.686$ in linear theory at this time.

While a density perturbation reaches infinity at the time of collapse in the spherical collapse model, there are always tiny departures from perfect spherical symmetry in reality. They lead to the formation of gravitationally-bound structures such as dark matter halos and filaments. A useful approximation for the time scale of the gravitational collapse of a spherically symmetric object is the free-fall time[32] [230]

$$t_{\mathrm{ff}} = \left(\frac{3\pi}{32G\bar{\rho}} \right)^{1/2} , \tag{2.113}$$

where $\bar{\rho}$ is the average density of the collapsing object. During the collapse, gravitational potential energy is converted into kinetic energy. Eventually, a halo will reach virial equilibrium meaning that the potential energy E_{pot} and the kinetic energy E_{kin} satisfy the virial theorem, $2E_{\mathrm{kin}} + E_{\mathrm{pot}} = 0$. This implies that a spherical object virialises at radius $r_{\mathrm{vir}} = R_{\mathrm{max}}/2$, i.e. at $\vartheta = 2\pi$, where the spherical collapse model predicts an overdensity of $\delta^{\mathrm{vir}} \simeq 178$ [230]. Numerical simulations revealed that the overdensity at virialisation $\Delta_{\mathrm{vir}} = \rho(t_{\mathrm{vir}})/\bar{\rho}(t_{\mathrm{vir}}) - 1$ in a flat ΛCDM universe is well described by [237–239]

$$\Delta_{\mathrm{vir}}(z) \approx \frac{18\pi^2 + 82x - 39x^2}{\Omega_m(z)} , \tag{2.114}$$

where z is the redshift of virialisation and $x = \Omega_m(z) - 1$ with

$$\Omega_m(z) = \frac{\Omega_{m,0}(1+z)^3}{\Omega_{m,0}(1+z)^3 + \Omega_{r,0}(1+z)^4 + \Omega_{\Lambda,0}} . \tag{2.115}$$

For a purely matter-dominated universe, the virial overdensity $\Delta_{\mathrm{vir}} = 18\pi^2 \approx 178$ does not depend on time and coincides with the result obtained from the spherical collapse model. In numerical simulations, this parameter is used to define the average density of a collapsed object. To avoid any dependency on the cosmological model, it is also quite common to use $\Delta_{\mathrm{vir}} = 200$ instead.

2.4.2 Press-Schechter Theory

The spherical collapse model tells us that a linearly evolved overdensity will collapse and form a halo once[33] $\delta(\mathbf{x}, t) > \delta_c = 1.686$. Working with the linearly extrapolated overdensity $\delta_0(\mathbf{x}) = \delta(\mathbf{x}, t)/D(t)$ where $D(t)$ is the linear growth factor normalised to unity at redshift $z = 0$, this is equivalent to $\delta_0(\mathbf{x}) > \delta_c/D(t) \equiv \delta_c(t)$. In fact, this simple collapse criterion can be used to estimate the mass distribution of halos. The ansatz of the Press-Schechter (PS) formalism [243] is to smooth the density field with a window

---

[32] This time scale defines the time it takes a uniform, pressure-free sphere to collapse [230].

[33] Note that this is only true in a matter-dominated universe. The collapse threshold is modified during radiation-domination which is relevant for axion minicluster formation [240–242].

function[34] $W(\mathbf{x}, R)$ such that it is filtered on a length scale R,

$$\delta_s(\mathbf{x}, R) = \int \delta_0(\mathbf{x}')W(\mathbf{x}+\mathbf{x}', R)\mathrm{d}^3\mathbf{x}' \,. \tag{2.116}$$

The filter scale can be related to a mass M and all points in space satisfying $\delta_s(\mathbf{x}, R) > \delta_c(t)$ are considered to be part of a halo. The idea is now to relate the probability that $\delta_s(\mathbf{x}, R) > \delta_c(t)$ to the fraction of the total mass contained within halos with a mass larger than M. Assuming a Gaussian density field as generated by inflation, the probability is [230]

$$\mathcal{P}[> \delta_c(t)] = \frac{1}{\sqrt{2\pi\sigma^2(R)}} \int_{\delta_c(t)}^{\infty} \mathrm{d}\delta \exp\left(-\frac{\delta^2}{2\sigma^2(R)}\right) . \tag{2.117}$$

The variance $\sigma^2(R)$ on scale R of the smoothed density field can be expressed in terms of the linear power spectrum $P(k)$ and the window function in Fourier space $W_R(k)$ as

$$\sigma^2(R) = \frac{1}{2\pi^2} \int_0^{\infty} P(k)W_R(k)k^2\mathrm{d}k \,. \tag{2.118}$$

Introducing the halo mass function (HMF) $\mathrm{d}n/\mathrm{d}\log M$, which is the comoving number density of halos per logarithmic mass bin, the mass fraction $F(> M)$ of halos with a mass larger than M can be written as [243]

$$F(> M) = \frac{1}{\bar{\rho}} \int_M^{\infty} \frac{\mathrm{d}n}{\mathrm{d}\log M'} M' \mathrm{d}\log M' \,, \tag{2.119}$$

where $\bar{\rho}$ is the comoving background density. Taking into account an additional factor of 2 and demanding that $F(> M) = 2\mathcal{P}[> \delta_c(t)]$, one obtains the Press-Schechter halo mass function[35] (PS-HMF) by differentiating Eq. (2.119) and Eq. (2.117) with respect to M [243],

$$\frac{\mathrm{d}n}{\mathrm{d}\log M} = -\frac{1}{2}\frac{\bar{\rho}}{M} f(\nu) \frac{\mathrm{d}\log\sigma^2}{\mathrm{d}\log M} \,. \tag{2.120}$$

Here, ν denotes the peak significance and $f(\nu)$ is the multiplicity function given by

$$f(\nu) = \sqrt{\frac{2\nu}{\pi}} \exp\left(-\frac{\nu}{2}\right) , \quad \text{with} \quad \nu = \frac{\delta_c^2(t)}{\sigma^2(R)} \,. \tag{2.121}$$

Note that there is a time dependence in the PS-HMF due to the "hidden" linear growth factor $D(t)$. The proposed multiplicity function in Eq. (2.121) assumes a spherical collapse

---

[34] For the sake of generality, we leave the exact shape of the window function undetermined at this point. In the case of spherical collapse, it is usually taken to be a top-hat function in real space.

[35] The "fudge factor" of 2 was originally introduced rather arbitrarily to account for the possibility that underdense regions can be contained within a larger overdense region [230]. However, this factor could be inferred naturally in the excursion set formalism [244], also known as extended Press-Schechter formalism, where a random walk process is applied to compute $F(> M)$.

of overdensities. However, it was discovered that considering ellipsoidal dynamics in terms of a different multiplicity function [245–247]

$$f_{\rm st}(\nu) = A_{\rm st}\sqrt{\frac{2q_{\rm st}\nu}{\pi}}\left(1 + (q_{\rm st}\nu)^{-p_{\rm st}}\right)\exp\left(-\frac{q_{\rm st}\nu}{2}\right), \tag{2.122}$$

with $p_{\rm st} = 0.3$, $A_{\rm st} = 0.3222$ and $q_{\rm st} = 0.707$, produces halo mass functions that are in better agreement with N-body simulations than the original PS-HMF. In any case, the HMF obtained from the Press-Schechter formalism strongly depends on the chosen window function $W(\mathbf{x}, R)$. A common choice to model the spherical collapse is the top-hat window function which corresponds to a sphere with radius $R_{\rm th}$ in real space. Correspondingly, the enclosed mass is given by $M_{\rm th} = 4\pi\bar{\rho}R_{\rm th}^3/3$. In Section 5.3.1, we will instead make use of the sharp-k window function that is defined as a top-hat sphere in Fourier space, $W_{\rm sk}(kR_{\rm sk}) = \Theta(1 - kR_{\rm sk})$. As this filter has contributions on all scales in real space, one cannot simply assign a mass to the filter scale $R_{\rm sk}$. How this issue can be resolved in order to obtain a PS-HMF with sharp-k filter is discussed in the context of Section 5.3.1.

2.4.3 N-body Simulations

Numerical N-body simulations have proven to be indispensable for studying the collapse of density fluctuations well into the nonlinear regime and for understanding the evolution of structures in our Universe. Under the assumption that a system consists of a self-gravitating collisionless fluid, which can be described by the 6-dimensional phase space density $f(\mathbf{x}, \mathbf{p}, t)$, where $\mathbf{p} = m\mathbf{v}$ is the momentum, the gravitational evolution of the system is given by the collisionless Boltzmann equation [248]

$$\frac{\partial f}{\partial t} + \frac{1}{ma^2}\mathbf{p}\cdot\nabla f - m\nabla V_N \cdot \frac{\partial f}{\partial \mathbf{p}} = 0\,. \tag{2.123}$$

Furthermore, the gravitational potential V_N obeys the Poisson equation (see Eq. (2.89))

$$\nabla^2 V_N = 4\pi G a^2(\rho - \bar{\rho})\,. \tag{2.124}$$

The system of these two equations is usually referred to as the Vlasov-Poisson equations. It is suited to describe the evolution of both CDM, such as axions (see Section 4.3), and the inflaton in the matter-dominated epoch following inflation (see Section 5.3). The approach of N-body simulations is to evolve an ensemble of sample particles under their own gravity. The phase-space distribution $f(\mathbf{x}, \mathbf{p}, t)$ can be approximated from the sample particles according to [248]

$$f(\mathbf{x}, \mathbf{p}, t) = \sum_{i=1}^{N} \delta_D(\mathbf{x} - \mathbf{x}_i(t))\delta_D(\mathbf{p} - \mathbf{p}_i(t))\,. \tag{2.125}$$

This can be understood as a Monte-Carlo sampling of the phase space distribution which provides a good approximation of the true solution of the Vlasov equation for a sufficiently large number N. In the first step of an N-body simulation, the initial conditions have to be specified. Based on an initial power spectrum the ZA or 2LPT (see Section 2.3.3) can be used to initialise particle positions and velocities. Subsequently, the Poisson equation is solved to compute the gravitational force on each particle in order to update their position and velocity until the simulation is completed. While usually a leapfrog integrator [249] is used to update particle positions and velocities at each half a time step, there are several approaches for the computation of the gravitational force. The latter is the most challenging part of an N-body simulation.

The simplest and the original approach to achieve this is known as the particle-particle (PP) method [250]. The force on a particle is obtained by directly summing the force contributions of all other particles,

$$\mathbf{F}_i = m_i \sum_{i \neq j} G m_j \frac{\mathbf{x}_i - \mathbf{x}_j}{|\mathbf{x}_i - \mathbf{x}_j|^3} \,. \tag{2.126}$$

Since this expression diverges once a close encounter between two particles occurs, one needs to *smooth* the force between two particles by introducing the softening length $\varepsilon_{\mathrm{soft}}$ such that [251]

$$\mathbf{F}_{ij} = G m_i m_j \frac{\mathbf{x}_i - \mathbf{x}_j}{(|\mathbf{x}_i - \mathbf{x}_j|^2 + \varepsilon_{\mathrm{soft}}^2)^{3/2}} \,, \tag{2.127}$$

This can be understood as replacing point particles with spherical particles of size $\varepsilon_{\mathrm{soft}}$. However, the PP method has a computational cost of $\mathcal{O}(N^2)$ evaluations that have to be performed at each time step. Because of this, it is not suitable for large cosmological simulations that require a large number of particles. A natural extension of the PP method is the usage of a tree algorithm [252] where particles are grouped together and treated as a single pseudo-particle instead. While the short-range force between a target particle and its nearby neighbours is computed via the PP method, one considers the distant pseudo-particles for the computation of the long-range force. In other words, a multipole expansion of clusters of particles is performed and truncated at a given order. Compared to the PP approach, this leads to reduced computational costs of $\mathcal{O}(N \log N)$.

In the completely different particle-mesh (PM) method [249], the computational volume with side length L is divided into a fixed grid of size N with N^3 cells such that the width of a cell is $\Delta x = L/N$. Interpolating between particles of fixed size and mass, one can deduce the density at each grid point. There are different approaches to do so, for example, nearest-grid-point, cloud-in-cell (CIC) and triangular-shaped-clouds. Particles are considered to be point-like in the nearest-grid-point approach and the particle mass is completely assigned to the grid cell where the particle is located. In the CIC scheme, particles instead have a fixed size of Δx and contribute mass to all intersecting cells. CIC particles are treated as cubes of uniform density in contrast to triangular-shaped-clouds particles, which have – as the name suggests – a triangular shape. Having a well-defined density, the Poisson equation can be solved very efficiently on the grid using the Fast Fourier transform (FFT). As this requires periodic boundary conditions the size of the simulation box has to be much larger than the scales of interest to prevent artificial interactions due to periodicity. Once the Poisson equation is solved, the forces on the grid points are interpolated back to the position of the particles. A PM algorithm is significantly faster than a PP method. However, the spatial resolution is limited by cell size Δx which corresponds to an effectively rather large softening length $\varepsilon_{\mathrm{soft}} \sim \Delta x$. To reach smaller softening lengths, one can make use of adaptive mesh refinement (AMR) which locally introduces additional grids with finer spacing [253, 254]. In regions of interest where the density is large, the spatial resolution is thus increased by a hierarchy of nested rectangular sub-grids. Other methods to increase the spatial resolution of the simple PM approach are for example the $\mathrm{P}^3\mathrm{M}$ and the TreePM scheme. The former combines PP and PM algorithms where the long-range forces are computed on the grid exploiting the speed of the FFT and the direct summation of interactions of nearby particles is used to calculate the short-range forces [249, 255]. The TreePM method is an additional improvement by adopting a tree algorithm instead of the PP algorithm for the small-range forces [256–259].

Commonly used tree codes are for example GADGET [259–261] and PKDGRAV [262, 263], while NYX [264], ENZO [265], ART [266] and RAMSES [267] are widely used AMR codes. It is important to verify that the outcome of simulations with different N-body codes starting from the same initial conditions closely resemble each other. This has been confirmed for the previously mentioned codes by the AGORA comparison project [268] and by recent NYX simulations that reproduce the patterns observed in the AGORA runs [269]. Due to the accordance among the different codes, one can work with the code that is geared to the needs of a given situation. In this thesis, the TreePM code GADGET-3, a precursor to the current version GADGET-4 [261], has been used for the first simulations of axion miniclusters (see Section 4.3) and NYX for the structure formation simulations in the post-inflationary universe (see Section 5.3).

Eventually, one needs to locate halos in the simulation volume to extract, for example, their mass distribution in terms of the halo mass function and to study their formation history and inner structure. N-body simulations cannot provide such important data on their own which is why additional algorithms have to be applied to find halos. The two halo finders that were used for this thesis are SUBFIND [270, 271], which is specialised to analyse GADGET simulation data, in the context of axion miniclusters in Section 4.3 and ROCKSTAR [272] to identify inflaton halos in the simulations from Section 5.3. The basis of both halo finders is a friends-of-friends algorithm [273] which groups particles together that are close to each other, i.e. their distance must be smaller than a certain linking length. Having identified a halo, gravitationally unbound particles are removed from it in order to find subhalos within a halo. An overview of different halo finders and how they perform can be found in Ref. [274]. They have in common that they characterise halos in terms of virial quantities. Under the assumption that a halo is spherically symmetric, one usually defines its radial size in terms of the virial radius r_{vir}, for which the average overdensity within the halo matches the virial parameter Δ_{vir} from Eq. (2.114). Then, the mass of a halo is approximated by the virial mass

$$M_{\mathrm{vir}} = \frac{4\pi}{3}\Delta_{\mathrm{vir}}\bar{\rho} r_{\mathrm{vir}}^3 \,, \tag{2.128}$$

and its circular velocity is given by the virial velocity [230]

$$v_{\mathrm{vir}} = \left(\frac{GM_{\mathrm{vir}}}{r_{\mathrm{vir}}}\right)^{1/2} . \tag{2.129}$$

Once a halo is located, it is of interest to study its internal structure. The mass distribution of a halo can be described by its density profile $\rho(r)$. For example, it was shown that the self-similar infall of an isolated initial density perturbation leads to the steep power-law profile [275]

$$\rho(r) \propto r^{-9/4} . \tag{2.130}$$

High-resolution cosmological N-body simulations have revealed that the density profile of objects forming from hierarchical structure formation can be described by the Navarro-Frenk-White (NFW) profile [71]

$$\rho_{\mathrm{NFW}}(r) = \frac{\rho_0}{(r/r_s)(1+r/r_s)^2} \,, \tag{2.131}$$

where r_s is the so-called scale radius and ρ_0 is a characteristic density. For small radii $r < r_s$, the NFW profile scales as $\rho \sim r^{-1}$ and for large $r > r_s$ it behaves as $\rho \sim r^{-3}$. Thus, the scale radius r_s represents the scale where the transition between the two asymptotic power-law profiles occurs. At this point one finds $\rho_0 = 4\rho(r_s)$, so only one free parameter in Eq. (2.131) is required in this model. Related to the scale radius is the concentration of an NFW halo which is defined by $c_{\mathrm{NFW}} = r_{\mathrm{vir}}/r_s$ and of $\mathcal{O}(10)$ for typical halos. Remarkably, the NFW profile is universal in the sense that it can describe the density profile of halos for any mass and in different cosmological scenarios [237, 276].

However, simulations have revealed that there are small but systematic deviations in the density profiles of halos compared to the NFW profile. In fact, the Einasto profile [277], which introduces an additional free parameter in the density profile, might provide a more suitable description [278, 279].

2.4.4 The Peak-Patch Method

Since large and high-resolution N-body simulations are computationally expensive, it is desirable to use approximate methods to generate large halo catalogues. This can be achieved by the Peak-Patch algorithm [280]. Instead of resolving the full gravitational evolution as N-body simulations do, the Peak-Patch method linearly extrapolates an initial density field and identifies regions with an overdensity larger than $\delta_c = 1.686$. In this way, peaks in the density field at any given time can be found. Since they can be compared to halos in an actual N-body simulation, the Peak-Patch method can be understood as a halo finder operating on the initial density field. As a result, one obtains a large halo catalogue having used only a fraction of the computation time and memory of an N-body simulation. In Section 5.3 we make use of M3P, which is based on the Peak-Patch algorithm from Refs. [280, 281] and has been adapted for studying axion miniclusters [240, 241], to validate the inflaton halo mass function obtained from N-body simulations. In contrast to the Peak-Patch methods from Refs. [280, 281], which take into account ellipsoidal collapse, M3P only applies the spherical collapse model.

Peaks in the linearly evolved density field are detected by smoothing it with a spherical top-hat filter in real space on various scales and storing all regions above the density threshold δ_c. It is important to make a wise choice as too few filters might miss potential halos. However, too many filters reduce the computational performance of the filtering procedure significantly. Optimally, the filter sizes should be logarithmically spaced and cover the mass range of the expected halos. Once peak candidates are identified, the maximum radius at which a spherical region around a given peak will gravitationally collapse determines both the size of a halo and its time of collapse. If, for example, the enclosed average density within a certain radius is smaller than the critical overdensity δ_c, the radius has to be decreased. As a result, the average density within a smaller enclosed region will eventually be large enough to fulfil the collapse criterion. The mass of the collapsed halo is then given by the average density within the collapse radius.

Since halos can overlap with each other and smaller collapsed objects might actually be contained within larger ones, a hierarchical Lagrangian exclusion and reduction algorithm is performed in the next step. This avoids any double-counting of mass and ensures that halo candidates are distinct. Beginning with the most massive halo candidates, any halo whose centre lies within the radius of the larger one is excluded from the list of halo candidates. Furthermore, overlapping halos are reduced in size to prevent double-counting of mass. Eventually, the displacement field $\boldsymbol{\Psi}(\mathbf{q})$ is computed from the density field to determine the final Eulerian position of the halos using either the ZA or 2LPT.

Chapter 3

Structure Formation with Nonrelativistic Scalar Fields

Having discussed the growth and collapse of matter density perturbations in the previous chapter, we now address self-gravitating scalar fields in the context of cosmological structure formation. As already noted in Chapter 1, the inflaton, the QCD axion and any other ALPs are described by scalar fields which can form gravitationally-bound objects in different cosmological scenarios. They have in common that they can be considered as cold – and thus nonrelativistic – matter, they have high occupation numbers which allows us to treat them as classical scalar fields, and their self-interactions can be neglected in our scenarios of interest.

The evolution equations of a nonrelativistic, self-gravitating scalar field are derived at the beginning of this chapter. We will see that the evolution is governed by the familiar Schrödinger equation. However, it is important to emphasise that purely *classical* scalar fields are considered and quantum effects do not exist. Instead, one should regard this analogy as a wavelike description of the scalar field with the associated wavelike behaviour on scales of the de Broglie wavelength. Aside from wave interference patterns, a prominent feature is the formation of bound solitonic objects. Exploring the nonlinear evolution of scalar field fluctuations requires large numerical simulations. Lately, there has been substantial progress in the development of different numerical schemes. They can be separated into particle-based approaches adopting a fluid formulation of the Schrödinger equation, grid-based approaches solving the wave equation directly with finite difference and pseudo-spectral methods, and a hybrid approach that aims to combine the advantages of the fluid and the field description.

The basis for the different approaches is provided in Section 3.1 where the Schrödinger and its fluid formulation are introduced. This is followed by a discussion of its relation to the Vlasov-Poisson equations that govern the evolution of nonrelativistic collisionless particles such as CDM. An overview of the available numerical toolbox is given in Section 3.2, including a brief description of the cosmology code AxioNyx [43] that was adapted for the Schrödinger simulations of the early Universe presented in Section 5.4.

3.1 Scalar Field Dynamics

Any real scalar field ϕ with mass m, which does not couple to other fields and does not interact with itself except for gravity, can be described by the action in Eq. (1.23) with Lagrangian[36]

$$\mathcal{L} = -\frac{1}{2} g^{\mu\nu} \partial_\mu \phi \partial_\nu \phi - \frac{1}{2} \frac{m^2}{\hbar^2} \phi^2 \, . \tag{3.1}$$

As before in Section 1.2.2, one can vary the action in Eq. (1.23) with respect to ϕ to obtain the Klein-Gordon equation

$$\Box \phi - \frac{m^2}{\hbar^2} \phi = 0 \, , \tag{3.2}$$

where we introduced the d'Alembertian operator [46]

$$\Box = \partial_\mu \partial^\mu = \frac{1}{\sqrt{-g}} \partial_\mu \left(\sqrt{-g} g^{\mu\nu} \partial_\nu \right) . \tag{3.3}$$

Considering the FLRW background metric, the perturbed line element in Newtonian gauge is (see Eq. (2.8))

$$\mathrm{d}s^2 = -(1 + 2V_N)\mathrm{d}t^2 + a^2(1 - 2V_N)(\mathrm{d}x^2 + \mathrm{d}y^2 + \mathrm{d}z^2) \, , \tag{3.4}$$

where we used that a scalar field has no anisotropic stress, i.e. $\Phi = \Psi$ (cf. Eq. (2.29) and Appendix B.3) and we identified the Newtonian potential as $V_N = \Phi$. We now consider the nonrelativistic limit of the Klein-Gordon equation to derive the evolution equation for a nonrelativistic scalar field.

3.1.1 Evolution Equations in the Nonrelativistic Limit

We start by taking the nonrelativistic limit of the d'Alembertian in Eq. (3.3). According to the post-Newtonian approximation, where the parameter $\varepsilon_{\mathrm{nr}}$ is introduced to account for

---

[36] This corresponds to using the quadratic inflaton potential from Eq. (1.38). In this chapter, we explicitly take the $\hbar$ dependence into account.

relativistic corrections, the gravitational potential scales as $V_N \sim \varepsilon_{\rm nr}^2$ [51]. Since the metric determinant is $\sqrt{-g} = a^3(1-2V_N)$ to $\mathcal{O}(\varepsilon_{\rm nr}^2)$ and $\partial_t\sqrt{-g} = 3H\sqrt{-g}$, the d'Alembertian can be expanded as [25]

$$\Box = -(1-2V_N)(\partial_t^2 + 3H\partial_t) + a^{-2}(1+2V_N)\nabla^2 + \mathcal{O}(\varepsilon_{\rm nr}^4)\,. \tag{3.5}$$

Apart from this, the nonrelativistic limit implies[37] that $m \gg H$ which motivates us to introduce another perturbative parameter $\varepsilon_{\rm WKB} \sim H/m$. In this limit, the Wentzel-Kramers-Brillouin (WKB) approximation can be applied to express ϕ in terms of the slowly varying and complex field ψ [282],

$$\phi(\mathbf{x},t) = \frac{\hbar}{\sqrt{2}m}\left(\psi(\mathbf{x},t)e^{-imt/\hbar} + \psi^*(\mathbf{x},t)e^{imt/\hbar}\right)\,. \tag{3.6}$$

As ϕ performs fast oscillations with frequency m, the idea of this ansatz is to factor out the oscillations and consider instead the equation of motion for the field ψ that obeys $|\hbar\partial_t\psi| \ll |m\psi|$. Calculating the derivatives $\partial_t\phi$, $\partial_t^2\phi$ and $\nabla^2\phi$ in terms of ψ up to first-order in $\varepsilon_{\rm WKB} = |\hbar\partial_t\psi|/|m\psi|$, inserting them into the Klein-Gordon Eq. (3.2) with the d'Alembertian from Eq. (3.5), and performing an expansion to $\mathcal{O}(\varepsilon_{\rm nr}^2, \varepsilon_{\rm WKB})$, the equation of motion for ψ reads[38] [25]

$$i\partial_t\psi + \frac{3}{2}iH\psi + \frac{\hbar}{2ma^2}\nabla^2\psi - \frac{m}{\hbar}V_N\psi = 0\,. \tag{3.7}$$

Making use of Eq. (1.25), the energy density of the scalar field can be computed from the stress-energy tensor up to $\mathcal{O}(\varepsilon_{\rm nr}^2)$,

$$\rho = -T^0_{\ 0} = \frac{1}{2}\left[(1-2V_N)(\partial_t\phi)^2 + a^{-2}(1+2V_N)\nabla^2\phi + \frac{m^2}{\hbar^2}\phi^2\right]\,. \tag{3.8}$$

Applying once more the WKB approximation and expanding the energy density to $\mathcal{O}(\varepsilon_{\rm nr}^2, \varepsilon_{\rm WKB})$ gives that $\rho = |\psi|^2$. This allows the Poisson equation to be expressed in terms of ψ as (see Eq. (2.89))

$$\nabla^2 V_N = 4\pi G a^2\left(|\psi|^2 - \langle|\psi|^2\rangle\right)\,, \tag{3.9}$$

where $\langle|\psi|^2\rangle = \bar{\rho}$ is the homogeneous background density. We now multiply Eq. (3.7) with $\hbar$ and consider the comoving field ψ instead of the physical field that are related by $\psi_{\rm phys} = a^{-3/2}\psi_{\rm comv}$. Then, we obtain the comoving Schrödinger-Poisson (SP) equations [283, 284],

$$i\hbar\partial_t\psi = -\frac{\hbar^2}{2ma^2}\nabla^2\psi + V_N m\psi\,, \tag{3.10}$$

$$\nabla^2 V_N = \frac{4\pi G}{a}(\rho - \bar{\rho})\,, \tag{3.11}$$

---

[37] In the nonrelativistic regime, the Hubble length $l_H = c/H$ is large compared to the Compton wavelength $\lambda_C = \hbar/(mc)$, so $H \ll m/\hbar$.

[38] Note that the equation of motion for ψ^* can be obtained accordingly.

Using the Madelung transformation which expresses ψ in terms of the density and the complex phase S [285],

$$\psi = \sqrt{\rho} e^{iSm/\hbar} , \tag{3.12}$$

it is possible to rewrite the Schrödinger Eq. (3.10) in the form of nonrelativistic fluid equations that are similar to the continuity and the Euler equation. Substituting the Madelung expression for ψ in Eq. (3.10) yields

$$\begin{aligned} i\hbar \frac{\partial_t \rho}{2\sqrt{\rho}} - \sqrt{\rho} m \partial_t S = &- \frac{\hbar^2}{2ma^2} \left[\nabla^2 \sqrt{\rho} - \sqrt{\rho} \frac{m^2}{\hbar^2} (\nabla S)^2 \right] + m V_N \sqrt{\rho} \\ &- \frac{i\hbar}{2a^2} \left[\frac{\nabla \rho}{\sqrt{\rho}} \nabla S + \sqrt{\rho} \nabla^2 S \right] . \end{aligned} \tag{3.13}$$

Defining the fluid velocity as $\mathbf{v} = \nabla S$, the imaginary part of Eq. (3.13) gives the comoving continuity equation [286]

$$\partial_t \rho + a^{-2} \nabla (\rho \mathbf{v}) = 0 . \tag{3.14}$$

Taking the real part of Eq. (3.13) leads to an evolution equation for the phase S,

$$\partial_t S = - \left(\frac{(\nabla S)^2}{2a^2} + V_N + Q \right) , \tag{3.15}$$

where

$$Q = - \frac{\hbar^2}{2m^2 a^2} \frac{\nabla^2 \sqrt{\rho}}{\sqrt{\rho}} \tag{3.16}$$

is often referred to as “quantum potential” or “quantum pressure” in the literature. This naming convention originates from the similarity of Q to the Bohm quantum potential [287]. Note that in this context, Q does not have a quantum origin but simply depends on the curvature of the amplitude of the wave function ψ. Taking the spatial derivative of Eq. (3.15) we obtain the comoving Euler equation,

$$\partial_t \mathbf{v} + a^{-2} \mathbf{v} (\nabla \cdot \mathbf{v}) = -\nabla (V_N + Q) , \tag{3.17}$$

where the hydrodynamic pressure is replaced by Q.

3.1.2 Structure Formation

Perturbing the continuity Eq. (3.14) and the Euler Eq. (3.17) in analogy to the procedure in Section 2.3.1 to linear order, the linearised equations are

$$0 = a^2 \partial_t \delta\rho + \bar{\rho} \, \nabla \cdot \mathbf{v} , \tag{3.18}$$

$$0 = \bar{\rho} \partial_t \mathbf{v} + \bar{\rho} \, \nabla V_N - \frac{\hbar^2}{4m^2 a^2} \nabla (\nabla^2 \delta\rho) . \tag{3.19}$$

Taking the time derivative of Eq. (3.18) and the divergence of Eq. (3.19), the resulting two equations can be combined with the Poisson Eq. (3.11) which yields the second-order differential equations for $\delta = \delta\rho/\bar{\rho}$,

$$0 = \partial_t(a^2\partial_t\delta) - \frac{4\pi G}{a}\bar{\rho}\delta + \frac{\hbar^2}{4m^2a^2}\nabla^2(\nabla^2\delta)\,. \tag{3.20}$$

This perturbation equation can be written in Fourier space as [286]

$$\ddot{\delta}_k + 2H\dot{\delta}_k + \left(\frac{\hbar^2k^4}{4m^2a^4} - \frac{4\pi G\bar{\rho}}{a^3}\right)\delta_k = 0\,, \tag{3.21}$$

and allows a stability analysis as done before in Section 2.3.1. Identifying a pressure and a gravity term in front of δ_k in Eq. (3.21), they compensate each other at the comoving Jeans scale [286]

$$k_J = \left(16\pi a G\bar{\rho}\frac{m^2}{\hbar^2}\right)^{1/4}\,. \tag{3.22}$$

As in Section 2.3.1, the pressure term can be omitted on large scales ($k < k_J$), and gravity leads to growing overdensities. Thus, a nonrelativistic scalar field behaves similarly to a pressureless fluid like CDM on large scales.[39] In contrast to a pressureless fluid, overdensities in a scalar field oscillate without growing on small scales ($k > k_J$) where gravity is subdominant, which prevents further collapse [286].

In fact, it is possible to relate the Jeans length $\lambda_J = 2\pi/k_J$ to the *de Broglie* wavelength $\lambda_{\mathrm{dB}} = 2\pi\hbar/(mv)$ of the ground state of a particle with mass m and velocity v in a potential well [26]. We now interpret the de Broglie wavelength as the minimum size of a collapsed object and consider a halo with size R and a characteristic velocity $v \simeq R/t_{\mathrm{ff}}$ given by its free-fall time t_{ff} (see Eq. (2.113)). By demanding $R = \lambda_{\mathrm{dB}}$ we then find that the characteristic physical de Broglie wavelength of a halo is [26]

$$\lambda_{\mathrm{dB}} = \frac{2\pi\hbar}{mv} = \left(\frac{3\pi^3a^3}{8G\bar{\rho}}\right)^{1/4}\left(\frac{\hbar}{m}\right)^{1/2}\,. \tag{3.23}$$

Comparing this expression with the physical Jeans wavelength by using Eq. (3.22),

$$\lambda_J = \frac{2\pi a}{k_J} = \left(\frac{\pi^3a^3}{G\bar{\rho}}\right)^{1/4}\left(\frac{\hbar}{m}\right)^{1/2}\,, \tag{3.24}$$

we can indeed confirm that $\lambda_{\mathrm{dB}} \simeq \lambda_J$. The quantum origin of the de Broglie wavelength might be used as a motivation to explain the stability below the Jeans scale with the

---

[39] Note that this is the prediction of linear perturbation theory. Taking into account higher-order perturbations leads to an enhanced growth rate instead of further suppression [288].

uncertainty principle. However, this is misleading since it is actually the gradient energy that is dominant on small scales and ensures gravitational stability. Note again that the evolution equations for a nonrelativistic scalar field are completely *classical*.

Structure formation with a nonrelativistic scalar field as an alternative to standard CDM was discussed by the authors of Ref. [282]. Based on this, the FDM model [26] was proposed to resolve the emerging small-scale problems of CDM. The authors of Ref. [26] showed that the linear power spectrum of FDM coincides with that of CDM on large scales while the suppression of gravitational growth on smaller scales produces a sharp cut-off in the power spectrum. A first estimate revealed that the power spectrum is suppressed by a factor of two at the scale $k_{1/2} = 4.5\,\mathrm{Mpc}^{-1}$ for an FDM mass of $m = 10^{-22}\,\mathrm{eV}$. The cut-off in the power spectrum translates to the suppression of halos below the corresponding mass scale. This provides an explanation for the missing satellite problem [18, 19] and the delayed collapse of small-scale structures affects the reionisation history [26]. Importantly, FDM predicts the formation of a core with a size given by the de Broglie wavelength inside a dark matter halo which alleviates the cusp-core problem of the ΛCDM model. The first cosmological simulations that proved the formation of stable solitonic cores in the centre of FDM halos were reported in Ref. [289]. Additional striking features of FDM that were observed for the first time in Ref. [289] are interference patterns that form along filaments and in collapsed halos. These fluctuations in the density field appear on scales of the de Broglie wavelength and are known as *granules*.

FDM has received much attention the past years since it can tackle several small-scale problems of ΛCDM at the same time by introducing only a single additional free parameter, the FDM mass m. This has led to a number of observational constraints on the FDM mass that cast doubt on whether FDM can actually solve the small-scale problems. Without going into great detail, there are constraints from early structure formation, such as observations of the Lyman-alpha forest [15, 290, 291], and from galactic structures (see e.g. Refs. [292–294]). Additional constraints can be derived from processes involving dynamical friction where it is assumed that the granular structure of FDM halos leads to the heating of stars in a galaxy (see e.g. Refs. [295–297]). An extensive overview of FDM mass constraints can be found for example in Ref. [298]. These observations are closing the mass window of FDM and some results already disfavour FDM masses that are required to solve the small-scale problems of ΛCDM. Note that the constraints are derived under the assumption that the total dark matter density consists of FDM. However, they are modified if FDM constitutes only a certain fraction of the total dark matter in the Universe. Simulations of a mixed dark matter model consisting of FDM and CDM with varying fractions of FDM were performed in Ref. [43] and showed that a solitonic core inside a halo still forms if the fraction of FDM is larger than 10%.

Independent of the possible exclusion of FDM, the scalar field description that leads to the formation of solitonic cores can be used to study the core formation in other cosmological scenarios. This includes, for example, axion stars inside axion miniclusters and inflaton stars in the centre of inflaton halos. The physics of the solitons is the same in each of these three cases and is discussed in the following section. However, their mass and size differ significantly from each other and their existence leads to different observational signatures. Axion stars and inflaton stars are further discussed in Section 4.4 and Section 5.4, respectively.

3.1.3 Solitonic Cores

To gain insight into the origin of the solitonic cores, one can consider a wave function of the form $\psi(\mathbf{x}, t) = \psi(\mathbf{x}) \exp(-iEt/\hbar)$. Inserting this ansatz in the SP equations (see Eqs. (3.10) and (3.11)) for $a = 1$ yields the time-independent SP equations,

$$E\psi = -\frac{\hbar^2}{2m}\nabla^2\psi + V_N m\psi\,, \tag{3.25}$$

$$\nabla^2 V_N = 4\pi G\psi^2\,. \tag{3.26}$$

Restricting ourselves to spherical solutions, the time-independent SP equations simplify to a system of ordinary differential equations [299]

$$\partial_r^2\psi + \frac{2\partial_r\psi}{r} = \frac{2m}{\hbar^2}(V_N m - E)\psi\,, \tag{3.27}$$

$$\partial_r^2 V_N + \frac{2\partial_r V_N}{r} = 4\pi G\psi^2\,, \tag{3.28}$$

that can be solved numerically to find spherically symmetric stationary solutions [299–304]. One can recognise the spherical SP equations as an eigenvalue problem. Its solutions are eigenstates ordered with increasing energy according to the number of nodal radii $n = 0, 1, 2, \ldots$ where the density $\rho = |\psi|^2$ vanishes. The ground state solution is the $n = 0$ eigenstate with minimum energy, known as *soliton*, while solutions with $n \geq 1$ are excited states. Depending on the cosmological context, the solitons are referred to as Bose or boson stars [28, 305–307], solitonic cores [289, 308, 309], axion stars [42, 310–312], or inflaton stars [38, 41]. The properties of the lowest eigenstates of Eqs. (3.27) and (3.28), such as their central density and the half-mass radius, can be found for example in Ref. [304]. Importantly, the SP equations themselves and thus also their ground state solution follow a scaling symmetry [299, 313]

$$\{t, r, V_N, \psi, \rho\} \;\longrightarrow\; \{\lambda^{-2}t, \lambda^{-1}r, \lambda^2 V_N, \lambda^2\psi, \lambda^4\rho\}\,. \tag{3.29}$$

Thus, the arbitrary scale parameter λ can be used to construct a family of soliton solutions. Note that the radial size of a soliton scales as $r \sim \rho^{-1/4}$, consistent with the scaling relation of the de Broglie wavelength in Eq. (3.23).

A perturbative treatment of solitonic solutions showed that the ground state is stable and that it is subject to strong quasi-normal oscillations when slightly perturbed [299]. By emitting scalar matter, a process known as gravitational cooling [299, 314, 315], soliton configurations in excited states eventually settle down to the ground state. Then, the soliton is in stationary equilibrium and fulfils the virial condition [303, 304], $2E_{\mathrm{kin}} + E_{\mathrm{pot}} = 0$, where the potential energy is given by

$$E_{\mathrm{pot}} = \frac{1}{2}\int V_N |\psi|^2 \mathrm{d}^3\mathbf{x} = \frac{1}{2}\int \rho V_N \mathrm{d}^3\mathbf{x}\,. \tag{3.30}$$

Making use of the Madelung transformation in Eq. (3.12) the kinetic energy can be written as [304]

$$E_{\mathrm{kin}} = \frac{\hbar^2}{2m^2}\int |\nabla\psi|^2 \mathrm{d}^3\mathbf{x} = \frac{1}{2}\int \rho \mathbf{v}^2 \mathrm{d}^3\mathbf{x} + \frac{\hbar^2}{2m^2}\int (\nabla\sqrt{\rho})^2 \mathrm{d}^3\mathbf{x}\,, \tag{3.31}$$

where the first term is the kinetic energy of a fluid. The second term is the gradient energy that arises from the term defined in Eq. (3.16) and prevents the soliton from gravitational collapse.

Groundbreaking numerical FDM simulations revealed that the radial density profile of a soliton in the centre of a halo can be well approximated by[40,41] [289]

$$\rho_*(r) \simeq \rho_{*,0}\left(1 + 0.091\left(\frac{r}{r_*}\right)^2\right)^{-8}\,. \tag{3.32}$$

Here, r_* is the physical core radius at which the density drops to half of its maximum value and $\rho_{*,0}$ is the physical central core density given by [289, 319]

$$\rho_{*,0} \simeq 3.1\times 10^{15}\left(\frac{2.5\times 10^{-22}\,\mathrm{eV}}{m}\right)^2\left(\frac{\mathrm{kpc}}{r_*}\right)^4\frac{M_\odot}{\mathrm{Mpc}^3}\,. \tag{3.33}$$

Defining the core mass M_* as the mass enclosed by r_* yields [289, 319]

$$M_* \simeq 8.64\times 10^6\left(\frac{2.5\times 10^{-22}\,\mathrm{eV}}{m}\right)^2\left(\frac{\mathrm{kpc}}{r_*}\right)M_\odot\,. \tag{3.34}$$

Hence, the core radius r_*, which can be roughly determined by the de Broglie wavelength corresponding to the local velocity in the centre of the host halo, fully determines both

---

[40] Boson stars have been studied before, for example in Refs. [283, 299, 305, 314, 316, 317].

[41] Note that the soliton profile can only be obtained numerically and that it is nearly a Gaussian as shown in Ref. [318].

the mass of the soliton and its density profile for a given particle mass m. While solitonic cores in the centre of FDM halos have masses of $\sim 10^7\,M_\odot$, typical axion star masses are smaller than $10^{-15}\,M_\odot$ [39, 42] and the mass of inflaton stars is of $\mathcal{O}(\mathrm{g})$ as shown in Section 5.4.

Since the velocity dispersion varies only mildly within the virial radius of a host halo, the velocities of the soliton $v_{\mathrm{vir},*}$ and of the halo $v_{\mathrm{vir},h}$ satisfy $v_{\mathrm{vir},*} = v_{\mathrm{vir},h}$ in virial equilibrium. This makes it possible to relate the core mass to the virial mass of its host halo and numerical simulations found that [308]

$$M_* = \frac{1}{4} a^{-1/2} \left(\frac{\Delta_{\mathrm{vir}}(z)}{\Delta_{\mathrm{vir}}(0)}\right)^{1/6} \left(\frac{M_h}{M_0}\right)^{1/3} M_0\,, \tag{3.35}$$

known as the core-halo mass relation. The virial parameter $\Delta_{\mathrm{vir}}(z)$ is given by Eq. (2.114) and the mass scale

$$M_0 = 32\pi\bar{\rho}_0 \left(\frac{\Delta_{\mathrm{vir}}(0)}{375\Omega_{m,0}^3}\right)^{1/4} \left(\frac{\hbar}{mH_0}\right)^{3/2} \sim 4.4\times10^7 \left(\frac{10^{-22}\,\mathrm{eV}}{m}\right)^{3/2} M_\odot \tag{3.36}$$

is approximately the present Jeans mass, i.e. the minimum possible halo mass. The core-halo mass relation is useful for predicting the expected core masses in a halo, however, it should be clear that it is only an approximation and other simulations favour the slightly different scaling relation $M_* \sim M_h^{5/9}$ [320]. Also, instead of using Eq. (3.35) it is actually more practical to express the core mass in terms of the virial velocity of its host halo. Applying a halo finder to an N-body simulation naturally outputs the virial velocity of each identified halo which, in a further step, can be immediately used to compute the corresponding soliton masses.[42] This is done in Section 5.4 to determine the mass distribution of inflaton stars from the inflaton halo mass function obtained from the N-body simulations presented in Section 5.3.

3.1.4 The Question of Soliton Formation

The cosmological FDM simulations by Ref. [289] proved the existence of solitonic cores in the centre of FDM halos. However, the physical processes that led to their formation in the first place were not discussed. The question of soliton formation was addressed in Ref. [307]. In this work, they studied numerically the evolution of a superposition of plane waves that are initially Gaussian distributed in momentum space. They considered the kinetic regime where the box size L of their simulation is much larger than the de

---

[42] Of course, pure N-body simulations cannot be used for simulations of soliton formation as this requires solving the SP equations.

Broglie wavelength, $L \gg \lambda_{\mathrm{dB}}$. Starting from the Wigner distribution of an ensemble of random classical fields [321]

$$f_W(\mathbf{x},\mathbf{p}) = \frac{1}{(\pi\hbar)^3}\int \mathrm{d}^3\mathbf{x}' \exp\left(\frac{2i}{\hbar}\mathbf{p}\cdot\mathbf{x}'\right)\langle\psi(\mathbf{x}+\mathbf{x}')\psi^*(\mathbf{x}-\mathbf{x}')\rangle\,, \tag{3.37}$$

taking the derivative of f_W and inserting the SP equations, one obtains the evolution equation [286]

$$\partial_t f_W + \frac{\mathbf{p}}{a^2 m}\nabla_{\mathbf{x}} f_W = \frac{im}{\pi^3\hbar^4}\int \mathrm{d}^3\mathbf{x}'\langle\psi(\mathbf{x}+\mathbf{x}')\psi^*(\mathbf{x}-\mathbf{x}')\left[V_N(\mathbf{x})+\mathbf{x}')-V_N(\mathbf{x}-\mathbf{x}')\right]\rangle\,. \tag{3.38}$$

Since the gravitational potential V_N is sourced by $|\psi|^2$ which corresponds to the non-local interaction of two ψ-fields, the integral actually consists of a correlator of four fields. Decomposing this correlator and expanding Eq. (3.38) in the parameter $\varepsilon_f = \lambda_{\mathrm{dB}}/R \ll 1$, where R is the size of a spatial inhomogeneity, one obtains that the evolution of f_W is described to linear order in ε_f by the Vlasov Eq. (2.123). At higher order the Landau scattering integral $\mathrm{St}\,f_W$ acts as a source of kinetic relaxation (see Ref. [307] for details). In fact, the scattering integral $\mathrm{St}\,f_W \sim f_W/\tau_{\mathrm{gr}}$ is determined by the kinetic relaxation time [307]

$$\tau_{\mathrm{gr}} = \frac{b\sqrt{2}}{12\pi^3}\frac{mv^6}{\hbar^3 G^2 n^2 \ln\Lambda}\,, \tag{3.39}$$

where v is a characteristic velocity, n the number density, $\ln\Lambda = \ln(mvR/\hbar)$ the Coulomb logarithm and $b \sim 1$ a coefficient that depends on the initial conditions and has to be computed numerically. The simulations in Ref. [307] showed that τ_{gr} is the relevant time scale for both the formation of a solitonic core with mass $M_{*,0}$ in the kinetic regime and for its subsequent mass growth,

$$M_*(t) \simeq M_{*,0}\left[\left(\frac{t}{\tau_{\mathrm{gr}}}\right)^{1/2}+1\right]\,. \tag{3.40}$$

Since a soliton is the ground state of the SP system and thus the state of lowest energy, one can interpret the relaxation process of a self-gravitating field described by the SP equations as Bose-Einstein condensation[43] [317, 327]. Hence, the time scale in Eq. (3.39) can be understood as a condensation time and the soliton formation as a kinetic process of classical wave condensation [307]. It is important to emphasise that solitonic cores can form in a cosmological setting actually at earlier times than predicted by the condensation

---

[43] Note that Bose-Einstein condensation is a well-known phenomenon arising for example also in the framework of wave turbulence and nonlinear optics [322–326].

time. This is possible since the kinetic description is not valid at all times in contrast to the idealised setup of the simulations in Ref. [307]. Starting from cold initial conditions, i.e. in the non-kinetic regime, the subsequent gravitational collapse of overdensities leads to the formation of halos during which the kinetic regime is eventually entered. This seems to be confirmed by the simulations in Ref. [42] which demonstrated that the kinetic description is applicable after the virialisation of the halos as the soliton mass growth – but not its formation time – is described by the condensation time. Nevertheless, further simulations are required to make more precise predictions.

Interestingly, the expression in Eq. (3.39) can be derived starting from classical two-body scattering. Considering a gravitational system of size R consisting of N particles with mass m, one can compute the interaction rate of two particles. In direct collisions, the velocity deflection $\delta\mathbf{v}$ of a particle with velocity $\mathbf{v}$ is of the same order, so $|\delta\mathbf{v}| \simeq |\mathbf{v}|$. One can show that the characteristic time scale of a direct collision is large compared to the time scale of the more relevant indirect collisions [230]. They are also called weak encounters[44] and satisfy $|\delta\mathbf{v}|/|\mathbf{v}| \ll 1$, in which case $|\delta\mathbf{v}|$ is perpendicular to $|\mathbf{v}|$. Taking into account many independent deflections, one obtains a measure of the mean-square velocity change $\Delta v_\perp^2$ for a complete crossing of the system by integrating $\delta v_\perp^2$ from the minimum impact parameter $b_{\min}$ to the system size R. Defining the relaxation time τ_r as the time at which $\Delta v_\perp^2$ has reached the typical velocity of a particle in the system,[45] one obtains that [248]

$$\tau_\mathrm{r} \simeq \frac{b\sqrt{2}v^3}{2\pi G^2 m^2 n \ln\Lambda}\,. \tag{3.41}$$

The parameter $b \sim 1$ depends on the details of the relaxation process[46] and $\ln\Lambda = \ln(R/b_{\min})$ is the Coulomb logarithm. Considering a system with total mass $M = Nm$ in virial equilibrium, one can express the relaxation time in terms of the crossing time $t_\mathrm{cr} = R/v_\mathrm{vir}$, as

$$\tau_\mathrm{r} \sim \frac{M}{m}\frac{t_\mathrm{cr}}{\ln\Lambda}\,, \tag{3.42}$$

which reveals that $\tau_\mathrm{r} \gg t_\mathrm{cr}$. In the limit of high occupation numbers, the expression in Eq. (3.41) needs to be modified to account for Bose statistics. This can be achieved by multiplying the Eq. (3.41) with the inverse of the phase space density [28, 305, 307, 317]

$$f_p = \frac{3\lambda_\mathrm{dB}^3 n}{4\pi} = \frac{6\pi^2\hbar^3 n}{m^3 v^3}\,, \tag{3.43}$$

---

[44] This means that long-range interactions in the gravitational potential scaling as $1/r$ are the dominant contribution. Hence, gravitational scattering is similar to Coulomb scattering.

[45] The typical velocity in a halo is given by the virial velocity.

[46] In an alternative derivation the N-body system is treated as a diffusion problem which allows the prefactor to be specified, see for example Refs. [248, 328].

such that $\tau_{\mathrm{gr}}^{-1} = (1 + f_p)\tau_{\mathrm{r}}^{-1}$. Thus, we have $\tau_{\mathrm{gr}} \simeq \tau_{\mathrm{r}}/f_p$ for a large phase space density which leads to the expression of the condensation time in Eq. (3.39). Additionally, one can derive Eq. (3.39) by treating the field fluctuations of de Broglie size in a collapsed halo as granular quasiparticles with mass $m_{\mathrm{gran}} \sim \rho\lambda_{\mathrm{dB}}^3$. Their mutual interactions can then source the relaxation process [304]. Taking m_{gran} as the particle mass in Eq. (3.42) gives

$$\tau_{\mathrm{r}} \sim \frac{m^3 v^6}{\hbar^3 G^2 \rho^2 \ln \Lambda}, \tag{3.44}$$

in accordance with Eq. (3.39). Interestingly, it was shown that the typical scalar field fluctuations increase the velocity dispersion of a test particle inside the gravitational potential sourced by the scalar field. This can be understood as "heating-up" the tracer particle and the heating rate can be expressed in terms of diffusion coefficients [328]. Applied to a star cluster inside a dwarf galaxy dominated by FDM, the heating of the star cluster sourced by the FDM density fluctuations was used to derive constraints on the FDM mass [297].

3.1.5 Schrödinger-Vlasov Correspondence

Cosmological structure formation simulations with FDM have shown that CDM and FDM are indistinguishable on scales larger than the de Broglie wavelength [289, 309]. This characteristic is known as the Schrödinger-Vlasov correspondence. In fact, even before the FDM model has been introduced the SP equations were proposed as an alternative method to simulate collisionless CDM [282] that is described by the Vlasov Eq. (2.123). This requires constructing a phase space distribution from the wave function. Due to its strong oscillations on de Broglie scales and the circumstance that it can have negative values, the Wigner distribution f_W (see Eq. (3.37)) is not suited for studying structure formation [282, 321, 329]. These issues are solved by coarse-graining f_W with a Gaussian filter with width σ_x and σ_p, both in real and momentum space [321, 329],

$$f_{\mathrm{FDM}}(\mathbf{x}, \mathbf{p}) = \frac{1}{(2\pi\sigma_x\sigma_p)^3} \int \mathrm{d}^3\mathbf{x}'\mathrm{d}^3\mathbf{p}' \exp\left(-\frac{(\mathbf{x}-\mathbf{x}')^2}{2\sigma_x^2} - \frac{(\mathbf{p}-\mathbf{p}')^2}{2\sigma_p^2}\right) f_W(\mathbf{x}', \mathbf{p}'). \tag{3.45}$$

It was demonstrated that f_{FDM} is strictly positive for $\sigma_x\sigma_p \geq \hbar/2$ [330]. Choosing $\sigma_x\sigma_p = \hbar/2$ defines the Husimi distribution function $f_H = |\psi_H|^2$, where the Husimi representation of the wave function is given by [321]

$$\psi_H(\mathbf{x}, \mathbf{p}) = \frac{1}{(2\pi\hbar)^{3/2}(2\pi\sigma_x^2)^{3/4}} \int \mathrm{d}^3\mathbf{x}' \exp\left[-\frac{i}{\hbar}\mathbf{p}\left(\mathbf{x}' - \frac{\mathbf{x}}{2}\right) - \frac{(\mathbf{x}-\mathbf{x}')^2}{4\sigma_x^2}\right] \psi(\mathbf{x}'). \tag{3.46}$$

Smoothing the Vlasov equation correspondingly and comparing it with the evolution equation for the Husimi distribution, revealed that the evolution equations are equal to each other to first order in σ_x^2 [321]. This means that deviations between CDM and FDM are suppressed by $(\hbar/m)^2$. As a result, the Schrödinger-Vlasov correspondence is even valid on length scales of halos as verified by the simulations in Ref. [309]. However, deviations are expected on de Broglie scales where solitonic cores form. The Schrödinger-Vlasov correspondence can be exploited to perform less expensive N-body simulations to model cosmological structure formation on large scales with nonrelativistic particles instead of running much more costly SP simulations. To resolve the correct wavelike behaviour on small scales, an SP solver needs to be applied. An overview of different simulation methods is given in the following.

3.2 Simulating Nonrelativistic Scalar Fields

In contrast to simulations of collisionless CDM where N-body methods are the most established tool for studying structure formation, several different approaches are used to simulate the gravitational evolution of nonrelativistic scalar fields. In the first instance, one can distinguish between the wave formulation, where the SP Eqs. (3.10) and (3.11) are solved directly, and the fluid formulation. The latter makes use of the Madelung transformation (see Eq. (3.12)) to evolve the density and velocity according to the fluid Eqs. (3.14) and (3.17). Since the first simulations solving the SP equations numerically were presented [282], in general four different approaches have emerged. Both Eulerian finite difference methods [43, 282, 288, 289, 308, 319, 331] and pseudo-spectral methods [43, 307, 320, 332–337] were used in the wave formulation, and particle-based schemes [288, 338–343] were applied to solve the fluid equations. Furthermore, hybrid methods which employ particle schemes on large scales and finite difference methods to solve the SP equations on small scales were introduced [269, 309].

In this section, the different approaches together with their advantages and disadvantages are briefly summarised. Originally developed in the context of FDM structure formation with the pioneering cosmological FDM simulations presented in Ref. [332], they are not restricted to this case and were also applied in the context of axion star formation [42, 307, 344] and for structure formation simulations in the post-inflationary Universe [37, 40, 41].

3.2.1 Schrödinger-Poisson Solvers

Since the gravitational evolution of a nonrelativistic scalar field is governed by the SP system in terms of the wave function ψ, the natural choice is to directly solve the SP Eqs. (3.10) and (3.11). One possible way of doing so is to discretise the spatial coordinates of the wave function on a grid in order to transform the partial differential equation into an ordinary one. Considering only one spatial dimension for convenience with Δx denoting the distance between two points on the grid, i.e. the spatial resolution, a spatial gradient of the wave function can be computed as

$$\nabla \psi(x) = \lim_{\Delta x \to \infty} \frac{\psi(x + \Delta x) - \psi(x)}{\Delta x} . \tag{3.47}$$

The discretised derivative converges to the analytical expression for a decreased Δx and thus for an increased spatial resolution. Denoting the wave function at the grid point j as ψ_j and the adjacent values separated spatially by Δx as ψ_{j+1} and ψ_{j-1} respectively, the second derivative in the Schrödinger Eq. (3.10) can be approximated as

$$\nabla^2 \psi_j = \frac{\psi_{j-1} - 2\psi_j + \psi_{j+1}}{(\Delta x)^2} . \tag{3.48}$$

Higher accuracy in the spatial derivatives can be achieved by taking into account information from more neighbouring grid points. In three dimensions, the standard approximation of the Laplacian corresponding to Eq. (3.48) is the 7-point stencil which involves the central point and its six closest neighbours. Employing, for example, the much more accurate 19-point stencil increases the allowed size of the time step in the time integration of the Schrödinger equation and reduces the numerical error significantly [345]. Using the same discretisation scheme for the time and writing the wave function at time t as $\psi_j^{(n)}$ and at a slightly later time $t + \Delta t$ as $\psi_k^{(n+1)}$, the Schrödinger Eq. (3.10) can be integrated to evolve the wave function in time,

$$\psi_j^{(n+1)} = i \left(\frac{\hbar}{2ma^2} \frac{\psi_{j-1} - 2\psi_j + \psi_{j+1}}{(\Delta x)^2} - \frac{m}{\hbar} V_N \psi_j \right) \Delta t + \psi_j^{(n)} , \tag{3.49}$$

where Eq. (3.48) was applied. This simple time integration scheme is known as the forward Euler method which, however, is only accurate to first-order. Also, it does not guarantee stability in the sense that small numerical errors in each time step pile up spoiling the numerical solution [346]. Sub-dividing the time step improves the stability significantly. The fourth-order Runge-Kutta time integration scheme (see for example Ref. [346]) is accurate to the fourth-order and is unconditionally stable for solving the Schrödinger equation if the Courant-Friedrichs-Lewy criterion [288, 319]

$$\Delta t \leq \min \left[\frac{m}{6\hbar} (\Delta x)^2 , \ \frac{\hbar}{m |V_{N,\mathrm{max}}|} \right] \tag{3.50}$$

is satisfied. Since the spatial resolution must be of at least the same size as the de Broglie wavelength, $\Delta x \lesssim \lambda_{\mathrm{dB}}$, to capture the wave effects of the Schrödinger equation, the criterion in Eq. (3.50) means that the time step must be smaller than the coherence time scale $t_c \sim (\Delta x)^2 m/\hbar \sim \hbar/(mv^2)$. Moreover, the Newtonian potential introduces another time criterion which ensures that only information between adjacent grid points is transmitted within each time step. Due to comparatively small de Broglie scales, high spatial resolution is required to correctly evolve the wave function. This additionally implies that only small time steps, which reduce quadratically with increased spatial resolution, are allowed. This is the reason why cosmological simulations with scalar fields cannot reach the spatial extent of N-body simulations, limiting the explorations to smaller length scales.

In pseudo-spectral methods, one exploits that a gradient in real space corresponds to multiplication with the wave number k in Fourier space. In contrast to finite difference methods, gradients can be computed without numerical approximations. Because of the finite spatial resolution of the grid in real space, the discrete Fourier transform (DFT) is limited to wave numbers smaller than the Nyquist frequency $k_{\text{max}} = \pi/\Delta x$. While requiring periodic boundary conditions and a uniform rectangular grid, DFTs can be efficiently computed using FFTs with numerical costs scaling as $\mathcal{O}(N \log N)$. Moreover, they are suited to be parallelised on a large number of processors. The time evolution of the wave function in the SP equations is given by the unitary transformation

$$\psi(t + \Delta t) = e^{-i\mathbf{H}\Delta t}\psi(t)\,, \tag{3.51}$$

where the Hamiltonian of the system $\mathbf{H} = \mathbf{K} + \mathbf{W}$ is split into a kinetic $\mathbf{K} = -\hbar\nabla^2/(2m)$ and a potential part $\mathbf{W} = V_N m/\hbar$. To second-order accuracy, the operator $e^{-i\mathbf{H}\Delta t}$ can be expanded as [320, 332, 336, 337]

$$e^{-i\mathbf{H}\Delta t} = e^{i\mathbf{W}\Delta t/2} e^{-i\mathbf{K}\Delta t} e^{i\mathbf{W}\Delta t/2}\,, \tag{3.52}$$

which is known as the leapfrog or *kick-drift-kick* method.[47] In the first step, the potential V_N needs to be computed which can be achieved by transforming the Poisson Eq. (3.11) to Fourier space and back. Then, the wave function is given a *kick* by half a time step in real space due to the potential term $\mathbf{W}$, followed by a full time step *drift* in Fourier space according to the kinetic term $\mathbf{K}$. Another *kick* by half a time step in real space completes the time step. Using fourth-order [335] or sixth-order schemes [43, 307] increases the accuracy of the time integration. From the requirement that the phase of the wave function varies less than π in a single time step [320, 336], one obtains the time step criterion (cf. Eq. (3.50))

$$\Delta t \leq 4\min\left[\frac{m}{\hbar}\frac{(\Delta x)^2}{2\pi}, \frac{\pi\hbar}{4m|V_{N,\text{max}}|}\right]. \tag{3.53}$$

---

[47] This is similar to the leapfrog solver used in N-body simulations to evolve particles.

As for the finite difference method, resolving the de Broglie wavelength requires high spatial resolution and small time steps which is why SP simulations in general are limited to much smaller box sizes than N-body simulations. If the resolution criteria $\Delta x \sim \hbar/(mv)$ and $\Delta t \sim \hbar/(mv^2)$ are not satisfied, the dynamics of the simulated system is not correctly evolved anymore. As a result, the dynamics is unphysically slowed down – also on well-resolved scales [288]. Due to their stability, pseudo-spectral methods are usually the preferred way to solve the SP equations on a uniform grid. In contrast to a finite difference solver they cannot be applied on higher levels in an AMR simulation, though. That is because pseudo-spectral methods require periodic boundary conditions that can be ensured only on the root grid. Nevertheless, one can combine both approaches by applying a pseudo-spectral method on the root grid and using AMR with a finite difference solver on higher resolved levels to zoom into regions of interest. The cosmology code AXIONYX [43] is capable of doing so and further described in Section 3.2.4.

3.2.2 Particle Based Solvers

To overcome the issue of spatially resolving the de Broglie wavelength, which is associated with high computational costs, a different approach is to solve the fluid Eqs. (3.14) and (3.17) instead of the SP equations. Then, the density ρ and the velocity of the fluid $\mathbf{v}$ are the variables of interest that can be discretised using particles with mass m_i and velocity $\mathbf{v}_i$. Generally, an interpolation kernel is used to compute the acceleration of each particle which explicitly takes into account the contribution from the quantum pressure in Eq. (3.16). There exist particle-based Lagrangian approaches [338, 340–342], in analogy to smoothed-particle hydrodynamics [347], and the particle-mesh scheme [339] in the literature that are built on already existing N-body methods. They are complemented by an Eulerian grid-based solver [343]. Being fully mass- and energy-conserving, simulations have shown that the fluid formulation correctly describes the dynamical evolution of the SP equations on large and intermediate scales without the need of resolving the de Broglie wavelength [288]. This is in contrast to SP solvers where the evolution on large scales is delayed when λ_{dB} is unresolved. However, the fluid schemes have difficulties with producing the typical interference patterns in SP simulations on small scales. This is related to a vanishing density $\rho = |\psi|^2$ resulting in a divergent quantum pressure term [288]. Since the Schrödinger-Vlasov correspondence (see Section 3.1.5) allows the use of pure N-body solvers to simulate structure formation on large scales, the fluid formalism basically extends the N-body description to smaller scales where the quantum pressure becomes relevant. An SP solver should be used on even smaller scales to correctly resolve the inner structure of a halo and its solitonic core.

3.2.3 Combining N-Body Particles with a Field Representation

The hybrid method introduced in Ref. [309] combines the efficiency of N-body simulations on large scales with the accuracy of the finite difference method to solve the SP equations on small scales. Since most of the simulation volume is covered by the N-body solver, the hybrid approach reduces the computational costs compared to a full wave description significantly, enabling simulations with larger box sizes. Selecting an isolated halo and using the N-body solver until it starts to gravitationally collapse, additional refinement levels are added to increase the spatial resolution in order to resolve the de Broglie wavelength on the higher refined levels. This is necessary for a correct description of the wavelike dynamics governed by the SP equations.

The essential aspect of this idea is the specification of the boundary conditions for the SP solver that are constructed from information provided by the N-body particles. Figuratively speaking, the particles have to be converted into a field representation. N-body particles cannot capture interference effects or the quantum pressure appearing in the fluid equations. Therefore, the conversion of the particles into a wave function has to take place in the single streaming regime far away from the centre of a collapsing halo where wavelike effects are suppressed. The resulting *classical wave function* (CWF) can be derived by omitting the quantum pressure in the evolution Eq. (3.15) for the complex phase S [348],

$$\partial_t S = -\frac{(\nabla S)^2}{2a^2} - V_N \,, \tag{3.54}$$

known as the classical Hamilton-Jacobi equation. The fluid representation of the SP equations originates from using the Madelung transformation (see Eq. (3.12)) to express the wave function in terms of the density $\rho = |\psi|^2$ and the phase S. Hence, subtracting the quantum pressure defined in Eq. (3.16) from the Schrödinger Eq. (3.10),

$$i\hbar\partial_t\psi = -\frac{\hbar^2}{2ma^2}\nabla^2\psi + V_N m\psi + \frac{\hbar^2}{2m^2a^2}\frac{\nabla^2|\psi|}{|\psi|} \,, \tag{3.55}$$

erases the “quantum effects” and leads to Eq. (3.54) after applying the Madelung transformation. This *classical* Schrödinger equation describes the evolution of the CWF and can be used as an approximation of the exact Schrödinger Eq. (3.10), provided the last term on the right-hand side of Eq. (3.55) is small. This corresponds to vanishing interference effects in which case the dynamics of the nonrelativistic scalar field can be simulated with N-body particles. Since wave interference cannot be neglected in the centre of collapsing halos, it is important to transform the N-body particles into the CWF in regions where the Schrödinger-Vlasov correspondence is still valid.

In order to construct the CWF from N-body particles, one requires – apart from particle masses m_i, positions $\mathbf{x}_i$ and velocities $\mathbf{v}_i$ – information about the phase S of the wave function. The initial phase S_i of each N-body particle is obtained from the initial particle velocity field $\mathbf{v} = a^{-1}\nabla S$ (in physical units) by solving the Poisson equation

$$\nabla \cdot \mathbf{v} = a^{-1}\nabla^2 S\,, \tag{3.56}$$

and interpolating S to the particle positions. Subsequently, the particle phases are evolved in each time step as

$$\frac{\mathrm{d}S_i}{\mathrm{d}t} = \frac{1}{2}\mathbf{v}_i^2 - V_N(\mathbf{x}_i)\,. \tag{3.57}$$

This corresponds to the classical Hamilton-Jacobi Eq. (3.54) that is applied to each particle and expressed in terms of the total derivative $\mathrm{d}S/\mathrm{d}t = \partial_t S + a^{-1}\mathbf{v}\nabla S = \partial_t S + \mathbf{v}^2$. In regions far outside of a collapsed halo, the amplitude of the CWF is given by the square root of the classical density [309]

$$|\psi(\mathbf{x})| = \left(\sum_i W(\mathbf{x} - \mathbf{x}_i)\right)^{1/2}\,. \tag{3.58}$$

The classical density on the grid is obtained by smoothing the N-body particle masses with the mass conserving interpolation kernel [309]

$$W(\mathbf{x} - \mathbf{x}_i) = m_i \frac{3}{\pi\xi^3}\left(1 - \frac{|\mathbf{x} - \mathbf{x}_i|}{\xi}\right) \tag{3.59}$$

for $|\mathbf{x} - \mathbf{x}_i| < \xi$ and 0 elsewhere. The parameter ξ can be thus understood as the smoothing radius for the interpolation of the particles onto the grid. Note that the definition of the CWF in Eq. (3.58) implies that interference effects are not contained in the boundary conditions. The phase of the CWF on the grid is approximated as the argument of the wave function resulting from a superposition of particles weighted by their interpolation kernel [309],

$$S(\mathbf{x}) = \frac{\hbar}{m}\arg\left(\sum_i \sqrt{W(\mathbf{x} - \mathbf{x}_i)}e^{i[S_i + \mathbf{v}_i \cdot a(\mathbf{x} - \mathbf{x}_i)]m/\hbar}\right)\,. \tag{3.60}$$

The author of this thesis implemented this hybrid method into the cosmology code AxioNyx and used it to study the formation of inflaton stars in the centre of inflaton halos. The results are presented in Section 5.4.

Recently, another hybrid scheme has been developed which allows the reconstruction of the wave function within the virial radius of a collapsed halo [269]. The idea of the so-called Gaussian beam method is to decompose the wave function into coherent Gaussian wave packets. Their superposition can correctly describe the evolution of the wave function also at times after shell-crossing. It was shown in Ref. [269] that using the wave function in Eq. (3.60) with a Gaussian kernel instead of the interpolation kernel in Eq. (3.59) produces the statistically correct interference patterns inside a collapsed halo. In contrast to the classical wave approximation from Ref. [309] where the wave function has to be constructed in regions where interference can be neglected, the Gaussian beam method can be applied deeply inside a collapsed halo. This decreases the domain where the SP equations are solved and thus reduces the computational costs significantly. Conversely, the Gaussian beam method provides the possibility to simulate much larger halos as proven by Ref. [269] where the solitonic core inside the most massive simulated FDM halo to date was resolved.

3.2.4 Structure Formation Simulations with AxioNyx

The simulations presented in Section 5.4 were performed with AxioNyx [43], which is an SP solver designed to work on adaptively refined regular meshes. Thus, AxioNyx is suited for structure formation simulations with nonrelativistic scalar fields over many length scales. It is an extension of the cosmology code Nyx [264] consisting of a particle-mesh N-body solver and built upon AMReX [349] which provides a framework for block-structured AMR. In this computationally efficient way, the spatial resolution can be considerably increased in regions of interest. To solve the SP equations AxioNyx contains both a second-order and a sixth-order pseudo-spectral method based on the schemes in Ref. [336] and Ref. [307], respectively. Furthermore, it includes a fourth-order Runge-Kutta finite difference algorithm that was implemented within Nyx in Ref. [319]. The most efficient way of performing pure SP simulations with AxioNyx is to apply the pseudo-spectral solver on the root grid, making use of the FFT routines contained in AMReX, and to use the finite difference method on higher levels of refinement [43].

For hybrid simulations as performed in Refs. [41, 269] with AxioNyx, most of the computational domain is evolved with the N-body solver of Nyx. The comoving position $\mathbf{x}_i$ and the peculiar proper velocity $\mathbf{v}_i$ of each N-body particle is advanced by a kick-drift-kick method which is symplectic and thus mass conserving [264]. Applying the multigrid Gauss-Seidel red-black Poisson solver,[48] the gravitational acceleration $\mathbf{g}_i$ of each particle is computed at the beginning of each time step. Then, the particle velocities at time $t^{(n)}$

---

[48] Note that this is in contrast to other N-body PM schemes where FFTs are used to solve the Poisson equation.

are updated by half a time step [264],

$$[a\mathbf{v}_i]^{(n+1/2)} = [a\mathbf{v}_i]^{(n)} + \frac{\Delta t}{2}\mathbf{g}_i^{(n)}\,, \tag{3.61}$$

which is followed by advancing the particle positions for a complete time step

$$\mathbf{x}_i^{(n+1)} = \mathbf{x}_i^{(n)} + \Delta t\left[a^{-1}\mathbf{v}_i\right]^{(n+1/2)}\,, \tag{3.62}$$

and completed by another velocity update

$$[a\mathbf{v}_i]^{(n+1)} = [a\mathbf{v}_i]^{(n+1/2)} + \frac{\Delta t}{2}\mathbf{g}_i^{(n+1)}\,, \tag{3.63}$$

after the gravitational potential has been computed at time $t^{(n+1)}$. Once the wave function is constructed in a comparatively small region of the full simulation volume via either the classical wave approximation or the Gaussian beam method, the wave function is evolved with the fourth-order Runge-Kutta SP solver. Inside the domain where the SP equations are solved, the N-body particles are passively co-evolved and do not contribute to the gravitational field. The density $\rho = |\psi|^2$ of the wave function acts as the source of gravity there.

Chapter 4

Axion Miniclusters

As discussed in Section 1.3, the QCD axion is a real scalar field which is the phase of the complex PQ field originally introduced to solve the so-called strong CP problem of QCD. If the breaking of the PQ symmetry occurs after inflation, the resulting distribution of the axion density field is characterised by large inhomogeneities. In contrast to much lighter ALPs such as FDM, which predicts the formation of prominent solitonic cores in the centre of galaxies with a size of several kpc, QCD axions behave like CDM on galactic scales. However, on smaller scales there can be significant deviations from standard CDM due to the formation of very dense axion miniclusters. They originate from the large isocurvature perturbations which gravitationally collapse already in the radiation-dominated epoch of the Universe.

Before gravitational structure formation becomes relevant, the early evolution of the axion field from PQ symmetry breaking until after the QCD phase transition is dominated by nonlinear axion self-interactions and the formation of topological defects. Eventually, the axion mass becomes relevant initialising the collapse into axion miniclusters accompanied by the formation of axion stars in their centre. Subsequently, the miniclusters merge to build larger-scale objects called axion minicluster halos (MCHs). It is assumed that a large amount of axion miniclusters still exists as substructures in galactic halos at the present time. Larger axion MCHs are more likely to be tidally disrupted forming streams of axions. Both axions gravitationally-bound in miniclusters and more loosely axions in streams are of significance for axion detection experiments.

The spherical collapse model that was originally used to model the collapse of a spherical overdense region into an axion minicluster is reviewed in Section 4.1. This is followed in Section 4.2 by a discussion of the early evolution of the axion field when gravity can still be neglected and a brief summary of the lattice simulations that were used to determine the distribution of the axion density field at redshift $z = 10^6$. At this time, gravitational interactions among the axion particles begin to dominate which can be studied with N-body simulations. The first results obtained from such simulations starting from the initial conditions described in Section 4.2 were published in Ref. [39]. They are presented as part of this thesis in Section 4.3. This includes the fraction of axions bound in miniclusters, their mass distribution as a function of time and an analysis of the structure of axion MCHs at the final redshift[49] $z = 99$. Since there remain some unanswered questions, suggestions for follow-up simulations are also examined. Finally, models of how axion miniclusters can be evolved to the present time and their observational consequences for axion detection experiments are discussed in Section 4.4.

4.1 Formation From Spherical Collapse

Patches of the size of the horizon with random values of the axion field θ are produced in the post-inflationary PQ breaking scenario. The size of a patch of constant θ increases until the axion mass becomes relevant and starts to oscillate (cf. Section 1.3). The gravitational collapse of these patches leads to the formation of axion miniclusters. Their size can be approximated as the horizon size H_{osc}^{-1} at the onset of oscillations and their mass can be thus defined as the mass enclosed in a sphere with radius H_{osc}^{-1}. Characteristic axion minicluster masses and radii are of the order $M_{\mathrm{mc}} \sim 10^{-12}\, M_{\odot}$ and $R_{\mathrm{mc}} \sim 10^{12}$ cm, respectively [27–30]. They are highly overdense objects that can collapse already before matter-radiation equality where the density fulfils $\rho_{\mathrm{eq}} = \rho_m(a_{\mathrm{eq}}) = \rho_r(a_{\mathrm{eq}})$. The axion density perturbation, i.e. the overdensity of the minicluster seeds, can be defined as $\Phi_a = \rho_a/\bar{\rho}_a - 1$ and is $\Phi_a \sim 1$ for typical miniclusters [27]. It can also reach much larger values and stays roughly constant during radiation-domination [28]. In fact, the spherical collapse model can be adapted to compute the minicluster density ρ_{mc} as a function of Φ_a [29]. Considering a flat universe consisting of nonrelativistic matter and radiation, the equation of motion for the radius r of a spherical region containing a matter perturbation is[50] [29]

$$\ddot{r} = -\frac{8\pi G\rho_r}{3} r - \frac{GM_{\mathrm{tot}}}{r^2}\,. \tag{4.1}$$

The mass enclosed by the radius r is denoted as M_{tot} and the radiation density ρ_r is assumed to be homogeneous. Changing to conformal time, and writing $r = a(\tau)R(\tau)\xi$ where ξ labels a comoving shell of the sphere and $R(\tau)$ represents the deviation of the

---

[49] At this time, density perturbations on the scale of the simulation volume have become nonlinear and the N-body simulations needed to be terminated (see Section 4.3.1 for details).

[50] Note that there is a missing r in Eq. (2.1) of Ref. [29].

shell motion from the Hubble flow, Eq. (4.1) can be expressed in terms of R and Φ_a [29],

$$y(1+y)\frac{\mathrm{d}^2R}{\mathrm{d}y^2}+\left(1+\frac{3}{2}y\right)\frac{\mathrm{d}R}{\mathrm{d}y}+\frac{1}{2}\left(\frac{1+\Phi_a}{R^2}-R\right)=0\,. \tag{4.2}$$

As in Eq. (2.96), we introduced the variable $y = a/a_{\mathrm{eq}}$ in this differential equation for R. To obtain Eq. (4.2), the total mass M_{tot} inside a shell was replaced with [29]

$$M_{\mathrm{tot}}=\frac{4\pi}{3}\rho_{\mathrm{eq}}a_{\mathrm{eq}}^3\left(1+\Phi_a\right)\xi^3\,. \tag{4.3}$$

With initial conditions $R_i = 1$, $\mathrm{d}R_i/\mathrm{d}x = 0$ one can solve the full Eq. (4.2) numerically, however, it is also illuminating to find an analytic solution by expanding R in a power series to second-order in y. Then, Eq. (4.2) reduces to [29]

$$R=1-\frac{\Phi_a y}{2}-\frac{\Phi_a^2y^2}{8}\,, \tag{4.4}$$

which reveals that at turn-around ($\dot{r} = 0$, cf. Section 2.4.1) we have $R + y\mathrm{d}R/\mathrm{d}y = 0$. Correspondingly, the scale factor and the density at turn-around are to second-order [29]

$$y_{\mathrm{ta}}=\frac{C_y}{\Phi_a}\,,\quad \text{and}\quad \rho_{\mathrm{ta}}=C_\rho\rho_{\mathrm{eq}}\frac{\Phi_a^3}{3\xi^2}\frac{\mathrm{d}}{\mathrm{d}\xi}(1+\Phi_a)\xi^3\,, \tag{4.5}$$

respectively. Note that the parameters C_y and C_ρ depend weakly on Φ_a and need to be determined numerically. Since the virial radius of a collapsed object is half of the turn-around radius, the virial density is eight times larger than ρ_{ta}. Using the numerical result that $C_\rho \sim 17$, one obtains an expression for the density of an axion minicluster [29],

$$\rho_{\mathrm{mc}}\simeq 140\rho_{\mathrm{eq}}\Phi_a^3(1+\Phi_a)\,. \tag{4.6}$$

This relation was used to estimate the destruction of axion miniclusters in a galaxy as a function of Φ_a in order to measure the event rate that a minicluster passes through Earth [350, 351]. This is a crucial quantity for axion detection experiments (see Section 4.4). Note, however, that this outcome for the overdensity of a minicluster deviates from the virial overdensity Δ_{vir} given by Eq. (2.114) that is used in simulations to determine the mass and size of gravitationally collapsed objects. So far it is still not understood how Eq. (4.6) could be used in a minicluster simulation, and we used Eq. (2.114) instead in the simulations presented in Section 4.3.

4.2 Minicluster Seeds

An accurate description of the evolution starting from PQ symmetry breaking until the QCD phase transition and beyond is crucial for the distribution of axion dark matter before gravity eventually becomes the dominant force leading to the formation of axion miniclusters. This requires not only solving the equation of motion for the axion field $\theta = \phi/f_a$ (cf. Eq. (1.72)) but additionally, the complex scalar PQ field $\phi_{\mathrm{PQ}} = |\phi_{\mathrm{PQ}}|e^{i\theta}$ needs to be evolved. Its equation of motion can be derived from the Lagrangian density [205]

$$\mathcal{L} = a^3 \left(\frac{1}{2} |\dot{\phi}_{\mathrm{PQ}}|^2 - \frac{1}{2a^2} |\nabla \phi_{\mathrm{PQ}}|^2 - V(\phi_{\mathrm{PQ}}) \right) . \tag{4.7}$$

The potential $V(\phi_{\mathrm{PQ}})$ can be decomposed into the sum of the PQ potential, depending only on the radial term $|\phi_{\mathrm{PQ}}|$, and the axion potential from Eq. (1.71) for the angular part of the PQ field [205],

$$V(\phi_{\mathrm{PQ}}) = \frac{\lambda}{8} \left(|\phi_{\mathrm{PQ}}|^2 - f_a^2 \right)^2 + \chi(T) \left(1 - \cos \frac{\phi}{f_a} \right) . \tag{4.8}$$

The temperature dependence of the QCD axion mass is encoded in the topological susceptibility $\chi(T)$. Immediately after PQ symmetry breaking, the complex PQ field acquires its vacuum expectation value $\langle \phi_{\mathrm{PQ}} \rangle = f_a$ and the phase of ϕ_{PQ}, i.e. the axion, takes random values in causally disconnected regions. This leads to the formation of an axion string network (see Section 1.3.2).

Large numerical lattice simulations have been performed to resolve the highly nonlinear processes over large length and time scales. The approach presented in Ref. [205] aims to determine the axion distribution consisting eventually of the seeds of miniclusters as precisely as possible and is further described below. Their procedure is in contrast to other studies where numerical simulations of the string network were used to compute the total dark matter density at the present time in order to obtain an estimate for the axion mass [199, 202]. The challenge for these kind of simulations is to resolve the string core whose radius stays physically constant while the Universe expands. For accurate results, this has to be achieved at least until the time of the QCD phase transition when the axion mass becomes relevant and the axion starts to oscillate. By then, the size of the Universe has increased enormously, and the simulations must be able to resolve a hierarchy of length scales. A common trick to simplify this task is to exploit the Press-Ryden-Spergel method [352, 353]. The idea is to make the mass of the radial field $|\phi_{\mathrm{PQ}}|$ explicitly time-dependent such that the radius of the string core remains constant in comoving coordinates. Evolving the simulations as long as possible after the QCD phase transition necessitates high spatial resolution to capture the important field fluctuations on small scales. Recently, progress has been made by applying AMR to resolve regions of interest [354].

In the simulations performed by Ref. [205], the complex PQ field is evolved until the string network has decayed completely which occurs after the QCD phase transition.

At earlier times, string loops also collapse emitting relativistic axion particles which transfers the string energy into the axion field. Once the axion mass becomes relevant and the axion field starts to oscillate, $H(T_{\rm osc}) \simeq m_a(T_{\rm osc})$ where [205]

$$T_{\rm osc} \simeq 1.694 \left(\frac{m_a}{50\,\mu\text{eV}}\right)^{0.1638} \text{GeV}\,, \tag{4.9}$$

domain walls start to form between the axion strings. This leads to an increased string tension initiating the destruction of the complete string network which generates both relativistic and nonrelativistic axions. Subsequently, the equation of motion for the axion field (see Eq. (1.72)) is solved. Due to the attractive axion self-interactions arising from the higher-order terms in the axion potential, so-called *axitons* form [28, 29, 355]. They are quasi-stable soliton-like objects similar to oscillons that can form during reheating (cf. Section 1.2.3). Axitons are subject to strong oscillations which, together with their eventual decay, lead to the emission of spherical waves of relativistic axions. Originating from overdensities generated by the decay of the string network in the first place, it was observed that they form chain-like structures on large scales [205]. Since their radius scales as m_a^{-1} and the axion mass increases with time, the axiton radius decreases. This poses another challenge for the simulations to spatially resolve them for a sufficient amount of time. If not properly resolved, the energy density transferred to the axions cannot be computed reliably. At late times when the axion mass has reached its zero-temperature value, the axiton radius stops shrinking and the axitons diffuse away. Due to limited spatial resolution, the simulations of Ref. [205] cannot reach such late times. Therefore, the axion self-interactions were set to zero at a time when the axitons were still well resolved to allow them to diffuse away and to ensure that all momentum modes become nonrelativistic. By solving the linear axion equations of motion analytically, the axion density field is evolved until a redshift of $z \simeq 10^6$ at which point its distribution is statistically fixed on essentially all scales.

It is argued in Ref. [205] that axions emitted from the well-resolved axitons at early times contribute to a significant fraction of the axion density field although the number density of axitons grows at late times. The axion density distribution on scales relevant for the formation of axion miniclusters does not depend on the contribution from late-time axiton emission. Thus, the adopted approach with essentially neglecting late-time axitons seems to be a valid approximation [205]. Nevertheless, it is desirable to be able to resolve the axiton evolution for a longer time which should be feasible with AMR. Lately, there have been some efforts in extending AxioNyx to run similar simulations as in Ref. [205] but with AMR instead of using a single, highly resolved uniform grid. It will be exceedingly interesting to see its effect on the obtained axion density distribution as it enables string cores and axitons to be resolved to a higher extent. Additionally, the performance of the computation should be improved which, in the next step, might allow for larger box sizes to evolve the simulations for a longer time. The first promising AMR simulations of the evolution of the axion field from PQ symmetry breaking and beyond the QCD phase transition were recently reported in Ref. [354].

The outcome of the simulations from Ref. [205] provides the distribution of axion dark matter at redshift $z = 10^6$ and serves as the initial conditions for the N-body simulations in Section 4.3 to study the gravitational collapse of the minicluster seeds into axion miniclusters. Due to the fast increase of the axion mass during the early Universe epoch, the axion field can be treated as CDM. The axion distribution consists of large homogeneous patches, where the axion field takes a similar value, which arise from the misalignment mechanism. The axion density field is complemented with typical $\mathcal{O}(1)$ overdensities reaching up to $\mathcal{O}(100)$ that originate from string decays and axitons. A projection of the final axion density field at $z \simeq 10^6$ for a comoving box size of $L = 24L_{\rm osc}$, where [205]

$$L_{\rm osc} = \frac{1}{H_{\rm osc}a_{\rm osc}} = 0.0362 \left(\frac{50\,\mu\text{eV}}{m_a}\right)^{0.167} \text{pc} \tag{4.10}$$

is the comoving size of the horizon when the axion starts to oscillate ($H(T_{\rm osc}) \simeq m_a(T_{\rm osc})$), is shown in the left panel of Fig. 4.1. Note that the original lattice simulation consisted

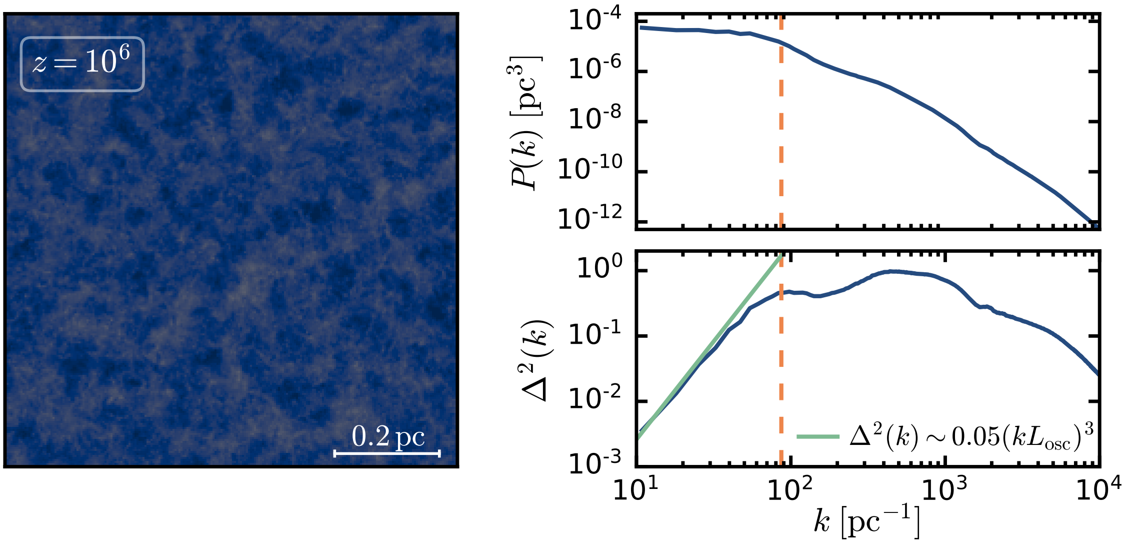

Figure 4.1 | Projected axion density field at redshift $z = 10^6$ for a simulation with box size $L = 24L_{\rm osc}$ (left) and corresponding power spectrum of density fluctuations both in physical (top right) and in dimensionless units (lower right). The dashed orange line denotes the scale $k \sim \pi/L_{\rm osc}$ where the first peak of $\Delta^2(k)$ is reached and below which it can be described by the white-noise power-law in Eq. (4.11).

of 8192^3 grid points which was smoothed to a 1024^3 grid for the purpose of performing subsequent N-body simulations. An analysis of the density field reveals that the dimensionless power spectrum of the density fluctuations (see right panel of Fig. 4.1) can be described by the white-noise power-law

$$\Delta^2(k) \sim 0.05(kL_{\mathrm{osc}})^3 \tag{4.11}$$

on scales larger than $k \sim \pi/L_{\mathrm{osc}}$. This means that the power spectrum $P(k)$ is independent of k on those scales which allows the interpretation that misalignment axions dominate the density field on large scales. The dimensionless power spectrum reaches a first peak at $k \sim \pi/L_{\mathrm{osc}}$, followed by a slight increase until another maximum at $k \sim 5\pi/L_{\mathrm{osc}}$, and slowly declines for higher k. This indicates that there are plenty of structures with small non-Gaussianities on small scales $k \gg \pi/L_{\mathrm{osc}}$ that can be ascribed to the axion production from strings, domain walls and axitons [205]. Hence, one can expect a large amount of substructure within typical miniclusters of size L_{osc}. By analysing the mass distribution of the minicluster seeds, it was found that a large number of them have high overdensities and masses significantly below the typical minicluster mass $M_{\mathrm{mc}} \sim 10^{-12}\,M_{\odot}$. This provides an estimate for the expected rich substructure within axion MCHs.

4.3 The First Simulations of Axion Miniclusters

It is desirable to predict the expected distribution of axion dark matter in the Milky Way at the present time as precisely as possible since this has direct implications for axion detection experiments [350, 356–360]. This requires not only an understanding of the axion density fluctuations generated in the early Universe (see Section 4.2) but also knowledge about their evolution when gravity becomes the dominating force. During this stage, axion overdensities collapse into gravitationally-bound axion miniclusters which subsequently merge into axion minicluster halos MCHs. Assuming Gaussian statistics for the axion density perturbations, semianalytical methods for structure formation were used to determine the minicluster halo mass function (MC-HMF) [361, 362]. Only numerical simulations can take into account nonlinear effects and provide the possibility to accurately determine the properties of axion MCHs. As long as the wavelike properties of the axion can be neglected, N-body simulations are suited to study the gravitational evolution of the minicluster seeds (see Section 3.1.5). Early N-body simulations presented in Ref. [363] observed the formation of axion miniclusters and were used to roughly determine their density profiles. However, the simulation consisted only of 100^3 particles and was thus limited to a rather low spatial resolution. Furthermore, their initial conditions did not consider the production of axions from topological defects.

Large N-body simulations of the gravitational collapse of axion density fluctuations into axion MCHs were reported in Ref. [39]. They start from the highly resolved, realistic initial conditions created by lattice simulations using the methods from Ref. [205] (see also Section 4.2). The obtained results are presented in this section, following and extending the discussion in Ref. [39].

4.3.1 Gravitational Collapse of Axion Density Fluctuations

The initial conditions for the subsequent N-body simulations are given by the frozen axion density field at redshift $z \simeq 10^6$ (see Fig. 4.1) resulting from early-universe lattice simulations with a comoving box side length of $L = 24\,L_{\mathrm{osc}}$. The original density field was converted into 1024^3 particles with initial velocities set to zero. The resulting power spectrum computed from the particle distribution coincides with the original power spectrum from the lattice simulations up to $k \sim 1.5 \times 10^3\,\mathrm{pc}^{-1}$ (see Fig. 4.5). For larger values of k, discretisation effects lead to a white-noise power spectrum where the original power spectrum actually decreases.

We used the N-body solver Gadget-3, which is a precursor of Gadget-4 [261], and chose a comoving box size of $L = 0.864\,\mathrm{pc}$ corresponding to $24L_{\mathrm{osc}}$ for an axion mass of $m_a = 50\,\mu\mathrm{eV}$ to follow the gravitational evolution of the system to a final redshift of $z = 99$. At this point, perturbations of the size of L have become nonlinear beyond which the N-body simulations cannot be trusted anymore (see Fig. 4.5). Each of the 1024^3 particles has a mass of $2.454 \times 10^{-17}\,M_\odot$ and the numerical softening length, which sets the limit of the spatial resolution, was adjusted to be $\varepsilon_{\mathrm{soft}} = 1\,\mathrm{AU}/h$ in comoving units. Since the simulation begins deep inside the radiation-dominated epoch, the background radiation terms were taken explicitly into account for the computation of the Hubble parameter. We used the parameters $\Omega_{m,0} = 0.3$, $\Omega_{r,0} = 8.486 \times 10^{-5}$, $\Omega_{\Lambda,0} = 0.7$ and $H_0 = 70\,\mathrm{km/s/Mpc}$ that are consisted with the ΛCDM model and we assumed that axions account for the total amount of CDM.

Axion MCHs and sub-miniclusters (sub-MCs) were identified with the Subfind halo finder [270, 271]. By definition, substructures are locally overdense, self-bound groups of particles that are contained within a larger parent halo. Applying a friends-of-friends algorithm with a linking length of 0.16 times the average particle separation, parent MCHs consisting of at least 32 particles are identified in the first step. A set of sub-halo candidates is obtained by estimating the local density of each particle in a parent MCH with an adaptive kernel interpolator and finding locally overdense regions in the resulting density field. The extent of a sub-halo candidate is given by a density contour passing through a saddle point of the global density field. Finally, all sub-halo candidates undergo

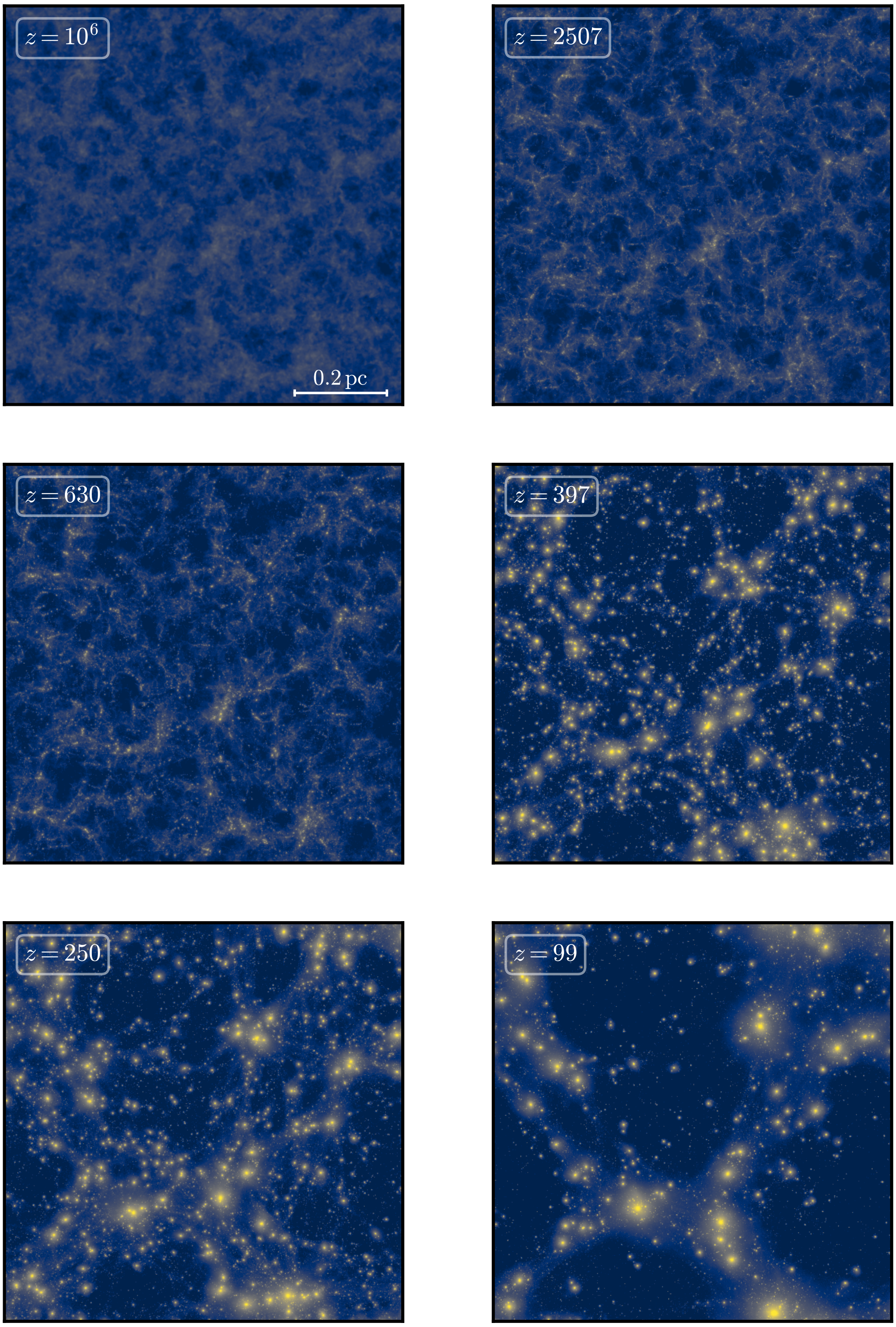

Figure 4.2 | Illustration of the projected axion density of the full simulation box starting from redshift $z = 10^6$ to $z = 99$. The projected density normalised to the average density spans over six orders of magnitude.

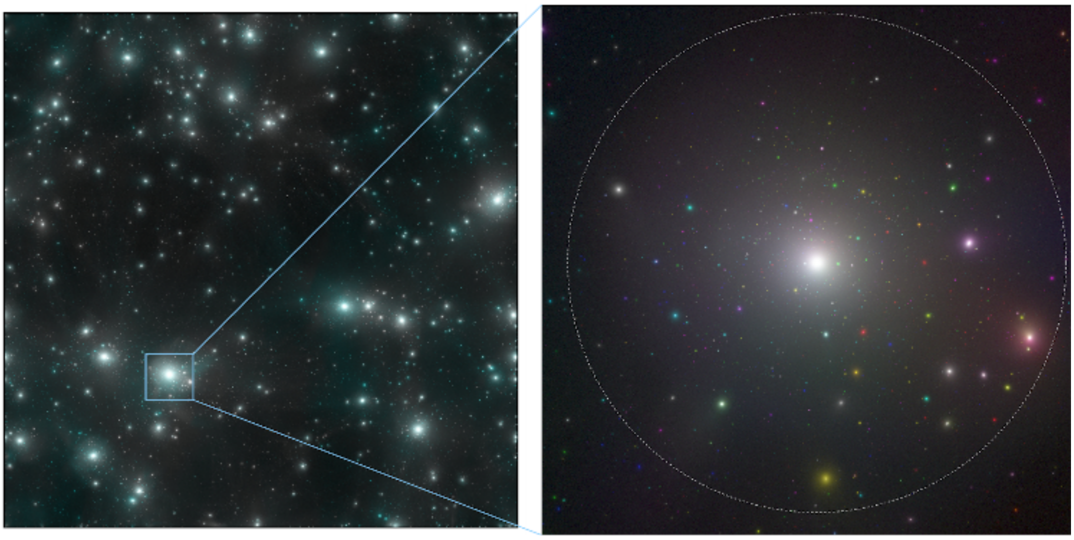

Figure 4.3 | Projected axion density at $z = 99$ and an enlargement of the largest axion MCH with a virial mass of $M_{\mathrm{MCH}} = 3 \times 10^{-9}\, M_{\odot}$ and a virial radius of $r_{\mathrm{vir}} = 92\,\mathrm{AU}$ that is indicated by the dashed circle. The sub-miniclusters are coloured according to their orbital velocity. Figure reproduced from Ref. [39].

a gravitational unbinding procedure such that only self-bound sub-MCs consisting of at least 20 gravitationally-bound particles are kept. In the following, parent MCHs are characterised by their virial mass M_{vir} (cf. Eq. (2.128)) and virial radius r_{vir}. Note that this is not the case for sub-MCs whose mass is determined by the number of self-bound particles.

The evolution of the axion density field is shown in Fig. 4.2. During the radiation-dominated epoch, initially large overdensities start to collapse forming compact axion miniclusters. After matter-radiation equality and, in particular, deep in the matter-dominated era large structures grow by hierarchical structure formation. This means that miniclusters merge to form larger axion MCHs. As visible from Fig. 4.3, the largest MCH in the simulation volume with a virial mass of $M_{\mathrm{MCH}} = 3 \times 10^{-9}\, M_{\odot}$ consists of a high number of sub-MCs. Overall, the masses and radii of the identified MCHs span the ranges $M_{\mathrm{MCH}} \in [2.5 \times 10^{-16},\ 3.0 \times 10^{-9}]\, M_{\odot}$ and $r_{\mathrm{vir}} \in [0.4,\ 92.0]\,\mathrm{AU}$, respectively. Their mass distribution is studied in Section 4.3.2.

To verify that the late evolution of axion miniclusters is indeed dominated by mergers, it is insightful to analyse the total fraction f_b of gravitationally-bound axions and the total number N_{MCH} of MCHs above different mass scales. Both quantities are shown as a function of redshift in the upper and lower panel of Fig. 4.4, respectively. Taking into account MCHs with at least 32 particles, Fig. 4.4 reveals that the bound mass fraction f_b slowly saturates to a value of $f_b \sim 0.75$ at the final redshift $z = 99$. The evolution of f_b and the final result at $z = 99$ agrees with the outcome of a simulation with 512^3

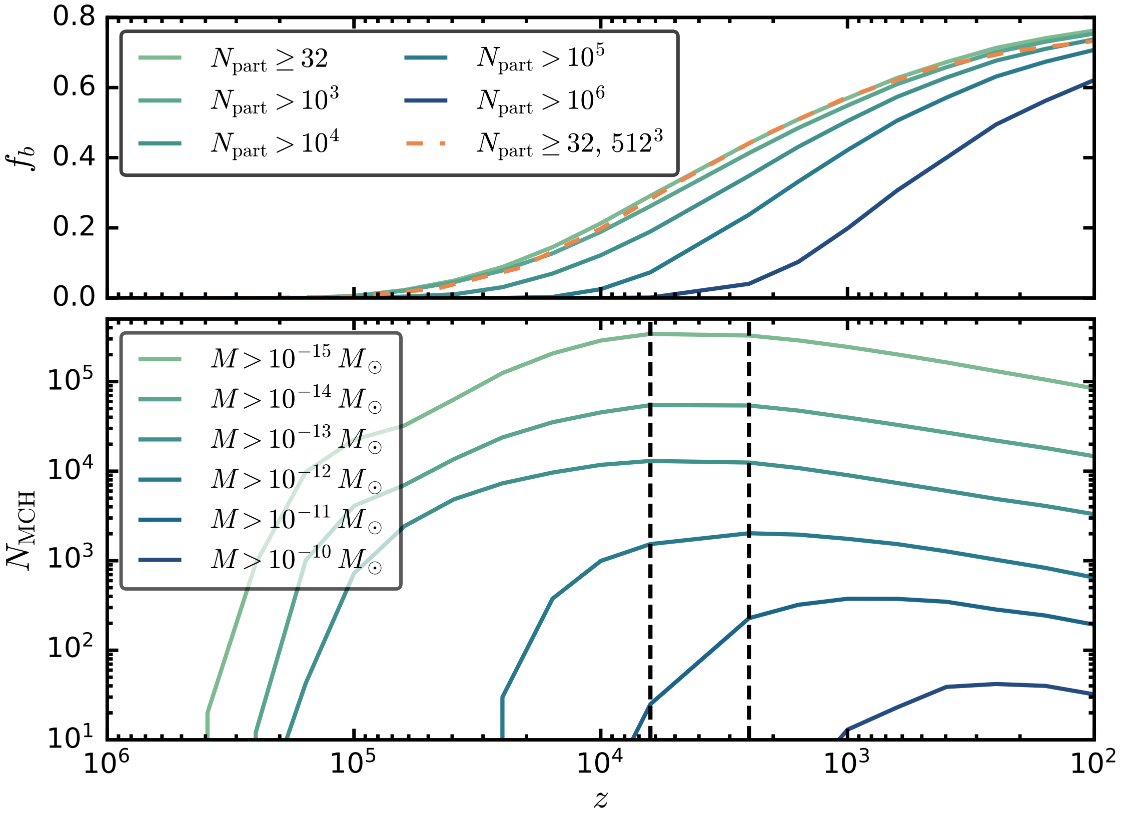

Figure 4.4 | Mass fraction f_b of gravitationally-bound axions considering axion MCHs with at least $N_{\rm part}$ as seen in the legend (upper panel) and the evolution of the total number $N_{\rm MCH}$ of MCHs above different mass scales (lower panel) as a function of redshift z. Convergence of mass resolution for the $N_{\rm part} = 32$ case is shown in the top panel by comparing simulations with 1024^3 and 512^3 particles (orange dashed line). The black dashed lines in the lower panel mark the transition from the radiation-dominated to the matter-dominated epoch. Figure adapted from Ref. [39].

particles only (orange dashed line in the top of Fig. 4.4). Hence, we observe convergence between different mass resolutions. Since MCHs consisting of only 32 particles are at the lower limit of the mass resolution, one should nevertheless compare the obtained result $f_b \sim 0.75$ with the bound mass fraction when only MCHs with a higher number of constituent particles, which do not suffer from the low-mass resolution limit, are considered. As is evident from Fig. 4.4, the behaviour of f_b does not significantly change when only MCHs with more than 10^3 particles are taken into account. Thus, this quantity is not sensitive to the low-mass miniclusters as it is dominated by high-mass MCHs. This is further confirmed by increasing the minimum particle number contained in an MCH to 10^6 which reveals that 60% of all axions are bound in such high-mass MCHs at $z = 99$. Note that the contribution becomes relevant only after matter-radiation equality. Focusing on the evolution of the total number of MCHs in the lower panel of Fig. 4.4 we, first of all, see that the first miniclusters form at $z \simeq 4 \times 10^5$. Their number increases drastically until matter-radiation equality and reduces afterwards as a result of merger events with other miniclusters. Distinguishing between N_{MCH} above certain mass scales allows us to observe at which redshift MCHs of different mass emerge. Miniclusters with masses up to $10^{-11}\,M_{\odot}$ form already in the radiation-dominated epoch while higher-mass MCHs arise only after matter-radiation equality. Throughout the matter-dominated era, the number of MCHs with masses below $10^{-11}\,M_{\odot}$ steadily decreases suggesting that they are subject to mergers producing higher-mass MCHs. Although outnumbering high-mass MCHs at $z = 99$ significantly, the lower-mass MCHs contribute only slightly to the total fraction of axions bound in MCHs.

The evolution of the power spectrum of axion density fluctuations computed from the distribution of N-body particles is shown in Fig. 4.5. The figure is complemented by the power spectrum of the original density field obtained from the early-universe lattice simulations. As mentioned already at the beginning of this section, the N-body power spectrum at $z = 10^6$ agrees with the original one up to large values of k where discretisation effects prevent the correct mapping. Nevertheless, the N-body simulations

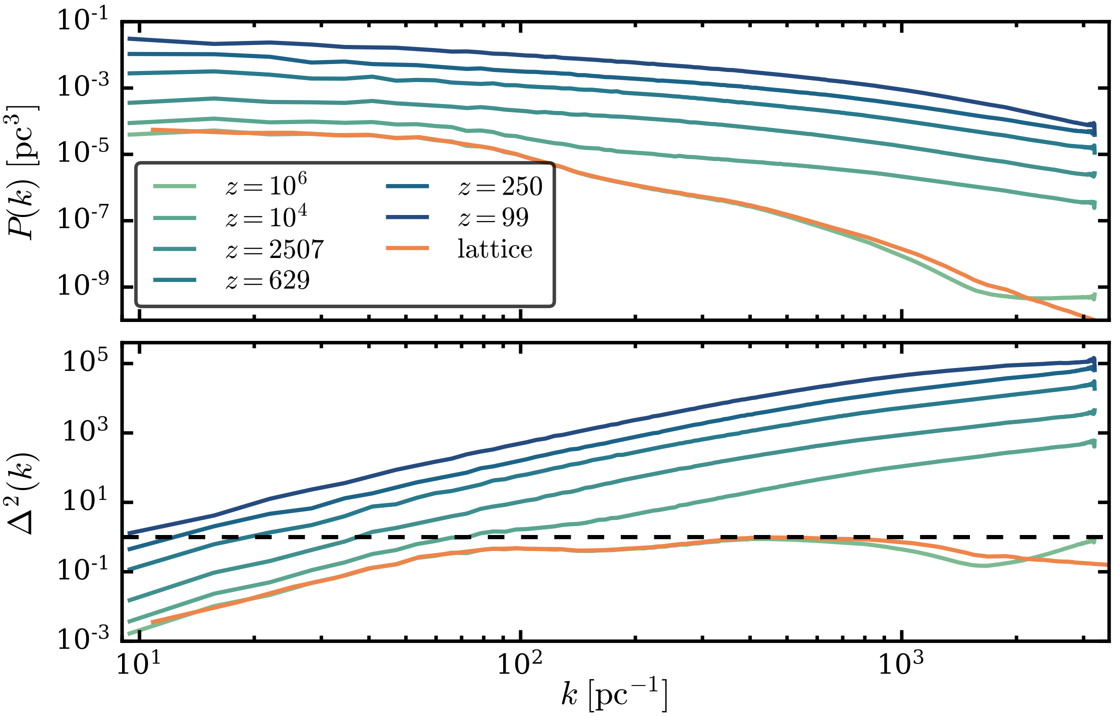

Figure 4.5 | Power spectrum of axion density fluctuations both in physical (upper panel) and dimensionless (lower panel) units for different redshifts. The orange line shows the power spectrum obtained directly from the axion density field of the early-universe lattice simulation with 8192^3 grid points for comparison. The black dashed horizontal line marks $\Delta^2 = 1$ where a density perturbation on a given scale can be considered to be nonlinear. Figure adapted from Ref. [39].

with 1024^3 particles have a large dynamical range and are sensitive to the small scales where the axion density fluctuations originate from the decay of topological defects and axitons. The scales where $\Delta^2(k)$ starts to decrease are thus still resolved. Comparing the power spectra at the beginning of the simulations and at $z = 10^4$, we observe a well-pronounced growth of perturbations on the small scales while the power on large scales increases only mildly. This is consistent with the previous observation that small-scale miniclusters collapse first. After matter-radiation equality, the power on large scales rises considerably which is related to the formation of larger-scale objects. As can be seen from the dimensionless power spectrum at $z = 99$, perturbations of the length of the simulation box are above $\Delta^2(k) \sim 1$ which means that the corresponding mode has become nonlinear. Figuratively speaking, the simulation box then reacts to the gravitational potential of its periodic boundaries and the simulation can no longer be trusted. During matter-domination, the linear growth of density perturbations can be described in terms of the growth factor (cf. Eq. (2.97))

$$D(a) = 1 + \frac{3}{2}\frac{1+z_{\mathrm{eq}}}{1+z}\,. \tag{4.12}$$

Note that slight deviations from this linear prediction arise on scales of the length of the simulation box already at larger redshifts than $z = 99$. No irregularities appeared at very late times in our simulation, so the arising nonlinearities do not seem to affect our simulation results. However, N-body simulations with a larger box size might be required for an independent verification.

4.3.2 Minicluster Halo Mass Function

To obtain a quantitative picture of the dynamics of MCH formation we study the MC-HMF, which is the comoving number density of gravitationally-bound MCHs per logarithmic mass interval as a function of MCH mass. The MC-HMF is shown for different redshifts in Fig. 4.6. The distinct cut-off for low masses at $M_{\mathrm{cut}} \sim 10^{-15}\,M_\odot$ originates from the low-mass resolution limit and is thus not physical but a numerical artefact. For simulations of higher resolution, the cut-off will be thus shifted to lower masses and it is expected that the number density of lower-mass miniclusters further increases. As already discussed in Section 4.3.1, this does not affect the fraction of axions bound in MCHs as this quantity is dominated by the highest-mass MCHs.

At times before matter-radiation equality (see left panel of Fig. 4.6) the MC-HMF grows quickly. It is dominated at first by halos near the low-mass resolution cut-off and develops a pronounced peak at $M_{\mathrm{mc}} \sim 2 \times 10^{-13}\,M_\odot$ when $z \simeq 4 \times 10^4$. The rapid growth can be understood as the collapse of initially deeply nonlinear density fluctuations and

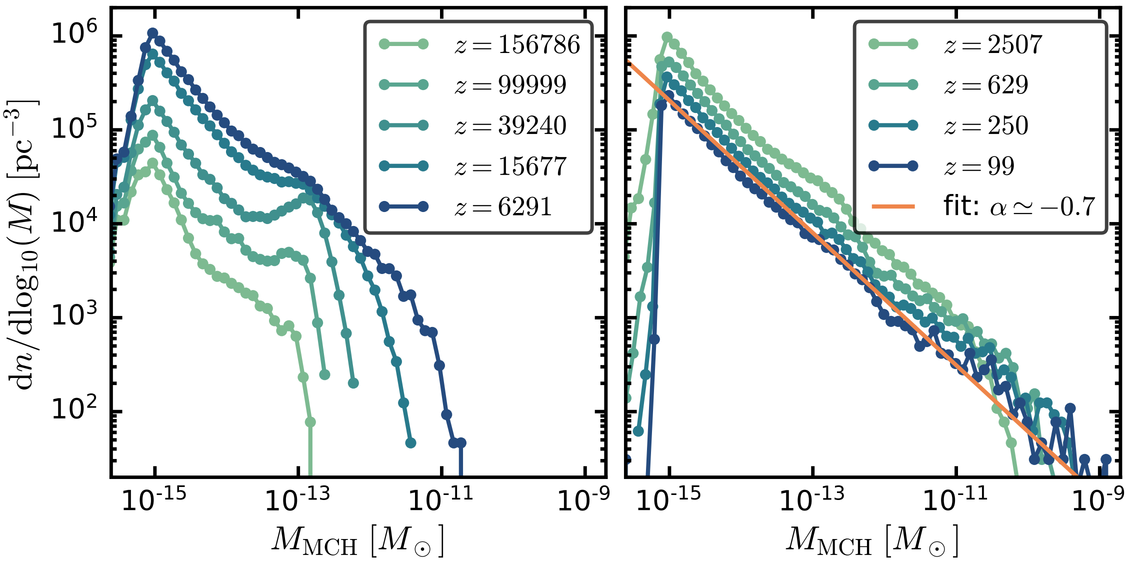

Figure 4.6 | Evolution of the MC-HMF separated into times before (left panel) and after matter-radiation equality (right panel). The slope of the MC-HMF at the final redshift $z = 99$ can be described by $\mathrm{d}n/\mathrm{d}\log_{10}(M) \sim M^\alpha$ with $\alpha \simeq -0.7$. Figure adapted from Ref. [39].

the peak at M_{mc} can be ascribed to the collapse of the largest nonlinear fluctuations. In fact, the mass peak can be directly related to the first peak occurring at $k \sim \pi/L_{\mathrm{osc}}$ in the initial dimensionless power spectrum. As discussed in Section 4.2, the density field at $k \lesssim \pi/L_{\mathrm{osc}}$, which corresponds to length scales larger than $L_{\mathrm{osc}}/2$, originates from misalignment axions. Since the mass contained within a patch of size L_{osc} is $M_{\mathrm{osc}} \sim 2 \times 10^{-12}\, M_\odot$ [205], the associated mass scale of $L_{\mathrm{osc}}/2$ is $M \sim 2.5 \times 10^{-13}\, M_\odot$ which is in agreement with the developed peak in the MC-HMF at $M_{\mathrm{mc}} \sim 2 \times 10^{-13}\, M_\odot$. Thus, this mass peak can be interpreted to result from “canonical” miniclusters that have formed from large-scale density fluctuations produced by misalignment axions. Correspondingly, the abundance of lower-mass miniclusters is the result of the collapse of small-scale axion density perturbations arising from the decay of topological defects and axitons.

The overall amplitude of the MC-HMF rises until matter-radiation equality, flattening out the peak at M_{mc} while extending towards higher masses. By the time of matter-radiation equality, the MC-HMF has developed into a power-law $\mathrm{d}n/\mathrm{d}\log_{10}(M) \sim M^\alpha$ with a slope of $\alpha \simeq -0.7$ and an exponential cut-off at $\sim 10^{-11} M_\odot$. This mass scale agrees with the mass of the largest canonical miniclusters which typically had an initial overdensity of order $O(1)$ [205]. During the evolution after matter-radiation equality (see right panel of Fig. 4.6) the high-mass cut-off continues to grow while the overall amplitude of the MC-HMF decreases. Fitting the MC-HMF to a power-law times a high-mass cut-off at redshift $z = 99$ still prefers the same overall slope $\alpha \simeq -0.7$. Using the semianalytic

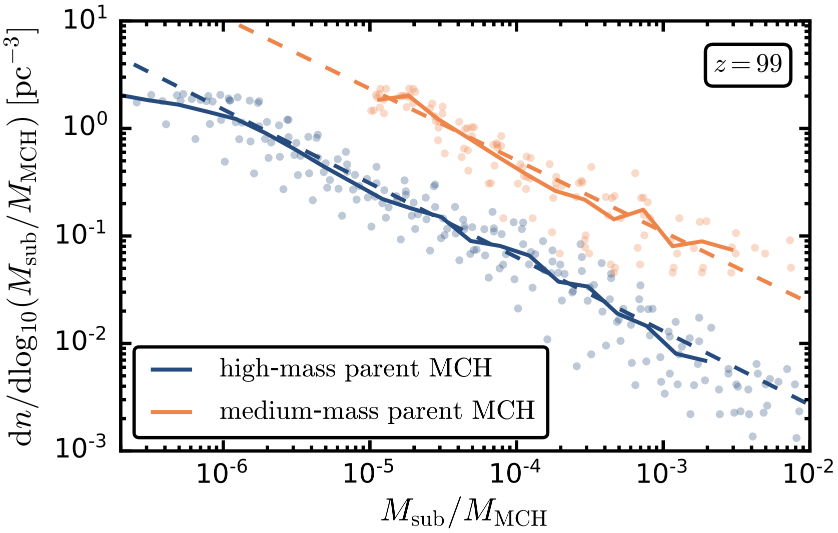

Figure 4.7 | Sub-MC-HMF of ten high-mass (blue data points) and medium-mass (orange data points) MCHs, normalised to the virial mass of the parent MCH at redshift $z = 99$. The solid line represents the average of the combined data for the high-mass and low-mass MCHs, respectively. The dashed lines are power-law fits to the data, both consistent with a slope parameter of $\alpha \simeq -0.7$. Figure adapted from Ref. [39].

Press-Schechter formalism and assuming a Gaussian distribution of density fluctuations, it was found that the MC-HMF then scales as $\mathrm{d}n/\mathrm{dlog}\, M \sim M^{-1/2}$ [361, 362]. Since the initial axion density field at $z = 10^6$ is approximately Gaussian on large scales, one might therefore expect that the MC-HMF behaves as a power-law with slope $\alpha = -0.5$ at high MCH masses. However, there exist only ~ 30 MCHs with $M_\mathrm{MCH} > 10^{-10}\, M_\odot$ in the full simulation volume (cf. Fig. 4.4), so the statistics is not sufficient for a suitable quantification and verification of this prediction. Furthermore, perturbations of the length of the simulation box have become nonlinear at $z = 99$ (see Fig. 4.5) which requires a careful treatment of the MC-HMF at high masses. Only N-body simulations with larger box sizes will allow a detailed study of the MC-HMF at the high-mass end.

In order to characterise the distribution of sub-MCs within the MCHs, we selected samples of different MCH masses separated according to Table 4.1. The substructure of ten high-mass and ten medium-mass MCHs[51] is compared in Fig. 4.7. For this, we identified all sub-MCs within the virial radius of each MCH and normalised the sub-MC masses to the virial mass of the corresponding parent MCH. Additionally, the resulting distribution was normalised to the size of the simulation box to obtain the number density per logarithmic mass interval which is the sub-MC-HMF. It is illustrated for each of the selected MCHs by the data points in Fig. 4.7 where the solid lines represent the average

---

[51] The small-mass sample from Table 4.1 was not included in this analysis because of the lack of a sufficient amount of sub-MCs contained in the small-mass MCHs.

Table 4.1 | Selected mass samples of axion MCHs, their respective concentration parameter c_{NFW} from an NFW fit and its sensitivity to the radial fit range (details in Section 4.3.3).

	M_{MCH} $[M_{\odot}]$	r_{vir} [AU]	c_{NFW}	sensitivity
high-mass	$[2.6 - 30.0] \times 10^{-10}$	$40.8 - 92.0$	160	3%
medium-mass	$[3.4 - 4.6] \times 10^{-11}$	$20.7 - 22.8$	400	6%
low-mass	$\sim 8 \times 10^{-12}$	~ 12.7	450	11%

sub-MC-HMF of the combined data. The slopes of the averaged sub-MC-HMFs are similar to that of the MC-HMF, $\alpha \simeq -0.7$, for both subsets. The independence of the slopes from the parent MCH mass agrees with previous results of subhalo mass functions in CDM simulations [271, 364].

4.3.3 Density Profiles of Minicluster Halos

We study the radial density profiles $\rho(r)$ of MCHs separated into the three mass samples from Table 4.1 at redshift $z = 99$ in Fig. 4.8. Since nonphysical effects arise on length scales of the numerical softening length $\varepsilon_{\mathrm{soft}}$, the density profiles on the left-hand side of Fig. 4.8 were truncated at a radial distance of $4\varepsilon_{\mathrm{soft}}$. This choice is in agreement with the resolution studies from Refs. [365, 366]. The upper right panel of Fig. 4.8 confirms for an exemplary MCH of each mass sample that the density profiles develop an unphysical core on scales smaller than $4\varepsilon_{\mathrm{soft}}$. The radial range $r < 4\varepsilon_{\mathrm{soft}}$ thus needs to be excluded, for example, in NFW fits (cf. Eq. (2.131)) and in the computation of the concentration parameter c_{NFW} of the MCHs.

The stacked radial density profiles of 20 MCHs in each sample are plotted in the upper left panel of Fig. 4.8 together with their best-fit NFW parameterisation. For comparison, we also show the best-fit power-law profile for the high-mass MCHs. As seen in the lower left panel of Fig. 4.8, high-mass MCHs are in good agreement with NFW profiles across the entire radial range, and the scale radius represented by the vertical line is well resolved. The best-fit power-law profile of the high-mass MCHs is given by $\rho \sim r^{-2.52}$ and exhibits larger deviations than the corresponding NFW fit. The medium-mass and low-mass MCHs, however, are slightly underdense at large radii $r \sim r_{\mathrm{vir}}/2$ compared to their NFW fits, and their scale radii are only close to or even below the spatial resolution limit. Note that the agreement with the NFW density profile is only valid on length scales larger than $4\varepsilon_{\mathrm{soft}}$ as shown on the right-hand side of Fig. 4.8. The deviations of the outer density profiles from the NFW fits, clearly visible in the lower panels of Fig. 4.8, might be explained by an increased accretion of mass onto the MCHs which is discussed in the context of standard CDM halos in Ref. [367]. Since MCHs with mass $M_{\mathrm{MCH}} \lesssim 10^{-11}\,M_{\odot}$

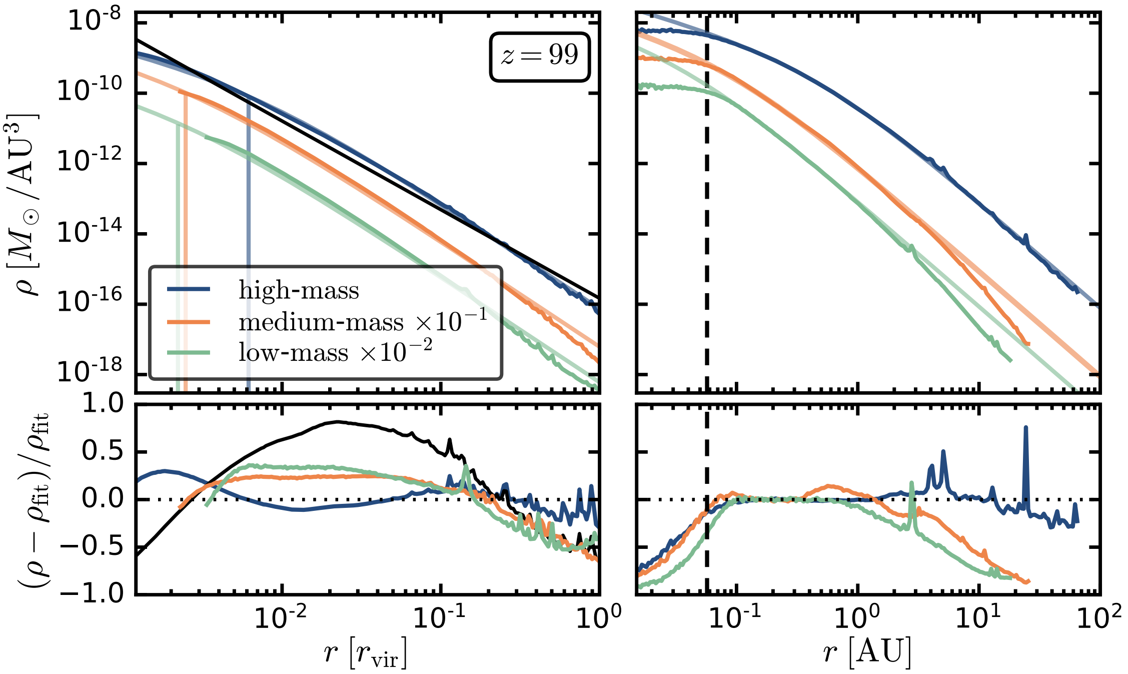

Figure 4.8 | Radial density profiles of high-, medium- and low-mass axion MCHs at redshift $z = 99$. Left: averaged density profiles of 20 MCHs in each mass sample (dark solid lines) truncated at a radial distance of $4\varepsilon_\mathrm{soft}$ together with NFW fits (light solid lines) where vertical lines mark the corresponding scale radii r_s (upper panel). The density profiles of the medium- and the low-mass MCHs are rescaled for illustration purposes. The black line shows the best-fit power-law $\rho \sim r^{-2.52}$ of the averaged density profile of the high-mass MCHs. Deviations from the NFW fits and the power-law fit are shown in the lower panel. Right: exemplary density profile of one MCH from each mass sample in physical units (dark solid lines) ranging from $\varepsilon_\mathrm{soft}$ to the corresponding virial radius together with their NFW fits (light solid lines). The black dashed line marks $4\varepsilon_\mathrm{soft}$. Deviations from the NFW fits are shown in the lower panel. The left-hand side of this figure is adapted from Ref. [39].

form from an initially nonlinear overdensity while larger MCHs originate from linear density seeds and a merger history, one can conjecture that the mass accretion is more pronounced for the lower-mass MCHs. This would provide an explanation for their underdense profiles at large radii.

The NFW fits allowed us to compute the concentration parameter $c_\mathrm{NFW} = r_\mathrm{vir}/r_s$ of the MCHs, which is of the order of several 10^2 (see Table 4.1) and increases for decreasing MCH masses, in agreement with CDM N-body simulations [278]. In order to examine the stability of the fits, their radial fit range was reduced by 5%, which varies the concentration parameter of the high-mass and medium-mass samples by a few per cent. The increased sensitivity for the low-mass sample is related to the fact that its scale radius it not resolved. This suggests that the density profile of the lower-mass MCHs is actually described by a single power-law instead of an NFW profile. The density profiles of MCHs with masses

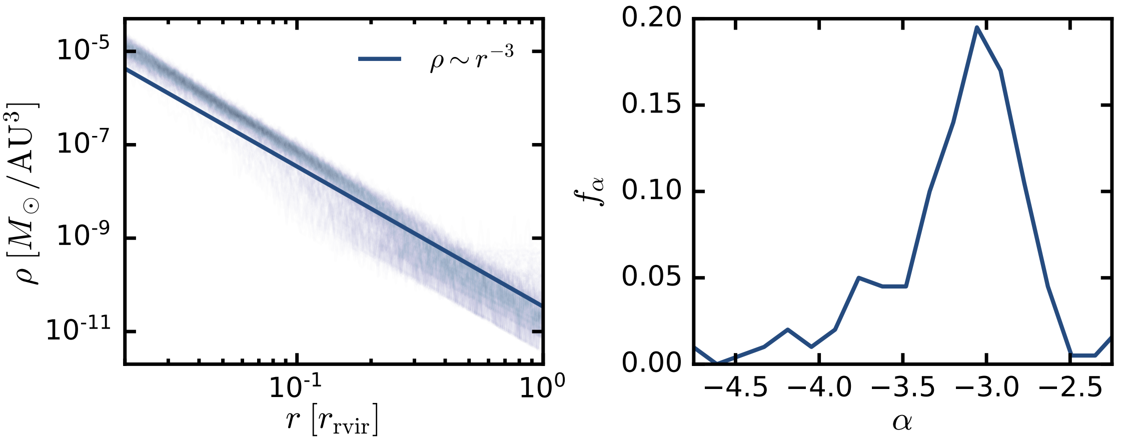

Figure 4.9 | Radial density profiles of all MCHs with masses between $10^{-12}\,M_\odot$ and $10^{-13}\,M_\odot$ at redshift $z = 99$ (left) and the normalised distribution of their slope parameters α obtained from the power-law fit $\rho \sim r^\alpha$ (right). Note that the dark line in the left panel is not a fit for the presented data but is used to guide the eye.

ranging from $10^{-12}\,M_\odot$ to $10^{-13}\,M_\odot$, which make up 9% of the total number of MCHs above the low-mass resolution cut-off, are presented in the left panel of Fig. 4.9. At first view, a large number of MCHs seems to be in agreement with a power-law of $\rho \sim r^{-3}$ although some MCHs even favour a steeper slope. This is confirmed in the right panel of Fig. 4.9 where the normalised distribution of the slope parameter α obtained from a power-law fit $\rho \sim r^\alpha$ to each MCH is shown. Evidently, the distribution peaks for a slope parameter of $\alpha = -3$, with a tail to steeper slopes. Only a tiny fraction of the density profiles of the MCHs in this sample are described by a shallower profile with slope parameter $\alpha \gtrsim -2.5$. A verification of whether MCHs with a r^{-3} slope converge to an NFW profile and a study of possible differences between MCHs and miniclusters formed from mergers or direct collapse require additional simulations with higher spatial resolution.

Nevertheless, we can conclude that the density profiles at $z = 99$ do not match a $\rho \sim r^{-9/4}$ power-law predicted for matter accretion onto a spherically symmetric perturbation from a homogeneous background [275]. This has previously been used to describe the density profile of axion miniclusters [29, 362]. The $\rho \sim r^{-9/4}$ profile was also used as an approximation for so-called ultracompact minihalos that can form in a similar manner to PBHs when a strong density perturbation crosses the horizon [368]. Due to their possible early formation and their large overdensities, ultracompact minihalos are similar to axion miniclusters. High-resolution simulations of the formation of ultracompact minihalos have revealed that they produce NFW density profiles when there are initially only slight deviations from a spherical symmetric perturbation [369]. Our results for the axion MCH density profiles are thus consistent with Ref. [369].

4.3.4 Discussion

We studied the formation of axion miniclusters and their clustering into MCHs from post-inflationary PQ symmetry breaking initial conditions. Our results are based on the highest-resolution simulations performed to date, both for the initial conditions and their gravitational evolution. Although our simulations cannot account for miniclusters at very low masses of $10^{-15}\,M_\odot$ and are not able to properly resolve the inner structure of MCHs with masses below $10^{-11}\,M_\odot$, they allow us to draw the following important conclusions. The total number of miniclusters is dominated by the lowest masses while the fraction of axions bound in miniclusters is $f_b \sim 0.75$ at $z = 99$ and is dominated by the highest-mass MCHs. Furthermore, the MC-HMF is nearly scale-invariant with a slope of $\alpha \simeq -0.7$ and the mass distribution of substructures within MCHs follows a similar scaling. Finally, the density profiles of MCHs are NFW-like at $z = 99$ at least for sufficiently massive MCHs with concentration parameters of an order of several hundred. Lower-mass density profiles are consistent with the power-law profile $\rho \sim r^{-3}$, excluding the previously used $r^{-9/4}$ density profile for axion miniclusters.

Neglected Adiabatic Perturbations and Initial Particle Velocities

It is important to mention that adiabatic density fluctuations generated from inflation were neglected in our N-body simulations. To verify that this is a justified assumption one should compare them with the size of the axion isocurvature density perturbations that were used as initial conditions. This requires relating the inflationary matter power spectrum, which is produced on much larger scales, to the small length scales that our simulations are sensitive to. For wave numbers larger than the one entering the horizon at matter-radiation equality, $k \gg k_{\mathrm{eq}} = a_{\mathrm{eq}} H_{\mathrm{eq}}$, the transfer function in the adiabatic matter power spectrum (see Eq. (2.105)) is [370]

$$T(k,a) = \frac{12k_{\mathrm{eq}}^2}{k^2} \ln\left(\frac{k}{8k_{\mathrm{eq}}}\right) D(a)\,. \tag{4.13}$$

Here, $D(a)$ is the growth factor in a matter-dominated universe that is given by Eq. (4.12). For redshifts $z \ll z_{\mathrm{eq}}$, the linear inflationary power spectrum at scales $k \gg k_{\mathrm{eq}}$ is thus (cf. Eq. (2.105))

$$\Delta_m^2(k,a) = \frac{4}{25}\left[12\frac{a}{a_{\mathrm{eq}}} \ln\left(\frac{k}{8k_{\mathrm{eq}}}\right)\right]^2 \Delta_{\mathcal{R}}^2\,, \tag{4.14}$$

where $\Delta_{\mathcal{R}}^2$ is the dimensionless curvature power spectrum from Eq. (2.71). To compare the adiabatic with the isocurvature power spectrum, we evolve the initial power spectrum of our N-body simulation linearly with the growth factor in Eq. (4.12) to the final redshift

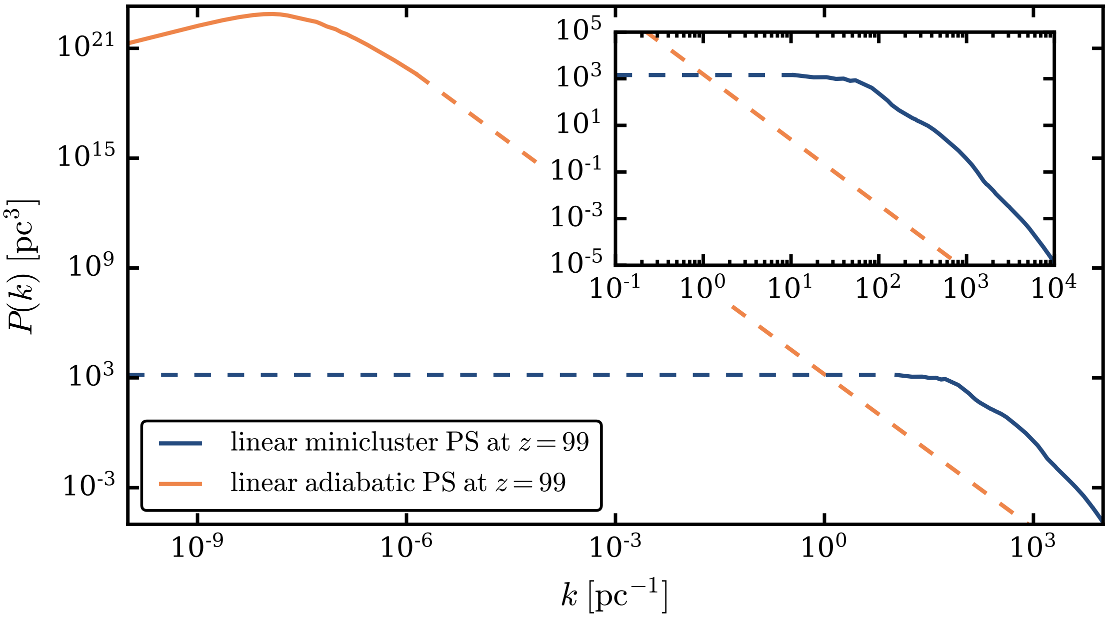

Figure 4.10 | Power spectra of isocurvature and adiabatic density fluctuations at redshift $z = 99$ in physical units. The adiabatic power spectrum was computed with Camb [231] and extrapolated to smaller scales (dashed orange line) while the isocurvature power spectrum corresponds to the initial conditions of our N-body simulations extrapolated to larger scales assuming a white-noise power spectrum (dashed blue line). An enlargement of the region where the two spectra become comparable to each other is shown in the inset.

$z = 99$. It can be easily extended to larger scales than covered by the simulation since it corresponds to a white-noise power spectrum on the largest resolved scales. Using the inflationary parameters given in Table 1.1 and a pivot scale of $k_p = 0.05\,\mathrm{Mpc}^{-1}$, we obtain that the two power spectra cross each other at $k_{\mathrm{cross}} \sim 1.2\,\mathrm{pc}^{-1}$. Since this is a factor of 6 smaller than the largest resolved wave number $k_L = 2\pi/L = 7.3\,\mathrm{pc}^{-1}$ in our simulation, the simulation box has to be a factor of 6 larger in order to start being sensitive to those scales. Hence, the adiabatic fluctuations can be safely neglected for the purpose of our N-body simulations. This is additionally illustrated in Fig. 4.10, where the adiabatic power spectrum from inflation at redshift $z = 99$ is extended to smaller scales and compared to the linearly evolved isocurvature power spectrum at the same redshift. Evidently, the isocurvature fluctuations clearly dominate over the adiabatic perturbations at our scales of interest.

Another detail that should be kept in mind is that the initial particle velocities were set to zero in the N-body simulation. In principle, axions obtain a velocity from the nonlinear evolution of the axion field at early times $z > 10^{12}$. Due to the expansion of space and the increasing axion mass during free-streaming, the axion density becomes frozen on all scales of interest at redshift $z = 10^6$ [39]. Since gravity is not considered in the generation of the initial conditions for the N-body simulations, one can argue one misses the contribution from the gravitational acceleration in the evolution from $z \sim 10^{12}$ to $z = 10^6$. It is assumed that once gravity is turned on at the beginning of the N-body simulations the particles obtain the correct velocity after a couple of e-folds [39]. Nevertheless, this approximation might lead to a delayed formation of small-scale structures at the low-mass end of the MC-HMF and one should treat the lowest-mass miniclusters carefully.

Prospective Simulations

The N-body simulation results presented above bring up questions that can only be answered by a more in-depth analysis complemented by follow-up simulations. For example, increased statistics are needed to sample the MC-HMF at the high-mass end in order to determine the slope parameter of the MC-HMF at those scales. Then, one could verify whether $\mathrm{d}n/\mathrm{d}\log M \sim M^{-1/2}$ is indeed the correct behaviour of the MC-HMF at high masses, as expected from Press-Schechter theory [361, 362]. A larger number of high-mass MCHs can be theoretically obtained when stacking the MC-HMF from multiple runs with slightly different initial conditions. From a computational point of view, this can be easily achieved in an efficient manner by reducing the number of N-body particles and making use of already existing simulation routines. However, one might run into the problem of the arising nonlinearities at $z = 99$ (see Fig. 4.5) which would manifest themselves at the high-mass end of the MC-HMF. To be insensitive to such numerical artefacts it is actually safer to run simulations with a larger box size as the simulation can then be evolved to later times.

Unfortunately, simulating larger boxes than $24L_{\mathrm{osc}}$ with the same code that originally produced the initial conditions for the N-body simulations does not seem to be possible at the moment.[52] This might be alleviated with the help of AMR though, as discussed in Section 4.2. Additional simulations with smaller box sizes and an increased number of particles to reach higher spatial resolution might be helpful for studies of the radial density profiles of MCHs with masses below $10^{-11}\,M_{\odot}$. Although the simulations could not be evolved until $z = 99$, they might resolve whether the MCHs with a slope of $\rho \sim r^{-3}$ in Fig. 4.9 are actually described by an NFW profile. Also, they can be used to identify differences in the morphology of the canonical miniclusters and MCHs and could verify the conjecture that the density profiles of MCHs converge towards an NFW profile for decreasing redshift. Such a resolution study also warrants a careful treatment of initial particle velocities since setting them to zero might affect the lower-mass miniclusters.

---

[52] Javier Redondo, private communication.

Therefore, the impact of including nonzero initial velocities on the morphology and the mass distribution of miniclusters should be a necessary ingredient of future examinations.

Another interesting avenue for future research is to focus on the white-noise part of the isocurvature power spectrum and to run simulations with an overall power spectrum that includes the adiabatic density fluctuations (cf. Fig. 4.10). This basically corresponds to generating a Gaussian density field as the initial condition for the axion density perturbations. A similar study was presented in Ref. [371] but they did not take the adiabatic power spectrum into account. In fact, their chosen comoving box side length of $L = 72\,\mathrm{pc}$ implies that the adiabatic power spectrum would actually dominate over the only considered isocurvature perturbations for the majority of their resolved k. This might affect their obtained MC-HMF, which agrees with our MC-HMF at late times indicating that the high-mass MCHs then drive the evolution, considerably. The miniclusters formed from isocurvature fluctuations at early times are small-scale objects and one assumes that they will end up as the substructures of galactic halos. They are composed of axion dark matter and originate from the adiabatic large-scale density fluctuations. This logic provides motivation to treat the two types of initial conditions independently from each other but considering both of them at relevant scales might gain some new insights.

This treatment could turn out to be irrelevant since very high-mass MCHs forming at late times are distinctly less dense than miniclusters produced at early times. Thus, they will be more vulnerable to being disrupted by tidal encounters with stars or other miniclusters in a galaxy [350, 351]. This also means that our result of 75% of all axions being bound in MCHs at $z = 99$ is not a robust prediction for the bound fraction of axion dark matter at the present time as a substantial amount could be ejected by the tidal disruption of axion miniclusters. This is highly relevant both for direct and indirect axion detection experiments (see Section 4.4). Sophisticated models for the distribution of axion dark matter in our Milky Way at the present time do not yet exist. Hopefully, our simulation results can be used as a starting point for model building as the overall problem is probably intractable with full simulations.

Axion Stars

Finally, we consider the predicted population of axion stars in the context of MCHs. Recent studies have shown that the formation of axion stars in the cores of axion MCHs is a firm prediction [42, 307]. Following the core-halo mass relation $M_* \sim M_{\mathrm{MCH}}^{1/3}$ (see Eq. (3.35)) between the mass M_* of the axion star and the host MCH found in simulations [42, 308, 309], we can expect axion stars with masses ranging from $10^{-17} - 10^{-15}\, M_\odot$ for the mass range of our MC-HMF. Although the expected masses of the axion stars and the smallest identified MCHs overlap, we note that our N-body simulations are by construction not capable of resolving them. Also, the value of the de Broglie wavelength λ_{dB} that determines the scale of the axion star radius does not exceed the numerical softening length across the entire mass range of the MCHs. Thus, our N-body simulations do not miss these small-scale effects accidentally.

4.4 Observational Signatures From Miniclusters

For axion detection experiments it is essential to know the distribution of axion miniclusters, their structure and the fraction of axions bound in them at the present time. Focusing on the formation of large-scale MCHs by starting from a Gaussian axion density field and neglecting the contribution from adiabatic density fluctuations, N-body simulations were recently performed until a redshift of $z = 19$ [371]. The resulting MC-HMF was extrapolated with a Press-Schechter method to $z = 0$. This can be regarded only as a rough approximation since no predictions about the substructure of the large-scale MCHs are made. More importantly, tidal interactions with stars that can lead to the complete destruction of an MCH were not taken into account at all.

While axion miniclusters can be disrupted by encounters with other miniclusters, the dominating contribution comes from interactions with stars in the late-time Universe. Based on studies of tidal interactions between small dark matter halos and stars [372, 373], an expression for the destruction probability of axion miniclusters inside a galactic halo was computed analytically [350, 351, 374]. In terms of the initial minicluster seed overdensity Φ_a, the destruction probability can be approximated as $P_d \simeq 10^{-2}\Phi_a^{-3/2}(1+\Phi_a)^{-1/2}$ [350, 351]. This suggests that roughly one per cent of the miniclusters with $\Phi_a \sim 1$ and approximately one third of $\Phi_a \sim 0.1$ miniclusters are destroyed. This matches the physical intuition that compact miniclusters are less likely to be disrupted. Hence, one can expect that a majority of the early collapsed miniclusters still exist as substructures at the present day.

Simulations of the stellar disruption of axion miniclusters in the Milky Way at the position of the Solar System revealed that the survival probability of MCHs with an NFW density profile is less than 50%, while 99% of the miniclusters with a power-law density profile survive. This emphasises the need for additional N-body simulations to precisely determine the structure of the so far not sufficiently resolved lower-mass MCHs. Note that the tidal destruction of a minicluster does not have to occur at once. Indirect encounters can lead to a gradual mass loss of the outer parts of an MCH whereas its inner part is not affected by tidal forces [372]. Several of these tidal stripping events results in a decreasing MCH mass and radius but the internal density profile, i.e. the core of the MCH, remains unaffected [351].

Axion Direct Detection and Gravitational Lensing

As a consequence of the destruction process, tidal streams with a lower density than their progenitors are produced which has significant implications for axion direct detection experiments. So-called haloscopes such as ADMX [375] and ORGAN [376] consist of a cavity surrounded by a strong magnetic field by which axions are converted into photons leading to a detectable signal [184]. As the strength of the signal depends on the local energy density of axions, the passage of a minicluster through the Earth will amplify the power of the signal enormously. However, this is expected to be a rare event occurring only once every 10^5 years [29, 350]. Nevertheless, the probability of detecting axions is drastically increased by the existence of tidal streams of axions since they fill a larger volume than a bound minicluster. It was estimated that crossing events with axion streams take place roughly every 20 years which increases the expected signal in a haloscope experiment by a factor of 10 [350]. For this reason, the estimates of the destruction probability of axion miniclusters and the distribution of tidal streams should be further improved, which can potentially be achieved by means of numerical simulations.

Furthermore, axion miniclusters could be detected by femto- and picolensing of gamma-ray bursts [30, 377] as well as by microlensing [362] events. The general idea of gravitational lensing is that the path of light of a distant light source is bent by the gravitational field of an object between the light source and the observer. This leads to multiple images of the source seen by the observer. It has been noted that femto- and picolensing of gamma-ray bursts with an axion minicluster serving as the lens is challenging as only a small fraction of gamma-ray bursts turned out to be suitable [377]. If separate images cannot be resolved, one speaks of microlensing. The light of the observed source is magnified when a minicluster, or any other compact object, passes close to its line of sight [362]. Using a modification of the peak-patch method presented in Section 2.4.4 together with the results from the N-body simulations in Section 4.3, merger trees were constructed to determine the collapse redshift of axion MCHs [240]. In the next step, a concentration-mass relation of the MCHs was obtained and extrapolated to the present time, under the assumption that the density profile of the MCHs is given by an NFW profile. Predicting concentrations of $\sim 10^4$ at $z = 0$, the MCHs are to diffuse to create a microlensing signal [240]. However, larger concentrations are expected in miniclusters that collapsed very early which are likely to end up as substructures in larger MCHs. The peak-patch method was additionally used to identify large overdense regions in the initial density field [241, 242]. The subsequent gravitational collapse of these regions was tracked with the N-body simulations from Section 4.3 to study their properties and their ability for microlensing.

As expected, miniclusters with a larger mass are more likely to survive disruption events. A correlation between the overdensity at the time of collapse and the survival rate was only observed for minicluster masses $\gtrsim 3 \times 10^{-13}\, M_\odot$ [241, 242]. This raises the question of the significance of Φ_a and whether it is a relevant quantity for predicting the properties of axion miniclusters. Consistent with the discussion of the density profiles in Section 4.3.3, the considered minicluster density profiles in Ref. [241, 242] are close to an NFW profile if the scale radius can be resolved. If this is not the case, they are described by the single power-law profile $\rho \sim r^{-2.9}$. The core-halo mass relation can be used to determine the mass and size of an axion star in the centre of an axion minicluster, which works as a cut-off for microlensing. Assuming the existence of an axion star in the centre of the miniclusters and extrapolating their overall density profiles to the present time it was found that neither miniclusters with an NFW profile nor a power-law profile with a slope of $\alpha = -2.9$ are able to produce a microlensing signal. However, this can be achieved if axions with a mass of $m_a \gtrsim 10^{-4}$ eV are considered [241, 242].

Additionally, another lensing diagnostic has been proposed based on the strong magnification of caustic transiting stars via a galaxy cluster lens. The existence of dark matter substructures imprints themselves as observable irregularities in the microlensing light curves. It was shown that this should be also perceivable for axion miniclusters in the post-inflationary PQ breaking scenario [378].

Pulsar Timing Arrays and Neutron Stars

Other possibilities to detect axion miniclusters are through Pulsar Timing Arrays and the resonant conversion of axions into photons in astrophysical magnetic fields. Pulsars are rotating neutron stars with strong magnetic fields and can be recognised from Earth as periodic emitters of electromagnetic radiation. The observed pulsar frequency will be different when an axion minicluster, or in general a dark matter subhalo, comes close to Earth or the pulsar. It was shown in Ref. [379] that the Square Kilometer Array observatory [380] is presumably not sensitive to the frequency shifts induced by axion miniclusters but this might be achievable with future experiments [371, 379].

Besides, a collision of an axion minicluster with a neutron star can lead to the resonant conversion of axions into photons in the magnetic field of a neutron star [381–383]. Recently, it has been estimated that encounters of axion miniclusters with neutron stars in the Milky Way should occur quite frequently with $\mathcal{O}(1 - 100)$ events per day [383].

They are expected to last several days and up to a few months and might be observable with existing telescopes [383]. Since the amount of generated photons depends on the number density of axions, stronger signals are predicted for dense miniclusters. Accordingly, axion stars in their centre might produce even stronger radio bursts [358, 384]. Collisions of axion stars with neutron stars could also source other observables, for instance, gravitational waves, the emission of neutrinos and electromagnetic radiation in a broad frequency range [385, 386].

Chapter 5

Gravitational Collapse in the Post-Inflationary Universe

In simple inflationary scenarios, the period of accelerated expansion comes to an end when the scalar inflaton field starts to oscillate around the minimum of its potential.[53] Although the precise details of the epoch following slow-roll inflation are unknown, the energy density stored in the inflaton field must eventually be converted into Standard Model particles. As mentioned in Section 1.2.3, the energy scale at which this so-called reheating phase is completed is barely constrained leaving room for a plethora of exciting physical processes prior to thermalisation. This allows, for example, the fragmentation of the initially nearly homogeneous inflaton field in a number of different preheating scenarios where parametric resonance can lead to efficient particle production (see Section 1.2.3). Even if couplings to other fields can be neglected at higher energy scales and become relevant only at later times, the inflaton fluctuations can be resonantly amplified by the strong oscillations of the inflaton field at the beginning of reheating, provided that self-interactions are present. In this case, long-lived excitations such as oscillons form and may populate the early Universe in large numbers.

In this chapter, we consider a scenario without any resonance. Inflaton self-interactions are omitted and the dominating inflaton interactions are gravitational. Provided that the reheating temperature is sufficiently low, inflation is then followed by a long period of matter-dominated expansion where initially small inflaton perturbations grow gravitationally on subhorizon scales. This is very similar to the formation of structures in the late-time Universe. Since the inflaton is a real scalar field in single-field models of inflation, we can adopt the same computational methods from Section 3.1.2 to study its

---

[53] Depending on the shape of the inflaton potential, the oscillations are performed around a possibly local minimum.

nonlinear evolution and the gravitational collapse of inflaton fluctuations in the non-relativistic limit. Using an N-body solver, we performed the largest-ever simulation of the smallest fraction of the Universe to obtain the first quantitative predictions for the mass distribution and the structure of collapsed objects which we call inflaton halos. These simulations were complemented by solving the SP equations on length scales of inflaton halos in order to prove furthermore the existence of solitonic cores, denoted in this context as inflaton stars, in their centre. The formation of inflaton halos in the post-inflationary Universe can source gravitational waves which imprint themselves in an SGWB. Furthermore, it is possible that subhorizon-sized PBHs are produced.

The scenario of gravitationally growing inflaton density perturbations on subhorizon scales is described in Section 5.1, including the calculation of the power spectrum at scales of interest. The simulation setup and the drawback of N-body simulations in this context are discussed in Section 5.2, followed by the presentation of the simulation results in Section 5.3 and Section 5.4, respectively. Large parts of Sections 5.2 to 5.4 are directly taken from the original work published in Refs. [40, 41]. Finally, it is shown in Section 5.5 how the SGWB generated from the formation and subsequent evolution of inflaton halos can be computed.

5.1 Post-Inflationary Dynamics

As in Section 1.2.3, we consider single-field slow-roll inflation and work with the quadratic inflaton potential from Eq. (1.38). In fact, the potential must actually be shallower than quadratic at large field values $\varphi > M_{\rm Pl}$ to be consistent with observations [89]. However, after the end of inflation, the inflaton oscillates around the minimum of its potential which can be approximated by its leading-order quadratic term. Under the assumption that higher-order terms of the full potential do not support resonance, we can use the results from Section 1.2.3 for the evolution of the inflaton field and the expansion of the universe. The evolution equations for the inflaton field and the Hubble parameter are given in Eq. (1.39). Averaged over several oscillations, the inflaton field evolves as $\varphi \sim a^{-3/2}$, the scale factor grows as $a(t) \sim t^{2/3}$, the Hubble parameter decreases as $H \sim a^{-3/2}$ and the energy density decreases as $\rho_\varphi \sim a^{-3}$ during the matter-dominated post-inflationary universe. This epoch continues until the Hubble parameter becomes eventually comparable to the decay rate Γ of the inflaton. This occurs only after multiple e-folds provided its coupling to other fields is small. Using Eq. (1.55) to relate the inflaton decay rate to the reheating temperature and that the Hubble parameter evolves as $H \simeq H_{\rm end}(a/a_{\rm end})^{-3/2} = H_{\rm end}\exp(-3\mathcal{N}/2)$ where $\mathcal{N}$ now denotes the number of e-folds after the end of inflation, one can estimate the duration of the matter-dominated epoch as

$$\mathcal{N} \simeq \frac{2}{3}\ln\left(\frac{H_{\mathrm{end}}}{\Gamma}\right) \simeq \frac{2}{3}\ln\left(\frac{H_{\mathrm{end}}M_{\mathrm{Pl}}}{3T_{\mathrm{reh}}^2}\right) . \tag{5.1}$$

For an exemplary reheating temperature of $T_{\mathrm{reh}} \simeq 10^7$ GeV the matter-dominated epoch lasts for $\mathcal{N} \simeq 25.6$ e-folds.

5.1.1 Evolution of Perturbations after Inflation

We are now interested in the evolution of the inflaton perturbations $\delta\varphi$ for which the equation of motion is given by the Mukhanov-Sasaki Eq. (2.57). Inflaton perturbations can be conveniently treated in the spatially flat gauge (see Appendix A.3) where the Mukhanov variable (see Eq. (2.56)) reads $q = a\delta\varphi$ [212]. Then, we can write the Mukhanov-Sasaki Eq. (2.57) in terms of $\delta\varphi$ as

$$\delta\varphi'' + 2\mathcal{H}\delta\varphi' + \left(\frac{a''}{a} - \nabla^2 - \frac{\zeta''}{\zeta}\right)\delta\varphi = 0\,, \tag{5.2}$$

where ζ''/ζ is given by Eq. (2.58). Inserting the slow-roll parameters ε and η into Eq. (2.58) and using Eq. (1.39) we see that

$$\frac{\zeta''}{\zeta} = 2a^2H^2 - a^2\frac{\partial^2 V(\bar{\varphi})}{\partial\bar{\varphi}^2} - \frac{a^2}{M_{\mathrm{Pl}}^2}\left(\frac{1}{2}\dot{\bar{\varphi}}^2 + \frac{\dot{\bar{\varphi}}^2}{H^2M_{\mathrm{Pl}}^2}V(\bar{\varphi}) + 2\frac{\dot{\bar{\varphi}}}{H}\frac{\partial V(\bar{\varphi})}{\partial\bar{\varphi}}\right) . \tag{5.3}$$

Here, $V(\bar{\varphi})$ denotes the quadratic inflaton potential from Eq. (1.38) for the background field $\bar{\varphi}$. Since $a''/a = 2a^2H^2 - a^2\dot{\bar{\varphi}}^2/(2M_{\mathrm{Pl}}^2)$, the perturbation Eq. (5.2) expressed in terms of derivatives with respect to physical time becomes [36]

$$\delta\ddot{\varphi} + 3H\dot{\varphi} + \left(m^2 + \frac{m^2\bar{\varphi}^2}{2M_{\mathrm{Pl}}^4}\frac{\dot{\bar{\varphi}}^2}{H^2} + \frac{2m^2\bar{\varphi}}{M_{\mathrm{Pl}}^2}\frac{\dot{\bar{\varphi}}}{H} - \frac{\nabla^2}{a^2}\right)\delta\varphi = 0\,. \tag{5.4}$$

In general, one needs to solve this equation numerically in Fourier space as done in Ref. [36] to compute the evolution of the inflaton perturbations over a wide range of k. However, it is insightful to consider approximations of Eq. (5.4) to find analytic solutions. Starting with modes that left the horizon already during inflation, one can make use of the slow-roll approximations, $\varepsilon \ll 1$, $\eta \ll 1$ and the fact that the Hubble parameter H is constant to simplify Eq. (5.4). According to Eq. (1.29), this then implies that the $\dot{\bar{\varphi}}/H$ terms in Eq. (5.4) can be dropped. Moreover, using the potential slow-roll parameter η_V from Eq. (1.33) makes clear that the mass term in Eq. (5.4) can be omitted as well. Hence, in this case, the perturbation equation simplifies in Fourier space to

$$\delta\ddot{\varphi}_k + 3H\delta\dot{\varphi}_k + \frac{k^2}{a^2}\delta\varphi_k = 0\,, \tag{5.5}$$

which has the solution [52]

$$\delta\varphi_k = \frac{1}{a\sqrt{2k}}\left(1 + i\frac{aH}{k}\right)\exp\left(\frac{ik}{aH}\right) . \tag{5.6}$$

Note that this is a solution that is valid for modes leaving the horizon well before the end of slow-roll inflation, $t \ll H_{\rm end}^{-1}$. We are, on the contrary, interested in the behaviour of perturbations in the matter-dominated post-inflationary epoch at times $t \gg H_{\rm end}^{-1}$ where the slow-roll approximation is not valid. Note that the time derivative of the background field given by Eq. (1.46) is

$$\dot{\bar{\varphi}} = \frac{\sqrt{6}M_{\rm Pl}}{m}(\dot{H}\sin(mt) + Hm\cos(mt)) , \tag{5.7}$$

where the Hubble parameter and its time derivative scale as $H \sim a^{-3/2}$ and $\dot{H} \sim a^{-3}$, respectively. Expanding the two $\bar{\varphi}$ dependent terms in the bracket of Eq. (5.4) in powers of $a^{-3/2}$ reveals that the dominating contribution of order $a^{-3/2}$ is

$$2\frac{m^2}{M_{\rm Pl}^2}\bar{\varphi}\frac{\dot{\bar{\varphi}}}{H} = 6Hm\sin(2mt) + \mathcal{O}(a^{-3}) , \tag{5.8}$$

whereas the other term decays as $\mathcal{O}(a^{-3})$ and can be neglected. Thus, the equation of motion in Fourier space takes the form [36]

$$\delta\ddot{\varphi}_k + 3H\delta\dot{\varphi}_k + \left(\frac{k^2}{a^2} + m^2 + 6Hm\sin(2mt)\right)\delta\varphi_k = 0 . \tag{5.9}$$

It was shown in Ref. [35] by writing Eq. (5.9) as a Mathieu equation (cf. Eq. (1.60)) that the last term in the brackets leads to a parametric amplification of $\delta\varphi_k$ within the resonance band $0 < k/a < (3Hm)^{1/2}$. This should not be confused with the parametric resonance from preheating which leads to an exponential growth of quantum fluctuations. In this case, the resonance results in a rather mild amplification of $\delta\varphi_k$ and is such that the comoving curvature perturbation $\mathcal{R}_k = H\delta\varphi_k/\dot{\bar{\varphi}}$ in the spatially flat gauge approaches a constant for all modes k within the identified resonance band. This is independent of whether they are inside or outside the horizon [36]. This means that both the background field $\bar{\varphi}$ and the perturbations $\delta\varphi$ evolve like in a matter-dominated universe in which $\mathcal{R}$ is constant on sub- and superhorizon scales (cf. Section 2.3.2). Note that an approximate solution of Eq. (5.9) directly shows that $\mathcal{R}$ approaches a constant at late times without the need of resolving this resonance [36].

5.1.2 Power Spectrum of Inflaton Perturbations

Based on the evolution Eqs. (5.5) and (5.9) it is possible to compute the power spectrum of the inflaton fluctuations in the limit of super- and subhorizon scales. We will see that the final result is independent of time, and therefore can be used to obtain the power spectrum at the end of inflation. For perturbations that leave the horizon during slow-roll inflation, the solution to Eq. (5.5) is given by Eq. (5.6) and therefore

$$|\delta\varphi_k|^2 = \frac{1}{2ka^2}\left(1+\frac{a^2H^2}{k^2}\right) = \frac{H^2}{2k^3}\left(1+\frac{k^2}{a^2H^2}\right) . \tag{5.10}$$

In the superhorizon limit, $k \ll aH$, this becomes $\delta\varphi_k \longrightarrow H/(2k^3)^{1/2}$ and the dimensionless curvature power spectrum at horizon crossing, $k = a_* H_*$, is

$$\Delta^2_{\mathcal{R}}(k) = \frac{k^3}{2\pi^2}|\mathcal{R}_k|^2 = \frac{H_*^2}{(2\pi)^2}\frac{H_*^2}{\dot{\bar\varphi}^2} , \tag{5.11}$$

where we used that $\mathcal{R}_k = H\delta\varphi_k/\dot{\bar\varphi}$ in the spatially flat gauge. Evidently, we recover the result from Eq. (2.68).

The calculation is much more involved for nonrelativistic modes ($k/a \ll m$) that never leave the horizon ($k \gg aH$). Deep in the matter-dominated epoch, the equation of motion for such density perturbations is described by Eq. (5.9) and one can find an approximate solution with the leading-order WKB ansatz [36]

$$\delta\varphi_k = \frac{1}{a^{3/2}\sqrt{2\omega(t)}}\exp\left(i\int \omega(t)\,\mathrm{d}t\right) , \quad \text{where} \quad \omega(t) = \left(\frac{k^2}{a^2}+m^2\right)^{1/2} . \tag{5.12}$$

Note that this approximation is only valid for modes $k/a \gg (3mH)^{1/2}$ and breaks down when parametric resonance sets in [35, 36]. Following Refs. [36, 387] and noting that $\omega = m$ in the nonrelativistic limit, $k/a \ll m$, a solution to Eq. (5.9) is of the form

$$\delta\varphi_k(t) = \frac{1}{a^{3/2}\sqrt{2m}}\left(A(t)e^{-imt} + B(t)e^{imt}\right) . \tag{5.13}$$

Both $A(t)$ and $B(t)$ are slowly varying functions, i.e. $\dot A/A \ll m$ and $\dot B/B \ll m$, and the time derivatives of $\delta\varphi_k(t)$ are

$$\sqrt{2m}a^{3/2}\delta\dot\varphi_k = \left(\dot A - \frac{3}{2}AH - imA\right)e^{-imt} + \left(\dot B - \frac{3}{2}BH + imB\right)e^{imt} , \tag{5.14}$$

and

$$\sqrt{2m}a^{3/2}\delta\ddot\varphi_k = \left(\ddot A - 3\dot A H - \frac{3}{2}A\dot H + \frac{9}{4}AH^2 - 2im\left(\dot A - \frac{3}{2}AH\right) - m^2A\right)e^{-imt} + \dots , \tag{5.15}$$

where the ellipse at the end of the second derivative corresponds to the Be^{imt} terms which are very similar and omitted for convenience. Expressing now the $\sin(2mt)$ term in

Eq. (5.9) as exponential functions, collecting all terms proportional to e^{-imt} and dropping all contributions that decay faster than a^{-2}, one obtains the coupled equation

$$\frac{k^2}{a^2}A + 3HmiB - 2im\dot{A} = 0\,. \tag{5.16}$$

Introducing the variable [387]

$$x = \frac{k^2}{Hma^2} = \frac{3k^2t}{2ma^2} \quad \text{with derivative} \quad \dot{x} = \frac{3k^2}{2ma^2}\left(1 - 2tH\right) = -\frac{k^2}{2ma^2}\,, \tag{5.17}$$

and performing a change of variables such that

$$\dot{A} = -\frac{k^2}{2ma^2}\frac{\mathrm{d}A}{\mathrm{d}x}\,, \tag{5.18}$$

one can write Eq. (5.16) as [387]

$$\frac{\mathrm{d}A}{\mathrm{d}x} + \frac{3B}{x} - iA = 0\,. \tag{5.19}$$

Similarly, one can collect the terms proportional to e^{imt} in Eq. (5.9) and one obtains

$$\frac{\mathrm{d}B}{\mathrm{d}x} + \frac{3A}{x} + iB = 0\,. \tag{5.20}$$

Thus, Eq. (5.9) has now turned in a coupled system of equations for A and B, which by replacing B and its derivative can be transformed into the second-order differential equation

$$x^2\frac{\mathrm{d}^2A}{\mathrm{d}x^2} + x\frac{\mathrm{d}A}{\mathrm{d}x} + (x^2 - ix - 9)A = 0\,. \tag{5.21}$$

The solution to this equation and the related expression for B are [387]

$$A = e^{ix}\left(1 + \frac{9i}{2} - \frac{9}{x^2} - \frac{15i}{2x^3}\right)\,, \quad \text{and} \quad B = e^{ix}\left(\frac{3i}{2x} - \frac{6}{x^2} - \frac{15i}{2x^3}\right)\,. \tag{5.22}$$

Since we are interested in the late-time behaviour of $\delta\varphi_k$, we consider $x \ll 1$ in which case the $-15i/(2x^3)$ term in A and B dominates. Hence, the inflaton perturbation approaches [36]

$$\delta\varphi_k \longrightarrow -\frac{1}{a^{3/2}\sqrt{2m}}\frac{15i}{2x^3}\left(e^{-imt} + e^{imt}\right) = -\frac{15i}{\sqrt{2m}}\frac{m^3H^3a^{9/2}}{k^6}\cos(mt) \tag{5.23}$$

in this limit. Using that $\dot{\bar{\varphi}} \longrightarrow \sqrt{6}M_{\mathrm{Pl}}H\cos(mt)$ at late times (see Eq. (5.7)), the comoving curvature perturbation becomes

$$\mathcal{R}_k = \frac{H}{\dot{\bar{\varphi}}}\delta\varphi_k = -\frac{15i}{\sqrt{12m}M_{\mathrm{Pl}}}\frac{m^3H^3a^{9/2}}{k^6}\,, \tag{5.24}$$

and therefore the curvature power spectrum on subhorizon scales is [36]

$$\Delta^2_{\mathcal{R}}(k) = \frac{k^3}{2\pi^2}|\mathcal{R}_k|^2 = \frac{75m^5}{8\pi^2}\frac{H^6}{M_{\mathrm{Pl}}^2}\frac{a^9}{k^9}\,. \tag{5.25}$$

Since H^6a^9 is constant during the post-inflationary epoch, it can be evaluated at any convenient time, particularly at the end of inflation. The subhorizon power spectrum of density perturbations (cf. Eq. (2.105))

$$\Delta^2_m(k) = \frac{4}{25}\left(\frac{k}{aH}\right)^4 \Delta^2_{\mathcal{R}}(k) \tag{5.26}$$

at the end of inflation thus scales as $\Delta^2_m \sim k^{-5}$.

5.2 Simulating the Early Matter-Dominated Epoch

The end of slow-roll inflation is defined by $\varepsilon(\varphi_{\mathrm{end}}) = 1$ which implies, for the quadratic inflaton potential from Eq. (1.38), that $\varphi_{\mathrm{end}} \approx \sqrt{2}M_{\mathrm{Pl}}$ and correspondingly $H_{\mathrm{end}} \sim m$ where m is the inflaton mass. Since the Hubble parameter decreases with $a^{-3/2}$ in the post-inflationary matter-dominated era, $H \ll m$ after only a few e-folds following the end of inflation. This provides motivation to consider the nonrelativistic limit of the Klein-Gordon Eq. (1.24) to study the evolution of the inflaton field under its own self-gravity without self-interactions or couplings to other fields. In addition, a large number density allows the inflaton field to be treated classically, complementing the situation that the SP Eqs. (3.10) and (3.11) are suited to evolve the inflaton field on subhorizon scales [37]. Adopting a pseudo-spectral method to solve the SP equations, numerical simulations of the matter-dominated epoch following inflation demonstrated the gravitational fragmentation of the inflaton field [37]. However, due to limitations in spatial resolution and the box size, the simulations could not be used to study the mass distribution of collapsed objects and to probe the formation of solitonic cores. Exploiting the analogy to cosmological structure formation with axion-like dark matter, the Press-Schechter formalism was adapted to estimate the mass distribution of gravitationally-bound inflaton halos and predicted typical masses of 10^{-3} kg [38]. Building on the work presented in Refs. [37, 38], we performed detailed N-body and SP simulations published in Ref. [40] and Ref. [41], respectively. The following two sections summarise the setup for our simulations and are taken to a high degree directly from Ref. [40].

5.2.1 Unit System and Initial Conditions

To facilitate comparison with Refs. [36, 38] the same assumptions about the model parameters are made. We chose an inflaton mass of $m = 6.35 \times 10^{-6}\, M_{\mathrm{Pl}}$ which assumes that a pivot scale of $k_p = 2 \times 10^{-3}\,\mathrm{Mpc}^{-1}$ crosses the horizon $\mathcal{N}_p = 60$ e-folds before the end of inflation. Note that a long matter-dominated epoch reduces the value of $\mathcal{N}_p$ (cf. Eq. (1.65)) and also m itself is weakly dependent on the energy scale when reheating is completed, so in principle $\mathcal{N}_p$ and m need to be solved self-consistently. The small corrections are neglected in the following as their numerical impact on our simulations from Sections 5.3 and 5.4 is limited. Furthermore, we assume that inflaton ends when $\varphi \approx M_{\mathrm{Pl}}$ and correspondingly $H_{\mathrm{end}} \approx m/\sqrt{6}$.

As the physical size of the horizon at the end of inflation is $H_{\mathrm{end}}^{-1} \sim 10^{-29}$ m, we need to introduce an appropriate unit system for our simulations. We define the comoving length unit l_u of our simulations by the physical size of the horizon $\mathcal{N} = 20$ e-folds after the end of inflation, i.e. $l_u = e^{20} H_{\mathrm{end}}^{-1} = 1.51 \times 10^{-20}$ m. Choosing the mass unit as $m_u = 10^{-10}$ g and taking the gravitational constant in the new unit system as $G = 10^{-10}\, l_u^3/(m_u t_u^2)$, the corresponding time unit is

$$t_u = \left[\frac{10^{-10}}{6.67 \times 10^{-11}} \left(\frac{l_u}{\mathrm{m}} \right)^3 \frac{\mathrm{g}}{m_u} \right]^{1/2} \mathrm{s} = 7.23 \times 10^{-24}\,\mathrm{s}\,. \tag{5.27}$$

The Hubble parameter at the end of the simulation is $H_{20} = e^{-30} H_{\mathrm{end}} = 6.49\, t_u^{-1}$, where the subscript “20” refers to quantities evaluated $\mathcal{N} = 20$ e-folds after the end of inflation. Using that $\rho_{20} = 3H_{20}^2/(8\pi G)$, the energy density at this time in physical units is $\rho_{20} = 5.02 \times 10^{10}\, m_u/l_u^3$. Additionally, the matter energy density is fixed at $\Omega_m = 1$ throughout the simulations.

The power spectrum of density perturbations at the end of inflation was computed in Section 5.1.2 in the super- and subhorizon limits. To obtain the precise shape of the power spectrum on intermediate scales, one in principle needs to compute it numerically as done in Ref. [36]. However, the nonlinear evolution of the inflaton fluctuations is not sensitive to its precise form [37] and therefore it is sufficient to interpolate between the sub- and superhorizon limits of the initial power spectrum [38], as shown in the upper panel of Fig. 5.1. As discussed in Section 5.1.1, the inflaton perturbations grow linearly with the scale factor during the post-inflationary epoch. This allows us to evolve the interpolated power spectrum forward from the end of inflation with the growth factor $D(a) \sim a$. Nonlinearities are expected to emerge after ~ 17 e-folds of growth [38] and therefore we take the linearly extrapolated power spectrum at $\mathcal{N} = 14$ e-folds after the end of inflation as the initial condition for our subsequent simulations. They are evolved for six additional e-folds until $\mathcal{N} = 20$ which is why we normalise the final scale factor to unity such that the initial scale factor corresponds to $a_{\mathrm{init}} = a_{14}/a_{20} = e^{-6}$. The N-body simulations presented in Section 5.3 were evolved with Nyx [264] with box side lengths of $L = 50\, l_u$ and $L = 100\, l_u$, respectively. The code AxioNyx [43] with a box size of $L = 50\, l_u$

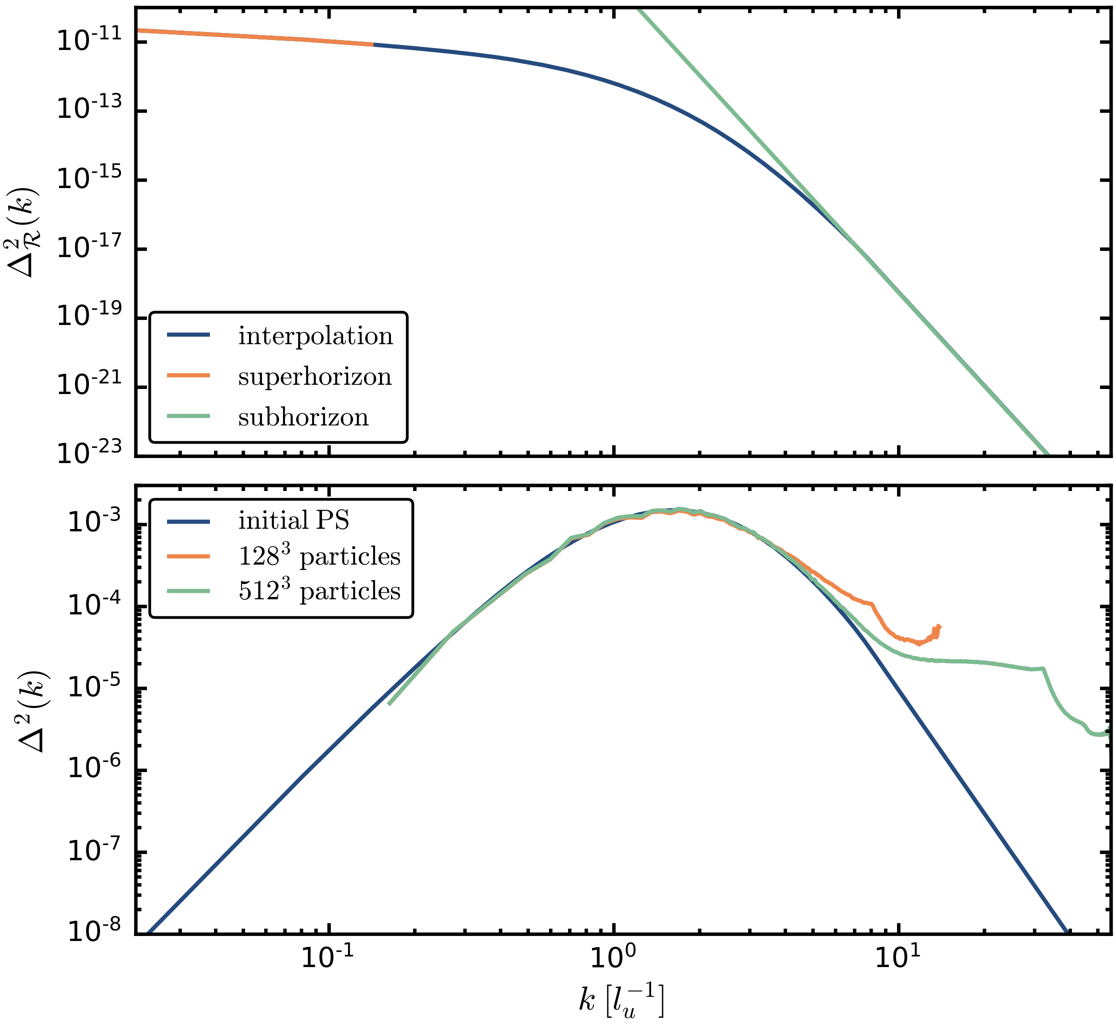

Figure 5.1 | Dimensionless curvature power spectrum at the end of inflation (upper panel) and dimensionless inflaton density power spectrum $\mathcal{N} = 14$ e-folds after the end of inflation (lower panel). The super- and subhorizon limits of the curvature power spectrum are given by Eq. (2.68) and Eq. (5.25), respectively. The interpolated dimensionless density power spectrum linearly evolved to $\mathcal{N} = 14$ e-folds after the end of inflation serves as the initial condition for the simulations. The computed power spectra from the initial density field for 128^3 and 512^3 particles are shown for comparison. The increasing deviations for large k from the input power spectrum arise due to discretisation effects (see text for details). The lower panel of the figure is adapted from Ref. [40].

was used for the SP simulations in Section 5.4. Initial particle positions and velocities are generated with Music [236] for the power spectrum shown in the lower panel of Fig. 5.1. As an input, Music requires a transfer function $T(k)$ which is related to the power spectrum $P(k)$ via

$$P(k) = \sigma_8 k^{n_s} T^2(k)\,, \tag{5.28}$$

where n_s is the spectral index (see Table 1.1) and σ_8 is the normalisation of the power spectrum. In the standard cosmology we have $\sigma_8 = 0.811$ [2, 236], however, since we use another power spectrum σ_8 has to be computed from

$$\sigma_8^2 = \frac{1}{2\pi^2} \int W(k)^2 k^2 P(k)\, \mathrm{d}k\,. \tag{5.29}$$

Here, $W(k)$ is the top-hat window function in Fourier space,

$$W(k) = \frac{3 j_1(kR_8)}{kR_8}\,, \tag{5.30}$$

where R_8 denotes a top-hat filter of radius $R_8 = 8\, l_u$ and j_1 is the first order spherical Bessel function

$$j_1(x) = \frac{\sin(x) - x\cos(x)}{x^2}\,. \tag{5.31}$$

Solving the integral in Eq. (5.29) and including the growth factor by adding a factor of $(a_{20}/a_{\mathrm{init}})^2 = (e^6)^2$ in the integral of Eq. (5.29) gives a normalisation of $\sigma_8 = 1.71$.

To verify the correct setup of the initial conditions we compare the power spectrum that was indirectly inserted in Music via the corresponding transfer function with the power spectrum calculated from the initial density field in Nyx. As can be seen in the lower panel of Fig. 5.1, the power spectra agree over a wide range of k but for large k there are deviations from the input power spectrum which are explained by two effects. The first is the sharp cut-off that arises at different k for different grid sizes. It is determined by the Nyquist frequency $k_{\mathrm{Ny}} = \pi N_{\mathrm{cell}}/L$, where N_{cell} denotes the grid size and $L = 50\, l_u$ is the size of the simulation box. For $N_{\mathrm{cell}} = 512$, $k_{\mathrm{Ny}} \simeq 32.2\, l_u^{-1}$ and for $N_{\mathrm{cell}} = 128$, $k_{\mathrm{Ny}} \simeq 8.05\, l_u^{-1}$. However, there is also an artefact arising from an interpolation used in Nyx to compute the particle mass density. This process requires roughly 3–4 cells and the deviations thus become apparent at $k \sim k_{\mathrm{Ny}}/3$. For a larger value of N_{cell} the deviation from the input power spectrum kicks in at larger k, as seen in Fig. 5.1.

5.2.2 N-body Simulations and Spurious Halos

In contrast to solving the full SP dynamics on all scales, we made use of the Schrödinger-Vlasov correspondence and have instead performed pure N-body in the first step (see Section 5.3). They are computationally less expensive and allow us to easily follow the evolution of the inflaton field deep into the nonlinear phase. This provides an accurate understanding of halo formation at the cost of neglecting small-scale wavelike dynamics, including solitonic cores in the centre of inflaton halos and granular density fluctuations at the de Broglie scale. In order to determine the mass distribution of inflaton halos in terms of their halo mass function (see Section 5.3.1), we adapt the Rockstar halo finder [272] to locate the inflaton halos in the simulation outputs. Their virial radii are calculated from

$$r_{\text{vir}} = v_{\text{max}} \left(\frac{4\pi}{3} G \rho_{\text{vir}} \right)^{-1/2} , \tag{5.32}$$

where $\rho_{\text{vir}} = \Delta_{\text{vir}} \bar{\rho}$ with mean density $\bar{\rho}$, $\Delta_{\text{vir}} = 18\pi^2$ for a matter-dominated background, and v_{max} is the halo's maximum circular velocity. The virial mass of the halos is then given by $M_{\text{vir}} = 4\pi/3 \Delta_{\text{vir}} \bar{\rho} r_{\text{vir}}^3$.

In addition to not being able to capture the detailed dynamics of wavelike matter, another downside is that N-body simulations generate so-called spurious halos [388–391] when the initial power spectrum has a well-resolved cut-off at small scales. These are found preferentially along filaments and can outnumber genuine physical halos below some mass scale. They are caused by artificial fragmentation of filaments and are common in WDM simulations [388–391] where the free-streaming of particles induces a cut-off in the matter power spectrum. The scale below which spurious halos dominate is [389]

$$M_{\text{lim}} = 10.1 \bar{\rho} \Delta x k_{\text{peak}}^{-2} , \tag{5.33}$$

where Δx is the effective spatial resolution of the simulation and k_{peak} is the wave number at which the dimensionless initial power spectrum has its maximum. These small-scale halos are resolution-dependent and are thus clearly unphysical [388], and must be filtered out of the halo catalogue. Algorithms that distinguish between artificial and genuine halos have been developed for WDM simulations.[54] We adopt a simplified but sufficient version for use here which works as follows.

To identify spurious halos and to remove them from the halo catalogue, we follow the procedure from Ref. [389]. In the first step, we trace all the particles that are in a parent halo at a certain $\mathcal{N}$ to their positions at the initial snapshot. This collection of particles is the so-called protohalo. As suggested in Refs. [272, 394, 395], the appropriate way of computing the ellipsis parameters of a (proto)halo is via the shape tensor S. Since all of the N-body particles in our simulation have the same mass, the shape tensor is

$$S_{ij} = \frac{1}{N} \sum_k x_{k,i} x_{k,j} , \tag{5.34}$$

where $x_{k,i}$ denotes the ith component of the position of the kth particle relative to the centre of mass of the protohalo. The sorted eigenvalues $(\lambda_a, \lambda_b, \lambda_c)$ of S are related to the ellipsis parameters $(c \leq b \leq a)$ of the protohalo as $\lambda_a = a^2/3$, $\lambda_b = b^2/3$ and $\lambda_c = c^2/3$,

---

[54] Instead of running a standard N-body simulation, it is also possible to trace dark matter sheets in phase space [392], significantly suppressing the formation of spurious halos [393].

and the sphericity of the protohalo is defined as $s = c/a = (\lambda_c/\lambda_a)^{1/2}$. Analysing the distribution of the sphericity s of all protohalos corresponding to the identified halos at a certain $\mathcal{N}$ allows a cut-off to be set below which protohalos are marked as spurious. The corresponding halos are then removed from the halo catalogue. This procedure removes most but not all of the artificial halos. In principle, one should also filter out halos that do not have a counterpart in simulations of the same initial conditions but with a different spatial resolution [389]. However, we only make the sphericity cut and additionally use the peak-patch code M3P (see Section 2.4.4) to cross-validate the N-body results as M3P results are unaffected by spurious low-mass halos.

5.3 Formation of Inflaton Halos

Adapting the cosmology code Nyx [264], we performed N-body simulations from $\mathcal{N} = 14$ to $\mathcal{N} = 20$ e-folds after the end of inflation to study the gravitational fragmentation of the inflaton field in the post-inflationary epoch. This allows us to obtain the inflaton halo mass function (IHMF) and to analyse the density distribution of the inflaton field as well as the density profiles of gravitationally-bound inflaton halos. Sufficient spatial resolution is required for accurate results while larger box sizes are needed to evolve the simulations to later times. Choosing a box size of $L = 50\, l_u$ with 512^3 particles we achieve a spatial resolution of $\Delta x = L/512 = 9.8 \times 10^{-2}\, l_u$. This choice ensures that the density profiles of the highest-mass halos can be well resolved. At the same time, it guarantees that the peak of the IHMF at $\mathcal{N} = 20$ is still resolved (see Fig. 5.4). We used this setup as our benchmark simulation. However, the largest scales of the $L = 50\, l_u$ simulation box start to become nonlinear around $\mathcal{N} \gtrsim 19$ (see Fig. 5.5). This is why an additional N-body simulation with a size of $L = 100\, l_u$ containing 512^3 particles has been performed. Suffering admittedly from a reduced spatial resolution, nonlinearities at scales of the size of the simulation box then appear at later times. This helps to compare the IHMF obtained from the peak-patch code M3P (see Section 2.4.4) with the N-body IHMF. Since inflaton halos are expected to form on comoving scales roughly equal to H_{end}^{-1}, the typical halo mass can be approximated by the mass contained within the horizon at the end of inflation,

$$M_{h,\mathrm{end}} = \frac{4\pi}{3}\bar{\rho}_{\mathrm{end}} H_{\mathrm{end}}^{-3} = \frac{4\pi M_{\mathrm{Pl}}^2}{H_{\mathrm{end}}} = 0.021\,\mathrm{kg}\,. \tag{5.35}$$

The evolution of the inflaton density field for the $L = 50\, l_u$ N-body simulation is shown in Fig. 5.2. The first gravitationally-collapsed objects already exist at $\mathcal{N} = 16.9$ which subsequently merge to form larger inflaton halos. At $\mathcal{N} = 20$ e-folds after the end of

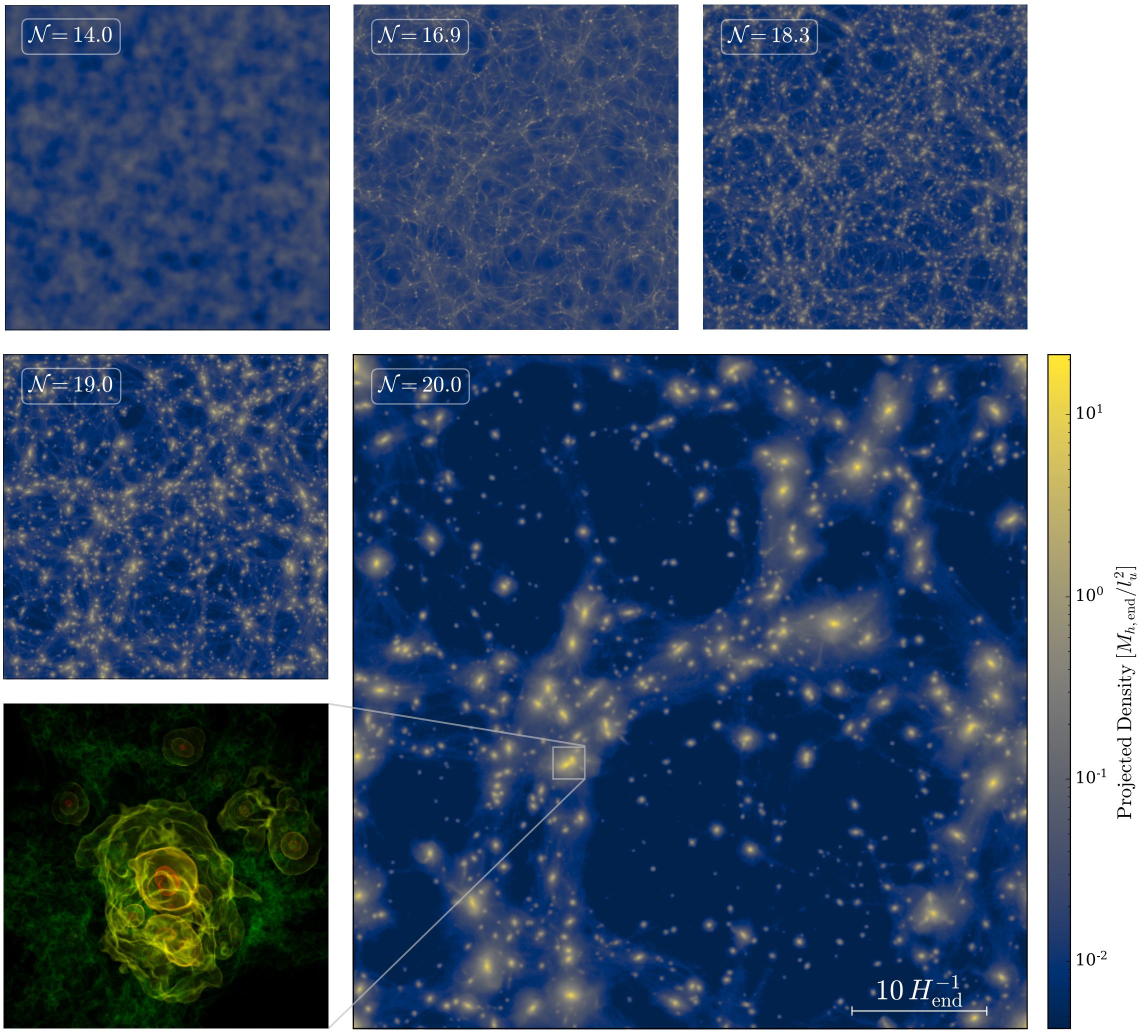

Figure 5.2 | Projected inflaton density of the full simulation box with a comoving size of $L = 50\,l_u$ from $\mathcal{N} = 14$ (upper left) to $\mathcal{N} = 20$ e-folds (lower right) after the end of inflation. Note that the colour bar only applies to the final snapshot. A volume rendering of the largest inflaton halo with virial mass of $1.2 \times 10^3\,M_{h,\rm end} \sim 20\,\rm kg$ is shown in the lower-left panel. Figure reproduced from Ref. [40].

inflation, 60% of the total mass is bound in inflaton halos with masses in the range $M_{\rm vir} \in [0.2,\,1.2 \times 10^3]\,M_{h,\rm end}$ and corresponding virial radii of $r_{\rm vir} \in [0.1,\,2.0]\,l_u$. A visualisation of the largest halo in the simulation volume with a virial mass of 20 kg can be also seen in Fig. 5.2.

5.3.1 Inflaton Halo Mass Function

As discussed in Section 5.2.2, N-body simulations produce spurious low-mass halos if the initial power spectrum has a well-resolved cut-off at small scales. This means that the N-body IHMF includes unphysical halos which need to be removed. According to Eq. (5.33) spurious halos dominate the IHMF below a mass scale of $M_{\mathrm{lim}} \sim 0.1\, M_{h,\mathrm{end}}$ for our spatial resolution of $\Delta x = 9.8 \times 10^{-2}\, l_u$ and for the scale $k_{\mathrm{peak}} = 1.7\, l_u^{-1}$ at which the dimensionless input power spectrum has its maximum (see Fig. 5.1). Following the procedure presented in Section 5.2.2, the constituent particles of every identified halo at a certain time are traced back to their initial positions in order to compute the sphericity of each protohalo. The resulting sphericity distribution of all protohalos corresponding to the identified halos at $\mathcal{N} = 20$ is shown in the left panel of Fig. 5.3 and reveals a strong increase in the number of protohalos with sphericity $s < 0.13$. Thus, we decided to set a cut-off at $s_{\mathrm{cut}} = 0.13$ below which protohalos are considered to be spurious. The corresponding halos are removed from the halo catalogue and the IHMF. Since this procedure does not remove all artificial halos, we additionally compare the N-body IHMFs with those computed using the M3P algorithm, and with Press-Schechter predictions of the IHMF. The latter adopts a sharp-k filter to account for the suppression in the initial power spectrum on small scales. The HMF in the Press-Schechter model given by Eq. (2.120) depends on the choice of the window function and the initial density power spectrum. Usually, the window function is taken to be a top-hat function with radius R_T in real space such that

$$W_T(kR_T) = \frac{3 j_1(kR_T)}{kR_T} \tag{5.36}$$

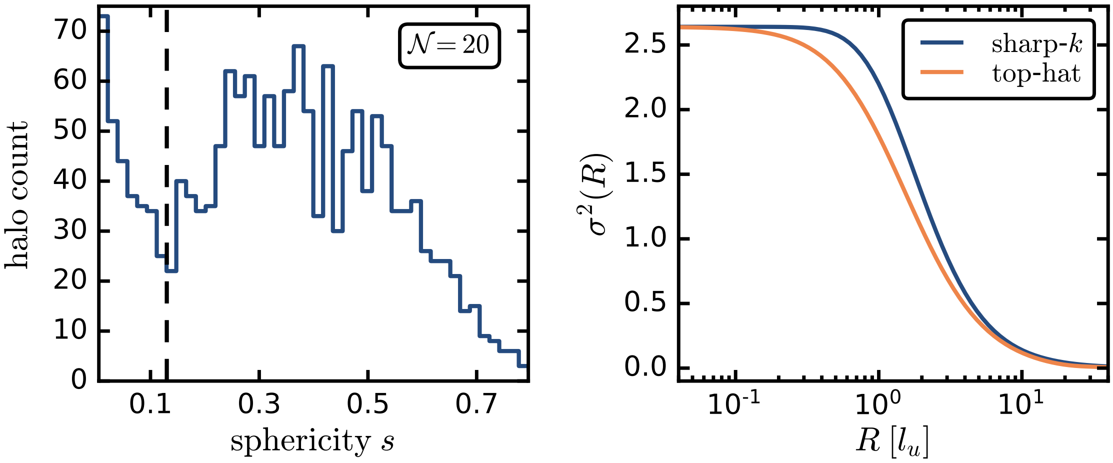

Figure 5.3 | Sphericity distribution of all inflaton protohalos in the simulation volume and variance of density perturbation for different window functions in the Press-Schechter formalism. Left: histogram of the sphericity of all protohalos that belong to the identified halos $\mathcal{N} = 20$ e-folds after the end of inflation. The dashed vertical black line marks the sphericity cut $s_{\mathrm{cut}} = 0.13$. Right: Variance of density perturbations $\sigma^2(R)$ (see Eq. (2.118)) using the sharp-k and the top-hat window function, respectively (see Eqs. (5.36) and (5.37)). Figure adapted from Ref. [40].

in Fourier space, where j_1 is the first order spherical Bessel function from Eq. (5.31). However, this approach is not able to match the HMF of simulations when the initial power spectrum has a resolved small-scale cut-off as is the case for WDM. It was shown in Refs. [390, 391] that using the sharp-k filter, which is defined as a top-hat window function with radius R in Fourier space as

$$W_k(kR) = \Theta(1 - kR)\,, \tag{5.37}$$

can, however, provide an accurate description of the HMF. Making use of this analogy and choosing Eq. (5.37), a direct calculation of the variance term in Eq. (2.120) yields

$$\frac{\mathrm{d}\log\sigma^2}{\mathrm{d}\log M} = -\frac{1}{6\pi^2\sigma^2}P(1/R)\frac{1}{R^3}\,. \tag{5.38}$$

Correspondingly, the PS-HMF from Eq. (2.120) simplifies to [38, 390, 391]

$$\frac{\mathrm{d}n}{\mathrm{d}\log M} = \frac{1}{12\pi^2\sigma^2}\frac{\bar{\rho}}{M}f(\nu)\frac{P(1/R)}{R^3} = \frac{1}{6}\frac{\bar{\rho}}{M}f(\nu)\nu\frac{\Delta^2(1/R)}{\delta_c^2}\,. \tag{5.39}$$

In contrast to the top-hat window function in real space, which allows us to directly define a mass scale $M_T = 4\pi\bar{\rho}R_T^3/3$ to the filter scale R_T, the sharp-k filter has contributions on all scales in real space. This makes it difficult to assign a mass to the filter scale and therefore a free parameter ϵ is added to the mass assignment such that

$$M = \frac{4\pi}{3}\bar{\rho}(\epsilon R)\,. \tag{5.40}$$

This free parameter is chosen so that the PS-HMF matches the numerical simulations. Similarly to Refs. [391, 396, 397], $\epsilon = 2.5$ provides a good fit to the numerical data and does not vary with time. Furthermore, we need to rescale the value of the critical density $\delta_c = 1.686$ originating from spherical top-hat collapse to consider any contributions from using the sharp-k filter instead of a top-hat. In order to do so, we follow Ref. [397] and compare the variance of density perturbations (see Eq. (2.118)) on a filter scale R using the window functions from Eqs. (5.36) and (5.37) in the right panel of Fig. 5.3. We found that $\sigma^2(R)$ using the sharp-k window function is larger by a factor of 1.44 for large R, i.e. for high masses. As discussed in Ref. [397], the critical density δ_c in Eq. (5.39) has to be adjusted correspondingly.

The IHMF from the Press-Schechter approach, as well as the N-body IHMF and the M3P outcome, is shown in Fig. 5.4 at four different times. Consistent with Eq. (5.33), spurious halos dominate the N-body IHMF for halos with masses lower than $M_{\mathrm{lim}} \sim 0.1\,M_{h,\mathrm{end}}$, and account for the strong increase of the IHMF for $M \lesssim M_{\mathrm{lim}}$, which becomes steeper for smaller $\mathcal{N}$. As mentioned before, the procedure of removing the spurious

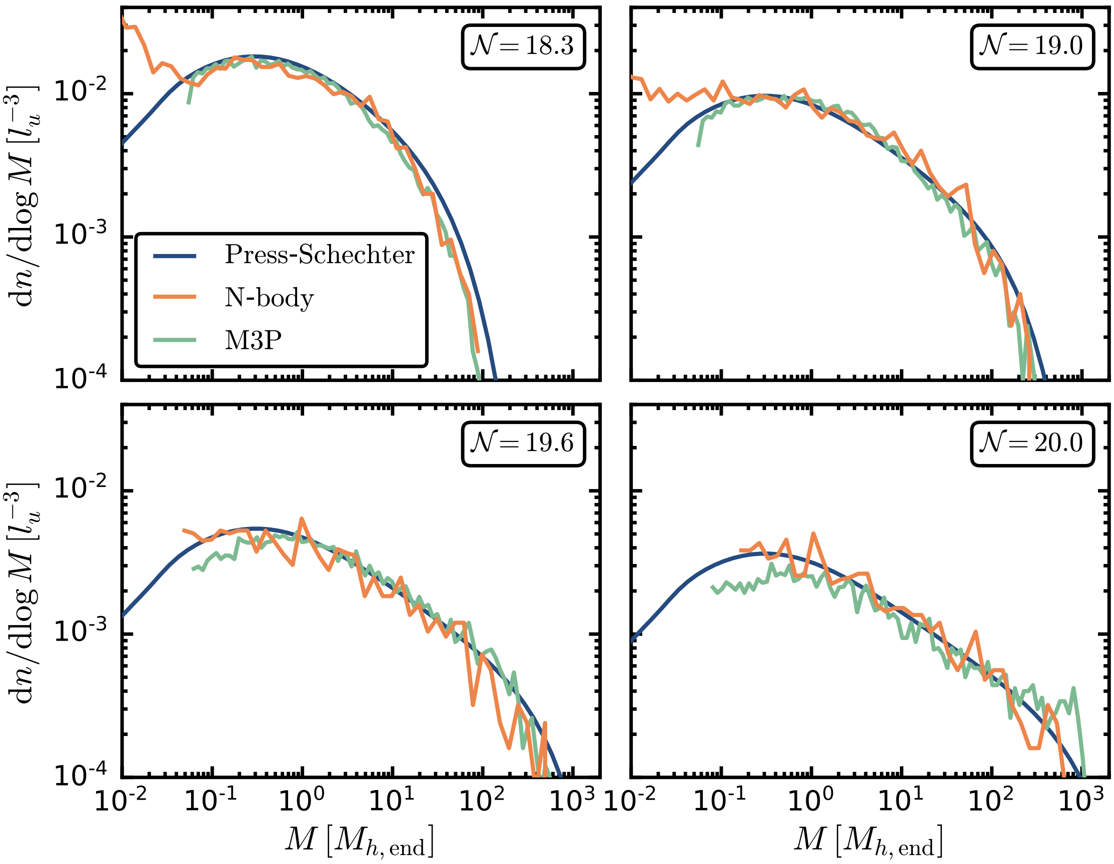

Figure 5.4 | Evolution of the IHMF predicted from the Press-Schechter formalism with $\epsilon = 2.5$ and obtained from N-body simulations with a $L = 50\,l_u$ simulation box and via the M3P algorithm with a box size of $L = 100\,l_u$, respectively. Figure adapted from Ref. [40].

halos is incomplete which explains the observed increase of the HMF at low masses. Apart from these unphysical deviations, the N-body results are in agreement with the PS-HMF at all times. Since the IHMFs generated with M3P are unaffected by spurious low-mass halos, they serve as a consistency check. Based on the mass range of the HMF from the N-body simulations we performed an M3P run with a total of 20 real space filters logarithmically spaced between $0.195\,l_u$ and $10\,l_u$. In order to adequately compare the M3P results to the N-body IHMF we chose a larger box size of $L = 100\,l_u$ for the M3P run, which is discussed below. As can be seen in Fig. 5.4, the corresponding IHMFs agree with the N-body IHMFs over the entire mass range down to M_{lim} for $\mathcal{N} \leq 19$. Notably, the low-mass end of the M3P-HMF is slightly underpopulated compared to both the N-body and the PS-HMF at $\mathcal{N} = 19.6$, which becomes more pronounced at $\mathcal{N} = 20$ when additionally more high-mass halos than expected are identified.

To understand why M3P reproduces the N-body and PS-HMF over the entire mass range at early times but cannot adequately do so at $\mathcal{N} \geq 19.6$ we now analyse the

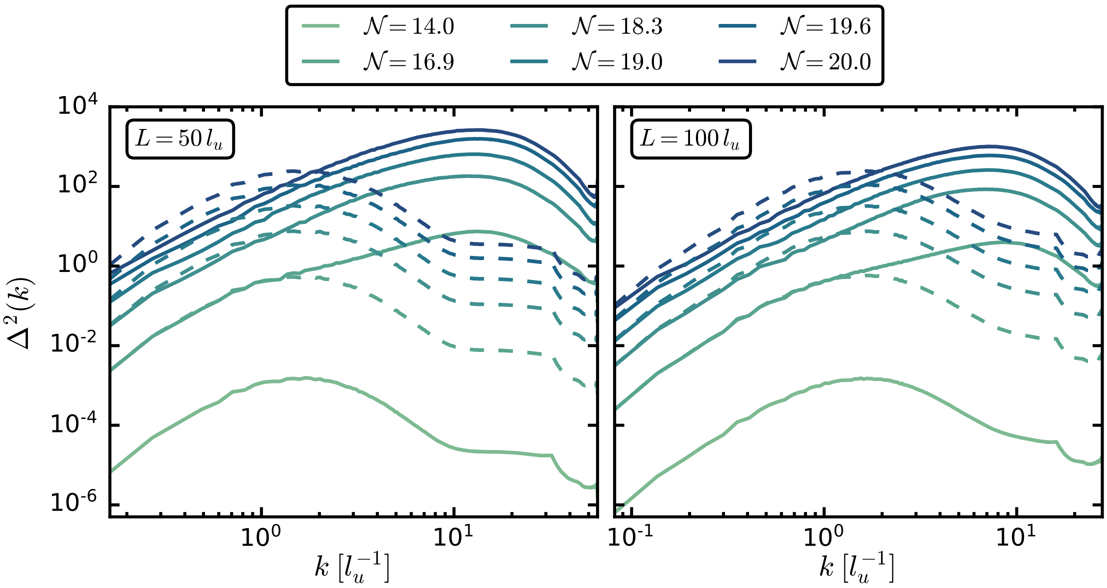

Figure 5.5 | Evolution of inflaton density power spectrum in dimensionless units for a simulation box size of $L = 50\, l_u$ (left panel) and $L = 100\, l_u$ (right panel). The dashed lines display the linearly evolved power spectra used by M3P, see Eq. (5.41). Figure adapted from Ref. [40].

evolution of the dimensionless power spectrum of density fluctuations. First of all, one can see in Fig. 5.5 by comparing the initial power spectrum of $L = 50\, l_u$ at $\mathcal{N} = 14$ with the one at $\mathcal{N} = 16.9$ that the discretisation artefacts at large k, which are discussed in Section 5.2.1, are washed out at $\mathcal{N} = 16.9$. Unsurprisingly, we observe an overall increase in power with time, particularly for high-k modes. The dotted lines in Fig. 5.5 show the M3P power spectrum. This is related to the initial power spectrum via the linear growth factor $D(a)$ so that

$$\Delta^2(k, a) = \left(\frac{a}{a_{\text{init}}}\right)^2 \Delta^2(k, a_{\text{init}})\,. \tag{5.41}$$

As expected, the N-body and M3P power spectra coincide for small k, i.e. in the linear regime for lower values of $\mathcal{N}$. However, at $\mathcal{N} \geq 19$ the M3P spectra differ significantly from the N-body spectra for $L = 50\, l_u$ even at small k, indicating that all scales are now nonlinear. Thus, the linearly evolved M3P power spectrum for $L = 50\, l_u$ at $\mathcal{N} \geq 19$ should not be used to obtain the corresponding IHMF. However, this issue can be resolved when a larger box size for the M3P runs is used. As expected, the $L = 100\, l_u$ M3P spectra shown in the right panel of Fig. 5.5 agree with the N-body power spectra at small k for a longer time. However, slight deviations on large scales are still observable at $\mathcal{N} \gtrsim 19.6$. This leads to inaccuracies in the M3P-IHMF in the sense that compared to the N-body results and the PS-HMF more high-mass and less low-mass halos are predicted at $\mathcal{N} = 20$, as can be seen in the lower right panel of Fig. 5.4. In other words, the N-body simulations are more resistant to numerical errors which arise from the largest scales becoming nonlinear.

5.3.2 Density Distribution and Halo Profiles

We determine the density distribution of the matter field, i.e. the one-point probability distribution function, by binning the normalised density $\rho_n = \rho/\bar{\rho} = 1 + \delta$, where δ is the overdensity, using a logarithmic bin width $\Delta \log(\rho_n) = 0.1$. The density distribution function $P(\rho_n)$ illustrates the relative frequency of overdensities. It is defined to be the normalised number of cells whose corresponding density value lies in a range given by $\Delta \log(\rho_n)$, i.e. $P(\rho_n) = \Delta N_{\mathrm{cell}}/\Delta \log(\rho_n) N_{\mathrm{cell}}^{-3}$ where $N_{\mathrm{cell}} = 512$ is the grid size.

The evolution of the density distribution in the $L = 50\, l_u$ simulation is shown in the left panel of Fig. 5.6. It can be seen that it is initially a narrow distribution, reflecting the shape of the power spectrum, which widens as the nonlinear phase continues. The observed maximal overdensity then increases, due to ongoing gravitational collapse, mergers, and accretion onto existing halos. As a consequence, the number of cells with a low mass density increases as raw material flows from these cells to the growing overdensities. At $\mathcal{N} = 20$, the densities range from roughly 10^{-6} to nearly 10^{5} and the distribution peaks at $\rho_n \sim 0.2$.

We now approximate the density distribution functions that we obtained from the numerical simulations. As a starting point, we introduce the log-normal distribution function [398]

$$P_{\mathrm{LN}}(\rho_n) = \frac{1}{\rho_n \sqrt{2\pi\sigma_{\mathrm{LN}}^2}} \exp\left(-\frac{(\ln(\rho_n) + \sigma_{\mathrm{LN}}^2/2)}{2\sigma_{\mathrm{LN}}^2}\right) , \tag{5.42}$$

where σ_{LN}^2 is the only free parameter. A fit for $\mathcal{N} = 16.4$ is shown in the right panel of Fig. 5.6. However, the log-normal distribution does not provide an accurate fit to the tails of the distribution function and does not align at all with the simulation results at later times. Consequently, we use a power-law $P(\rho_n) \sim \rho_n^{\alpha}$ with slope parameter α truncated on small and large densities with exponential terms [398] to model the distribution for $\rho_n \leq 0.2$ and another power-law with an exponential cut-off for $\rho_n > 0.2$. Specifically, the distribution functions are [398]

$$P(\rho_n) = A\rho_n^{\alpha} \exp\left(-(\rho_1/\rho_n)^{1.1}\right) \exp\left(-(\rho_n/\rho_2)^{0.55}\right) , \tag{5.43}$$

for $\rho_n \leq 0.2$ and

$$P(\rho_n) = B\rho_n^{\beta} \exp\left(-b\rho_n/\rho_3\right) , \tag{5.44}$$

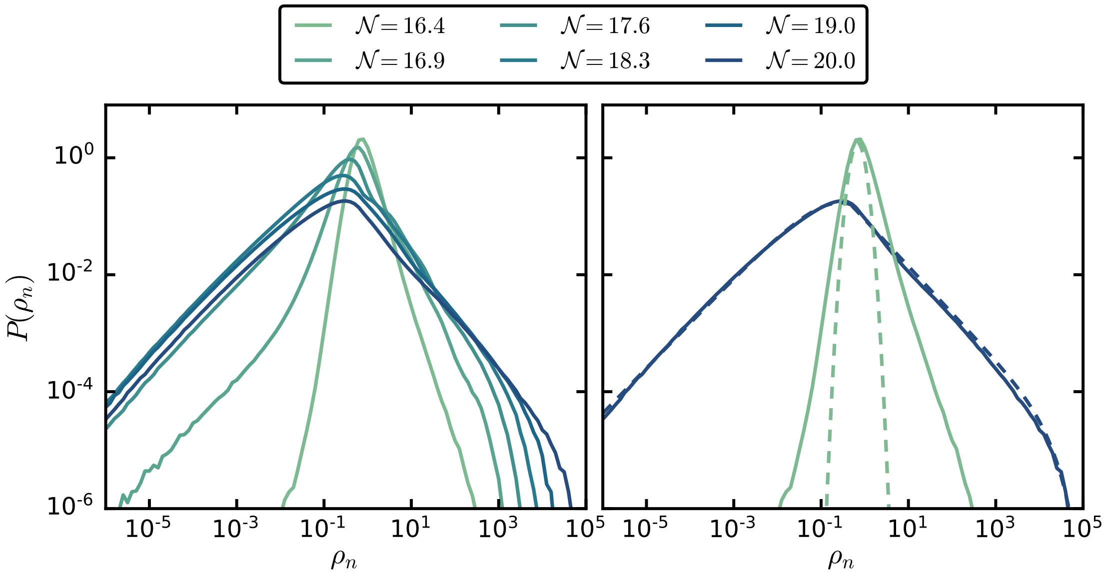

Figure 5.6 | Distribution of the inflaton density field for different $\mathcal{N}$. The left panel shows the evolution from $\mathcal{N} = 16.4$ to $\mathcal{N} = 20.0$ and fits to the distribution at these two instants of time are shown on the right. The dashed lines represent a log-normal fit for $\mathcal{N} = 16.4$ (see Eq. (5.42)) and a combined fit consisting of a power-law times a double exponential for $\rho_n \leq 0.2$ (see Eq. (5.43)) and a power-law times a single exponential for $\rho_n > 0.2$ (see Eq. (5.44)) for $\mathcal{N} = 20.0$, respectively. Figure adapted from Ref. [40].

for $\rho_n > 0.2$. In these two expressions A, B, α, β, b, ρ_1, ρ_2 and ρ_3 are free fitting parameters. With slope parameters of $\alpha = 0.8$ and $\beta = -0.8$, the numerical data can be modelled accurately over the entire range of ρ_n. The combination of Eqs. (5.43) and (5.44) is also suited to describe the density distribution at earlier times, i.e. this approach is not limited to the $\mathcal{N} = 20.0$ case.

Furthermore, we study the density profiles of the halos in our final snapshot in two mass regimes. Since we are limited by spatial resolution, we focus on inflaton halos at the high-mass end of the IHMF and separate between the mass regimes $M > 5 \times 10^2\, M_{h,\mathrm{end}}$ and $M \in [2, 3] \times 10^2\, M_{h,\mathrm{end}}$ at $\mathcal{N} = 20$ in the $L = 50\, l_u$ simulation. The averaged radial density profiles of ten inflaton halos in each mass sample are shown in Fig. 5.7. Black dashed lines represent NFW fits (see Eq. (2.131)) and the total range in the sample is shown by the coloured regions. The deviations of the averaged density profiles from the NFW fits are displayed in the lower panel of Fig. 5.7. There is a very good agreement for inflaton halos with $M > 5 \times 10^2\, M_{h,\mathrm{end}}$ deviating not more than $\sim 20\%$ even for large r. For lower-mass halos, the NFW fit is less accurate at large r where the averaged density profile is slightly underdense compared to the NFW fit. Nevertheless, the density profiles are NFW-like and exhibit concentrations of $c \in [10, 13.5]$. This result emphasises again the analogy of the early matter-dominated post-inflationary era to gravitational structure

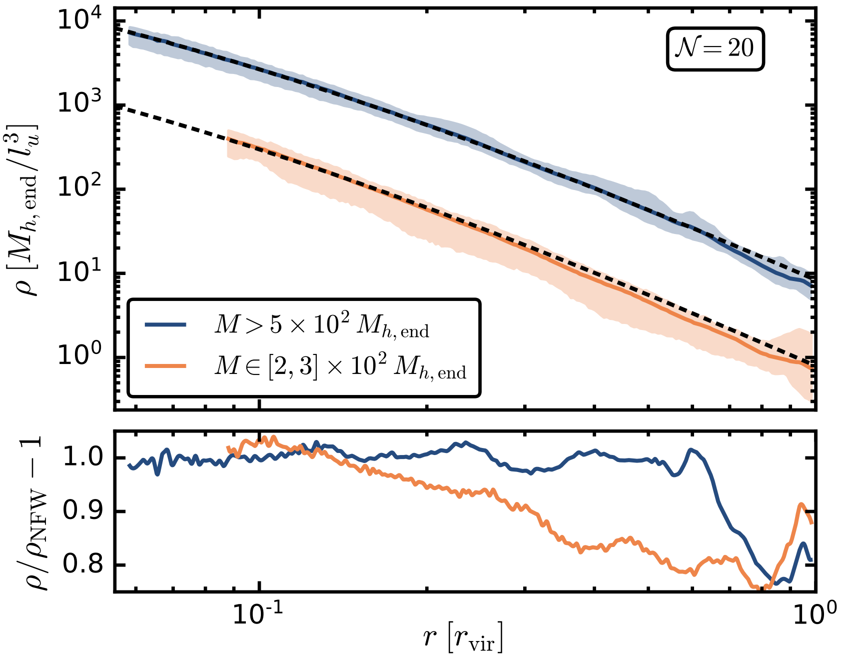

Figure 5.7 | Averaged radial density profiles (upper panel) of ten inflaton halos $\mathcal{N} = 20$ e-folds after the end of inflation in two different mass regimes (solid lines). The density profiles of the inflaton halos of masses $M \in [2,3] \times 10^2\,M_{h,\mathrm{end}}$ are rescaled by a factor of 10^{-1} for illustration purposes. The shaded regions display the area filled by all ten density profiles in the two mass bins. The black dashed lines represent NFW fits, the deviations from the fits are shown in the lower panel. Figure adapted from Ref. [40].

formation in the late-time Universe. Consistent with standard CDM simulations, the concentration parameter increases for a decreasing halo mass.

5.3.3 Discussion

The presented N-body simulation results provide quantitative predictions for the mass and density statistics of gravitationally-collapsed objects in the matter-dominated post-inflationary Universe. The inflaton halos in the simulation volume have masses up to $\sim 20\,\mathrm{kg}$ and their mass distribution is in agreement with the prediction of the mass-Peak Patch algorithm and with the PS-HMF as proposed in Ref. [38] after the first 1-3 e-folds of nonlinear growth. As expected from dark matter N-body simulations, the density profiles of the inflaton halos are NFW-like with concentrations of $\mathcal{O}(10)$ at $\mathcal{N} = 20$. Overall, the inflaton density field $\mathcal{N} = 20$ e-folds after the end of inflation reaches overdensities close to 10^5. Importantly, the simulation results do not depend on an explicit choice of parameters and on the precise form of the inflaton potential. For example, a smaller amplitude of the power spectrum at the end of inflation implies that gravitational structure formation will be delayed and a shifted peak of the power spectrum will shift the inflaton halo mass distribution accordingly. As long as the resonant amplification of the inflaton itself can be neglected after the end of inflation and the inflaton couplings to other particle species are small compared to the Hubble parameter for a large number of *e*-folds after inflation, there will be a long phase of matter-dominated expansion associated with the formation of gravitationally-bound structures on subhorizon scales before the Universe thermalises.

Certainly, the presence of gravitationally-bound structures in the post-inflationary Universe will modify the dynamics of reheating in ways that are yet to be properly explored. Furthermore, their formation and subsequent nonlinear evolution can source the production of gravitational waves that lead to a potentially observable SGWB [128]. Thus, a natural extension of the presented work is to compute the SGWB from the N-body simulations which is discussed in Section 5.5. Since the matter-dominated phase in the early Universe can last for a long time during which objects with increasing masses form, it is possible that eventually a threshold is reached beyond which an object becomes gravitationally unstable and might collapse into a PBH. The result that the IHMF in the post-inflationary Universe can be well described by a PS-HMF allows for the extrapolation of the IHMF to much later times where high-mass objects appear that are in principle massive enough to form a PBH. In the next section, we explore the formation of inflaton stars in the centre of inflaton halos. We make use of the Press-Schechter formalism to compute the mass distribution of inflaton stars and to study their potential to produce PBHs. It is expected that the possible collapse of an inflaton star requires a corresponding halo mass that is smaller than the necessary mass for a complete halo to collapse into a PBH [151]. This stresses the significance of inflaton stars in the early Universe.

5.4 Formation of Inflaton Stars

In order to confirm the hypothesis that inflaton stars form in the post-inflationary Universe [38] in analogy to solitonic cores in the centre of FDM halos, high-resolution simulations of the SP equations have to be performed. Since solving the SP equations directly on all length scales and resolving the de Broglie wavelength throughout the full simulation is much more computationally expensive, we instead make use of the hybrid method from Section 3.2.3. Implementing the classical wave approximation within AxioNyx [43] enables us to solve the SP equations on adaptively refined regular grids while the standard N-body solver is used for most of the simulation volume. This reduces the computation time significantly while resolving the wavelike properties of the inflaton field in regions of interest which cover only $1.5 \times 10^{-3}\%$ of the full simulation domain.

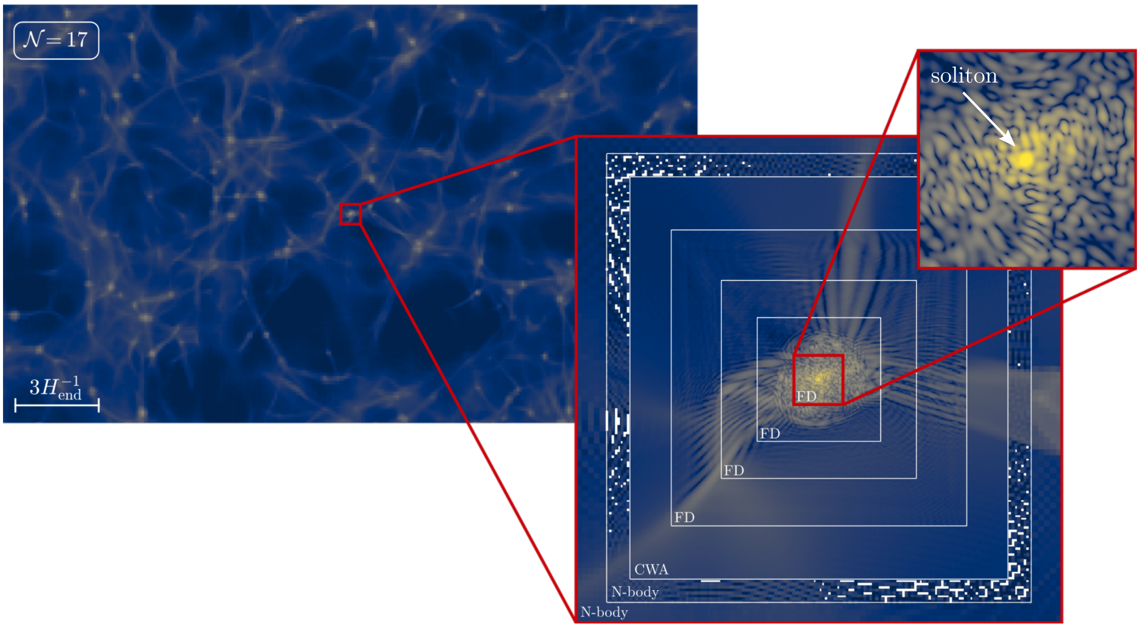

Figure 5.8 | Scaled sequence of the inflaton density $\mathcal{N} = 17$ e-folds after the end of inflation. The rectangular region shows the projected inflaton density of 15% of the full simulation box centred on a selected halo. A slice through the maximum density of the halo illustrates the setup of several refinement levels in our simulation. Note that the white space in the last N-body level corresponds to cells without any particles. On the next higher level, the wave function is constructed using the classical wave approximation (CWA) which is followed by levels where the SP equations are solved with finite difference (FD) methods. The spatial resolution of the finest FD level, which is displayed in an enlargement in the upper right panel, is increased by a factor of $2^8 = 256$ compared to the root grid. One can clearly recognise the interference patterns in the filaments, the granular structure inside the collapsed inflaton halo and the solitonic core (inflaton star) in its centre. Figure reproduced from Ref. [41].

The same model parameters, initial power spectrum and unit system as described in Section 5.2.1 are used. Extending the previous N-body simulations, the same comoving length $L = 50\, l_u$ of the simulation box is chosen and the simulations are initialised $\mathcal{N} = 14$ e-folds after the end of inflation. We make use of one special trick to ensure that the numerical simulations are tractable. The overall cosmological parameters from Section 5.2.1 are set relative to the choice $m = 6.35 \times 10^{-6}\, M_{\rm Pl}$. However, we artificially increase the de Broglie wavelength $\lambda_{\rm dB}$ in the simulations by reducing m by a factor of 80, so that $\hbar/m = 9.84 \times 10^{-3}\, l_u^2/t_u$. This increases the lengths at which wave effects become apparent and reduces the number of nested levels we need to resolve, and allows a larger time step within the simulation. Taken together these choices prevent the simulations from becoming computationally intractable. This approach is justified given the scaling symmetry of the SP equations (see Section 3.1.3) which maps soliton quantities to rescaled inflaton masses. Hence, our simulation results are qualitatively independent of the inflaton mass.

The 512^3 unigrid N-body simulations described in Section 5.3 are used to determine the Lagrange patches of five isolated halos that experience no major mergers during the entire simulation time. In five separate simulations, these regions are individually refined with two additional initial, static refinement levels with a comoving side length of up to $7.5\, l_u$. The number of particles in these regions is increased accordingly. As before, we employ the Music code [236] to generate particle positions and velocities for these nested initial conditions.

Initially, the particles are in the single-streaming regime and can be evolved with the N-body solver until $\mathcal{N} \approx 16.5$ without further refinement. As the selected halos start to collapse, we add three additional refinement levels tracing the halos' central positions. The first is an additional N-body level, followed by a level with a cubic grid of comoving side length $1.5\, l_u$ on which the CWF is constructed with a smoothing radius of $\xi = 6\,\Delta x$, where Δx denotes the level's cell width. The initial CWF is interpolated onto the finest level and then evolved with the SP equations via a fourth-order Runge-Kutta algorithm. Since the Schrödinger-Vlasov correspondence does not hold in the centre of a collapsing halo, it is important to construct the CWF far beyond it, as noted in Section 3.2.3. The evolution of the N-body particles is tracked inside the SP domain but the source of gravity is the density $\rho = |\psi|^2$ of the wave function. Once the halo has formed up to three additional finite difference levels are added to ensure that the de Broglie wavelength is resolved throughout our simulations. This yields a total of eight refinement levels with a refinement factor of two at each step, six of which dynamically trace the position of the selected halo. The level setup is illustrated in Fig. 5.8.

5.4.1 Properties of Inflaton Stars

We simulate the formation of five inflaton halos covering a mass range between 8.5 g and 225 g at $\mathcal{N} = 17.3$. Analogously to FDM halos, a solitonic core forms in the centre of each collapsing inflaton halo surrounded by incoherent granular density fluctuations, as shown in Fig. 5.8. The solitonic core is identified by its radial density profile given by Eq. (3.32) where the central core density $\rho_{*,0}$ in our unit system from Section 5.2.1 reads

$$\rho_{*,0} = 3.3 \times 10^{13} \left(\frac{1.546 \times 10^{22}\,\mathrm{eV}}{m}\right)^2 \left(\frac{10^{-3}\, l_u}{r_*}\right)^4 \frac{m_u}{l_u^3}\,, \tag{5.45}$$

with r_* denoting the physical radius of the solitonic core. Fig. 5.9 shows the radial density profiles centred around the point of maximal density of the five simulated halos at different $\mathcal{N}$. They are well fitted by Eq. (3.32) in the innermost region, transitioning to outer profiles indistinguishable from the results of the corresponding pure N-body simulations. This confirms the hypothesised existence of inflaton stars in the post-inflationary universe [38]

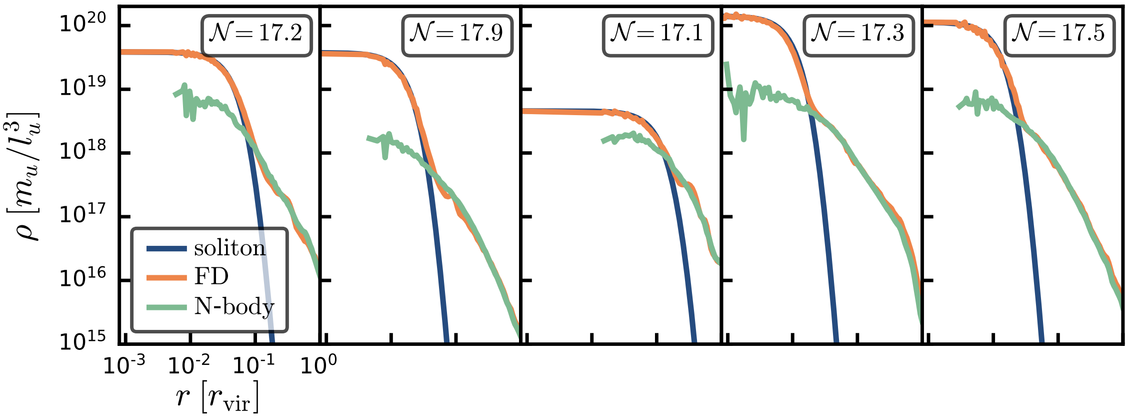

Figure 5.9 | Radial density profiles of five simulated halos at different numbers of *e*-folds after the end of inflation. The orange curves represent the profiles produced by solving the Schrödinger-Poisson equations with the finite difference method while the blue curves are given by the theoretical soliton density profiles from Eq. (3.32). For comparison, the halo profiles from a pure N-body simulation are shown in green. Figure reproduced from Ref. [41].

and demonstrates the validity of the Schrödinger-Vlasov correspondence in the outer parts of the halos.

The velocity distributions of the lowest-, highest- and a medium-mass halo from our sample are shown in Fig. 5.10 for both the wave function ψ within a cube defined by the halo's virial radius r_{vir} and for the corresponding pure N-body simulation. The former is given by [309]

$$f(\mathbf{v}) = \frac{1}{N}\left|\int \mathrm{d}^3\mathbf{x}\exp\left(-im\mathbf{v}\cdot\mathbf{x}/\hbar\right)\psi(\mathbf{x})\right|^2, \tag{5.46}$$

where N is a normalisation factor. These velocity distributions are almost indistinguishable, again confirming the Schrödinger-Vlasov correspondence, and are well fitted by a Maxwellian distribution

$$f_M(v)\mathrm{d}v = 3\left(\frac{6}{\pi}\right)^{1/2}\frac{v^2}{v_0^3}\exp\left(-\frac{3}{2}\frac{v^2}{v_0^2}\right)\mathrm{d}v\,, \tag{5.47}$$

with free parameter v_0. They peak at $v_{\mathrm{vir}} = (2/3)^{1/2}v_0$. It was previously found that the core radii r_* are correlated with the peaks of the velocity distributions of their host halos,

$$r_* = \frac{2\pi}{7.5}\frac{\hbar}{mv_{\mathrm{vir}}}, \tag{5.48}$$

once the cores are in virial equilibrium with their surroundings [43, 320]. In practice, this means that the soliton velocity satisfies $v_* = v_{\mathrm{vir}}$ [286]. We use Eq. (5.48) to compute v_* from r_* for each of the three halos. The soliton velocities are displayed as vertical dashed lines in Fig. 5.10. While the soliton velocities inside the lower-mass halos agree

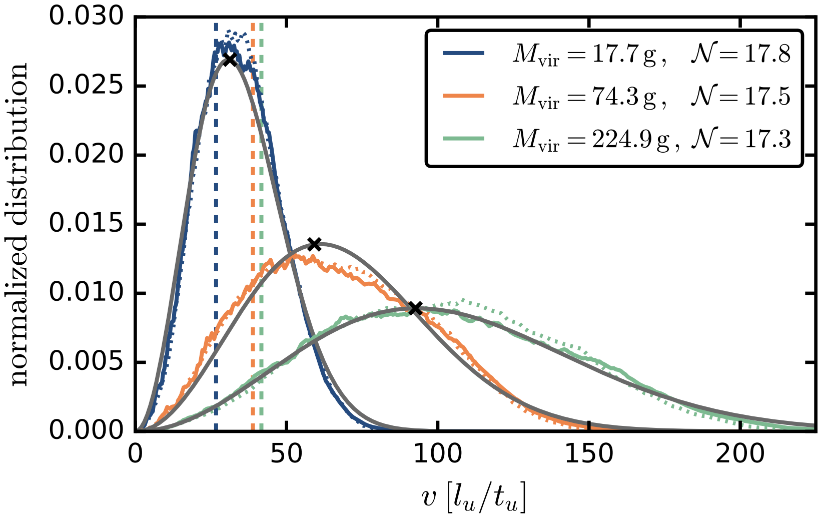

Figure 5.10 | Velocity spectra of three inflaton halos inside their respective virial radii for the wave function (solid) and for N-body particles (dotted) in the same region. Fits of Maxwellian distribution functions (cf. Eq. (5.47)) are displayed in grey. The vertical dashed lines show the soliton velocities v_* that are computed from the core radius r_* via Eq. (5.48). The crosses mark $v_{\rm vir}$ of the respective halos which closely align with the peaks of the Maxwellian distribution. Figure reproduced from Ref. [41].

well with $v_{\rm vir}$ at their respective $\mathcal{N}$, v_* of the heaviest halo at an earlier time is only half the peak velocity, implying that this core needs to double its mass before reaching virial equilibrium (cf. Eq. (5.50)).

We define the mass of a solitonic core as the mass enclosed by r_* [304],

$$M_* = 3.9251 \frac{\hbar^2}{G r_* m^2} \,. \tag{5.49}$$

For the density profiles shown in Fig. 5.9 we find core masses ranging from 0.95 g to 1.90 g. Inserting r_* from Eq. (5.49) into Eq. (5.48), we obtain a relation between the core mass and the virial velocity of the halo,

$$M_* = 4.69 \frac{\hbar}{m} \frac{v_{\rm vir}}{G} \,. \tag{5.50}$$

Note that by replacing $v_{\rm vir}$ in Eq. (5.50) with the virial velocity $v_{\rm vir} = (GM_h/r_{\rm vir})^{1/2}$ of a halo with mass M_h, one recovers the core-halo mass relation $M_* \sim M_h^{1/3}$ from Eq. (3.35). Since Eq. (5.50) is only accurate when the soliton radii approach Eq. (5.48) the core masses from the two lighter halos in Fig. 5.10 are 15% and 35% smaller than expected from Eq. (5.50), while the most massive core has only half of its expected mass.

The mass increase of the respective solitonic core inside a low-mass (blue), a medium-mass (orange) and a high-mass halo (green) is shown in Fig. 5.11. The soliton masses are normalised by their initial masses $M_{*,0}$ when the radial density profile starts to be

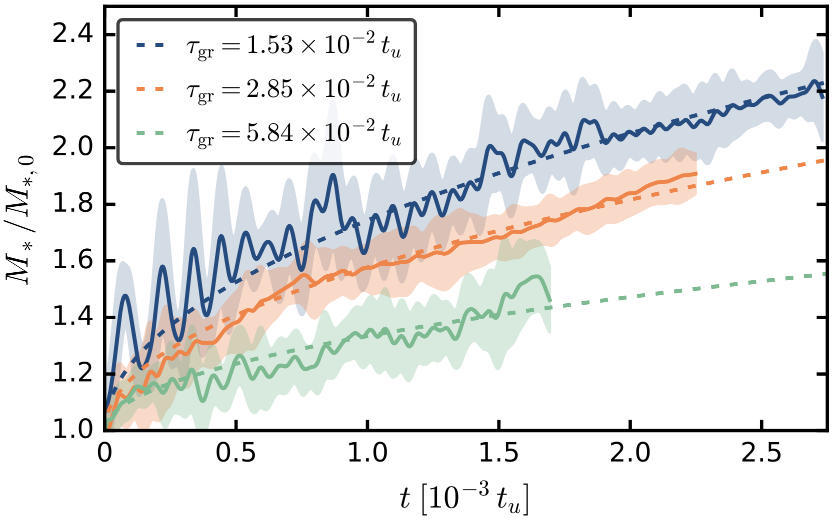

Figure 5.11 | Mass increase of three inflaton stars relative to their mass $M_{*,0}$ at formation. Due to the strong oscillations of the solitonic cores, the simulation data was smoothed with a Gaussian kernel with a standard deviation of $\sigma = 2 \times 10^{-5}\, t_u$. The mean and its 1σ deviation band are displayed by the solid lines and the shaded regions, respectively. As shown by the dashed lines, the mass growth obeys Eq. (5.52) with time scale $\tau_{\rm gr}$ given by Eq. (5.51). Figure adapted from Ref. [41].

well described by the soliton profile defined in Eq. (3.32). The growth rate depends on the condensation time scale (see Eq. (3.39)) which can be expressed in terms of virial quantities as [307]

$$\tau_{\rm gr} = \frac{0.7\sqrt{2}}{12\pi^3}\left(\frac{m}{\hbar}\right)^3 \frac{v_{\rm vir}^6}{G^2\rho^2 \ln\Lambda}\,. \tag{5.51}$$

Similar to Eq. (3.39), $\ln\Lambda = \ln(m v_{\rm vir} r_{\rm vir}/\hbar)$ is the Coulomb logarithm and $\rho = \Delta_{\rm vir}\bar{\rho}$ is the mean density of the host halo. Computing $\tau_{\rm gr}$ at soliton formation time, we recover the expected growth rate (cf. Eq. (3.40))

$$M_* = M_{*,0}\left[c_{\rm gr}\left(\frac{t}{\tau_{\rm gr}}\right)^{1/2} + 1\right], \tag{5.52}$$

where $c_{\rm gr} \simeq 3$ was determined from fitting Eq. (5.52) to the growth curves. As is noticeable from Fig. 5.11 and expected from Eqs. (5.51) and (5.52), larger halo masses lead to larger values of $\tau_{\rm gr}$ and thus to a relatively slower mass growth of the solitonic core. It was conjectured in Ref. [42] and confirmed in Ref. [344] that the mass growth proportional to $\sim t^{1/2}$ comes to an end once the soliton is in virial equilibrium with its halo and that it afterwards proceeds with the reduced growth rate $\sim t^{1/8}$. However, our simulations are limited by spatial resolution and it is too computationally expensive to verify this in our setup.

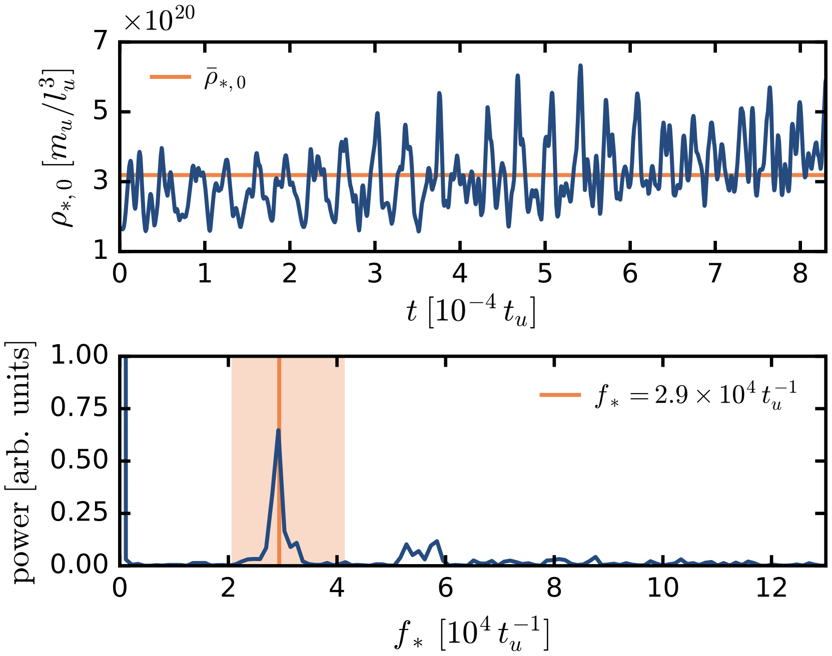

Figure 5.12 | Frequency analysis of an oscillating inflaton star. The central soliton density as a function of time is shown in the upper panel and its corresponding power spectrum in the lower panel. Boundaries of the shaded region are determined by the quasi-normal frequencies (see Eq. (5.53)) using the maximum and minimum $\rho_{*,0}$. The spectrum peaks at the frequency $f_* = 2.9\times 10^4\,t_u$ corresponding to $\bar{\rho}_{*,0}$ in the lower panel. Figure adapted from Ref. [41].

From Fig. 5.11 we see that strong soliton oscillations cause M_* to vary over time by up to 20%. Analysing the oscillations with high temporal resolution reveals that the central soliton density oscillates with amplitudes of more than a factor of two and a density-dependent frequency. A representative frequency analysis can be seen in Fig. 5.12 showing the fluctuating soliton density and its temporal Fourier transform. In agreement with previous studies (see Refs. [42, 43, 309]) the frequency spectrum of the oscillations peaks at the quasi-normal mode of the excited soliton [299]

$$f_* = 5.2\times 10^4 \left(\frac{\bar{\rho}_{*,0}}{10^{21}\,m_u/l_u^3}\right)^{1/2} t_u^{-1}\,, \tag{5.53}$$

where $\bar{\rho}_{*,0}$ is the time-averaged value of the central soliton density, $\rho_{*,0}$. This means that inflaton stars do not form in a stationary but in a highly excited oscillatory state in which the frequency is governed by Eq. (5.53).

5.4.2 Inflaton Star Mass Function

The mass distribution of inflaton stars can be predicted using the mass distribution of inflaton halos and their radii at different times found in the N-body simulations from

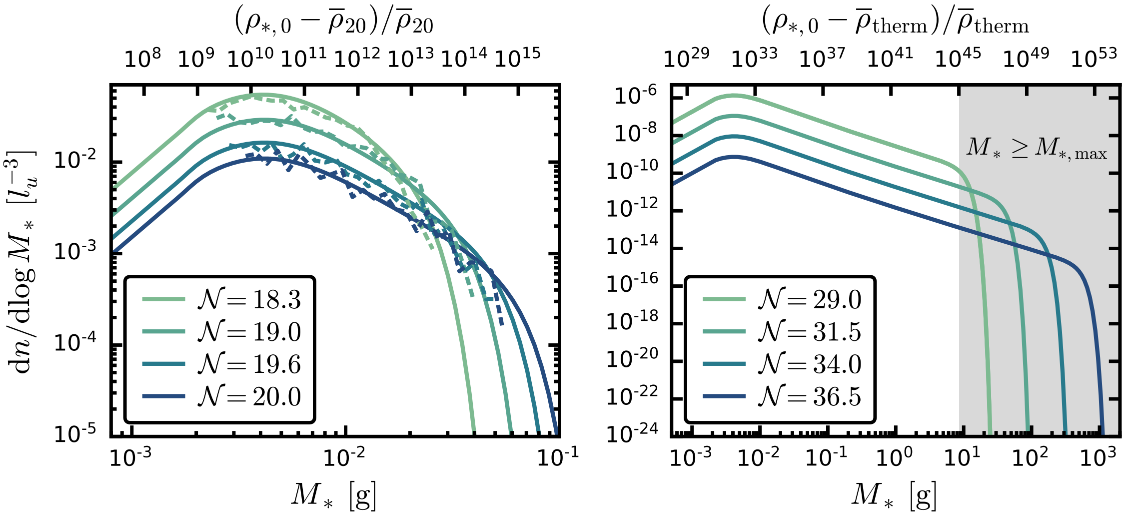

Figure 5.13 | Inflaton star mass function at different number of e-folds after the end of inflation for an inflaton mass of $m = 6.35 \times 10^{-6}\,M_{\mathrm{Pl}}$. Left: solid lines represent the ISMF obtained from the Press-Schechter formalism, while dashed lines display the corresponding ISMF derived from the numerical IHMF (see Section 5.3.1). The upper axis shows the inflaton star overdensity relative to the average density 20 e-folds after the end of inflation. Right: ISMF from Press-Schechter theory until thermalisation at $T = 1$ TeV ($\mathcal{N} = 36.5$) with overdensities relative to the mean density $\bar{\rho}_{\mathrm{therm}}$ at thermalisation. The grey shaded area highlights masses larger than $M_{*,\mathrm{max}}$ (see Eq. (5.54)). Figure adapted from Ref. [41].

Section 5.3. We compute the expected mass of an inflaton star in each halo with Eq. (5.50). The resulting inflaton star mass function (ISMF) $\mathrm{d}n/\mathrm{d}\log M_*$, defined as the comoving number density of inflaton stars per logarithmic mass interval,[55] is shown in the left panel of Fig. 5.13 from $\mathcal{N} = 18.3$ to $\mathcal{N} = 20.0$. Inserting the obtained masses M_* into Eqs. (5.45) and (5.49), we relate them to their central densities and determine their overdensities relative to the mean density $\bar{\rho}$. As is evident from the upper axis in the left panel of Fig. 5.13, the distribution of overdensities associated with inflaton stars when $\mathcal{N} = 20.0$ peaks at around 10^{10} and can reach values as high as 10^{15} before dropping exponentially.

As shown in Section 5.3.1, the numerical IHMF can be well described by adapting the Press-Schechter formalism with a sharp-k filter. Assuming that each halo contains an inflaton star with a mass given by Eq. (5.50), the ISMF retains in general the shape of the PS-HMF for the inflaton halos (cf. Fig. 5.4) but is shifted to correspondingly smaller masses. As evident from the left panel in Fig. 5.13, the corresponding ISMFs agree with each other at different $\mathcal{N}$. This allows us to extrapolate the ISMF and their distribution of overdensities to even later times in the post-inflationary Universe, as shown in the right panel of Fig. 5.13. Assuming that thermalisation occurs at a temperature of 1 TeV, the

---

[55] Note that a similar procedure is also applicable to determine the mass distributions of solitonic cores in FDM halos and axion stars in axion miniclusters, respectively.

early matter-dominated epoch lasts for $\mathcal{N} = 36.5$ e-folds (cf. Eq. (5.1)) allowing typical overdensities at the centre of inflaton stars to be as large as 10^{32} at the end of the matter-dominated phase. An inflaton star, like any boson star, has a maximum possible mass, beyond which its radius approaches the Schwarzschild radius $r_\mathrm{S} = 2GM/c^2$. Applying the uncertainty principle to an inflaton star with maximum momentum $p = mc$ and size r_S, one obtains an estimate for the upper mass limit [316, 399]

$$M_{*,\mathrm{max}} = \frac{1}{2}\frac{\hbar}{m}\frac{c}{G}\,, \tag{5.54}$$

above which an inflaton star becomes gravitationally unstable, potentially dispersing or collapsing into a black hole depending on the details of its prior evolution [316, 400]. As is shown in the right panel of Fig. 5.13, this condition is met for a range of inflaton stars for $\mathcal{N} \geq 29$ e-folds after the end of inflation.

Integrating the ISMF yields an estimate for the mass $M_{*,\mathrm{tot}}$ per unit volume that is attributed to the sum of the masses of all inflaton stars,

$$M_{*,\mathrm{tot}} = \int_0^{M_{*,\mathrm{max}}} \frac{\mathrm{d}n}{\mathrm{d}\log M_*}\,\mathrm{d}M_*\,. \tag{5.55}$$

Performing the integration for the PS-HMF to obtain the fraction of mass bound in inflaton halos, we find that this quantity rapidly converges to 70% already at $\mathcal{N} = 25$. At the same time, the mass fraction of inflaton stars decreases linearly with scale factor from 10^{-5} at $\mathcal{N} = 20.0$ to 10^{-12} at $\mathcal{N} = 36.5$. This is reasonable since overall $\mathrm{d}n/\mathrm{d}\log M_* \sim a^{-1}$ while the cut-off at the high-mass end of the ISMF (see right panel of Fig. 5.13), which effectively acts as the upper limit in Eq. (5.55) when $M_{*,\mathrm{max}}$ is not yet reached, increases only weakly with a. Setting the lower limit in the integral to $M_{*,\mathrm{max}}$ and integrating to $M_* \to \infty$ yields the integrated mass of inflaton stars with $M \geq M_{*,\mathrm{max}}$. The maximal fraction of 3×10^{-11} is reached at $\mathcal{N} = 30$, afterwards it decreases. Importantly, this quantity is not the mass fraction of PBHs since (i) not every unstable inflaton star collapses into a black hole and (ii) this approach does not capture black hole evolution via accretion, mergers or evaporation. With maximal possible masses of only 1 kg assuming thermalisation at $T = 1\,\mathrm{TeV}$, any such black holes would evaporate in less than 10^{-18} s [401].

5.4.3 Discussion

Using a hybrid method combining an N-body scheme on large scales with a finite difference solver for the Schrödinger-Poisson equations on small scales, we performed highly refined simulations of the effective matter-dominated era in the post-inflationary Universe. Extending the N-body simulations from Section 5.3 to much smaller length scales by zooming into selected halos enabled us to properly resolve their interior structure. Taking a sample of five halos with masses ranging from 8.5 g to 225 g at $\mathcal{N} = 17.3$ e-folds after the end of inflation, we confirm the existence of inflaton stars in the very early Universe. In agreement with their late-time analogues in FDM halos [289, 308, 309] and axion miniclusters [42, 307], we find that inflaton stars are subject to strong quasi-normal oscillations and that their masses after formation increase as $t^{1/2}$. The radial density profiles in the outer regions of the simulated halos and the velocity distribution inside them are consistent with their counterparts in pure N-body simulations. This confirms the validity of the Schrödinger-Vlasov correspondence on scales larger than the de Broglie wavelength.

Making use of the numerically obtained IHMF in Section 5.3.1 and the Press-Schechter formalism we predict the mass distribution of inflaton stars in the post-inflationary Universe until thermalisation at temperature $T = 1$ TeV. Since halo masses increase over time and more massive inflaton halos collapse at later times, inflaton stars eventually reach an upper mass limit suggesting that they can collapse into PBHs. Given their masses, all these black holes evaporate prior to BBN. Any particle coupled to gravity with a mass below the Hawking temperature can be produced in this process [402]. Hence, a decaying PBH population provides a production mechanism for dark matter [403–408] and also for dark radiation [401, 407]. Even if the fraction of produced PBHs is rather small, particle creation through their evaporation can be efficient enough to constitute the observed dark matter relic abundance [407, 408].

The possible formation of PBHs from the gravitational instability of nonrelativistic scalar fields was already studied in Ref. [140] and the same formation mechanism as presented in Section 5.4.2 was recently discussed in Ref. [151]. In this work, the authors of Ref. [151] derived mass limits both for the collapse of an inflaton halo and an inflaton star into a PBH and showed that lower halo masses are required for the soliton collapse. Furthermore, their results suggest that taking into account attractive inflaton self-interactions increases the probability of PBH formation. Nevertheless, this treatment can be considered only as a starting point and more sophisticated approaches are required to eventually obtain constraints on reheating models from bounds to the PBH abundance. A full analysis of PBH production and their subsequent evolution should also include the expected rapid mass growth of PBHs after formation through accretion. A detailed study of solitons exceeding the bound of Eq. (5.54) presumably involves fully relativistic simulations as in Refs. [400, 409]. It is also worthwhile to compare the PBH scenario from the gravitational fragmentation of the inflaton field with other PBH formation mechanisms in the post-inflationary Universe [141–150]. For example, it is also possible that PBHs are produced via oscillons [410, 411] in models where a phase of parametric resonance follows the end of inflation. In the standard PBH production scenario, an inflationary perturbation collapses into a PBH provided the perturbation is above a critical limit when it re-enters the horizon during radiation-domination (see Section 1.2.1). In contrast to this, subhorizon-sized PBHs can already form during reheating in scenarios where the inflaton field is subject to fragmentation.

Finally, it is important to mention that the existence of a phase of parametric resonance does not exclude the formation of inflaton stars. Instead, an oscillon-dominated era after inflation can serve as initial conditions for the subsequent nonrelativistic evolution in the matter-dominated phase. Thus, one can expect a rich phenomenology of inflaton halos and inflaton stars prior to thermalisation in a broad class of inflationary scenarios, provided the reheating temperature is sufficiently low. Moreover, if the inflaton has weak self-couplings during this phase, the SP equations will need to be generalised to the Gross–Pitaevskii equations to take the self-interactions into account. Separately, there are likely analogues of the resonant decay of axion stars into photons for inflaton stars coupled to external fields [412, 413].

5.5 Gravitational Wave Spectrum

In addition to the gravitational wave spectrum that originates from the quantisation of inflationary tensor perturbations (see Section 2.2.5), *classical* gravitational waves can be produced through a number of different processes in the post-inflationary era. These yield an SGWB that might be observable at the present time [120–131]. In all generation scenarios, the inhomogeneities in the fragmented inflaton density field act as a source term for tensor perturbations. In particular, the gravitational collapse of inflaton density fluctuations on subhorizon scales in the matter-dominated epoch following inflation is a potential origin of gravitational waves [127, 128]. So far there exist only analytical estimates of the expected signal, however, we can make use of our N-body simulations to refine the bounds obtained in Ref. [128]. In this section, the formalism to calculate the gravitational wave spectrum is presented and how our N-body simulations from Section 5.3 can be adapted to compute the SGWB from the gravitational fragmentation of the inflaton field. Finally, the first preliminary simulation results are discussed. A more detailed description can be found in Ref. [414].

5.5.1 Generation of Gravitational Waves after Inflation

The equation of motion for tensor perturbations is given by Eq. (2.73), where the source term Σ_{ij}^{TT} is the traceless and transverse part of the anisotropic stress tensor which can be expressed as [123, 229]

$$a^2\Sigma_{ij} = T_{ij} - \bar{p}a^2(\delta_{ij} + h_{ij})\,. \tag{5.56}$$

Here, T_{ij} denotes the spatial components of the stress-energy tensor of the inhomogeneous inflaton field and $\bar{p}$ the background pressure. Since the $\bar{p}\delta_{ij}$ in Eq. (5.56) is pure trace, it does not contribute to Σ^{TT}_{ij}. Also, the term that includes the metric perturbation h_{ij} turns out to be negligible on subhorizon scales and does not add to the traceless and transverse part of the anisotropic stress tensor [123]. Thus, Σ^{TT}_{ij} can be well approximated by the traceless and transverse component of the stress-energy tensor T_{ij} of the inflaton field for our purposes. Importantly, it can be evaluated at any time step in an N-body simulation as only the inflaton density field and the velocity fields are required (see Eq. (5.75) and Section 5.5.3 for details).

Introducing now the variable $\widetilde{h}_{ij} = ah_{ij}$ and working in Fourier space with the convention that

$$T_{ij}(\mathbf{k}) = \int \frac{\mathrm{d}^3\mathbf{x}}{(2\pi)^{3/2}} T_{ij}(\mathbf{x}) e^{i\mathbf{k}\mathbf{x}}\,, \tag{5.57}$$

the evolution Eq. (2.73) becomes in comoving units [123]

$$\widetilde{h}''_{ij}(\mathbf{k}) + \left(k^2 - \frac{a''}{a}\right)\widetilde{h}_{ij}(\mathbf{k}) = 16\pi G a T^{TT}_{ij}(\mathbf{k})\,. \tag{5.58}$$

The transverse traceless part of $T_{ij}(\mathbf{k})$ can be obtained in Fourier space by the projection [123]

$$T^{TT}_{ij}(\mathbf{k}) = O_{ijlm}(\mathbf{k}) T_{lm}(\mathbf{k})\,, \tag{5.59}$$

where the projection operator $O_{ijlm}(\mathbf{k})$ is given by

$$O_{ijlm}(\mathbf{k}) = P_{il}(\mathbf{e_k})P_{jm}(\mathbf{e_k}) - \frac{1}{2}P_{ij}(\mathbf{e_k})P_{lm}(\mathbf{e_k}) \tag{5.60}$$

with

$$P_{ij}(\mathbf{e_k}) = \delta_{ij} - e_{\mathbf{k},i}e_{\mathbf{k},j}\,, \tag{5.61}$$

and $\mathbf{e_k} = \mathbf{k}/k$ is the unit vector in $\mathbf{k}$-direction. Since $a''/a \sim a^2H^2$ during matter-domination and $a^2H^2 \ll k^2$ on subhorizon scales, one can safely neglect this term and Eq. (5.58) reduces to

$$\widetilde{h}''_{ij}(\mathbf{k}) + k^2\widetilde{h}_{ij}(\mathbf{k}) = 16\pi G a T^{TT}_{ij}(\mathbf{k})\,. \tag{5.62}$$

Assuming that gravitational waves are sourced in the time interval $\tau_i < \tau < \tau_f$, where τ_i and τ_f denote the initial and final time of the N-body simulations, this equation is solved by [123, 128]

$$\widetilde{h}_{ij}(\mathbf{k}) = A_{ij}(\mathbf{k}) \sin[k(\tau - \tau_f)] + B_{ij}(\mathbf{k}) \cos[k(\tau - \tau_f)] , \tag{5.63}$$

where

$$A_{ij}(\mathbf{k}) = \frac{16\pi G}{k} \int_{\tau_i}^{\tau_f} \mathrm{d}\tau \cos[k(\tau_f - \tau)] a(\tau) T_{ij}^{TT}(\tau, \mathbf{k}) , \tag{5.64}$$

$$B_{ij}(\mathbf{k}) = \frac{16\pi G}{k} \int_{\tau_i}^{\tau_f} \mathrm{d}\tau \sin[k(\tau_f - \tau)] a(\tau) T_{ij}^{TT}(\tau, \mathbf{k}) . \tag{5.65}$$

The energy density of the gravitational waves ρ_{gw} is then defined as an average over the volume $V = L^3$ covered by the simulation box with a comoving side length of L as [123]

$$\rho_{\mathrm{gw}} = \frac{1}{32\pi G a^4} \langle \widetilde{h}'_{ij}(\tau, \mathbf{x}) \widetilde{h}'_{ij}(\tau, \mathbf{x}) \rangle_V = \frac{1}{32\pi G a^4} \frac{1}{V} \int \mathrm{d}^3\mathbf{k} \widetilde{h}'_{ij}(\tau, \mathbf{k}) \widetilde{h}'^{*}_{ij}(\tau, \mathbf{k}) . \tag{5.66}$$

Inserting the derivative of $\widetilde{h}_{ij}(\mathbf{k})$ into Eq. (5.66), one can show that the energy density can be expressed as [123]

$$\begin{aligned} \rho_{\mathrm{gw}} = \frac{4\pi G}{V a^4} \int \mathrm{d}^3\mathbf{k} \sum_{i,j} \Bigg[& \left| \int_{\tau_i}^{\tau_f} \mathrm{d}\tau \cos(k\tau) a(\tau) T_{ij}^{TT}(\tau, \mathbf{k}) \right|^2 \\ & + \left| \int_{\tau_i}^{\tau_f} \mathrm{d}\tau \sin(k\tau) a(\tau) T_{ij}^{TT}(\tau, \mathbf{k}) \right|^2 \Bigg] . \end{aligned} \tag{5.67}$$

Since $\mathrm{d}^3\mathbf{k} = k^3 \mathrm{d}(\ln k) \mathrm{d}\Omega_k$, where Ω_k is the solid angle in Fourier space, it will be numerically convenient to consider instead the energy density per logarithmic k-interval [123]

$$\left(\frac{\mathrm{d}\rho_{\mathrm{gw}}}{\mathrm{d}\ln k} \right)_{\tau > \tau_f} = \frac{S_k(\tau_f)}{a^4(\tau)} , \tag{5.68}$$

with

$$\begin{aligned} S_k(\tau_f) = \frac{4\pi G k^3}{V} \int \mathrm{d}\Omega_k \sum_{i,j} \Bigg[& \left| \int_{\tau_i}^{\tau_f} \mathrm{d}\tau \cos(k\tau) a(\tau) T_{ij}^{TT}(\tau, \mathbf{k}) \right|^2 \\ & + \left| \int_{\tau_i}^{\tau_f} \mathrm{d}\tau \sin(k\tau) a(\tau) T_{ij}^{TT}(\tau, \mathbf{k}) \right|^2 \Bigg] . \end{aligned} \tag{5.69}$$

This quantity is independent of the subsequent cosmological evolution and is thus suited to be computed in an N-body simulation. Afterwards, $S_k(\tau_f)$ can be used to obtain the fractional contribution of the gravitational wave spectrum per logarithmic k-interval to the critical density [123],

$$\Omega_{\mathrm{gw}}(k) = \frac{1}{\rho_c}\frac{\mathrm{d}\rho_{\mathrm{gw}}}{\mathrm{d}\ln k}\,. \tag{5.70}$$

This yields the gravitational wave spectrum at the final time of the simulations. However, we are interested in the spectrum at the present time which requires taking into account the subsequent cosmological evolution.

5.5.2 Spectrum at the Present Time

In order to compute the gravitational wave spectrum at the present time, the comoving wave numbers k need to be converted to physical frequencies and the numerically obtained spectrum has to be redshifted. Denoting the scale factor at the end of the N-body simulations as a_f, we thus need to find an expression for a_f/a_0 which depends on the evolution of the equation of state parameter. Eventually, the inflaton decays and thermal equilibrium is established at temperature T_{reh}. At this time the Hubble parameter is (cf. Eq. (1.54))

$$H_{\mathrm{reh}}^2 = \frac{\rho_{\mathrm{reh}}}{3M_{\mathrm{Pl}}^2} = \frac{g_*\pi^2 T_{\mathrm{reh}}^4}{90 M_{\mathrm{Pl}}^2}\,. \tag{5.71}$$

Since $g_* a^3 T^3 = \mathrm{const}$ at thermal equilibrium, the expansion factor from T_{reh} to $T_0 = 2.7\,\mathrm{K} = 2.3267 \times 10^{-4}\,\mathrm{eV}$ is [120]

$$\frac{a_{\mathrm{reh}}}{a_0} = \left(\frac{g_0}{g_*}\right)^{1/3}\frac{T_0}{T_{\mathrm{reh}}} = \frac{g_0^{1/3}}{g_*^{1/12}}\left(\frac{\pi^2}{90}\right)^{1/4}\frac{T_0}{(M_{\mathrm{Pl}}H_{\mathrm{reh}})^{1/2}}\,, \tag{5.72}$$

where Eq. (5.71) was used to replace T_{reh}. In the time interval $a_f < a < a_{\mathrm{reh}}$ the Universe could be in principle either matter- or radiation-dominated. The Hubble parameter evolves as $H \sim a^{-\alpha}$ with $\alpha = 2$ for radiation- and $\alpha = 3/2$ for matter-domination such that at thermalisation $H_{\mathrm{reh}} = H_f(a_f/a_{\mathrm{reh}})^{\alpha}$. Taking this into account, the expansion factor from a_f until a_0 can be expressed as

$$\frac{a_f}{a_0} = \frac{a_f}{a_{\mathrm{reh}}}\frac{a_{\mathrm{reh}}}{a_0} = \left(\frac{g_0^{1/3}}{g_*^{1/12}}\right)\left(\frac{\pi^2}{90}\right)^{1/4}\frac{T_0}{(M_{\mathrm{Pl}}H_f)^{1/2}}\left(\frac{a_f}{a_{\mathrm{reh}}}\right)^{1-\alpha/2}\,. \tag{5.73}$$

Therefore, if the matter-dominated epoch continues after the end of the N-body simulations an additional contribution $(a_f/a_{\mathrm{reh}})^{1/4}$ has to be taken into account when computing the expected gravitational wave spectrum at the present time. Using Eq. (5.73), the wave numbers today are $k_0 = k_f a_f/a_0$ and the corresponding physical frequencies are

$f = k_0/(2\pi)$. The spectrum of the gravitational wave energy density at the present time is thus

$$\Omega_{\mathrm{gw}}(t_0, k) = \frac{1}{\rho_{c,0}} S_k(\tau_f) \left(\frac{a_f}{a_0}\right)^4 . \tag{5.74}$$

with a_f/a_0 given by Eq. (5.73).

5.5.3 N-body Simulations

We use the N-body solver of AxioNyx to evolve the inflaton field and to compute the quantity $S_k(\tau_f)$ defined in Eq. (5.69) numerically. Aiming to evolve the simulation from $\mathcal{N} = 16$ until $\mathcal{N} = 25$ e-folds after the end of inflation, we choose a length unit of $l_u = H_{\mathrm{end}}^{-1} \exp(25) = 2.25 \times 10^{-18}$ m and left both the mass unit $m_u = 10^{-10}$ g and the value of the gravitational constant $G = 10^{-10}\, l_u^3/(m_u t_u^2)$ unchanged. The corresponding time unit is then $t_u = 1.3 \times 10^{-20}$ s so that the Hubble parameter 25 e-folds after inflation is $H_{25} = 6.49\, t_u^{-1}$ in this unit system and the mean density is $\rho_{25} = 5.02 \times 10^{10}\, m_u/l_u^3$. We take a comoving box size of $L = 1200\, l_u$ with 512^3 particles to ensure that the peak of the initial power spectrum in Fig. 5.1 is still resolved while the turnover to higher k is not sampled anymore to avoid the formation of spurious halos.

The crucial part is the calculation of the stress-energy tensor T_{ij} and the extraction of its transverse traceless part in Fourier space. After the end of inflation, the inflaton oscillates at the bottom of its potential and the pressure vanishes on average, thus it is justified to approximate T_{ij} as a perfect fluid with vanishing pressure [128],

$$T_{ij} = \rho \mathbf{v}_i \mathbf{v}_j . \tag{5.75}$$

Here, ρ is the energy density in the rest-frame of the fluid and $\mathbf{v}$ the velocity relative to the rest-frame. The matter density field and the velocity fields can be directly obtained from the particle information in AxioNyx which enables us to compute T_{ij} at each time step. Each component of the stress-energy tensor is transformed to Fourier space and applying the projection operator $\mathcal{O}_{ijlm}(\mathbf{k})$ yields T_{ij}^{TT} in the next step. This requires the specification along which direction in Fourier space the projection is performed. Similar to Ref. [123], we consider the six different diagonal directions $1/\sqrt{2}[(1,1,0), (1,0,1), (0,1,1), (-1,1,0), (-1,0,1), (0,-1,1)]$. Subsequently, the two time integrals in Eq. (5.69) are summed up in each time step and S_k is calculated along each considered direction. Assuming that thermalisation is reached immediately after the end of the N-body simulations at $\mathcal{N} = 25$ we eventually use Eq. (5.74) to compute the gravitational wave spectrum $\Omega_{\mathrm{gw},0}$ at the present time. This is found to be independent of the different $\mathbf{k}$-directions in agreement with the spectrum obtained from preheating

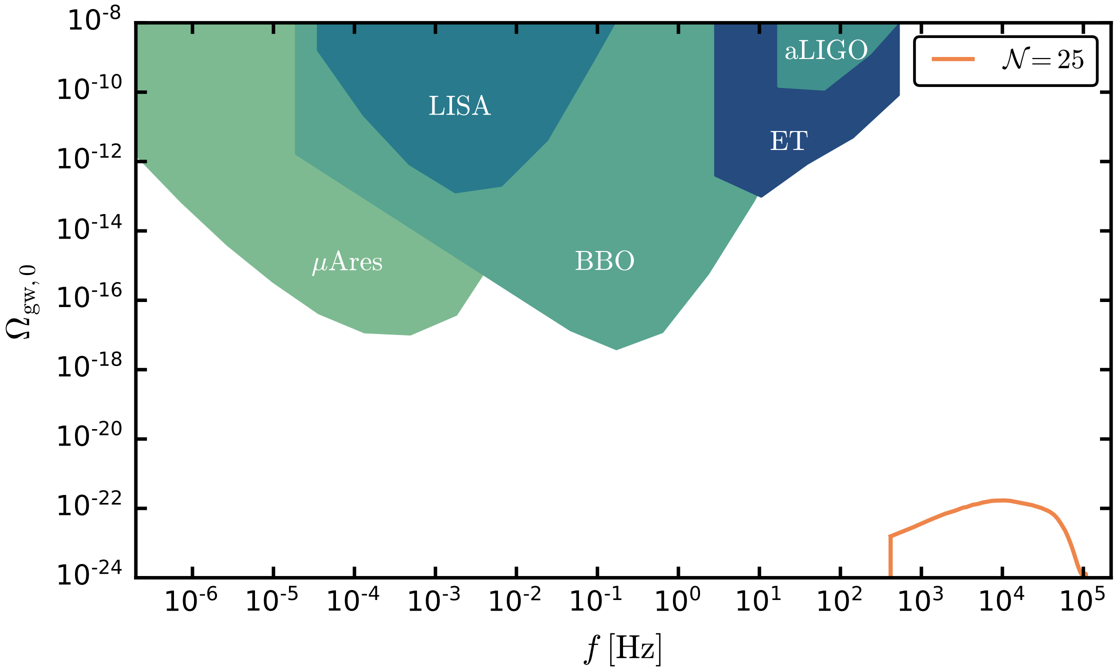

Figure 5.14 | Numerically obtained SGWB $\mathcal{N} = 25$ e-folds after the end of inflation extrapolated to present time with Eq. (5.74). We assumed instantaneous thermalisation at $\mathcal{N} = 25$ which corresponds to a reheating temperature of $T_{\mathrm{reh}} = 1.6 \times 10^7$ GeV (cf. Eq. (5.1)). The sensitivity curves on the energy density of gravitational waves for the experiments LISA [220], BBO [223], advanced LIGO [226, 227], μAres [415] and ET [416] are shown for comparison. The data of the experimental limits were taken from Ref. [417] (see also https://github.com/pcampeti/SGWBProbe).

simulations in Ref. [123]. The numerically obtained SGWB is shown in Fig. 5.14 together with the parameter space which is predicted to be visible by a range of experiments. Evidently, the signal is not within reach of these observations. A detailed analysis and discussion of the spectrum can be found in Ref. [414]. Note that we computed the SGWB for a specific choice of input parameters and under the assumption that instantaneous reheating occurs at the end of our simulations which corresponds to a reheating temperature of $T_{\mathrm{rh}} = 1.6 \times 10^7$ GeV. For reheating temperatures as low as $T_{\mathrm{rh}} \sim$ MeV the era of gravitational structure formation will continue for several e-folds. This leads to a strongly increased gravitational wave signal that is additionally shifted to smaller frequencies. It might thus be possible to reach the experimental sensitivity curves shown in Fig. 5.14. Furthermore, the first nonlinear inflaton structures will start to collapse at considerably earlier times if, for example, the amplitude of the initial power spectrum is increased. Similarly, this results in an enhanced SGWB.

Apart from the dependence of the computed spectrum on the initial power spectrum and the reheating temperature, it should be noted that the spatial extent and the duration of the N-body simulations are highly limited. Larger $\mathcal{N}$ can only be reached for larger box sizes at the cost of not being able to resolve the structures on scales of the peak of the initial power spectrum when the particle number is not increased accordingly. To be independent of numerical limitations, it is therefore desirable to find a semi-analytical description of the SGWB in order to extrapolate it to later times and to lower frequencies. This was achieved in Ref. [414] where it was discovered that the numerically obtained SGWB is well described by semi-analytical estimates that are based on the collapse and the subsequent tidal evolution of inflaton halos.

Additional contributions on the SGWB that our simulations cannot take into account are the formation of inflaton stars. Since they reach considerably larger overdensities than their host halos, one can also expect that mergers of inflaton stars leave a characteristic imprint on the SGWB. Another source of gravitational waves originates from the potential collapse of inflaton halos or inflaton stars into PBHs which would be an interesting area for future studies.

CHAPTER 6

Conclusions

The work presented in this thesis focused on gravitational structure formation with nonrelativistic scalar fields in two different cosmological scenarios. We considered the gravitational collapse of primordial axion density perturbations into axion miniclusters, their subsequent evolution, and the gravitational fragmentation of the inflaton field during an extended matter-dominated epoch following inflation. There exists a strong analogy between the nonlinear dynamics of the very early Universe and structure formation with axion-like dark matter. This makes it possible to adopt the same numerical methods to explore the rich phenomenology of gravitationally-bound structures in both scenarios employing large simulations.

Our simulation results provide the first insights into the statistics and structure of both axion miniclusters and gravitationally-collapsed inflaton halos in the post-inflationary Universe. Furthermore, our high-resolution simulations show for the first time the formation of inflaton stars in the very early Universe. While the distribution of axion miniclusters within the Milky Way is highly relevant for axion detection experiments, the nonlinear inflaton structures decay into other forms of matter and radiation during reheating. Thus, they do not leave a direct imprint on the Universe after thermalisation. However, the gravitational collapse of the inflaton field in the post-inflationary era enables the production of primordial black holes and additionally generates a stochastic gravitational wave background that might be observable in the future.

To strengthen the understanding of axion structure formation and to extract observational signatures from the post-inflationary Universe, future investigations will rely heavily on numerical simulations. Nevertheless, more advanced models need to be developed to determine, for example, the distribution of axion miniclusters within the Milky Way at the present time and the impact of gravitationally-bound inflaton structures on the dynamics of reheating. The simulation results presented in this thesis provide an important starting point for gaining further insight into both considered scenarios. In the following, the main findings of the performed simulations are summarised and we address a few interesting steps for prospective studies.

6.1 Summary of Results

Based on N-body simulations with the greatest level of spatial resolution and the largest physical box size to date, numerical results on the gravitational collapse of axion density perturbations into axion miniclusters were discussed in Section 4.3. Starting from realistic initial conditions that take into account the production of axion dark matter from the decay of topological defects, the N-body solver GADGET-3 was used to gravitationally evolve the axion field from an initial redshift of $z = 10^6$ to $z = 99$. At the final redshift, perturbations on the length scale of the size $L = 0.846\,\mathrm{pc}$ of the simulation box have become nonlinear and the simulations were terminated. Confirming theoretical expectations, the first axion miniclusters form already in the radiation-dominated epoch with masses up to $10^{-11}\,M_\odot$. After matter-radiation equality, this early distribution of miniclusters merges into larger axion minicluster halos reaching masses of $10^{-9}\,M_\odot$. At $z = 99$ the fraction of axions bound in miniclusters is roughly 75% and their mass distribution is described by a nearly scale-invariant mass function with an overall slope of $\alpha \simeq -0.7$. It is expected from Press-Schechter theory that the minicluster halo mass function scales as $M^{-0.5}$ for high masses. However, the statistics of the high-mass minicluster halos in the simulation volume is not sufficient to verify this prediction. We observed that large axion minicluster halos have a rich substructure and that the mass distribution of these sub-miniclusters follows a scaling relation similar to the slope of minicluster halo mass function. Furthermore, an analysis of the radial density profiles of the most massive axion minicluster halos revealed that they are NFW-like. The scale radius of the lower-mass ones could not be properly resolved but their density profiles largely agree with the slope $\rho \sim r^{-3}$ of an NFW profile at large r.

To study the dynamics of the non-resonant inflaton field in the post-inflationary matter-dominated era considering only gravitational interactions among the inflaton field, the cosmology code NYX was adapted to perform N-body simulations of the gravitational fragmentation of the inflaton field (see Section 5.3). With a final physical box size of only $\sim 10^{-18}\,\mathrm{m}$, they are presumably the largest simulations of the smallest part of the Universe that have ever been carried out. Evolving the inflaton field from 14 to 20 e-folds after the end of inflation, we observed its collapse into gravitationally-bound inflaton halos. Forming roughly $10^{-24}\,\mathrm{s}$ after the end of inflation, they have typical masses of only a few grams and radii of the order of 10^{-20} m. We found that their mass distribution can be well approximated with Press-Schechter methods. This allows for the extrapolation of the inflaton halo mass function to even later times in the post-inflationary epoch. Furthermore, the inflaton density field reaches overdensities close to 10^5 and the radial density profiles of sufficiently resolved inflaton halos are NFW-like, as expected from standard cold dark matter N-body simulations.

As is known from axion-like or fuzzy dark matter, the wavelike behaviour of a nonrelativistic scalar field on scales comparable to the de Broglie wavelength leads to the occurrence of interference patterns along filaments and in collapsed halos. Another prominent and fascinating feature is the formation of a solitonic core, often also denoted as boson star, in the centre of a collapsing halo. The parallels between structure formation with axion-like dark matter and with the nonrelativistic inflaton in the matter-dominated epoch succeeding inflation thus suggest the existence of inflaton stars in the very early Universe. To confirm this, we made use of a hybrid approach that has been used before in the context of fuzzy dark matter simulations. This method combines an N-body scheme on large scales with a finite difference solver on small scales to properly resolve the wavelike interior structure of inflaton halos. Using the code AxioNyx enabled us to extend the previous N-body simulations to much smaller length scales and we indeed found that inflaton stars form in the centre of inflaton halos (see Section 5.4). Based on the previously obtained inflaton halo mass function in Section 5.3.1 and the Press-Schechter formalism we computed the mass distribution of inflaton stars and evolved the inflaton star mass function to later times. Already 29 e-folds after inflation, the first inflaton stars cross the mass limit beyond which they are expected to become gravitationally unstable. This suggests that the gravitational collapse of inflaton stars may lead to a population of primordial black holes prior to thermalisation.

In addition to this, the gravitational fragmentation of the inflaton field leads to the production of gravitational waves and the generation of a stochastic gravitational wave background. So far, this gravitational wave spectrum has only been estimated analytically. Adapting the N-body solver of AxioNyx to include the computation of the gravitational wave spectrum, we obtained first preliminary numerical results in Section 5.5. The generated spectrum was extrapolated to the present time and reaches an amplitude of $\Omega_{\mathrm{gw},0} \sim 10^{-22}$. It is located at frequencies of $\mathcal{O}(\mathrm{kHz})$ and is not within reach of the sensitivity curves of existing and proposed experiments if reheating takes place 25 e-folds after the end of inflation. However, the gravitational wave signal will be increased and shifted to smaller frequencies for lower reheating temperatures and might reach the parameter space that is accessible to detectors. Note that we computed the gravitational wave background for a specific inflationary model. The initial spectrum of density perturbations in other models may differ significantly from the one assumed in Section 5.5. As a consequence, nonlinear structures might form at earlier times in certain scenarios leading potentially to an enhanced gravitational wave signal.

6.2 Outlook

Several possibilities for future studies arise from the results of this thesis. As mentioned in Section 4.3.4, the N-body simulations of axion minicluster formation were limited by spatial resolution and need to be complemented by follow-up simulations to explore the morphology of lower-mass minicluster halos. This should also include an extensive analysis of the minicluster halo density profiles as a function of redshift to verify that they converge towards an NFW shape for decreasing redshift. Additionally, it is of particular interest to understand the evolution of early collapsed miniclusters. They exhibit high concentrations and a large number of them should survive merging processes and persist as substructures in large axion minicluster halos.

Revealing the history of individual miniclusters requires the construction of merger trees as already done with a peak-patch code in Refs. [240–242]. Based on the N-body simulations from Section 4.3 it was shown that the survival probability is larger for miniclusters with higher concentration [241, 242]. Being able to accurately resolve those miniclusters is highly relevant for a precise estimation of their capability to produce observable microlensing events [241, 242]. In a first step, N-body simulations with higher spatial resolution might be sufficient to provide new insights but ultimately, only hybrid simulations as in Section 5.4 will be able to unveil the detailed structure of miniclusters relevant for microlensing. In particular, this will include the possible formation of axion stars in the centre of small-scale miniclusters which crucially affects the expected microlensing signal. Fortunately, AxioNyx already contains all the necessary ingredients to conduct these types of challenging simulations.

Currently, efforts are underway to generate axion initial conditions similar to the ones in Section 4.2 but with the help of adaptive mesh refinement. This should permit the creation of much larger box sizes for subsequent N-body simulations of axion structure formation. Hence, they could be evolved to redshifts smaller than $z = 99$ which will clarify the scaling relation of the minicluster halo mass function at high masses (see Section 4.3.2). Beyond that, running simulations to later times would reduce uncertainties in the estimation of the present-day axion dark matter distribution within the Milky Way. It must be noted that tidal interactions of axion miniclusters with stars have eventually to be taken into account for a more precise prediction.

Further follow-up work is also on hand in the context of structure formation in the matter-dominated era following inflation. For a start, a deeper understanding of the stochastic gravitational wave background computed in Section 5.5 needs to be acquired. It is necessary to identify the dominant processes that are responsible for the evolution and the overall shape of the spectrum. This could be used to extrapolate the gravitational wave spectrum to later times. Furthermore, the inflationary model parameters such as the inflaton mass and the energy scale at the end of inflation should be varied to explore the possible gravitational wave frequency range in different scenarios.

Exploring the possibility of primordial black hole formation in the post-inflationary epoch is another exciting avenue for future research. Instead of running N-body simulations, a convenient approach is to adopt the computationally efficient peak-patch method (see Section 2.4.4) to build merger trees of inflaton halos. Similarly to their central inflaton stars, the inflaton halos can become gravitationally unstable, potentially leading to the production of primordial black holes (see Section 5.4.2). The merger trees can be used to keep track of gravitationally unstable inflaton halos to estimate the population of primordial black holes. Another related but presumably highly demanding task would be to initialise simulations capable of including relativistic effects with a solitonic core close to the gravitational instability to see whether it will indeed collapse into a black hole or disperse.

So far we have assumed that inflaton self-interactions can be neglected and that there is thus no preheating instability driving the formation of oscillons. Such a resonant phase would result in a strongly inhomogeneous inflaton field with large overdensities. It would be interesting to study their subsequent gravitational collapse using numerical simulations similar to those of Section 5.3 and Section 5.4 and to compute the associated gravitational wave background in this scenario. Compared to the results in Section 5.5, one can expect a gravitational wave spectrum with a significantly increased amplitude. Independently, combined simulations of preheating and a subsequent epoch of gravitational structure formation will presumably reveal new intriguing phenomena that can occur in the very early Universe prior to thermalisation. Evidently, exciting and promising future opportunities for studies are ahead of us.

Appendix A

Aspects of Cosmological Perturbation Theory

In this appendix, important concepts of cosmological perturbation theory such as the SVT-decomposition and gauge transformations are summarised. They are used in the derivation of the Einstein equations for scalar perturbations in the conformal Newtonian gauge. This chapter thus provides useful background for Sections 2.1 and 2.2, and for Appendix B.

A.1 SVT-Decomposition

Perturbations in the metric and in the stress-energy tensor are related to each other via the Einstein equations which leads to highly complicated equations of motion. Exploiting the rotational symmetry of the flat FLRW background metric it is possible to decompose the perturbations into scalar, vector and tensor components. Then, these contributions are not coupled by the Einstein equations anymore which allows us to treat the equations of motion for scalar, vector and tensor components separately from each other.

The SVT-decomposition can be done both in Fourier and in real space. Here, we summarise the results from Ref. [211] for the decomposition of a vector field and a tensor field in real space. In principle, any vector field **B** can be divided into a part with vanishing curl and another one with vanishing divergence, i.e.

$$\mathbf{B} = \mathbf{B}^S + \mathbf{B}^V \,, \quad \text{with} \quad \nabla \times \mathbf{B}^S = 0 \quad \text{and} \quad \nabla \cdot \mathbf{B}^V = 0 \,. \tag{A.1}$$

Thus, $\mathbf{B}^S$ can be expressed as a gradient of a scalar field B and therefore

$$B_i = -\partial_i B + B_i^V \,, \quad \text{with} \quad \delta_{ij}\partial_j B_i^V = 0 \,. \tag{A.2}$$

In a similar manner, a symmetric traceless tensor field E_{ij} can be decomposed into scalar, vector and tensor parts

$$E_{ij} = E^S_{ij} + E^V_{ij} + E^T_{ij}\,, \tag{A.3}$$

where

$$E^S_{ij} = (\partial_i\partial_j - \frac{1}{3}\delta_{ij}\nabla^2)E\,, \tag{A.4}$$

$$E^V_{ij} = -\frac{1}{2}\left(\partial_j E_i + \partial_i E_j\right)\,, \quad \text{with} \quad \delta_{ij}\partial_j E_i = \nabla \cdot \mathbf{E} = 0\,. \tag{A.5}$$

Thus, E^S_{ij} is symmetric and traceless while E^V_{ij} is symmetric, traceless and divergenceless. Furthermore, the tensor E^T_{ij} is transverse and traceless, i.e.

$$\delta_{ik}\partial_k E^T_{ij} = 0\,, \quad \text{and} \quad \delta_{ij}E^T_{ij} = 0\,. \tag{A.6}$$

Since only scalar perturbations are responsible for structure formation in the Universe, Eqs. (A.2) and (A.4) are used several times in this thesis to consider only the scalar contribution of any vector or tensor perturbation. An analysis of the decomposition in Fourier space provides further insight. For example, it allows the decomposition theorem to be proven that scalar, vector and tensor perturbations evolve independently from each other in an FLRW universe [211].

A.2 Gauge Transformations

A gauge transformation is a coordinate transformation between different coordinate systems x, $\tilde{x}$ that leaves the perturbed spacetime $\delta g_{\mu\nu}$ very small. In general, a gauge transformation can be written as [53]

$$x^\mu \longrightarrow \tilde{x}^\mu = x^\mu + \xi^\mu(x)\,, \tag{A.7}$$

where $\xi^\mu(x) = (\xi^0, \xi^i)$ are small functions of space and time. As mentioned in Section 2.1, cosmological perturbations are generally coordinate-dependent. Thus, transformation rules are required when changing the coordinate system from x to $\tilde{x}$. In the following, we collect the transformation rules for scalar, vector and tensor perturbations.

A scalar quantity $s(x)$ does not change under a coordinate transformation, i.e. $\tilde{s}(\tilde{x}) = s(x)$. Thus, one can write

$$\tilde{s}(\tilde{x}) = s(x) = s(\tilde{x} - \xi) = s(\tilde{x}) - \partial_\mu s(\tilde{x})\xi^\mu(\tilde{x})\,. \tag{A.8}$$

Using that a generic scalar perturbation can be defined as $\delta s(\tilde{x}) = s(\tilde{x}) - \bar{s}(\tilde{x})$ and $\delta\tilde{s}(\tilde{x}) = \tilde{s}(\tilde{x}) - \bar{s}(\tilde{x})$, and keeping only terms up to linear order in ξ^μ, one finds that scalar perturbations transform as [53]

$$\delta\tilde{s}(\tilde{x}) = \delta s(\tilde{x}) - \partial_\mu \bar{s}(\tilde{x})\xi^\mu(\tilde{x})\,. \tag{A.9}$$

A vector v_μ transforms as [211]

$$\tilde{v}_\mu(\tilde{x}) = \frac{\partial x^\alpha}{\partial \tilde{x}^\mu} v_\alpha(x) \quad \text{with} \quad \frac{\partial x^\alpha}{\partial \tilde{x}^\mu} = \delta^\alpha_\mu - \partial^\alpha \xi_\mu(\tilde{x})\,, \tag{A.10}$$

and one obtains

$$\tilde{v}_\mu(\tilde{x}) = \frac{\partial x^\alpha}{\partial \tilde{x}^\mu} v_\alpha(\tilde{x} - \xi) = v_\mu(\tilde{x}) - \partial_\beta v_\mu(\tilde{x})\xi^\beta(\tilde{x}) - v_\alpha(\tilde{x})\partial_\mu \xi^\alpha(\tilde{x})\,. \tag{A.11}$$

Since $\delta v_\mu(\tilde{x}) = v_\mu(\tilde{x}) - \bar{v}_\mu(\tilde{x})$ and $\delta\tilde{v}_\mu(\tilde{x}) = \tilde{v}_\mu(\tilde{x}) - \bar{v}_\mu(\tilde{x})$, one finds the transformation rule for vector perturbations,

$$\delta\tilde{v}_\mu(\tilde{x}) = \delta v_\mu(\tilde{x}) - \partial_\beta \bar{v}_\mu(\tilde{x})\xi^\beta(\tilde{x}) - \bar{v}_\alpha(\tilde{x})\partial_\mu \xi^\alpha(\tilde{x})\,, \tag{A.12}$$

when only terms linear in δv_μ and ξ^μ are considered. In a similar manner, one can derive the transformation behaviour for tensor perturbations. Using that the tensors $t_{\mu\nu}$ and t^μ_ν transform as

$$\tilde{t}_{\mu\nu}(\tilde{x}) = \frac{\partial x^\alpha}{\partial \tilde{x}^\mu}\frac{\partial x^\beta}{\partial \tilde{x}^\nu} t_{\mu\nu}(\tilde{x}) \quad \text{and} \quad \tilde{t}^\mu_\nu(\tilde{x}) = \frac{\partial \tilde{x}^\mu}{\partial x^\alpha}\frac{\partial x^\beta}{\partial \tilde{x}^\nu} t^\mu_\nu(\tilde{x})\,, \tag{A.13}$$

respectively, the gauge transformation laws for the tensor perturbations are [53]

$$\delta\tilde{t}_{\mu\nu}(\tilde{x}) = \delta t_{\mu\nu}(\tilde{x}) - \partial_\beta \bar{t}_{\mu\nu}(\tilde{x})\xi^\beta(\tilde{x}) - \bar{t}_{\mu\beta}(\tilde{x})\partial_\nu \xi^\beta(\tilde{x}) - \bar{t}_{\alpha\nu}\partial_\mu \xi^\alpha(\tilde{x})\,, \tag{A.14}$$

$$\delta\tilde{t}^\mu{}_\nu(\tilde{x}) = \delta t^\mu{}_\nu(\tilde{x}) - \partial_\beta \bar{t}^\mu{}_\nu(\tilde{x})\xi^\beta(\tilde{x}) - \bar{t}^\mu{}_\beta(\tilde{x})\partial_\nu \xi^\beta(\tilde{x}) + \bar{t}^\alpha{}_\nu \partial_\alpha \xi^\mu(\tilde{x})\,. \tag{A.15}$$

A.2.1 Gauge Transformations of Metric Perturbations

We can now directly apply the transformation rule in Eq. (A.14) to the metric tensor $g_{\mu\nu} = \bar{g}_{\mu\nu} + \delta g_{\mu\nu}$. Using that the background metric $\bar{g}_{\mu\nu} = a^2\eta_{\mu\nu}$, where $\eta_{\mu\nu}$ denotes the Minkowski metric, only depends on time the spatial derivatives in the second term of Eq. (A.14) vanish and one obtains [212]

$$\delta\tilde{g}_{\mu\nu} = \delta g_{\mu\nu} - a^2\left(2\mathcal{H}\eta_{\mu\nu}\xi^0 + \eta_{\mu\beta}\partial_\nu \xi^\beta + \eta_{\alpha\nu}\partial_\mu \xi^\alpha\right)\,. \tag{A.16}$$

Writing the perturbed part of the metric as (cf. Eq. (2.3))

$$[\delta g_{\mu\nu}] = a^2 \begin{bmatrix} -2A & -B_i \\ -B_i & -2D\delta_{ij} + 2E_{ij} \end{bmatrix}\,,$$

and considering the components of $\delta\tilde{g}_{\mu\nu}$ individually, one can derive the transformation rules for the metric perturbations A, D, B_i and E_{ij}. Exploiting the invariance of the spacetime interval, $\mathrm{d}s^2 = g_{\mu\nu}\mathrm{d}x^\mu\,\mathrm{d}x^\nu = \tilde{g}_{\mu\nu}\mathrm{d}\tilde{x}^\mu\,\mathrm{d}\tilde{x}^\nu$, one finds that [212]

$$\delta\tilde{g}_{00} = -2a^2\tilde{A} = \delta g_{00} = -2a^2\left(A - \xi^{0\prime} - \mathcal{H}\xi^0\right)\,, \tag{A.17}$$

and therefore

$$\tilde{A} = A - \xi^{0\prime} - \mathcal{H}\xi^0\,. \tag{A.18}$$

Similarly, studying δg_{0i} yields [212]

$$\tilde{B}_i = B_i + \xi^{i\prime} - \partial_i\xi^0\,, \tag{A.19}$$

and δg_{ij} gives that

$$\tilde{D} = D + \frac{1}{3}\partial_k\xi^k + \mathcal{H}\xi^0\,, \tag{A.20}$$

$$\tilde{E}_{ij} = E_{ij} - \frac{1}{2}\left(\partial_j\xi^i + \partial_i\xi^j\right) + \frac{1}{3}\delta_{ij}\partial_k\xi^k\,. \tag{A.21}$$

Scalar Perturbations

Considering now only scalar perturbations, we are interested in how the scalar perturbations A, B, D and E that appear in the metric given by Eq. (2.4) behave under an arbitrary gauge transformation $\xi^\mu = (\xi^0, \xi^i)$. Decomposing ξ^i in analogy to the shift vector B_i in Eq. (A.2) into a scalar part and a vector part, i.e.

$$\xi^i = -\delta^{ij}\partial_j\xi + \xi^i_V\,, \tag{A.22}$$

and keeping only the scalar contribution ξ, the gauge transformation from Eq. (A.7) reads

$$\tilde{\tau} = \tau + \xi^0\,, \tag{A.23}$$

$$\tilde{x}^i = x^i - \delta^{ij}\partial_j\xi\,. \tag{A.24}$$

Applying this to the gauge transformation rules of A, B, D and E in Eqs. (A.18) to (A.21), we directly obtain [212]

$$\tilde{A} = A - \xi^{0\prime} - \mathcal{H}\xi^0\,, \tag{A.25}$$

$$\tilde{B} = B + \xi' + \xi^0\,, \tag{A.26}$$

$$\tilde{D} = D - \frac{1}{3}\nabla^2\xi + \mathcal{H}\xi^0\,, \tag{A.27}$$

$$\tilde{E} = E + \xi\,. \tag{A.28}$$

A.2.2 Gauge Transformations of Matter Perturbations

Similar to metric perturbations, matter perturbations are also gauge-dependent. Applying the transformation rule in Eq. (A.15) to the perturbed stress-energy tensor in Eqs. (2.11), (2.13) and (2.14), one finds that [212]

$$\delta\tilde{\rho} = \delta\rho - \bar{\rho}'\xi^0 \,, \tag{A.29}$$

$$\delta\tilde{p} = \delta p - \bar{p}'\xi^0 \,, \tag{A.30}$$

$$\tilde{v}_i = v_i + \xi^{i\,\prime} \,, \tag{A.31}$$

$$\tilde{\Sigma}^i{}_j = \bar{p}\,\tilde{\Pi}^i{}_j = \bar{p}\,\Pi^i{}_j = \Sigma^i{}_j \,. \tag{A.32}$$

Note that the anisotropic stress is gauge-invariant. Considering only the scalar component, we have $v_i = -\partial_i v$ (see Eq. (A.2)) and $\xi^i = -\delta^{ij}\partial_j\xi$ (see Eq. (A.22)). Thus, we immediately see that the scalar perturbations transform as

$$\tilde{v} = v + \xi' \,, \tag{A.33}$$

$$\tilde{\Pi} = \Pi \,. \tag{A.34}$$

A.3 Particular Gauges

In principle, one is free to use any gauge since the physical quantities are gauge-invariant anyway. Each gauge has certain benefits, so a wise gauge choice in a suited situation can simplify the computations enormously. In the following, we introduce the conformal Newtonian gauge, the comoving gauge and the spatially flat gauge as they are used in Chapters 2 and 5. Further details can be found for example in Refs. [52, 211, 212].

Conformal Newtonian Gauge

The conformal Newtonian or longitudinal gauge is defined by setting the scalar metric perturbations in Eq. (2.4) to zero, i.e. $B^N = E^N = 0$. As can be seen from the gauge transformations rules in Eqs. (A.25) to (A.28), this requires that $\xi = -E$ and $\xi^0 = -B + E'$. Choosing this gauge, the scalar metric perturbations in Eq. (2.4) are given by the gauge-invariant Bardeen potentials (see Eq. (2.8)). This allows the derivation of gauge-invariant equations in the Newtonian gauge. Using Eqs. (A.29), (A.30), (A.33) and (A.34), the scalar perturbations that appear in the stress-energy tensor then read in the Newtonian gauge [52]

$$\delta\rho^N = \delta\rho + \bar{\rho}(B - E')\,, \tag{A.35}$$

$$\delta p^N = \delta p + \bar{p}(B - E')\,, \tag{A.36}$$

$$v^N = v - E\,, \tag{A.37}$$

$$\Pi^N = \Pi\,. \tag{A.38}$$

Comoving Gauge

The comoving gauge is defined by setting the scalar perturbations $v^C = B^C = 0$. From their gauge transformation behaviour given by Eq. (A.33) and Eq. (A.26), respectively, it becomes obvious that the corresponding gauge conditions are $\xi' = -v$ and $\xi^0 = v - B$. Using them, one finds that the curvature perturbation (cf. Eq. (2.5)), which transforms according to Eq. (2.6), is in this gauge given by [212]

$$\psi_{\mathcal{R}}^C = \psi_{\mathcal{R}} + \mathcal{H}(v - B)\,. \tag{A.39}$$

This defines the *comoving* curvature perturbation $\mathcal{R} \equiv \psi_{\mathcal{R}}^C$ which can be expressed in terms of the Bardeen potentials in Eq. (2.7) and is therefore a gauge-invariant quantity. It is of particular interest when discussing inflationary perturbations in Section 2.2. If the universe is filled by a scalar field $\varphi = \bar{\varphi} + \delta\varphi$ (e.g. during inflation), then it is possible to express ξ^0 and thus $\mathcal{R}$ in terms of a scalar field perturbation $\delta\varphi$, as shown in Appendix B.4. The comoving curvature perturbation then is [212]

$$\mathcal{R} = \psi_{\mathcal{R}} + \mathcal{H}\frac{\delta\varphi}{\bar{\varphi}'}\,. \tag{A.40}$$

Spatially Flat Gauge

The spatially flat gauge is defined by setting the curvature perturbation $\psi_{\mathcal{R}} = 0$. According to the transformation rule in Eq. (2.6), this means that $\xi^0 = -\mathcal{H}^{-1}\psi_{\mathcal{R}}$. Importantly, the comoving curvature perturbation in Eq. (A.40) is then directly related to the perturbation of the scalar field,

$$\mathcal{R} = \mathcal{H}\frac{\delta\varphi}{\bar{\varphi}'}\,. \tag{A.41}$$

This is especially useful for inflationary perturbations since then all scalar perturbations can be described by $\delta\varphi$.

A.4 Perturbed Einstein Tensor in Newtonian Gauge

In this section, the perturbed connection coefficients from Eqs. (2.19) to (2.24) are used to compute the scalar perturbations of the Einstein tensor $\delta G^{\mu}{}_{\nu}$ in Newtonian gauge to linear order. Perturbing the Ricci tensor $R_{\mu\nu} = \bar{R}_{\mu\nu} + \delta R_{\mu\nu}$, it can be written as (cf. Eq. (1.2))

$$R_{\mu\nu} = \bar{R}_{\mu\nu} + \partial_\alpha \delta\Gamma^{\alpha}{}_{\nu\mu} - \partial_\nu \delta\Gamma^{\alpha}{}_{\alpha\mu} + \bar{\Gamma}^{\alpha}{}_{\alpha\beta}\delta\Gamma^{\beta}{}_{\nu\mu} + \bar{\Gamma}^{\beta}{}_{\nu\mu}\delta\Gamma^{\alpha}{}_{\alpha\beta} - \bar{\Gamma}^{\alpha}{}_{\nu\beta}\delta\Gamma^{\beta}{}_{\alpha\mu} - \bar{\Gamma}^{\beta}{}_{\alpha\mu}\delta\Gamma^{\alpha}{}_{\nu\beta} \,.$$

Since $R^{\mu}{}_{\nu} = g^{\mu\alpha}R_{\alpha\nu} = (\bar{g}^{\mu\alpha} + \delta g^{\mu\alpha})(\bar{R}_{\alpha\nu} + \delta R_{\alpha\nu}) = \bar{R}^{\mu}{}_{\nu} + \delta g^{\mu\alpha}\bar{R}_{\alpha\nu} + \bar{g}^{\mu\alpha}\delta R_{\alpha\nu}$ an explicit calculation with $g^{\mu\nu}$ given by Eq. (2.8) yields [213]

$$\begin{aligned}
R^{0}{}_{0} &= a^{-2}\left(3\mathcal{H}' - 3\Psi'' - \nabla^2\Phi - 3\mathcal{H}(\Phi' + \Psi') - 6\mathcal{H}'\Phi\right) \,, && \text{(A.42)}\\
R^{i}{}_{0} &= 2a^{-2}\partial_i(\Psi' + \mathcal{H}\Phi) \,, && \text{(A.43)}\\
R^{i}{}_{j} &= a^{-2}\left(\mathcal{H}' + 2\mathcal{H}^2 - \Psi'' + \nabla^2\Psi - \mathcal{H}(\Phi' + 5\Psi') - (2\mathcal{H}' + 4\mathcal{H}^2)\Phi\right)\delta^i_j \\
&\quad + a^{-2}\partial_i\partial_j(\Psi - \Phi) \,. && \text{(A.44)}
\end{aligned}$$

Hence, the perturbed Ricci curvature scalar to linear order is [213]

$$\begin{aligned}
R &= R^{0}{}_{0} + R^{i}{}_{i} \\
&= a^{-2}\left(-6\Psi'' + 2\nabla^2(2\Psi - \Phi) - 6\mathcal{H}(\Phi' + 3\Psi') - 12(\mathcal{H}' + \mathcal{H}^2)\right) + 6a^{-2}(\mathcal{H}' + \mathcal{H}^2) \\
&\quad + 6a^{-2}(\mathcal{H}' + \mathcal{H}^2) \,. && \text{(A.45)}
\end{aligned}$$

Using Eqs. (A.42) to (A.45), one finally obtains the components of the Einstein tensor (cf. Eq. (1.1) for its definition)

$$\begin{aligned}
G^{0}{}_{0} &= a^{-2}\left(-3\mathcal{H}^2 - 2\nabla^2\Psi + 6\mathcal{H}\Psi' + 6\mathcal{H}^2\Phi\right) \,, && \text{(A.46)}\\
G^{i}{}_{0} &= 2a^{-2}\partial_i(\Psi' + \mathcal{H}\Phi) \,, && \text{(A.47)}\\
G^{i}{}_{j} &= a^{-2}\left(-2\mathcal{H}' - \mathcal{H}^2 + 2\Psi'' + \nabla^2(\Phi - \Psi) + \mathcal{H}(2\Phi' + 4\Psi') + (4\mathcal{H}' + 2\mathcal{H}^2)\Phi\right)\delta^i_j \\
&\quad + a^{-2}\partial_i\partial_j(\Psi - \Phi) \,. && \text{(A.48)}
\end{aligned}$$

Appendix B

Scalar Perturbations From Inflation

This appendix provides useful identities and derivations in the context of the scalar inflaton field. Starting with the derivation of some valuable relations used in Section 2.2 and Section 5.1.1, the perturbed Klein-Gordon equation and the perturbed Einstein equations for the inflaton field are obtained. Afterwards, the gauge-invariant comoving curvature perturbation is expressed in terms of the inflaton perturbation which is made use of in Section 5.1.1. Finally, we derive the Mukhanov-Sasaki equation that is relevant for Section 2.2 and Section 5.1.1.

B.1 Useful Identities

In this section, we only consider homogeneous background quantities and collect some expedient expressions. Often computations are simplified when evolution equations are considered in conformal time τ instead of the physical time t. They are related to each other via $\mathrm{d}\tau = \mathrm{d}t/a$ and the Friedmann Eqs. (1.6) and (1.7) in conformal time for a flat universe read

$$\mathcal{H}^2 = \left(\frac{a'}{a}\right)^2 = \frac{8\pi G}{3}\bar{\rho}a^2\,, \quad \mathcal{H}' = -\frac{4\pi G}{3}(\bar{\rho} + 3\bar{p})a^2\,. \tag{B.1}$$

Since $\mathcal{H} = a'/a = aH = \dot{a}$, the derivative of the conformal Hubble parameter is

$$\mathcal{H}' = \frac{a''}{a} - \mathcal{H}^2\,. \tag{B.2}$$

Using the equation of state parameter $w = \bar{p}/\bar{\rho}$, the continuity Eq. (1.8) can be written in conformal time as

$$\bar{\rho}' = -3\mathcal{H}(\bar{\rho} + \bar{p}) = -3\mathcal{H}(1 + w)\bar{\rho}\,. \tag{B.3}$$

Combining the two conformal Friedmann equations, one directly obtains this useful background relation

$$\mathcal{H}' = -\frac{1}{2}(1+3w)\mathcal{H}^2\,, \quad \text{so} \quad w = -\frac{1}{3}\left(1 + 2\frac{\mathcal{H}'}{\mathcal{H}^2}\right)\,. \tag{B.4}$$

Taking the time derivative of $w = \bar{p}/\bar{\rho}$ and using Eq. (B.3) gives

$$w' = \frac{\bar{\rho}'}{\bar{\rho}}(c_s^2 - w) = -3\mathcal{H}(1+w)(c_s^2 - w) \quad \Rightarrow \quad \frac{w'}{1+w} = 3\mathcal{H}(w - c_s^2)\,, \tag{B.5}$$

where c_s^2 denotes the speed of sound $c_s^2 = \bar{p}'/\bar{\rho}'$. Turning now to the homogeneous inflaton field, its energy density and pressure in conformal time are (cf. Eq. (1.26))

$$\bar{\rho} = \frac{1}{2}\frac{\bar{\varphi}'^{\,2}}{a^2} + V(\bar{\varphi}) \quad \text{and} \quad \bar{p} = \frac{1}{2}\frac{\bar{\varphi}'^{\,2}}{a^2} - V(\bar{\varphi})\,. \tag{B.6}$$

Taking their conformal derivatives and applying the conformal Klein-Gordon equation

$$\bar{\varphi}'' + 2\mathcal{H}\bar{\varphi}' + a^2\frac{\partial V(\bar{\varphi})}{\partial\bar{\varphi}} = 0\,, \tag{B.7}$$

the speed of sound is

$$c_s^2 = 1 - \frac{2}{3}\left(\frac{\bar{\varphi}''}{\mathcal{H}\bar{\varphi}'} + 2\right) = -\frac{1}{3\mathcal{H}}\left(\mathcal{H} + 2\frac{\bar{\varphi}''}{\bar{\varphi}'}\right)\,. \tag{B.8}$$

This allows us to write the ratio $\bar{\varphi}''/\bar{\varphi}'$ as

$$\frac{\bar{\varphi}''}{\bar{\varphi}'} = -\frac{1}{2}(3\mathcal{H}c_s^2 + \mathcal{H})\,. \tag{B.9}$$

Furthermore, multiplying the first Friedmann equation in Eq. (B.1) with a factor of 2 and subtracting $4\pi G\bar{\varphi}'^{\,2}$, we find that

$$2\mathcal{H}^2 - 4\pi G\bar{\varphi}'^2 = -\frac{8\pi G}{6}\bar{\varphi}'^2 + \frac{16\pi G}{3}V(\bar{\varphi})a^2\,. \tag{B.10}$$

Using the second Friedmann equation in Eq. (B.1) and Eq. (B.2), we thus obtain the relation

$$\frac{a''}{a} - 2\mathcal{H}^2 = \mathcal{H}' - \mathcal{H}^2 = -4\pi G\bar{\varphi}'^2\,. \tag{B.11}$$

B.2 Perturbed Klein-Gordon Equation

The Klein-Gordon equation for the inflaton field φ with potential $V(\varphi)$ can be written as [46]

$$\partial_\mu\partial^\mu\varphi - \frac{\mathrm{d}V}{\mathrm{d}\varphi} = \frac{1}{\sqrt{-g}}\partial_\mu(\sqrt{-g}\partial^\mu\varphi) - \frac{\mathrm{d}V}{\mathrm{d}\varphi} = 0\,. \tag{B.12}$$

Using the perturbed FLRW metric in Newtonian gauge (see Eq. (2.8)), the metric determinant $\sqrt{-g}$ to linear order in perturbations is

$$\sqrt{-g} = a^4 \left((1+2\Phi)(1-2\Psi)^3\right)^{1/2} = a^4(1+2\Phi-6\Psi)^{1/2} \approx a^4(1+\Phi-3\Psi)\,, \tag{B.13}$$

where in the last expression the Taylor expansion of the square root to linear order was used. Expanding the potential and its derivative $\partial_\varphi V$ to first-order in the field perturbation $\delta\varphi = \varphi - \bar{\varphi}$, they read

$$V(\varphi) = V(\bar{\varphi}+\delta\varphi) = \bar{V} + (\partial_\varphi \bar{V})\delta\varphi\,, \quad \text{and} \quad \partial_\varphi V(\varphi) = \partial_\varphi \bar{V} + (\partial_{\varphi\varphi}\bar{V})\delta\varphi\,, \tag{B.14}$$

respectively, where $V(\bar{\varphi}) = \bar{V}$. Switching now from conformal to cosmological time for convenience, the metric is $g_{\mu\nu} = (-(1+2\Phi), a^2(1-2\Psi), a^2(1-2\Psi), a^2(1-2\Psi))$ or $g^{\mu\nu} = (-1+2\Phi, a^2(1+2\Psi), a^2(1+2\Psi), a^2(1+2\Psi))$. Then, its determinant is $\sqrt{-g} = a^3(1+\Phi-3\Psi)$ and the derivatives that appear in Eq. (B.12) are

$$\begin{aligned}
\partial_0(\sqrt{-g}g^{0\nu}\partial_\nu\varphi) &= (3H\sqrt{-g} + a^3(\dot{\Phi}-3\dot{\Psi}))(-1+2\Phi)\dot{\varphi} + \sqrt{-g}(2\dot{\Phi}\dot{\varphi} + (2\Phi-1)\ddot{\varphi})\,,\\
\partial_i(\sqrt{-g}g^{i\nu}\partial_\nu\varphi) &= -\sqrt{-g}(a^{-2}(1+2\Psi)\nabla^2\varphi)\,.
\end{aligned}$$

Inserting these two expressions together with Eq. (B.14) into Eq. (B.12) and keeping only terms to first-order in perturbations, we obtain

$$-3H\dot{\bar{\varphi}} - 3H\delta\varphi + 6H\Phi\dot{\bar{\varphi}} + (\dot{\Phi}+3\dot{\Psi})\dot{\bar{\varphi}} - \ddot{\bar{\varphi}} - \delta\ddot{\varphi} + 2\Phi\ddot{\bar{\varphi}} + a^{-2}\nabla^2\delta\varphi = \partial_\varphi\bar{V} + \partial_{\varphi\varphi}\bar{V}\,.$$

Subtracting the background Klein-Gordon Eq. (2.42), the perturbation equation of the scalar field to linear order in Newtonian gauge is [52]

$$\delta\ddot{\varphi}^N + 3H\delta\dot{\varphi}^N + 2\Phi\partial_\varphi\bar{V} - a^{-2}\nabla^2\delta\varphi^N - (\dot{\Phi}+3\dot{\Psi})\dot{\bar{\varphi}} + (\partial_{\varphi\varphi}\bar{V})\delta\varphi^N = 0\,. \tag{B.15}$$

Switching back to conformal time gives Eq. (2.44).

B.3 Perturbed Einstein Equation

The stress-energy tensor of a scalar field (see Eq. (1.25)) to linear order in perturbations is [52]

$$\begin{aligned}
T^\mu{}_\nu &= g^{\alpha\mu}\partial_\alpha\bar{\varphi}\partial_\nu\bar{\varphi} + g^{\alpha\mu}\partial_\alpha\bar{\varphi}\partial_\nu\delta\varphi + g^{\alpha\mu}\partial_\alpha\delta\varphi\partial_\nu\bar{\varphi}\\
&\quad - \frac{1}{2}\delta^\mu_\nu\partial_\rho\bar{\varphi}g^{\rho\alpha}\partial_\alpha\bar{\varphi} - \delta^\mu_\nu\partial_\rho\bar{\varphi}g^{\rho\alpha}\partial_\alpha\delta\varphi - \delta^\mu_\nu V(\bar{\varphi}) - \delta^\mu_\nu(\partial_\varphi\bar{V})\delta\varphi\,.
\end{aligned} \tag{B.16}$$

Subtracting the background tensor and choosing the Newtonian gauge, one obtains the linear perturbations [212]

$$\delta T^0_{\ 0} = a^{-2}\Psi\bar{\varphi}'^2 - a^{-2}\bar{\varphi}'\left(\delta\varphi^N\right)' - (\partial_\varphi \bar{V})\delta\varphi^N , \tag{B.17}$$

$$\delta T^i_{\ 0} = a^{-2}\bar{\varphi}'\partial_i\delta\varphi^N , \tag{B.18}$$

$$\delta T^i_{\ j} = \left(a^{-2}\bar{\varphi}'\left(\delta\varphi^N\right)' - a^{-2}\Psi\bar{\varphi}'^2 - (\partial_\varphi \bar{V})\delta\varphi^N\right)\delta^i_j . \tag{B.19}$$

Obviously, $\delta T^i_{\ j}$ has only diagonal components which means that $\delta T^\mu_{\ \nu}$ has no anisotropic stress. According to the Einstein Eq. (2.29) this implies that $\Psi = \Phi$. Inserting Eqs. (B.17) to (B.19) into Eqs. (2.26), (2.30) and (2.31), the perturbed Einstein equations $\delta G^\mu_{\ \nu} = 8\pi G\delta T^\mu_{\ \nu}$ for a scalar field are [212]

$$-\nabla^2 + 3\mathcal{H}\Psi' + 3\mathcal{H}^2\Psi = 4\pi G\left(\Psi\bar{\varphi}'^2 - \bar{\varphi}'\left(\delta\varphi^N\right)' - a^2(\partial_\varphi \bar{V})\delta\varphi^N\right) , \tag{B.20}$$

$$\Psi' + \mathcal{H}\Psi = 4\pi G\bar{\varphi}'\delta\varphi^N , \tag{B.21}$$

$$\Psi'' + 3\mathcal{H}\Psi' + (\mathcal{H}^2 + 2\mathcal{H}')\Psi = -4\pi G\left(\Psi\bar{\varphi}'^2 - \bar{\varphi}'\left(\delta\varphi^N\right)' + a^2(\partial_\varphi \bar{V})\delta\varphi^N\right) . \tag{B.22}$$

B.4 Comoving Curvature Perturbation

The comoving curvature perturbation has its origin in the comoving gauge (see Appendix A.3). It is defined in terms of the curvature perturbation $\psi_{\mathcal{R}}$ and the gauge condition $\xi^0 = v - B$ of the comoving gauge [52],

$$\mathcal{R} = \psi_{\mathcal{R}} + \mathcal{H}\xi^0 = \psi_{\mathcal{R}} + \mathcal{H}(v - B) . \tag{B.23}$$

This quantity is of special interest since it is possible to write it in terms of the Bardeen potentials, thus $\mathcal{R}$ is gauge-invariant (see Section 2.2.2). We now express ξ^0 in terms of the scalar field perturbation $\delta\varphi$. The comoving gauge requires a vanishing velocity perturbation which can be written as (see Eq. (2.13))

$$\partial_i v = \frac{\delta T^i_{\ 0}}{\bar{\rho} + \bar{p}} . \tag{B.24}$$

Using the transformation rule for $\delta T^i_{\ 0}$ (cf. Eq. (A.15)),

$$\delta\tilde{T}^i_{\ 0} = \delta T^i_{\ 0} - (\bar{\rho} + \bar{p})\partial_i\xi^0 . \tag{B.25}$$

and demanding $\delta\tilde{T}^i_{\ 0} = 0$ for the velocity perturbation to vanish, it follows that [52]

$$\partial_i\xi^0 = \frac{\delta T^i_{\ 0}}{\bar{\rho} + \bar{p}} = \frac{\partial_i\delta\varphi}{\bar{\varphi}'} , \tag{B.26}$$

where it was made use of Eqs. (B.6) and (B.18) to express $\bar{\rho}$, $\bar{p}$ and $\delta T^i{}_0$ in terms of $\bar{\varphi}$ and $\delta\varphi$. Consequently, we have $\xi^0 = \delta\varphi/\bar{\varphi}$ and the comoving curvature perturbation is given by Eq. (A.40). In the spatially flat gauge where $\psi_{\mathcal{R}}$ vanishes, it reduces to $\mathcal{R} = \mathcal{H}\delta\varphi/\bar{\varphi}'$ which is particularly useful for computing the matter power spectrum from inflation on subhorizon scales (see Section 5.1.2).

B.5 Derivation of the Mukhanov-Sasaki Equation

In this section, Eq. (2.52) is expressed in terms of the Mukhanov-Sasaki variable $q = \zeta\mathcal{R}$ (see Eq. (2.56)). Making use of the first Friedmann equation in conformal time (see Eq. (B.1)), we find the following expression for the equation of state parameter,

$$1 + w = \frac{2\bar{\varphi}'^2}{\bar{\varphi}'^2 + 2a^2 V(\bar{\varphi})} = \frac{\bar{\varphi}'^2}{3M_{\mathrm{Pl}}^2\mathcal{H}^2}\,. \tag{B.27}$$

Thus, the left-hand side of Eq. (2.52) can be written as

$$\frac{3}{2}(1+w)\mathcal{H}\mathcal{R}' = \frac{\bar{\varphi}'^2}{2M_{\mathrm{Pl}}^2\mathcal{H}}\frac{\mathrm{d}}{\mathrm{d}\tau}\left(\frac{q}{\zeta}\right) = \frac{\bar{\varphi}'}{2M_{\mathrm{Pl}}^2}\frac{\zeta}{a}\frac{\mathrm{d}}{\mathrm{d}\tau}\left(\frac{q}{\zeta}\right) = \nabla^2\Psi\,. \tag{B.28}$$

In the next step, we express the second Einstein Eq. (B.21) in terms of q. From Eq. (B.11) one can see that

$$2\mathcal{H} - \frac{a''}{a\mathcal{H}} - \frac{\bar{\varphi}'^2}{2M_{\mathrm{Pl}}^2\mathcal{H}} = 2\mathcal{H} - \frac{1}{\mathcal{H}}\left(2\mathcal{H}^2 - \frac{\bar{\varphi}'^2}{2M_{\mathrm{Pl}}^2\mathcal{H}}\right) - \frac{\bar{\varphi}'^2}{2M_{\mathrm{Pl}}^2\mathcal{H}} = 0\,. \tag{B.29}$$

Since this is a vanishing expression, one can simply multiply it with Ψ and add it to the left-hand side of Eq. (B.21) which then becomes

$$\Psi' + \mathcal{H}\Psi + \left(2\mathcal{H} - \frac{a''}{a\mathcal{H}} - \frac{\bar{\varphi}'^2}{2M_{\mathrm{Pl}}^2\mathcal{H}}\right)\Psi = \Psi' + 2\mathcal{H}\Psi - \frac{\mathcal{H}'}{\mathcal{H}}\Psi - \frac{\bar{\varphi}'^2}{2M_{\mathrm{Pl}}^2\mathcal{H}}\Psi \tag{B.30}$$

$$= \frac{\mathcal{H}}{a^2}\frac{\mathrm{d}}{\mathrm{d}\tau}\left(\frac{a^2}{\mathcal{H}}\Psi\right) - \frac{\bar{\varphi}'^2}{2M_{\mathrm{Pl}}^2\mathcal{H}}\Psi\,. \tag{B.31}$$

Consequently, Eq. (B.21) reads in terms of q

$$\frac{\mathcal{H}}{a}\frac{\mathrm{d}}{\mathrm{d}\tau}\left(\frac{a^2}{\mathcal{H}}\Psi\right) = \frac{a\bar{\varphi}'}{2M_{\mathrm{Pl}}^2}\left(\delta\varphi + \frac{\bar{\varphi}'}{\mathcal{H}}\Psi\right) = \frac{\bar{\varphi}'}{2M_{\mathrm{Pl}}^2}q\,. \tag{B.32}$$

Taking ∇^2 on both sides of Eq. (B.32) and replacing $\nabla^2\Psi$ with the expression in Eq. (B.28), leads us to the Mukhanov-Sasaki equation [214, 216]

$$\frac{\mathrm{d}}{\mathrm{d}\tau}\left[\zeta^2\frac{\mathrm{d}}{\mathrm{d}\tau}\left(\frac{q}{\zeta}\right)\right] = z\nabla^2 q\,. \tag{B.33}$$

Bibliography

[1] E. Hubble. A Relation between Distance and Radial Velocity among Extra-Galactic Nebulae. *Proceedings of the National Academy of Science*, 15.3 (1929). DOI: 10.1073/pnas.15.3.168.

[2] N. Aghanim et al. Planck 2018 results. VI. Cosmological parameters. *A&A*, 641 (2020). DOI: 10.1051/0004-6361/201833910.

[3] F. Zwicky. On the Masses of Nebulae and of Clusters of Nebulae. *ApJ*, 86 (1937). DOI: 10.1086/143864.

[4] V. C. Rubin and J. Ford W. Kent. Rotation of the Andromeda Nebula from a Spectroscopic Survey of Emission Regions. *ApJ*, 159 (1970). DOI: 10.1086/150317.

[5] V. C. Rubin, J. Ford W. K., and N. Thonnard. Rotational properties of 21 SC galaxies with a large range of luminosities and radii, from NGC 4605 ($R = 4\,\mathrm{kpc}$) to UGC 2885 ($R = 122\,\mathrm{kpc}$). *ApJ*, 238 (1980). DOI: 10.1086/158003.

[6] J. Einasto, A. Kaasik, and E. Saar. Dynamic evidence on massive coronas of galaxies. *Nature*, 250.5464 (1974). DOI: 10.1038/250309a0.

[7] G. F. Smoot et al. Structure in the COBE Differential Microwave Radiometer First-Year Maps. *ApJL*, 396 (1992). DOI: 10.1086/186504.

[8] C. L. Bennett et al. Four-Year COBE DMR Cosmic Microwave Background Observations: Maps and Basic Results. *ApJ*, 464.1 (1996). DOI: 10.1086/310075.

[9] H. Hoekstra, H. Yee, and M. Gladders. Current status of weak gravitational lensing. *New Astron. Rev.*, 46 (2002). DOI: 10.1016/S1387-6473(02)00245-2.

[10] A. D. Lewis, D. A. Buote, and J. T. Stocke. Chandra Observations of A2029: The Dark Matter Profile Down to below 0.01 r_{vir} in an Unusually Relaxed Cluster. *ApJ*, 586.1 (2003). DOI: 10.1086/367556.

[11] D. Clowe et al. A Direct Empirical Proof of the Existence of Dark Matter. *ApJ*, 648.2 (2006). DOI: 10.1086/508162.

[12] C. L. Bennett et al. Nine-year Wilkinson Microwave Anisotropy Probe (WMAP) Observations: Final Maps and Results. *ApJS*, 208.2 (2013). DOI: 10.1088/0067-0049/208/2/20.

[13] P. J. E. Peebles. Large-scale background temperature and mass fluctuations due to scale-invariant primeval perturbations. *ApJL*, 263 (1982). DOI: 10.1086/183911.

[14] M. Taoso, G. Bertone, and A. Masiero. Dark matter candidates: a ten-point test. *Journal of Cosmology and Astroparticle Physics*, 2008.03 (2008). DOI: 10.1088/1475-7516/2008/03/022.

[15] V. Iršič et al. First Constraints on Fuzzy Dark Matter from Lyman-α Forest Data and Hydrodynamical Simulations. *Phys. Rev. Lett.*, 119.3 (2017). DOI: 10.1103/PhysRevLett.119.031302.

[16] R. A. Flores and J. R. Primack. Observational and Theoretical Constraints on Singular Dark Matter Halos. *ApJL*, 427 (1994). DOI: 10.1086/187350.

[17] B. Moore. Evidence against dissipation-less dark matter from observations of galaxy haloes. *Nature*, 370.6491 (1994). DOI: 10.1038/370629a0.

[18] A. A. Klypin et al. Where are the missing Galactic satellites? *ApJ*, 522 (1999). DOI: 10.1086/307643.

[19] B. Moore et al. Dark matter substructure within galactic halos. *ApJL*, 524 (1999). DOI: 10.1086/312287.

[20] M. Boylan-Kolchin, J. S. Bullock, and M. Kaplinghat. Too big to fail? The puzzling darkness of massive Milky Way subhaloes. *MNRAS*, 415.1 (2011). DOI: 10.1111/j.1745-3933.2011.01074.x.

[21] M. Boylan-Kolchin, J. S. Bullock, and M. Kaplinghat. The Milky Way's bright satellites as an apparent failure of ΛCDM. *MNRAS*, 422.2 (2012). DOI: 10.1111/j.1365-2966.2012.20695.x.

[22] J. S. Bullock and M. Boylan-Kolchin. Small-Scale Challenges to the ΛCDM Paradigm. *ARA&A*, 55 (2017). DOI: 10.1146/annurev-astro-091916-055313.

[23] L. Roszkowski, E. M. Sessolo, and S. Trojanowski. WIMP dark matter candidates and searches—current status and future prospects. *Reports on Progress in Physics*, 81.6 (2018). DOI: 10.1088/1361-6633/aab913.

[24] A. M. Green and B. J. Kavanagh. Primordial black holes as a dark matter candidate. *Journal of Physics G: Nuclear and Particle Physics*, 48.4 (2021). DOI: 10.1088/1361-6471/abc534.

[25] D. J. E. Marsh. Axion cosmology. *Phys. Rep.*, 643 (2016). DOI: 10.1016/j.physrep.2016.06.005.

[26] W. Hu, R. Barkana, and A. Gruzinov. Fuzzy Cold Dark Matter: The Wave Properties of Ultralight Particles. *Phys. Rev. Lett.*, 85.6 (2000). DOI: 10.1103/PhysRevLett.85.1158.

[27] C. J. Hogan and M. J. Rees. Axion Miniclusters. *Phys. Lett. B*, 205 (1988). DOI: 10.1016/0370-2693(88)91655-3.

[28] E. W. Kolb and I. I. Tkachev. Axion miniclusters and Bose stars. *Phys. Rev. Lett.*, 71.19 (1993). DOI: 10.1103/PhysRevLett.71.3051.

[29] E. W. Kolb and I. I. Tkachev. Large-amplitude isothermal fluctuations and high density dark matter clumps. *Phys. Rev. D*, 50.2 (1994). DOI: 10.1103/PhysRevD.50.769.

[30] E. W. Kolb and I. I. Tkachev. Femtolensing and Picolensing by Axion Miniclusters. *ApJ*, 460.1 (1996). DOI: 10.1086/309962.

[31] A. Starobinsky. A new type of isotropic cosmological models without singularity. *Phys. Lett. B*, 91.1 (1980). DOI: https://doi.org/10.1016/0370-2693(80)90670-X.

[32] A. H. Guth. Inflationary universe: A possible solution to the horizon and flatness problems. *Phys. Rev. D*, 23.2 (1981). DOI: 10.1103/PhysRevD.23.347.

[33] A. Linde. A new inflationary universe scenario: A possible solution of the horizon, flatness, homogeneity, isotropy and primordial monopole problems. *Phys. Lett. B*, 108.6 (1982). DOI: https://doi.org/10.1016/0370-2693(82)91219-9.

[34] A. Linde. Chaotic inflation. *Phys. Lett. B*, 129.3 (1983). DOI: https://doi.org/10.1016/0370-2693(83)90837-7.

[35] K. Jedamzik, M. Lemoine, and J. Martin. Collapse of small-scale density perturbations during preheating in single field inflation. *JCAP*, 2010.09 (2010). DOI: 10.1088/1475-7516/2010/09/034.

[36] R. Easther, R. Flauger, and J. B. Gilmore. Delayed Reheating and the Breakdown of Coherent Oscillations. *JCAP*, 1104 (2011). DOI: 10.1088/1475-7516/2011/04/027.

[37] N. Musoke, S. Hotchkiss, and R. Easther. Lighting the Dark: Evolution of the Postinflationary Universe. *Phys. Rev. Lett.*, 124.6 (2020). DOI: 10.1103/PhysRevLett.124.061301.

[38] J. C. Niemeyer and R. Easther. Inflaton clusters and inflaton stars. *JCAP*, 2020.07 (2020). DOI: 10.1088/1475-7516/2020/07/030.

[39] B. Eggemeier et al. First Simulations of Axion Minicluster Halos. *Phys. Rev. Lett.*, 125.4 (2020). DOI: 10.1103/PhysRevLett.125.041301.

[40] B. Eggemeier, J. C. Niemeyer, and R. Easther. Formation of inflaton halos after inflation. *Phys. Rev. D*, 103.6 (2021). DOI: 10.1103/PhysRevD.103.063525.

[41] B. Eggemeier et al. Gravitational collapse in the postinflationary Universe. *Phys. Rev. D*, 105.2 (2022). DOI: 10.1103/PhysRevD.105.023516.

[42] B. Eggemeier and J. C. Niemeyer. Formation and mass growth of axion stars in axion miniclusters. *Phys. Rev. D*, 100.6 (2019). DOI: 10.1103/PhysRevD.100.063528.

[43] B. Schwabe et al. Simulating mixed fuzzy and cold dark matter. *Phys. Rev. D*, 102.8 (2020). DOI: 10.1103/PhysRevD.102.083518.

[44] E. A. Milne. A Newtonian Expanding Universe. *The Quarterly Journal of Mathematics*, 5.1 (1934). DOI: 10.1093/qmath/os-5.1.64.

[45] A. Einstein. Die Grundlage der allgemeinen Relativitätstheorie. *Annalen der Physik*, 354.7 (1916). DOI: 10.1002/andp.19163540702.

[46] S. M. Carroll. *Spacetime and Geometry: An Introduction to General Relativity.* Addison Wesley, 2004.

[47] A. Friedmann. Über die Krümmung des Raumes. *Zeitschrift für Physik*, 10.1 (1922). DOI: 10.1007/BF01332580.

[48] A. G. Lemaître. A Homogeneous Universe of Constant Mass and Increasing Radius accounting for the Radial Velocity of Extra-galactic Nebulae. *MNRAS*, 91.5 (1931). DOI: 10.1093/mnras/91.5.483.

[49] H. P. Robertson. Kinematics and World-Structure. *ApJ*, 82 (1935). DOI: 10.1086/143681.

[50] A. G. Walker. On Milne's Theory of World-Structure. *Proceedings of the London Mathematical Society*, 42.1 (1937). DOI: 10.1112/plms/s2-42.1.90.

[51] S. Weinberg. *Cosmology.* Oxford University Press, 2008.

[52] A. R. Liddle and D. H. Lyth. *Cosmological Inflation and Large-Scale Structure.* Cambridge University Press, 2000. DOI: 10.1017/CBO9781139175180.

[53] V. Mukhanov. *Physical Foundations of Cosmology.* Cambridge University Press, 2005. DOI: 10.1017/CBO9780511790553.

[54] A. G. Riess et al. Observational Evidence from Supernovae for an Accelerating Universe and a Cosmological Constant. *AJ*, 116.3 (1998). DOI: 10.1086/300499.

[55] S. Perlmutter et al. Measurements of Ω and Λ from 42 High-Redshift Supernovae. *ApJ*, 517.2 (1999). DOI: 10.1086/307221.

[56] P. Brax. What makes the Universe accelerate? A review on what dark energy could be and how to test it. *Reports on Progress in Physics*, 81.1 (2017). DOI: 10.1088/1361-6633/aa8e64.

[57] K. S. Dawson et al. The Baryon Oscillation Spectroscopic Survey of SDSS-III. *AJ*, 145.1 (2012). DOI: 10.1088/0004-6256/145/1/10.

[58] É. Aubourg et al. Cosmological implications of baryon acoustic oscillation measurements. *Phys. Rev. D*, 92.12 (2015). DOI: 10.1103/PhysRevD.92.123516.

[59] A. G. Riess et al. New Parallaxes of Galactic Cepheids from Spatially Scanning the Hubble Space Telescope: Implications for the Hubble Constant. *ApJ*, 855.2 (2018). DOI: 10.3847/1538-4357/aaadb7.

[60] L. Knox and M. Millea. Hubble constant hunter's guide. *Phys. Rev. D*, 101.4 (2020). DOI: 10.1103/PhysRevD.101.043533.

[61] E. Di Valentino et al. In the realm of the Hubble tension—a review of solutions. *Class. Quant. Grav.*, 38.15 (2021). DOI: 10.1088/1361-6382/ac086d.

[62] E. Di Valentino, A. Melchiorri, and J. Silk. Planck evidence for a closed Universe and a possible crisis for cosmology. *Nature Astronomy*, 4 (2020). DOI: 10.1038/s41550-019-0906-9.

[63] S. Vagnozzi et al. The galaxy power spectrum take on spatial curvature and cosmic concordance. *Physics of the Dark Universe*, 33 (2021). DOI: 10.1016/j.dark.2021.100851.

[64] W. Handley. Curvature tension: evidence for a closed universe. *Phys. Rev. D*, 103.4 (2021). DOI: 10.1103/PhysRevD.103.L041301.

[65] Y. B. Zel'dovich, A. Krasinski, and Y. B. Zeldovich. The Cosmological constant and the theory of elementary particles. *Sov. Phys. Usp.*, 11 (1968). DOI: 10.1007/s10714-008-0624-6.

[66] S. Weinberg. The cosmological constant problem. *Rev. Mod. Phys.*, 61.1 (1989). DOI: 10.1103/RevModPhys.61.1.

[67] J. Martin. Everything you always wanted to know about the cosmological constant problem (but were afraid to ask). *Comptes Rendus Physique*, 13.6 (2012). DOI: 10.1016/j.crhy.2012.04.008.

[68] T. Clifton et al. Modified gravity and cosmology. *Physics Reports*, 513.1 (2012). DOI: https://doi.org/10.1016/j.physrep.2012.01.001.

[69] K. Koyama. Cosmological tests of modified gravity. *Reports on Progress in Physics*, 79.4 (2016). DOI: 10.1088/0034-4885/79/4/046902.

[70] A. Klypin et al. Abundance of field galaxies. *MNRAS*, 454.2 (2015). DOI: 10.1093/mnras/stv2040.

[71] J. F. Navarro, C. S. Frenk, and S. D. White. The Structure of cold dark matter halos. *ApJ*, 462 (1996). DOI: 10.1086/177173.

[72] S. Y. Kim, A. H. G. Peter, and J. R. Hargis. Missing Satellites Problem: Completeness Corrections to the Number of Satellite Galaxies in the Milky Way are Consistent with Cold Dark Matter Predictions. *Phys. Rev. Lett.*, 121 (2018). DOI: 10.1103/PhysRevLett.121.211302.

[73] J. R. Bond and A. S. Szalay. The collisionless damping of density fluctuations in an expanding universe. *ApJ*, 274 (1983). DOI: 10.1086/161460.

[74] S. Dodelson and L. M. Widrow. Sterile neutrinos as dark matter. *Phys. Rev. Lett.*, 72.1 (1994). DOI: 10.1103/PhysRevLett.72.17.

[75] S. Colombi, S. Dodelson, and L. M. Widrow. Large-Scale Structure Tests of Warm Dark Matter. *ApJ*, 458 (1996). DOI: 10.1086/176788.

[76] P. Bode, J. P. Ostriker, and N. Turok. Halo Formation in Warm Dark Matter Models. *ApJ*, 556.1 (2001). DOI: 10.1086/321541.

[77] E. D. Carlson, M. E. Machacek, and L. J. Hall. Self-interacting Dark Matter. *ApJ*, 398 (1992). DOI: 10.1086/171833.

[78] W. Rindler. Visual Horizons in World Models. *MNRAS*, 116.6 (1956). DOI: 10.1093/mnras/116.6.662.

[79] C. W. Misner. The Isotropy of the Universe. *ApJ*, 151 (1968). DOI: 10.1086/149448.

[80] R. H. Dicke and P. J. E. Peebles. The big bang cosmology - enigmas and nostrums. *General Relativity: An Einstein centenary survey*. Ed. by S. W. Hawking and W. Israel. 1979.

[81] B. J. Carr and S. W. Hawking. Black Holes in the Early Universe. *MNRAS*, 168.2 (1974). DOI: 10.1093/mnras/168.2.399.

[82] B. J. Carr. The primordial black hole mass spectrum. *ApJ*, 201 (1975). DOI: 10.1086/153853.

[83] A. D. Linde. Hybrid inflation. *Phys. Rev. D*, 49.2 (1994). DOI: 10.1103/PhysRevD.49.748.

[84] E. Pajer and M. Peloso. A review of axion inflation in the era of Planck. *Classical and Quantum Gravity*, 30.21 (2013). DOI: 10.1088/0264-9381/30/21/214002.

[85] K. Freese, J. A. Frieman, and A. V. Olinto. Natural inflation with pseudo Nambu-Goldstone bosons. *Phys. Rev. Lett.*, 65.26 (1990). DOI: 10.1103/PhysRevLett.65.3233.

[86] F. C. Adams et al. Natural inflation: Particle physics models, power-law spectra for large-scale structure, and constraints from the Cosmic Background Explorer. *Phys. Rev. D*, 47.2 (1993). DOI: 10.1103/PhysRevD.47.426.

[87] D. Wands. Multiple field inflation. *Lect. Notes Phys.*, 738 (2008). DOI: 10.1007/978-3-540-74353-8_8.

[88] D. H. Lyth. What Would We Learn by Detecting a Gravitational Wave Signal in the Cosmic Microwave Background Anisotropy? *Phys. Rev. Lett.*, 78.10 (1997). DOI: 10.1103/PhysRevLett.78.1861.

[89] Y. Akrami et al. Planck 2018 results. X. Constraints on inflation. *A&A*, 641 (2020). DOI: 10.1051/0004-6361/201833887.

[90] A. Albrecht et al. Reheating an Inflationary Universe. *Phys. Rev. Lett.*, 48 (1982). DOI: 10.1103/PhysRevLett.48.1437.

[91] L. Kofman, A. Linde, and A. A. Starobinsky. Towards the theory of reheating after inflation. *Phys. Rev. D*, 56.6 (1997). DOI: 10.1103/PhysRevD.56.3258.

[92] A. D. Dolgov and A. D. Linde. Baryon Asymmetry in Inflationary Universe. *Phys. Lett. B*, 116 (1982). DOI: 10.1016/0370-2693(82)90292-1.

[93] L. Abbott, E. Farhi, and M. B. Wise. Particle production in the new inflationary cosmology. *Phys. Lett. B*, 117.1 (1982). DOI: https://doi.org/10.1016/0370-2693(82)90867-X.

[94] J. H. Traschen and R. H. Brandenberger. Particle Production During Out-of-equilibrium Phase Transitions. *Phys. Rev. D*, 42.8 (1990). DOI: 10.1103/PhysRevD.42.2491.

[95] Y. Shtanov, J. H. Traschen, and R. H. Brandenberger. Universe reheating after inflation. *Phys. Rev. D*, 51.10 (1995). DOI: 10.1103/PhysRevD.51.5438.

[96] L. Kofman, A. Linde, and A. A. Starobinsky. Reheating after Inflation. *Phys. Rev. Lett.*, 73.24 (1994). DOI: 10.1103/PhysRevLett.73.3195.

[97] N. W. McLachlan. *Theory and application of Mathieu functions.* Dover, New York, 1961.

[98] R. A. Alpher, H. Bethe, and G. Gamow. The Origin of Chemical Elements. *Phys. Rev.*, 73.7 (1948). DOI: 10.1103/PhysRev.73.803.

[99] G. M. Fuller, G. J. Mathews, and C. R. Alcock. Quark-hadron phase transition in the early Universe: Isothermal baryon-number fluctuations and primordial nucleosynthesis. *Phys. Rev. D*, 37.6 (1988). DOI: 10.1103/PhysRevD.37.1380.

[100] M. Kawasaki, K. Kohri, and N. Sugiyama. Cosmological Constraints on Late-time Entropy Production. *Phys. Rev. Lett.*, 82.21 (1999). DOI: 10.1103/PhysRevLett.82.4168.

[101] S. Hannestad. What is the lowest possible reheating temperature? *Phys. Rev. D*, 70.4 (2004). DOI: 10.1103/PhysRevD.70.043506.

[102] P. F. de Salas et al. Bounds on very low reheating scenarios after Planck. *Phys. Rev. D*, 92.12 (2015). DOI: 10.1103/PhysRevD.92.123534.

[103] R. Allahverdi et al. Reheating in Inflationary Cosmology: Theory and Applications. *Ann. Rev. Nucl. Part. Sci.*, 60 (2010). DOI: 10.1146/annurev.nucl.012809.104511.

[104] S. Khlebnikov and I. Tkachev. Resonant Decay of Cosmological Bose Condensates. *Phys. Rev. Lett.*, 79.9 (1997). DOI: 10.1103/PhysRevLett.79.1607.

[105] G. N. Felder and I. Tkachev. LATTICEEASY: A Program for lattice simulations of scalar fields in an expanding universe. *Comput. Phys. Commun.*, 178.12 (2008). DOI: 10.1016/j.cpc.2008.02.009.

[106] A. V. Frolov. DEFROST: A New Code for Simulating Preheating after Inflation. *JCAP*, 2008.11 (2008). DOI: 10.1088/1475-7516/2008/11/009.

[107] R. Easther, H. Finkel, and N. Roth. PSPECTRE: A Pseudo-Spectral Code for Preheating. *JCAP*, 2010.10 (2010). DOI: 10.1088/1475-7516/2010/10/025.

[108] M. A. Amin et al. Nonperturbative Dynamics Of Reheating After Inflation: A Review. *Int. J. Mod. Phys. D*, 24 (2014). DOI: 10.1142/S0218271815300037.

[109] M. Gleiser. Pseudostable bubbles. *Phys. Rev. D*, 49.6 (1994). DOI: 10.1103/PhysRevD.49.2978.

[110] E. J. Copeland, M. Gleiser, and H. .-R. Muller. Oscillons: Resonant configurations during bubble collapse. *Phys. Rev. D*, 52.4 (1995). DOI: 10.1103/PhysRevD.52.1920.

[111] M. A. Amin, R. Easther, and H. Finkel. Inflaton fragmentation and oscillon formation in three dimensions. *JCAP*, 2010.12 (2010). DOI: 10.1088/1475-7516/2010/12/001.

[112] M. A. Amin et al. Oscillons after Inflation. *Phys. Rev. Lett.*, 108.24 (2012). DOI: 10.1103/PhysRevLett.108.241302.

[113] K. D. Lozanov and M. A. Amin. Equation of State and Duration to Radiation Domination after Inflation. *Phys. Rev. Lett.*, 119.6 (2017). DOI: 10.1103/PhysRevLett.119.061301.

[114] K. D. Lozanov and M. A. Amin. Self-resonance after inflation: oscillons, transients and radiation domination. *Phys. Rev. D*, 97.2 (2018). DOI: 10.1103/PhysRevD.97.023533.

[115] K. D. Lozanov and M. A. Amin. Gravitational perturbations from oscillons and transients after inflation. *Phys. Rev. D*, 99.12 (2019). DOI: 10.1103/PhysRevD.99.123504.

[116] J. Garcia-Bellido, M. Garcia Perez, and A. Gonzalez-Arroyo. Symmetry breaking and false vacuum decay after hybrid inflation. *Phys. Rev. D*, 67 (2003). DOI: 10.1103/PhysRevD.67.103501.

[117] G. N. Felder and L. Kofman. Nonlinear inflaton fragmentation after preheating. *Phys. Rev. D*, 75.4 (2007). DOI: 10.1103/PhysRevD.75.043518.

[118] I. Tkachev et al. Cosmic strings from preheating. *Phys. Lett. B*, 440 (1998). DOI: 10.1016/S0370-2693(98)01094-6.

[119] A. R. Liddle and S. M. Leach. How long before the end of inflation were observable perturbations produced? *Phys. Rev. D*, 68 (2003). DOI: 10.1103/PhysRevD.68.103503.

[120] S. Y. Khlebnikov and I. I. Tkachev. Relic gravitational waves produced after preheating. *Phys. Rev. D*, 56.2 (1997). DOI: 10.1103/PhysRevD.56.653.

[121] R. Easther and E. A. Lim. Stochastic gravitational wave production after inflation. *JCAP*, 2006.04 (2006). DOI: 10.1088/1475-7516/2006/04/010.

[122] R. Easther, J. T. Giblin Jr., and E. A. Lim. Gravitational Wave Production At The End Of Inflation. *Phys. Rev. Lett.*, 99.22 (2007). DOI: 10.1103/PhysRevLett.99.221301.

[123] J. F. Dufaux et al. Theory and Numerics of Gravitational Waves from Preheating after Inflation. *Phys. Rev. D*, 76.12 (2007). DOI: 10.1103/PhysRevD.76.123517.

[124] J. Garcia-Bellido and D. G. Figueroa. A stochastic background of gravitational waves from hybrid preheating. *Phys. Rev. Lett.*, 98.6 (2007). DOI: 10/bnfrgn.

[125] J. Garcia-Bellido, D. G. Figueroa, and A. Sastre. A Gravitational Wave Background from Reheating after Hybrid Inflation. *Phys. Rev. D*, 77.4 (2008). DOI: 10.1103/PhysRevD.77.043517.

[126] J.-F. Dufaux et al. Gravity Waves from Tachyonic Preheating after Hybrid Inflation. *JCAP*, 2009.03 (2009). DOI: 10.1088/1475-7516/2009/03/001.

[127] H. Assadullahi and D. Wands. Gravitational waves from an early matter era. *Phys. Rev. D*, 79.8 (2009). DOI: 10.1103/PhysRevD.79.083511.

[128] K. Jedamzik, M. Lemoine, and J. Martin. Generation of gravitational waves during early structure formation between cosmic inflation and reheating. *JCAP*, 2010.04 (2010). DOI: 10.1088/1475-7516/2010/04/021.

[129] D. G. Figueroa, J. Garcia-Bellido, and A. Rajantie. On the Transverse-Traceless Projection in Lattice Simulations of Gravitational Wave Production. *JCAP*, 2011.11 (2011). DOI: 10.1088/1475-7516/2011/11/015.

[130] S.-Y. Zhou et al. Gravitational Waves from Oscillon Preheating. *JHEP*, 2013.10 (2013). DOI: 10.1007/JHEP10(2013)026.

[131] S. Antusch, F. Cefala, and S. Orani. Gravitational waves from oscillons after inflation. *Phys. Rev. Lett.*, 118.1 (2017). DOI: 10.1103/PhysRevLett.118.011303.

[132] A. Dolgov and K. Freese. Calculation of particle production by Nambu Goldstone bosons with application to inflation reheating and baryogenesis. *Phys. Rev. D*, 51.6 (1995). DOI: 10.1103/PhysRevD.51.2693.

[133] A. Dolgov et al. Baryogenesis during reheating in natural inflation and comments on spontaneous baryogenesis. *Phys. Rev. D*, 56.10 (1997). DOI: 10.1103/PhysRevD.56.6155.

[134] J. Garcia-Bellido et al. Nonequilibrium electroweak baryogenesis from preheating after inflation. *Phys. Rev. D*, 60.12 (1999). DOI: 10.1103/PhysRevD.60.123504.

[135] S. Davidson, M. Losada, and A. Riotto. A New perspective on baryogenesis. *Phys. Rev. Lett.*, 84.19 (2000). DOI: 10.1103/PhysRevLett.84.4284.

[136] A. Tranberg and J. Smit. Baryon asymmetry from electroweak tachyonic preheating. *JHEP*, 2003.11 (2003). DOI: 10.1088/1126-6708/2003/11/016.

[137] K. D. Lozanov and M. A. Amin. End of inflation, oscillons, and matter-antimatter asymmetry. *Phys. Rev. D*, 90.8 (2014). DOI: 10.1103/PhysRevD.90.083528.

[138] K. Enqvist. Primordial magnetic fields. *Int. J. Mod. Phys. D*, 7.03 (1998). DOI: 10.1142/S0218271898000243.

[139] A. Diaz-Gil et al. Magnetic field production during preheating at the electroweak scale. *Phys. Rev. Lett.*, 100.24 (2008). DOI: 10.1103/PhysRevLett.100.241301.

[140] M. Y. Khlopov, B. A. Malomed, and Y. B. Zeldovich. Gravitational instability of scalar fields and formation of primordial black holes. *MNRAS*, 215.4 (1985). DOI: 10.1093/mnras/215.4.575.

[141] J. Garcia-Bellido, A. D. Linde, and D. Wands. Density perturbations and black hole formation in hybrid inflation. *Phys. Rev. D*, 54.10 (1996). DOI: 10.1103/PhysRevD.54.6040.

[142] A. M. Green, A. R. Liddle, and A. Riotto. Primordial black hole constraints in cosmologies with early matter domination. *Phys. Rev. D*, 56.12 (1997). DOI: 10.1103/PhysRevD.56.7559.

[143] A. M. Green and K. A. Malik. Primordial black hole production due to preheating. *Phys. Rev. D*, 64.2 (2001). DOI: 10.1103/PhysRevD.64.021301.

[144] B. A. Bassett and S. Tsujikawa. Inflationary preheating and primordial black holes. *Phys. Rev. D*, 63.12 (2001). DOI: 10.1103/PhysRevD.63.123503.

[145] E. Torres-Lomas et al. Formation of subhorizon black holes from preheating. *Phys. Rev. D*, 89.8 (2014). DOI: 10.1103/PhysRevD.89.083008.

[146] T. Harada et al. Primordial Black Hole Formation in the Matter-dominated Phase of the Universe. *ApJ*, 833.1 (2016). DOI: 10.3847/1538-4357/833/1/61.

[147] J. C. Hidalgo et al. Collapse threshold for a cosmological Klein-Gordon field. *Phys. Rev. D*, 96.6 (2017). DOI: 10.1103/PhysRevD.96.063504.

[148] B. Carr et al. Primordial black hole formation during slow reheating after inflation. *Phys. Rev. D*, 97.12 (2018). DOI: 10.1103/PhysRevD.97.123535.

[149] J. Martin, T. Papanikolaou, and V. Vennin. Primordial black holes from the preheating instability in single-field inflation. *JCAP*, 2020.1 (2020). DOI: 10.1088/1475-7516/2020/01/024.

[150] K. Carrion et al. Complex Scalar Field Reheating and Primordial Black Hole production. *JCAP*, 2021.07 (2021). DOI: 10.1088/1475-7516/2021/07/001.

[151] L. E. Padilla, J. C. Hidalgo, and K. A. Malik. New mechanism for primordial black hole formation during reheating. *Phys. Rev. D*, 106.2 (2022). DOI: 10.1103/PhysRevD.106.023519.

[152] J. C. Hidalgo, L. E. Padilla, and G. German. Production of PBHs from inflaton structure. *ArXiv e-prints* (2022). arXiv: 2208.09462.

[153] S. Weinberg. The U(1) problem. *Phys. Rev. D*, 11.12 (1975). DOI: 10.1103/PhysRevD.11.3583.

[154] G. ’t Hooft. Computation of the quantum effects due to a four-dimensional pseudoparticle. *Phys. Rev. D*, 14.12 (1976). DOI: 10.1103/PhysRevD.14.3432.

[155] M. D. Schwartz. *Quantum Field Theory and the Standard Model.* Cambridge University Press, 2014.

[156] R. Crewther et al. Chiral estimate of the electric dipole moment of the neutron in quantum chromodynamics. *Phys. Lett. B*, 88.1 (1979). DOI: https://doi.org/10.1016/0370-2693(79)90128-X.

[157] C. Abel et al. Measurement of the Permanent Electric Dipole Moment of the Neutron. *Phys. Rev. Lett.*, 124.8 (2020). DOI: 10.1103/PhysRevLett.124.081803.

[158] R. D. Peccei and H. R. Quinn. CP Conservation in the Presence of Pseudoparticles. *Phys. Rev. Lett.*, 38.25 (1977). DOI: 10.1103/PhysRevLett.38.1440.

[159] R. D. Peccei and H. R. Quinn. Constraints imposed by CP conservation in the presence of pseudoparticles. *Phys. Rev. D*, 16.6 (1977). DOI: 10.1103/PhysRevD.16.1791.

[160] S. Weinberg. A New Light Boson? *Phys. Rev. Lett.*, 40.4 (1978). DOI: 10.1103/PhysRevLett.40.223.

[161] F. Wilczek. Problem of Strong *P* and *T* Invariance in the Presence of Instantons. *Phys. Rev. Lett.*, 40.5 (1978). DOI: 10.1103/PhysRevLett.40.279.

[162] T. W. Donnelly et al. Do axions exist? *Phys. Rev. D*, 18.5 (1978). DOI: 10.1103/PhysRevD.18.1607.

[163] J. E. Kim. Light Pseudoscalars, Particle Physics and Cosmology. *Phys. Rept.*, 150 (1987). DOI: 10.1016/0370-1573(87)90017-2.

[164] J. E. Kim. Weak-Interaction Singlet and Strong CP Invariance. *Phys. Rev. Lett.*, 43.2 (1979). DOI: 10.1103/PhysRevLett.43.103.

[165] M. Shifman, A. Vainshtein, and V. Zakharov. Can confinement ensure natural CP invariance of strong interactions? *Nuclear Physics B*, 166.3 (1980). DOI: 10.1016/0550-3213(80)90209-6.

[166] M. Dine, W. Fischler, and M. Srednicki. A simple solution to the strong CP problem with a harmless axion. *Phys. Lett. B*, 104.3 (1981). DOI: https://doi.org/10.1016/0370-2693(81)90590-6.

[167] A. R. Zhitnitsky. On Possible Suppression of the Axion Hadron Interactions. *Sov. J. Nucl. Phys.*, 31 (1980).

[168] J. Preskill, M. B. Wise, and F. Wilczek. Cosmology of the invisible axion. *Phys. Lett. B*, 120.1 (1983). DOI: https://doi.org/10.1016/0370-2693(83)90637-8.

[169] L. Abbott and P. Sikivie. A cosmological bound on the invisible axion. *Physics Letters B*, 120.1 (1983). DOI: https://doi.org/10.1016/0370-2693(83)90638-X.

[170] M. Dine and W. Fischler. The not-so-harmless axion. *Phys. Lett. B*, 120.1-3 (1983). DOI: 10.1016/0370-2693(83)90639-1.

[171] G. Grilli di Cortona et al. The QCD axion, precisely. *JHEP*, 2016.01 (2016). DOI: 10.1007/JHEP01(2016)034.

[172] M. Gorghetto and G. Villadoro. Topological susceptibility and QCD axion mass: QED and NNLO corrections. *JHEP*, 2019.3 (2019). DOI: 10.1007/JHEP03(2019)033.

[173] J. W. Brockway, E. D. Carlson, and G. G. Raffelt. SN1987A gamma-ray limits on the conversion of pseudoscalars. *Phys. Lett. B*, 383 (1996). DOI: 10.1016/0370-2693(96)00778-2.

[174] J. A. Grifols, E. Masso, and R. Toldra. Gamma-rays from SN1987A due to pseudoscalar conversion. *Phys. Rev. Lett.*, 77.12 (1996). DOI: 10.1103/PhysRevLett.77.2372.

[175] A. Arvanitaki, M. Baryakhtar, and X. Huang. Discovering the QCD Axion with Black Holes and Gravitational Waves. *Phys. Rev. D*, 91.8 (2015). DOI: 10.1103/PhysRevD.91.084011.

[176] D. J. E. Marsh and S. Hoof. Astrophysical Searches and Constraints. *The Search for Ultralight Bosonic Dark Matter*. Springer International Publishing, 2023. DOI: 10.1007/978-3-030-95852-7_3.

[177] O. Wantz and E. P. S. Shellard. Axion cosmology revisited. *Phys. Rev. D*, 82.12 (2010). DOI: 10.1103/PhysRevD.82.123508.

[178] S. Borsanyi et al. Calculation of the axion mass based on high-temperature lattice quantum chromodynamics. *Nature*, 539 (2016). DOI: 10.1038/nature20115.

[179] P. Petreczky, H.-P. Schadler, and S. Sharma. The topological susceptibility in finite temperature QCD and axion cosmology. *Phys. Lett. B*, 762 (2016). DOI: 10.1016/j.physletb.2016.09.063.

[180] P. Svrcek and E. Witten. Axions in string theory. *JHEP*, 2006.6 (2006). DOI: 10.1088/1126-6708/2006/06/051.

[181] A. Arvanitaki et al. String axiverse. *Phys. Rev. D*, 81.12 (2010). DOI: 10.1103/PhysRevD.81.123530.

[182] M. Cicoli, M. D. Goodsell, and A. Ringwald. The type IIB string axiverse and its low-energy phenomenology. *JHEP*, 2012.10 (2012). DOI: 10.1007/JHEP10(2012)146.

[183] T. W. B. Kibble. Topology of cosmic domains and strings. *Journal of Physics A: Mathematical and General*, 9.8 (1976). DOI: 10.1088/0305-4470/9/8/029.

[184] P. Sikivie. Experimental Tests of the “Invisible” Axion. *Phys. Rev. Lett.*, 51.16 (1983). DOI: 10.1103/PhysRevLett.51.1415.

[185] D. J. E. Marsh and P. G. Ferreira. Ultralight scalar fields and the growth of structure in the Universe. *Phys. Rev. D*, 82.10 (2010). DOI: 10.1103/PhysRevD.82.103528.

[186] P. Fox, A. Pierce, and S. D. Thomas. Probing a QCD string axion with precision cosmological measurements. *ArXiv e-prints* (2004). arXiv:hep-th/0409059.

[187] L. Visinelli and P. Gondolo. Dark Matter Axions Revisited. *Phys. Rev. D*, 80.3 (2009). DOI: 10.1103/PhysRevD.80.035024.

[188] R. L. Davis. Goldstone bosons in string models of galaxy formation. *Phys. Rev. D*, 32.12 (1985). DOI: 10.1103/PhysRevD.32.3172.

[189] R. L. Davis. Cosmic Axions from Cosmic Strings. *Phys. Lett. B*, 180 (1986). DOI: 10.1016/0370-2693(86)90300-X.

[190] D. Harari and P. Sikivie. On the Evolution of Global Strings in the Early Universe. *Phys. Lett. B*, 195 (1987). DOI: 10.1016/0370-2693(87)90032-3.

[191] C. Hagmann and P. Sikivie. Computer simulations of the motion and decay of global strings. *Nucl. Phys. B*, 363 (1991). DOI: 10.1016/0550-3213(91)90243-Q.

[192] R. A. Battye and E. P. S. Shellard. Global string radiation. *Nucl. Phys. B*, 423 (1994). DOI: 10.1016/0550-3213(94)90573-8.

[193] R. A. Battye and E. P. S. Shellard. Axion string constraints. *Phys. Rev. Lett.*, 73.22 (1994). DOI: 10.1103/PhysRevLett.73.2954.

[194] M. Yamaguchi, M. Kawasaki, and J. Yokoyama. Evolution of axionic strings and spectrum of axions radiated from them. *Phys. Rev. Lett.*, 82.23 (1999). DOI: 10.1103/PhysRevLett.82.4578.

[195] C. Hagmann, S. Chang, and P. Sikivie. Axion radiation from strings. *Phys. Rev. D*, 63.12 (2001). DOI: 10.1103/PhysRevD.63.125018.

[196] T. Hiramatsu, M. Kawasaki, and K. Saikawa. Evolution of String-Wall Networks and Axionic Domain Wall Problem. *JCAP*, 2008.08 (2011). DOI: 10.1088/1475-7516/2011/08/030.

[197] T. Hiramatsu et al. Improved estimation of radiated axions from cosmological axionic strings. *Phys. Rev. D*, 83.12 (2011). DOI: 10.1103/PhysRevD.83.123531.

[198] T. Hiramatsu et al. Production of dark matter axions from collapse of string-wall systems. *Phys. Rev. D*, 85.10 (2012). DOI: 10.1103/PhysRevD.85.105020.

[199] M. Kawasaki, K. Saikawa, and T. Sekiguchi. Axion dark matter from topological defects. *Phys. Rev. D*, 91.6 (2015). DOI: 10.1103/PhysRevD.91.065014.

[200] L. Fleury and G. D. Moore. Axion dark matter: strings and their cores. *JCAP*, 2016.01 (2016). DOI: 10.1088/1475-7516/2016/01/004.

[201] V. B. Klaer and G. D. Moore. How to simulate global cosmic strings with large string tension. *JCAP*, 2017.10 (2017). DOI: 10.1088/1475-7516/2017/10/043.

[202] V. B. . Klaer and G. D. Moore. The dark-matter axion mass. *JCAP*, 2017.11 (2017). DOI: 10.1088/1475-7516/2017/11/049.

[203] M. Gorghetto, E. Hardy, and G. Villadoro. Axions from Strings: the Attractive Solution. *JHEP*, 2018.07 (2018). DOI: 10.1007/JHEP07(2018)151.

[204] M. Gorghetto, E. Hardy, and G. Villadoro. More axions from strings. *SciPost Phys.*, 10.2 (2021). DOI: 10.21468/SciPostPhys.10.2.050.

[205] A. Vaquero, J. Redondo, and J. Stadler. Early seeds of axion miniclusters. *JCAP*, 2019.04 (2019). DOI: 10.1088/1475-7516/2019/04/012.

[206] M. Buschmann, J. W. Foster, and B. R. Safdi. Early-Universe Simulations of the Cosmological Axion. *Phys. Rev. Lett.*, 124.16 (2020). DOI: 10.1103/PhysRevLett.124.161103.

[207] M. Srednicki. Axion couplings to matter: (I). CP-conserving parts. *Nuclear Physics B*, 260.3 (1985). DOI: https://doi.org/10.1016/0550-3213(85)90054-9.

[208] M. S. Turner. Early-Universe Thermal Production of Not-So-Invisible Axions. *Phys. Rev. Lett.*, 59.21 (1987). DOI: 10.1103/PhysRevLett.59.2489.

[209] S. Chang and K. Choi. Hadronic axion window and the big bang nucleosynthesis. *Phys. Lett. B*, 316 (1993). DOI: 10.1016/0370-2693(93)90656-3.

[210] S. Hannestad, A. Mirizzi, and G. Raffelt. New cosmological mass limit on thermal relic axions. *JCAP*, 2005.07 (2005). DOI: 10.1088/1475-7516/2005/07/002.

[211] C. Knobel. An Introduction into the Theory of Cosmological Structure Formation. *ArXiv e-prints* (2012). arXiv:1208.5931.

[212] D. Baumann. Inflation. *Theoretical Advanced Study Institute in Elementary Particle Physics: Physics of the Large and the Small.* 2011. DOI: 10.1142/9789814327183_0010.

[213] D. Baumann. Lecture Notes on Cosmology, University of Amsterdam. URL: http://cosmology.amsterdam/education/cosmology/ (last visited March 23, 2022).

[214] V. F. Mukhanov, H. A. Feldman, and R. H. Brandenberger. Theory of cosmological perturbations. *Phys. Rep.*, 215.5-6 (1992). DOI: 10.1016/0370-1573(92)90044-Z.

[215] R. Arnowitt, S. Deser, and C. W. Misner. Dynamical Structure and Definition of Energy in General Relativity. *Phys. Rev.*, 116.5 (1959). DOI: 10.1103/PhysRev.116.1322.

[216] M. Sasaki. Large Scale Quantum Fluctuations in the Inflationary Universe. *Progress of Theoretical Physics*, 76.5 (1986). DOI: 10.1143/PTP.76.1036.

[217] E. D. Stewart and D. H. Lyth. A More accurate analytic calculation of the spectrum of cosmological perturbations produced during inflation. *Phys. Lett. B*, 302 (1993). DOI: 10.1016/0370-2693(93)90379-V.

[218] V. Acquaviva et al. Second order cosmological perturbations from inflation. *Nucl. Phys. B*, 667 (2003). DOI: 10.1016/S0550-3213(03)00550-9.

[219] J. M. Maldacena. Non-Gaussian features of primordial fluctuations in single field inflationary models. *JHEP*, 2003.05 (2003). DOI: 10.1088/1126-6708/2003/05/013.

[220] P. Amaro-Seoane et al. Laser Interferometer Space Antenna. *ArXiv e-prints* (2017). arXiv:1702.00786.

[221] S. Sato et al. DECIGO: The Japanese space gravitational wave antenna. *Journal of Physics: Conference Series*, 154 (2009). DOI: 10.1088/1742-6596/154/1/012040.

[222] S. Sato et al. The status of DECIGO. *Journal of Physics: Conference Series*, 840 (2017). DOI: 10.1088/1742-6596/840/1/012010.

[223] C. Cutler and D. E. Holz. Ultrahigh precision cosmology from gravitational waves. *Phys. Rev. D*, 80.10 (2009). DOI: 10.1103/PhysRevD.80.104009.

[224] B. Abbott et al. Searching for a Stochastic Background of Gravitational Waves with LIGO. *ApJ*, 659 (2007). DOI: 10.1086/511329.

[225] J. R. Smith et al. The path to the enhanced and advanced LIGO gravitational-wave detectors. *Classical and Quantum Gravity*, 26.11 (2009). DOI: 10.1088/0264-9381/26/11/114013.

[226] G. M. Harry et al. Advanced LIGO: the next generation of gravitational wave detectors. *Classical and Quantum Gravity*, 27.8 (2010). DOI: 10.1088/0264-9381/27/8/084006.

[227] J. Aasi et al. Advanced LIGO. *Classical and Quantum Gravity*, 32.7 (2015). DOI: 10.1088/0264-9381/32/7/074001.

[228] F. Acernese et al. Advanced Virgo: a second-generation interferometric gravitational wave detector. *Classical and Quantum Gravity*, 32.2 (2015). DOI: 10.1088/0264-9381/32/2/024001.

[229] C. Caprini and D. G. Figueroa. Cosmological backgrounds of gravitational waves. *Classical and Quantum Gravity*, 35.16 (2018). DOI: 10.1088/1361-6382/aac608.

[230] H. Mo, F. van den Bosch, and S. White. *Galaxy Formation and Evolution*. Cambridge University Press, 2010. DOI: 10.1017/CBO9780511807244.

[231] A. Lewis, A. Challinor, and A. Lasenby. Efficient computation of CMB anisotropies in closed FRW models. *ApJ*, 538 (2000). DOI: 10.1086/309179.

[232] F. Bernardeau et al. Large scale structure of the universe and cosmological perturbation theory. *Phys. Rept.*, 367.1 (2002). DOI: 10.1016/S0370-1573(02)00135-7.

[233] F. Bernardeau. The evolution of the large-scale structure of the universe: beyond the linear regime. *100e Ecole d'Ete de Physique: Post-Planck Cosmology*. 2015. DOI: 10.1093/acprof:oso/9780198728856.003.0002.

[234] Y. B. Zeldovich. Gravitational instability: An Approximate theory for large density perturbations. *A&A*, 5 (1970).

[235] R. Scoccimarro. Transients from initial conditions: a perturbative analysis. *MNRAS*, 299 (1998). DOI: 10.1046/j.1365-8711.1998.01845.x.

[236] O. Hahn and T. Abel. Multi-scale initial conditions for cosmological simulations. *MNRAS*, 415.3 (2011). DOI: 10.1111/j.1365-2966.2011.18820.x.

[237] S. Cole and C. G. Lacey. The Structure of dark matter halos in hierarchical clustering models. *MNRAS*, 281 (1996). DOI: 10.1093/mnras/281.2.716.

[238] V. R. Eke, S. Cole, and C. S. Frenk. Cluster evolution as a diagnostic for Ω. *MNRAS*, 282.1 (1996). DOI: 10.1093/mnras/282.1.263.

[239] G. L. Bryan and M. L. Norman. Statistical Properties of X-Ray Clusters: Analytic and Numerical Comparisons. *ApJ*, 495.1 (1998). DOI: 10.1086/305262.

[240] D. Ellis, D. J. E. Marsh, and C. Behrens. Axion Miniclusters Made Easy. *Phys. Rev. D*, 103.8 (2021). DOI: 10.1103/PhysRevD.103.083525.

[241] D. Ellis. Axion Miniclusters: Formation, Structure and Observational Signatures. PhD Thesis, University of Göttingen (2021).

[242] D. Ellis et al. Structure of axion miniclusters. *Phys. Rev. D*, 106 (2022). DOI: 10.1103/PhysRevD.106.103514.

[243] W. H. Press and P. Schechter. Formation of Galaxies and Clusters of Galaxies by Self-Similar Gravitational Condensation. *ApJ*, 187 (1974). DOI: 10.1086/152650.

[244] J. R. Bond et al. Excursion set mass functions for hierarchical Gaussian fluctuations. *ApJ*, 379 (1991). DOI: 10.1086/170520.

[245] R. K. Sheth and G. Tormen. Large-scale bias and the peak background split. *MNRAS*, 308.1 (1999). DOI: 10.1046/j.1365-8711.1999.02692.x.

[246] R. K. Sheth, H. J. Mo, and G. Tormen. Ellipsoidal collapse and an improved model for the number and spatial distribution of dark matter haloes. *MNRAS*, 323.1 (2001). DOI: 10.1046/j.1365-8711.2001.04006.x.

[247] R. K. Sheth and G. Tormen. An excursion set model of hierarchical clustering: ellipsoidal collapse and the moving barrier. *MNRAS*, 329.1 (2002). DOI: 10.1046/j.1365-8711.2002.04950.x.

[248] J. Binney and S. Tremaine. *Galactic Dynamics: Second Edition.* Princeton University Press, 2008.

[249] R. W. Hockney and J. W. Eastwood. *Computer simulations using particles.* CRC Press, 1988.

[250] S. J. Aarseth. *Gravitational N-Body Simulations: Tools and Algorithms.* Cambridge University Press, 2003. DOI: 10.1017/CBO9780511535246.

[251] S. J. Aarseth and F. Hoyle. Dynamical Evolution of Clusters of Galaxies, I. *MNRAS*, 126.3 (1963). DOI: 10.1093/mnras/126.3.223.

[252] J. Barnes and P. Hut. A hierarchical $O(N \log N)$ force-calculation algorithm. *Nature*, 324.6096 (1986). DOI: 10.1038/324446a0.

[253] J. V. Villumsen. A New Hierarchical Particle-Mesh Code for Very Large Scale Cosmological N-Body Simulations. *ApJS*, 71 (1989). DOI: 10.1086/191380.

[254] C. Jessop, M. Duncan, and W. Chau. Multigrid Methods for N-Body Gravitational Systems. *Journal of Computational Physics*, 115.2 (1994). DOI: https://doi.org/10.1006/jcph.1994.1200.

[255] G. Efstathiou et al. Numerical techniques for large cosmological N-body simulations. *ApJS*, 57 (1985). DOI: 10.1086/191003.

[256] G. Xu. A New Parallel N-Body Gravity Solver: TPM. *ApJS*, 98 (1995). DOI: 10.1086/192166.

[257] J. S. Bagla. A TreePM code for cosmological N-body simulations. *J. Astrophys. Astron.*, 23 (2002). DOI: 10.1007/BF02702282.

[258] P. Bode, J. P. Ostriker, and G. Xu. The Tree Particle-Mesh N -Body Gravity Solver. *ApJS*, 128.2 (2000). DOI: 10.1086/313398.

[259] V. Springel. The Cosmological simulation code GADGET-2. *MNRAS*, 364.4 (2005). DOI: 10.1111/j.1365-2966.2005.09655.x.

[260] V. Springel, N. Yoshida, and S. D. M. White. GADGET: A Code for collisionless and gasdynamical cosmological simulations. *New Astron.*, 6.2 (2001). DOI: 10.1016/S1384-1076(01)00042-2.

[261] V. Springel et al. Simulating cosmic structure formation with the GADGET-4 code. *MNRAS*, 506.2 (2021). DOI: 10.1093/mnras/stab1855.

[262] J. Stadel et al. Quantifying the heart of darkness with GHALO – a multibillion particle simulation of a galactic halo. *MNRAS: Letters*, 398.1 (2009). DOI: 10.1111/j.1745-3933.2009.00699.x.

[263] D. Potter, J. Stadel, and R. Teyssier. PKDGRAV3: Beyond Trillion Particle Cosmological Simulations for the Next Era of Galaxy Surveys (2016).

[264] A. Almgren et al. Nyx: A Massively Parallel AMR Code for Computational Cosmology. *ApJ*, 765 (2013). DOI: 10.1088/0004-637X/765/1/39.

[265] G. L. Bryan et al. ENZO: An Adaptive Mesh Refinement Code for Astrophysics. *ApJS*, 211.2 (2014). DOI: 10.1088/0067-0049/211/2/19.

[266] A. V. Kravtsov, A. A. Klypin, and A. M. Khokhlov. Adaptive refinement tree: A New high resolution N body code for cosmological simulations. *ApJS*, 111 (1997). DOI: 10.1086/313015.

[267] R. Teyssier. Cosmological hydrodynamics with adaptive mesh refinement: a new high resolution code called ramses. *A&A*, 385 (2002). DOI: 10.1051/0004-6361:20011817.

[268] J.-h. Kim et al. The AGORA High-Resolution Galaxy Simulations Comparison Project. *ApJS*, 210 (2013). DOI: 10.1088/0067-0049/210/1/14.

[269] B. Schwabe and J. C. Niemeyer. Deep Zoom-In Simulation of a Fuzzy Dark Matter Galactic Halo. *Phys. Rev. Lett.*, 128.18 (2022). DOI: 10.1103/PhysRevLett.128.181301.

[270] V. Springel et al. Populating a cluster of galaxies. 1. Results at z = 0. *MNRAS*, 328.3 (2001). DOI: 10.1046/j.1365-8711.2001.04912.x.

[271] K. Dolag et al. Substructures in hydrodynamical cluster simulations. *MNRAS*, 399.2 (2009). DOI: 10.1111/j.1365-2966.2009.15034.x.

[272] P. S. Behroozi, R. H. Wechsler, and H.-Y. Wu. The ROCKSTAR phase-space temporal halo finder and the velocity offsets of cluster cores. *ApJ*, 762.2 (2012). DOI: 10.1088/0004-637x/762/2/109.

[273] M. Davis et al. The evolution of large-scale structure in a universe dominated by cold dark matter. *ApJ*, 292 (1985). DOI: 10.1086/163168.

[274] A. Knebe et al. Haloes gone MAD: The Halo-Finder Comparison Project. *MNRAS*, 415.3 (2011). DOI: 10.1111/j.1365-2966.2011.18858.x.

[275] E. Bertschinger. Self-similar secondary infall and accretion in an Einstein-de Sitter universe. *ApJS*, 58 (1985). DOI: 10.1086/191028.

[276] G. Tormen, F. R. Bouchet, and S. D. M. White. The Structure and dynamical evolution of dark matter halos. *MNRAS*, 286.4 (1997). DOI: 10.1093/mnras/286.4.865.

[277] J. Einasto. On the Construction of a Composite Model for the Galaxy and on the Determination of the System of Galactic Parameters. *Trudy Astrofizicheskogo Instituta Alma-Ata*, 5 (1965).

[278] J. F. Navarro et al. The Inner structure of Lambda-CDM halos 3: Universality and asymptotic slopes. *MNRAS*, 349.3 (2004). DOI: 10.1111/j.1365-2966.2004.07586.x.

[279] V. Springel et al. The Aquarius Project: the subhaloes of galactic haloes. *MNRAS*, 391.4 (2008). DOI: 10.1111/j.1365-2966.2008.14066.x.

[280] J. R. Bond and S. T. Myers. The Peak-Patch Picture of Cosmic Catalogs. I. Algorithms. *ApJS*, 103 (1996). DOI: 10.1086/192267.

[281] G. Stein, M. A. Alvarez, and J. R. Bond. The mass-Peak Patch algorithm for fast generation of deep all-sky dark matter halo catalogues and its N-body validation. *MNRAS*, 483.2 (2018). DOI: 10.1093/mnras/sty3226.

[282] L. M. Widrow and N. Kaiser. Using the Schroedinger Equation to Simulate Collisionless Matter. *ApJL*, 416 (1993). DOI: 10.1086/187073.

[283] R. Ruffini and S. Bonazzola. Systems of Self-Gravitating Particles in General Relativity and the Concept of an Equation of State. *Phys. Rev.*, 187.5 (1969). DOI: 10.1103/PhysRev.187.1767.

[284] Y. Nambu and M. Sasaki. Quantum treatment of cosmological axion perturbations. *Phys. Rev. D*, 42.12 (1990). DOI: 10.1103/PhysRevD.42.3918.

[285] E. Madelung. Quantentheorie in hydrodynamischer Form. *Zeitschrift für Physik*, 40.3 (1927). DOI: 10.1007/BF01400372.

[286] J. C. Niemeyer. Small-scale structure of fuzzy and axion-like dark matter. *Progress in Particle and Nuclear Physics*, 113 (2020). DOI: https://doi.org/10.1016/j.ppnp.2020.103787.

[287] D. Bohm. A Suggested Interpretation of the Quantum Theory in Terms of "Hidden" Variables. *Phys. Rev.*, 85.2 (1952). DOI: 10.1103/PhysRev.85.166.

[288] X. Li, L. Hui, and G. L. Bryan. Numerical and Perturbative Computations of the Fuzzy Dark Matter Model. *Phys. Rev. D*, 99.6 (2019). DOI: 10.1103/PhysRevD.99.063509.

[289] H.-Y. Schive, T. Chiueh, and T. Broadhurst. Cosmic Structure as the Quantum Interference of a Coherent Dark Wave. *Nature Phys.*, 10 (2014). DOI: 10.1038/nphys2996.

[290] T. Kobayashi et al. Lyman-α constraints on ultralight scalar dark matter: Implications for the early and late universe. *Phys. Rev. D*, 96.12 (2017). DOI: 10.1103/PhysRevD.96.123514.

[291] E. Armengaud et al. Constraining the mass of light bosonic dark matter using SDSS Lyman-α forest. *MNRAS*, 471.4 (2017). DOI: 10.1093/mnras/stx1870.

[292] N. Bar et al. Galactic rotation curves versus ultralight dark matter: Implications of the soliton-host halo relation. *Phys. Rev. D*, 98.8 (2018). DOI: 10.1103/PhysRevD.98.083027.

[293] V. H. Robles, J. S. Bullock, and M. Boylan-Kolchin. Scalar Field Dark Matter: Helping or Hurting Small-Scale Problems in Cosmology? *MNRAS*, 483.1 (2019). DOI: 10.1093/mnras/sty3190.

[294] A. Burkert. Fuzzy Dark Matter and Dark Matter Halo Cores. *ApJ*, 904.2 (2020). DOI: 10.3847/1538-4357/abb242.

[295] B. Bar-Or, J.-B. Fouvry, and S. Tremaine. Relaxation in a Fuzzy Dark Matter Halo. *ApJ*, 871.1 (2019). DOI: 10.3847/1538-4357/aaf28c.

[296] B. V. Church, P. Mocz, and J. P. Ostriker. Heating of Milky Way disc stars by dark matter fluctuations in cold dark matter and fuzzy dark matter paradigms. *MNRAS*, 485.2 (2019). DOI: 10.1093/mnras/stz534.

[297] D. J. E. Marsh and J. C. Niemeyer. Strong Constraints on Fuzzy Dark Matter from Ultrafaint Dwarf Galaxy Eridanus II. *Phys. Rev. Lett.*, 123.5 (2019). DOI: 10.1103/PhysRevLett.123.051103.

[298] L. Hui. Wave Dark Matter. *ARA&A*, 59 (2021). DOI: 10.1146/annurev-astro-120920-010024.

[299] F. S. Guzman and L. A. Urena-Lopez. Evolution of the Schrödinger-Newton system for a selfgravitating scalar field. *Phys. Rev. D*, 69.12 (2004). DOI: 10.1103/PhysRevD.69.124033.

[300] I. M. Moroz, R. Penrose, and P. Tod. Spherically-symmetric solutions of the Schrödinger-Newton equations. *Classical and Quantum Gravity*, 15.9 (1998). DOI: 10.1088/0264-9381/15/9/019.

[301] D. H. Bernstein, E. Giladi, and K. R. W. Jones. Eigenstates of the Gravitational Schrödinger Equation. *Mod. Phys. Lett. A*, 13.29 (1998). DOI: 10/c935vx.

[302] R. Harrison, I. Moroz, and K. P. Tod. A numerical study of the Schrödinger-Newton equations. *Nonlinearity*, 16.1 (2002). DOI: 10.1088/0951-7715/16/1/307.

[303] P.-H. Chavanis. Mass-radius relation of Newtonian self-gravitating Bose-Einstein condensates with short-range interactions. I. Analytical results. *Phys. Rev. D*, 84.4 (2011). DOI: 10.1103/PhysRevD.84.043531.

[304] L. Hui et al. Ultralight scalars as cosmological dark matter. *Phys. Rev. D*, 95.4 (2017). DOI: 10.1103/PhysRevD.95.043541.

[305] I. Tkachev. On the possibility of Bose-star formation. *Phys. Lett. B*, 261.3 (1991). DOI: https://doi.org/10.1016/0370-2693(91)90330-S.

[306] P. Jetzer. Boson stars. *Phys. Rep.*, 220.4 (1992). DOI: 10.1016/0370-1573(92)90123-H.

[307] D. G. Levkov, A. G. Panin, and I. I. Tkachev. Gravitational Bose-Einstein Condensation in the Kinetic Regime. *Phys. Rev. Lett.*, 121.15 (2018). DOI: 10.1103/PhysRevLett.121.151301.

[308] H.-Y. Schive et al. Understanding the Core-Halo Relation of Quantum Wave Dark Matter from 3D Simulations. *Phys. Rev. Lett.*, 113.26 (2014). DOI: 10.1103/PhysRevLett.113.261302.

[309] J. Veltmaat, J. C. Niemeyer, and B. Schwabe. Formation and structure of ultralight bosonic dark matter halos. *Phys. Rev. D*, 98.4 (2018). DOI: 10.1103/PhysRevD.98.043509.

[310] E. Braaten, A. Mohapatra, and H. Zhang. Dense Axion Stars. *Phys. Rev. Lett.*, 117.12 (2016). DOI: 10.1103/PhysRevLett.117.121801.

[311] L. Visinelli et al. Dilute and dense axion stars. *Phys. Lett. B*, 777 (2018). DOI: 10.1016/j.physletb.2017.12.010.

[312] P.-H. Chavanis. Phase transitions between dilute and dense axion stars. *Phys. Rev. D*, 98.2 (2018). DOI: 10.1103/PhysRevD.98.023009.

[313] S. U. Ji and S. J. Sin. Late time phase transition and the galactic halo as a bose liquid: 2. The Effect of visible matter. *Phys. Rev. D*, 50.6 (1994). DOI: 10.1103/PhysRevD.50.3655.

[314] E. Seidel and W.-M. Suen. Formation of solitonic stars through gravitational cooling. *Phys. Rev. Lett.*, 72.16 (1994). DOI: 10.1103/PhysRevLett.72.2516.

[315] F. S. Guzman and L. A. Urena-Lopez. Gravitational cooling of self-gravitating Bose-Condensates. *ApJ*, 645 (2006). DOI: 10.1086/504508.

[316] E. Seidel and W.-M. Suen. Dynamical evolution of boson stars: Perturbing the ground state. *Phys. Rev. D*, 42.2 (1990). DOI: 10.1103/PhysRevD.42.384.

[317] I. I. Tkachev. Coherent Scalar-Field Oscillations Forming Compact Astrophysical Object. *Soviet Astronomy Letters*, 12 (1986).

[318] D. J. E. Marsh and A.-R. Pop. Axion dark matter, solitons and the cusp–core problem. *MNRAS*, 451.3 (2015). DOI: 10.1093/mnras/stv1050.

[319] B. Schwabe, J. C. Niemeyer, and J. F. Engels. Simulations of solitonic core mergers in ultralight axion dark matter cosmologies. *Phys. Rev. D*, 94.4 (2016). DOI: 10.1103/PhysRevD.94.043513.

[320] P. Mocz et al. Galaxy formation with BECDM – I. Turbulence and relaxation of idealized haloes. *MNRAS*, 471.4 (2017). DOI: 10.1093/mnras/stx1887.

[321] C. Uhlemann, M. Kopp, and T. Haugg. Schrödinger method as N-body double and UV completion of dust. *Phys. Rev. D*, 90.2 (2014). DOI: 10.1103/PhysRevD.90.023517.

[322] S. Nazarenko. *Wave Turbulence.* Springer Berlin Heidelberg, 2011. DOI: 10.1007/978-3-642-15942-8_1.

[323] S. Dyachenko et al. Optical turbulence: weak turbulence, condensates and collapsing filaments in the nonlinear Schrödinger equation. *Physica D: Nonlinear Phenomena*, 57.1-2 (1992). DOI: 10.1016/0167-2789(92)90090-A.

[324] C. Connaughton et al. Condensation of Classical Nonlinear Waves. *Phys. Rev. Lett.*, 95.26 (2005). DOI: 10.1103/PhysRevLett.95.263901.

[325] G. Düring, A. Picozzi, and S. Rica. Breakdown of weak-turbulence and nonlinear wave condensation. *Physica D Nonlinear Phenomena*, 238.16 (2009). DOI: 10.1016/j.physd.2009.04.014.

[326] C. Sun et al. Observation of the kinetic condensation of classical waves. *Nature Physics*, 8.6 (2012). DOI: 10.1038/nphys2278.

[327] D. V. Semikoz and I. I. Tkachev. Condensation of bosons in kinetic regime. *Phys. Rev. D*, 55.2 (1997). DOI: 10.1103/PhysRevD.55.489.

[328] B. Bar-Or, J.-B. Fouvry, and S. Tremaine. Relaxation in a Fuzzy Dark Matter Halo. *ApJ*, 871.1 (2019). DOI: 10.3847/1538-4357/aaf28c.

[329] K. Takahashi. Distribution Functions in Classical and Quantum Mechanics. *Progress of Theoretical Physics Supplement*, 98 (1989). DOI: 10.1143/PTPS.98.109.

[330] N. Cartwright. A non-negative Wigner-type distribution. *Physica A: Statistical Mechanics and its Applications*, 83.1 (1976). DOI: https://doi.org/10.1016/0378-4371(76)90145-X.

[331] M. Mina, D. F. Mota, and H. A. Winther. SCALAR: an AMR code to simulate axion-like dark matter models. *A&A*, 641 (2020). DOI: 10.1051/0004-6361/201936272.

[332] T.-P. Woo. High Resolution Simulation on Structure Formation with Extremely Light Bosonic Dark Matter. *ApJ*, 697 (2009). DOI: 10.1088/0004-637X/697/1/850.

[333] P. Mocz et al. Schrödinger-Poisson–Vlasov-Poisson correspondence. *Phys. Rev. D*, 97.8 (2018). DOI: 10.1103/PhysRevD.97.083519.

[334] P. Mocz et al. First star-forming structures in fuzzy cosmic filaments. *Phys. Rev. Lett.*, 123.14 (2019). DOI: 10.1103/PhysRevLett.123.141301.

[335] X. Du et al. Tidal disruption of fuzzy dark matter subhalo cores. *Phys. Rev. D*, 97.6 (2018). DOI: 10.1103/PhysRevD.97.063507.

[336] F. Edwards et al. PyUltraLight: a pseudo-spectral solver for ultralight dark matter dynamics. *JCAP*, 2018.10 (2018). DOI: 10.1088/1475-7516/2018/10/027.

[337] S. May and V. Springel. Structure formation in large-volume cosmological simulations of fuzzy dark matter: impact of the non-linear dynamics. *MNRAS*, 506.2 (2021). DOI: 10.1093/mnras/stab1764.

[338] P. Mocz and S. Succi. Numerical solution of the nonlinear Schrödinger equation using smoothed-particle hydrodynamics. *Phys. Rev. E*, 91.5 (2015). DOI: 10.1103/PhysRevE.91.053304.

[339] J. Veltmaat and J. C. Niemeyer. Cosmological particle-in-cell simulations with ultralight axion dark matter. *Phys. Rev. D*, 94.12 (2016). DOI: 10.1103/PhysRevD.94.123523.

[340] M. Nori and M. Baldi. AX-GADGET: a new code for cosmological simulations of Fuzzy Dark Matter and Axion models. *MNRAS*, 478.3 (2018). DOI: 10.1093/mnras/sty1224.

[341] M. Nori et al. Lyman α forest and non-linear structure characterization in Fuzzy Dark Matter cosmologies. *MNRAS*, 482.3 (2019). DOI: 10.1093/mnras/sty2888.

[342] J. Zhang et al. The Importance of Quantum Pressure of Fuzzy Dark Matter on Lyman-Alpha Forest. *ApJ*, 863 (2018). DOI: 10.3847/1538-4357/aacf3f.

[343] P. F. Hopkins. A Stable Finite-Volume Method for Scalar-Field Dark Matter. *MNRAS*, 489.2 (2019). DOI: 10.1093/mnras/stz1922.

[344] J. Chen et al. New insights into the formation and growth of boson stars in dark matter halos. *Phys. Rev. D*, 104.8 (2021). DOI: 10.1103/PhysRevD.104.083022.

[345] M. Dowle, R. M. Mantel, and D. Barkley. Fast Simulations of Waves in Three-Dimensional Excitable Media. *International Journal of Bifurcation and Chaos*, 07 (1997).

[346] W. H. Press et al. *Numerical Recipes 3rd Edition: The Art of Scientific Computing*. Cambridge University Press, 2007.

[347] J. J. Monaghan. Smoothed particle hydrodynamics. *Reports on Progress in Physics*, 68.8 (2005). DOI: 10.1088/0034-4885/68/8/r01.

[348] R. E. Wyatt. *Quantum Dynamics with Trajectories: Introduction to Quantum Hydrodynamics*. Interdisciplinary Applied Mathematics. 2005. DOI: 10.1007/0-387-28145-2.

[349] A. Almgren et al. AMReX 21.07. Zenodo, 2021. DOI: 10.5281/zenodo.5055695.

[350] P. Tinyakov, I. Tkachev, and K. Zioutas. Tidal streams from axion miniclusters and direct axion searches. *JCAP*, 2016.1 (2016). DOI: 10.1088/1475-7516/2016/01/035.

[351] V. I. Dokuchaev, Y. N. Eroshenko, and I. I. Tkachev. Destruction of axion miniclusters in the Galaxy. *Soviet Journal of Experimental and Theoretical Physics*, 125.3 (2017). DOI: 10.1134/S1063776117080039.

[352] W. H. Press, B. S. Ryden, and D. N. Spergel. Dynamical Evolution of Domain Walls in an Expanding Universe. *ApJ*, 347 (1989). DOI: 10.1086/168151.

[353] J. N. Moore, E. P. S. Shellard, and C. J. A. P. Martins. Evolution of Abelian-Higgs string networks. *Phys. Rev. D*, 65.2 (2001). DOI: 10.1103/PhysRevD.65.023503.

[354] M. Buschmann et al. Dark matter from axion strings with adaptive mesh refinement. *Nature Communications*, 13 (2022). DOI: 10.1038/s41467-022-28669-y.

[355] E. W. Kolb and I. I. Tkachev. Nonlinear axion dynamics and the formation of cosmological pseudosolitons. *Phys. Rev. D*, 49.10 (1994). DOI: 10.1103/PhysRevD.49.5040.

[356] C. A. J. O'Hare and A. M. Green. Axion astronomy with microwave cavity experiments. *Phys. Rev. D*, 95.6 (2017). DOI: 10.1103/PhysRevD.95.063017.

[357] S. Knirck et al. Directional axion detection. *JCAP*, 2018.11 (2018). DOI: 10.1088/1475-7516/2018/11/051.

[358] I. I. Tkachev. Fast radio bursts and axion miniclusters. *JEPT Lett.*, 101.1 (2015). DOI: 10.1134/S0021364015010154.

[359] M. S. Pshirkov. May axion clusters be sources of fast radio bursts? *Int. J. Mod. Phys. D*, 26.7 (2017). DOI: 10.1142/S0218271817500687.

[360] B. J. Kavanagh et al. Stellar disruption of axion miniclusters in the Milky Way. *Phys. Rev. D*, 104.6 (2021). DOI: 10.1103/PhysRevD.104.063038.

[361] J. Enander, A. Pargner, and T. Schwetz. Axion minicluster power spectrum and mass function. *JCAP*, 2017.12 (2017). DOI: 10.1088/1475-7516/2017/12/038.

[362] M. Fairbairn et al. Structure formation and microlensing with axion miniclusters. *Phys. Rev. D*, 97.8 (2018). DOI: 10.1103/PhysRevD.97.083502.

[363] K. M. Zurek, C. J. Hogan, and T. R. Quinn. Astrophysical Effects of Scalar Dark Matter Miniclusters. *Phys. Rev. D*, 75.2 (2007). DOI: 10.1103/PhysRevD.75.043511.

[364] G. de Lucia et al. Substructures in cold dark matter haloes. *MNRAS*, 348.1 (2004). DOI: 10.1111/j.1365-2966.2004.07372.x.

[365] C. Power et al. The Inner structure of Lambda CDM halos. 1. A Numerical convergence study. *MNRAS*, 338.1 (2003). DOI: 10.1046/j.1365-8711.2003.05925.x.

[366] T. Zhang et al. The optimal gravitational softening length for cosmological N-body simulations. *MNRAS*, 487.1 (2019). DOI: 10.1093/mnras/stz1370.

[367] B. Diemer and A. V. Kravtsov. Dependence of the outer density profiles of halos on their mass accretion rate. *ApJ*, 789 (2014). DOI: 10.1088/0004-637X/789/1/1.

[368] M. Ricotti and A. Gould. A new probe of dark matter and high-energy universe using microlensing. *ApJ*, 707.2 (2009). DOI: 10.1088/0004-637x/707/2/979.

[369] M. Gosenca et al. 3D simulations with boosted primordial power spectra and ultracompact minihalos. *Phys. Rev. D*, 96.12 (2017). DOI: 10.1103/PhysRevD.96.123519.

[370] S. Dodelson. *Modern cosmology.* Academic Press, 2003. DOI: 10.1016/B978-0-12-219141-1.X5019-0.

[371] H. Xiao, I. Williams, and M. McQuinn. Simulations of axion minihalos. *Phys. Rev. D*, 104.2 (2021). DOI: 10.1103/PhysRevD.104.023515.

[372] T. Goerdt et al. The survival and disruption of cold dark matter microhaloes: implications for direct and indirect detection experiments. *MNRAS*, 375.1 (2007). DOI: 10.1111/j.1365-2966.2006.11281.x.

[373] A. M. Green and S. P. Goodwin. On mini-halo encounters with stars. *MNRAS*, 375.3 (2007). DOI: 10.1111/j.1365-2966.2007.11397.x.

[374] V. S. Berezinsky, V. I. Dokuchaev, and Y. N. Eroshenko. Formation and internal structure of superdense dark matter clumps and ultracompact minihaloes. *JCAP*, 2013.11 (2013). DOI: 10.1088/1475-7516/2013/11/059.

[375] G. Rybka et al. Direct detection searches for axion dark matter. *Physics of the Dark Universe*, 4 (2014). DOI: https://doi.org/10.1016/j.dark.2014.05.003.

[376] B. T. McAllister et al. The ORGAN Experiment: An axion haloscope above 15 GHz. *Phys. Dark Univ.*, 18 (2017). DOI: 10.1016/j.dark.2017.09.010.

[377] A. Katz et al. Femtolensing by Dark Matter Revisited. *JCAP*, 2018.12 (2018). DOI: 10.1088/1475-7516/2018/12/005.

[378] L. Dai and J. Miralda-Escudé. Gravitational Lensing Signatures of Axion Dark Matter Minihalos in Highly Magnified Stars. *AJ*, 159.2 (2020). DOI: 10.3847/1538-3881/ab5e83.

[379] V. S. H. Lee et al. Probing Small-Scale Power Spectra with Pulsar Timing Arrays. *JHEP*, 2021.06 (2021). DOI: 10.1007/JHEP06(2021)028.

[380] P. E. Dewdney et al. The Square Kilometre Array. *IEEE Proceedings*, 97.8 (2009). DOI: 10.1109/JPROC.2009.2021005.

[381] M. S. Pshirkov and S. B. Popov. Conversion of Dark matter axions to photons in magnetospheres of neutron stars. *J. Exp. Theor. Phys.*, 108 (2009). DOI: 10.1134/S1063776109030030.

[382] J. W. Foster et al. Green Bank and Effelsberg Radio Telescope Searches for Axion Dark Matter Conversion in Neutron Star Magnetospheres. *Phys. Rev. Lett.*, 125.17 (2020). DOI: 10.1103/PhysRevLett.125.171301.

[383] T. D. P. Edwards et al. Transient Radio Signatures from Neutron Star Encounters with QCD Axion Miniclusters. *Phys. Rev. Lett.*, 127.13 (2021). DOI: 10.1103/PhysRevLett.127.131103.

[384] A. Iwazaki. Axion stars and fast radio bursts. *Phys. Rev. D*, 91.2 (2015). DOI: 10.1103/PhysRevD.91.023008.

[385] S. Raby. Axion star collisions with Neutron stars and Fast Radio Bursts. *Phys. Rev. D*, 94.10 (2016). DOI: 10.1103/PhysRevD.94.103004.

[386] T. Dietrich et al. Neutron star–axion star collisions in the light of multimessenger astronomy. *MNRAS*, 483.1 (2019). DOI: 10.1093/mnras/sty3158.

[387] D. Polarski and A. Starobinsky. Spectra of perturbations produced by double inflation with an intermediate matter-dominated stage. *Nuclear Physics B*, 385.3 (1992). DOI: https://doi.org/10.1016/0550-3213(92)90062-G.

[388] J. Wang and S. D. White. Discreteness effects in simulations of Hot/Warm dark matter. *MNRAS*, 380.1 (2007). DOI: 10.1111/j.1365-2966.2007.12053.x.

[389] M. R. Lovell et al. The properties of warm dark matter haloes. *MNRAS*, 439.1 (2014). DOI: 10.1093/mnras/stt2431.

[390] A. Schneider, R. E. Smith, and D. Reed. Halo mass function and the free streaming scale. *MNRAS*, 433.2 (2013). DOI: 10.1093/mnras/stt829.

[391] A. Schneider. Structure formation with suppressed small-scale perturbations. *MNRAS*, 451.3 (2015). DOI: 10.1093/mnras/stv1169.

[392] T. Abel, O. Hahn, and R. Kaehler. Tracing the dark matter sheet in phase space. *MNRAS*, 427.1 (2012). DOI: 10.1111/j.1365-2966.2012.21754.x.

[393] R. E. Angulo, O. Hahn, and T. Abel. The warm dark matter halo mass function below the cut-off scale. *MNRAS*, 434.4 (2013). DOI: 10.1093/mnras/stt1246.

[394] B. Allgood et al. The shape of dark matter halos: dependence on mass, redshift, radius, and formation. *MNRAS*, 367.4 (2006). DOI: 10.1111/j.1365-2966.2006.10094.x.

[395] M. Zemp et al. On Determining the Shape of Matter Distributions. *ApJS*, 197.2 (2011). DOI: 10.1088/0067-0049/197/2/30.

[396] A. J. Benson et al. Dark matter halo merger histories beyond cold dark matter – I. Methods and application to warm dark matter. *MNRAS*, 428.2 (2012). DOI: 10.1093/mnras/sts159.

[397] M. Kulkarni and J. P. Ostriker. What is the halo mass function in a fuzzy dark matter cosmology? *MNRAS*, 510.1 (2021). DOI: 10.1093/mnras/stab3520.

[398] A. Klypin et al. Density distribution of the cosmological matter field. *MNRAS*, 481.4 (2018). DOI: 10.1093/mnras/sty2613.

[399] S. L. Liebling and C. Palenzuela. Dynamical Boson Stars. *Living Rev. Rel.*, 15 (2012). DOI: 10.12942/lrr-2012-6.

[400] T. Helfer et al. Black hole formation from axion stars. *JCAP*, 2017.3 (2017). DOI: 10.1088/1475-7516/2017/03/055.

[401] D. Hooper, G. Krnjaic, and S. D. McDermott. Dark Radiation and Superheavy Dark Matter from Black Hole Domination. *JHEP*, 2019.08 (2019). DOI: 10.1007/JHEP08(2019)001.

[402] S. W. Hawking. Particle Creation by Black Holes. *Commun. Math. Phys.*, 43 (1975). DOI: 10.1007/BF02345020.

[403] T. Fujita et al. Baryon asymmetry, dark matter, and density perturbation from primordial black holes. *Phys. Rev. D*, 89.10 (2014). DOI: 10.1103/PhysRevD.89.103501.

[404] O. Lennon et al. Black hole genesis of dark matter. *JCAP*, 2018.04 (2018). DOI: 10.1088/1475-7516/2018/04/009.

[405] R. Allahverdi, J. Dent, and J. Osinski. Nonthermal production of dark matter from primordial black holes. *Phys. Rev. D*, 97.5 (2018). DOI: 10.1103/PhysRevD.97.055013.

[406] L. Morrison, S. Profumo, and Y. Yu. Melanopogenesis: dark matter of (almost) any mass and baryonic matter from the evaporation of primordial black holes weighing a ton (or less). *JCAP*, 2019.05 (2019). DOI: 10.1088/1475-7516/2019/05/005.

[407] I. Masina. Dark matter and dark radiation from evaporating primordial black holes. *Eur. Phys. J. Plus*, 135.7 (2020). DOI: 10.1140/epjp/s13360-020-00564-9.

[408] A. Cheek et al. Primordial black hole evaporation and dark matter production. I. Solely Hawking radiation. *Phys. Rev. D*, 105.1 (2022). DOI: 10.1103/PhysRevD.105.015022.

[409] E. de Jong, J. C. Aurrekoetxea, and E. A. Lim. Primordial black hole formation with full numerical relativity. *JCAP*, 2022.3 (2022). DOI: 10.1088/1475-7516/2022/03/029.

[410] E. Cotner, A. Kusenko, and V. Takhistov. Primordial Black Holes from Inflaton Fragmentation into Oscillons. *Phys. Rev. D*, 98.8 (2018). DOI: 10.1103/PhysRevD.98.083513.

[411] E. Cotner et al. Analytic Description of Primordial Black Hole Formation from Scalar Field Fragmentation. *JCAP*, 2019.10 (2019). DOI: 10.1088/1475-7516/2019/10/077.

[412] M. P. Hertzberg and E. D. Schiappacasse. Dark Matter Axion Clump Resonance of Photons. *JCAP*, 2018.11 (2018). DOI: 10.1088/1475-7516/2018/11/004.

[413] D. G. Levkov, A. G. Panin, and I. I. Tkachev. Radio-emission of axion stars. *Phys. Rev. D*, 102.2 (2020). DOI: 10.1103/PhysRevD.102.023501.

[414] B. Eggemeier et al. Stochastic Gravitational Waves from Post-inflationary Structure Formation. *ArXiv e-prints* (2022). arXiv: 2212.00425.

[415] A. Sesana et al. Unveiling the gravitational universe at μ-Hz frequencies. *Experimental Astronomy*, 51.3 (2021). DOI: 10.1007/s10686-021-09709-9.

[416] S. Hild et al. Sensitivity Studies for Third-Generation Gravitational Wave Observatories. *Class. Quant. Grav.*, 28 (2011). DOI: 10.1088/0264-9381/28/9/094013.

[417] P. Campeti et al. Measuring the spectrum of primordial gravitational waves with CMB, PTA and laser interferometers. *JCAP*, 2021.1 (2021). DOI: 10.1088/1475-7516/2021/01/012.

Acknowledgements

The last words of my thesis are dedicated to all the people who supported my journey for the past thousand and thirty-eight days. First of all, I thank my supervisor Jens Niemeyer for the freedom he gave me to conduct independent research and for his helpful suggestions when I ran into problems. In particular, I am thankful for his continuous support and guidance.

I want to thank Doddy Marsh for being the second reviewer of this thesis and for his advice during the process of my doctoral studies. The latter also applies to Steffen Schumann who accompanied me since my time as an undergraduate student. I also thank my collaborators Richard Easther, Bodo Schwabe, Javier Redondo, Klaus Dolag and Alejandro Vaquero for their contributions to the publications presented in this thesis and for numerous insightful discussions.

I am grateful to Sebastian Hoof, David Ellis, Mona Dentler, Bodo and my brother Alexander for reading parts of my thesis and giving me valuable feedback. Another big thank you to my long-time office mate Bodo for all the fruitful and enlightening discussions during our coffee breaks. Likewise, I thank Sebastian for our always joyful coffee meetings and the “friends of the institute” for their coffee visits.

Finally, I thank my parents, my brothers, my friends and, especially, my girlfriend Felicitas for their incredible support and for cheering me up in dark times. This work would have been impossible without you.